Thèse n° 9306

Turbulent transport regimes in the tokamak boundary

Présentée le 21 janvier 2022

Faculté des sciences de base
SPC - Théorie
Programme doctoral en physique

pour l'obtention du grade de Docteur ès Sciences

par

Maurizio GIACOMIN

Acceptée sur proposition du jury

Prof. A. Pasquarello, président du jury
Prof. P. Ricci, directeur de thèse
Prof. H. Zohm, rapporteur
Prof. N. Loureiro, rapporteur
Prof. C. Theiler, rapporteur

École
polytechnique
fédérale
de Lausanne

2022

Acknowledgements

This thesis is the result of a journey lasted four years at the Swiss Plasma Center (SPC), where I had the opportunity to meet excellent scientists, who helped me to grow as a person and as a physicist. In particular, I would like to thank my thesis advisor Prof. Paolo Ricci. This thesis would not have been possible without his continuous guidance and support, even during the lockdown imposed by the spreading of COVID-19 and the consequent closure of EPFL. I am extremely grateful for his constant availability and advice as well as for the many discussions we had during these four years.

I would also like to thank the people with whom I collaborated during these four years, Jose Boedo, Antonio Coelho, Thomas Eich, Gilles Fourstey, Davide Galassi, Jan Horacek, Emmanuel Lanti, Joaquim Loizu, Davide Mancini, Alessandro Pau, Holger Reimerdes, Nicolas Richart, Olivier Sauter, Christian Theiler, Cedric Tsui and Nicola Varini. The collaboration with all of them was extremely pleasant and fruitful, resulting in a number of publications.

I am very thankful to the people of the Edge Theory group, in particular to Baptiste Frei and Rogerio Jorge, with whom I shared the office and had very pleasant conversations not only about plasma physics, Carrie Beadle and André Coroado, with whom I discussed many times about GBS simulations and enjoyed my time both in Switzerland and abroad, and Paola Paruta, who helped me a lot with GBS when I arrived at SPC.

During these four years, I had the opportunity to work with many master students who I would like to thank for their work. In particular, I am very grateful to Adriano Stagni and Louis Stenger for their important contribution to this thesis.

I would like to thank all my fellow colleagues at SPC for making this a very nice and stimulating place where to work.

A special thank to my family, always present to support, motivate and advise me, especially during difficult times.

Finally, I would like to thank Alessandra Ivaldi for supporting and advising me as well as bearing with me. She motivated me when I needed it most, listening to my constant complaints, always finding the positive aspect of everything and pushing me to give my best.

Abstract

The overall performance of a tokamak strongly depends on phenomena that take place in a thin region between the main plasma and the vessel wall, which is denoted as tokamak boundary. In fact, the formation of transport barriers in this region can significantly improve plasma confinement and, therefore, the tokamak fusion performance. In addition, the tokamak boundary determines the peak heat flux to the wall, an essential quantity for the design and the operation of fusion power plants, as well as the level of impurities in the core, the removal of fusion ash and the dynamics of neutral particles.

The dynamics in the plasma boundary is strongly nonlinear and characterized by a wide range of length and time scales as well as by a complex magnetic field geometry that may feature one or more nulls of the poloidal magnetic field. Large-scale, three-dimensional turbulence simulations are therefore often required to disentangle the complex physical mechanisms that govern this region.

The thesis is focused on the analysis of the different turbulent transport regimes present in the plasma boundary as they appear from three-dimensional, flux-driven, global, two-fluid turbulence simulations carried out by using the GBS code, which is significantly extended here to allow the self-consistent simulation of the plasma dynamics coupled to a kinetic single-species neutral model in arbitrarily complex magnetic geometries. Considering single-null magnetic configurations, three turbulent transport regimes are identified: (i) a regime of suppressed turbulent transport at low values of collisionality and large values of heat source, (ii) a regime of developed turbulent transport at intermediate values of collisionality and heat source, and (iii) a regime of very large turbulent transport at high value of collisionality and density, which can be associated to the crossing of the density limit.

By leveraging the results of GBS simulations, theory-based scaling laws of the pressure and density decay lengths in the near and far scrape-off layer are derived in the developed transport regime from a balance among heat source, turbulent transport across the separatrix and parallel losses at the vessel wall. The theoretical scaling of the pressure decay length in the near scrape-off layer is successfully validated against a multi-machine database of SOL width measurements at the outer target.

By carefully analysing the transition to the regime of large turbulent transport, we show that the density limit can be explained by an enhancement of turbulent transport at the tokamak boundary when the density increases. This analysis leads to a theory-based scaling law of the maximum edge density achievable in tokamaks, which is in better agreement with a multi-machine database than the widely used Greenwald empirical scaling, thus significantly improving our understanding and predictive capability of the density limit, with important implications for the design and the operation of future fusion power plants.

The thesis concludes by presenting the first turbulent simulations carried out in various snowflake magnetic configurations, which are used to investigate the effect of turbulence and equilibrium flow on the heat flux distribution among the different strike points. In particular, the presence of an equilibrium $\mathbf{E} \times \mathbf{B}$ convective cell around the second order null is found to play an important role for the activation of the unconnected strike points, especially in the case of the exact snowflake.

Keywords: plasma physics, controlled fusion, tokamak boundary, plasma turbulence, turbulent transport, fluid simulations, density limit, snowflake

Résumé

Les performances globales d'un tokamak dépendent fortement des phénomènes qui se produisent dans une région entre le plasma au centre et la paroi de la machine, appelée le bord du plasma. En effet, la formation de barrières de transport dans cette région permet d'améliorer significativement le confinement du plasma et donc les performances de fusion. De plus, le bord du tokamak controle le pic de chaleur sur la paroi, une quantité essentielle pour la conception et le fonctionnement des centrales à fusion, ainsi que le niveau d'impuretés au noyau du tokamak, l'élimination des résidus de fusion et la dynamique des particules neutres.

La dynamique dans le bord du plasma est fortement non linéaire et caractérisée par une large gamme d'échelles de longueur et de temps ainsi que par une géométrie complexe du champ magnétique qui peut avoir un ou plusieurs zéros du champ magnétique poloïdal. Les simulations tridimensionnelles de turbulence du plasma sont donc nécessaires pour étudier les mécanismes physiques qui régissent la dynamique du plasma dans cette région.

Cette thèse analyse différents régimes de transport turbulent présents au bord du plasma tels qu'ils apparaissent dans des simulations tridimensionnelles de turbulences réalisées en utilisant le code GBS. Ce code est considérablement étendu pour permettre la simulation de manière cohérente de la dynamique du plasma, couplée à un modèle cinétique des particules neutres dans des géométries magnétiques complexess.

En considérant une géométrie "single-null", trois régimes de transport turbulent sont identifiés : (i) un régime à basse collisionnalité et à forte source de chaleur où le transport turbulent est réduit, (ii) un régime à des valeurs intermédiaires de collisionnalité où le transport turbulent est bien développé, et (iii) un régime de très grand transport turbulent à haute collisionnalité et densité, qui peut être associé au dépassement de la limite de densité.

En utilisant les résultats des simulations de GBS, on dérive des lois théoriques pour calculer les longueurs de décroissance de la pression et de la densité dans le "scrape-off layer". Ces lois sont dérivées dans le régime de turbulences développées à partir d'un équilibre entre la source de chaleur, le transport turbulent à travers la séparatrice et les pertes parallèles de chaleur à la paroi de la machine. Les prédictions théoriques de la longueur de décroissance de la pression dans le "scrape-off layer" sont comparées aux données expérimentales provenant de différentes machines, montrant un bon accord entre

théorie et expériences.
En analysant la transition vers le régime de grand transport turbulent, on montre que la limite de densité peut être considérée comme le résultat d'une augmentation du transport turbulent au bord du tokamak lorsque la densité augmente. Cette analyse conduit à une loi théorique pour la densité maximale qui peut être atteinte dans les machines à fusion. Cette loi est capable de reproduire les données expérimentales de différentes machines d'une meilleure manière que la loi empirique de Greenwald, qui est souvent utilisée. La théorie proposée dans cette thèse améliore remarquablement notre compréhension et notre capacité de prédiction de la limite de densité, et conduit à des importantes implications pour la conception et l'exploitation des futures centrales à fusion.
La thèse se termine par la présentation des premières simulations turbulentes réalisées dans diverses configurations magnétiques de "snowflake", qui sont utilisées pour étudier l'effet de la turbulence et du flux d'équilibre sur la distribution du flux de chaleur entre les différents points de contact. En particulier, la présence d'une cellule convective d'équilibre autour du zéro d'ordre deux du champ magnétique poloïdal s'avère jouer un rôle important pour l'activation des points d'impact non connectés, notamment dans le cas du "snowflake" exact.

Mots clefs : physique des plasmas, fusion contrôlée, bord du tokamak, turbulence de plasma, transports turbulents, simulations de fluides, limite de densité, snowflake.

Contents

Acknowledgements **i**

Abstract (English/Français) **iii**

1 Introduction **1**

1.1 Thermonuclear fusion 2
1.2 The tokamak device 5
1.3 The plasma boundary 7
1.4 Scope and outline of the thesis 8

2 The GBS code for plasma boundary turbulence simulations **11**

2.1 Introduction 11
2.2 The neutral model 13
2.3 The plasma model 14
  2.3.1 Braginskii equations 15
  2.3.2 Drift-reduced Braginskii equations 19
2.4 Implementation of the physical model in GBS 24
  2.4.1 The GBS plasma model 24
  2.4.2 The GBS neutral model 28
  2.4.3 Differential operators 31
  2.4.4 Boundary and initial conditions 35
2.5 Numerical implementation and optimization of the GBS model 36
  2.5.1 Spatial discretization of the plasma equations 37
  2.5.2 Implementation and optimization of the Poisson and Ampère equations 39
  2.5.3 Implementation and optimization of neutral model in diverted geometry 40
2.6 Verification of GBS implementation 43
  2.6.1 Verification of the plasma model 43
  2.6.2 Verification of the neutral model 45
2.7 Parallelisation scalability tests 49
2.8 Convergence properties 52
2.9 First simulation results in an experimentally-relevant scenario 54

2.10 Conclusions 58

3 Turbulent transport regimes in the tokamak edge 59

3.1 Introduction 59
3.2 Overview of simulation results 61
3.3 Mechanisms regulating the equilibrium electrostatic potential 66
3.4 Developed transport regime 70
3.5 Suppressed transport regime 74
3.6 Degraded confinement regime 77
3.7 Heat source threshold to access the suppressed transport regime 79
3.8 Conclusions 83

4 Theory-based scaling of L-mode near and far SOL decay lengths 85

4.1 Introduction 85
4.2 Simulation results: turbulence in the near and far SOL 88
4.3 Theoretical derivation of the near and far SOL decay lengths 91
  4.3.1 Near SOL decay length 91
  4.3.2 Far SOL decay length 94
4.4 Validation of the theoretical scaling laws 100
  4.4.1 Near SOL validation 100
  4.4.2 Far SOL validation 103
4.5 Conclusions 104

5 Electromagnetic phase space of edge turbulence and density limit 107

5.1 Introduction 107
5.2 Overview of the simulation results 111
5.3 Electromagnetic phase space of edge turbulence 114
5.4 Theory-based scaling of the density limit 118
  5.4.1 Pressure decay length in the conduction regime and theory-based scaling for the density limit 119
  5.4.2 Comparison with experimental data 121
5.5 Conclusions 123

6 Turbulence and flows in snowflake magnetic configurations 125

6.1 Introduction 125
6.2 The snowflake magnetic equilibrium 127
6.3 Heat flux distribution at the target plates 129
6.4 The role of turbulence in the heat flux distribution 133
6.5 Conclusions 136

7 Conclusions and outlook 137

Bibliography 141

Curriculum Vitae **163**

1 Introduction

The continuous increase of the population and the fast economical growth of developing countries is leading to a dramatic rise of the energy demand, which is expected to double by 2100. Nowadays, more than 80% of the world energy production is based on fossil fuels such as oil, gas, or coal (see Fig. 1.1). The decrease of the available resources is expected to strongly increase the price of energy, enlarging the gap between developed and developing countries. In addition, the combustion of fossil fuels produces greenhouse gasses that contribute to global warming and climate changes. For example, the global emission of CO_2 doubled in the period 1975-2017 (see Fig. 1.2) and is expected to triple by 2040 [36]. There is an urgent need to develop sustainable energy sources.

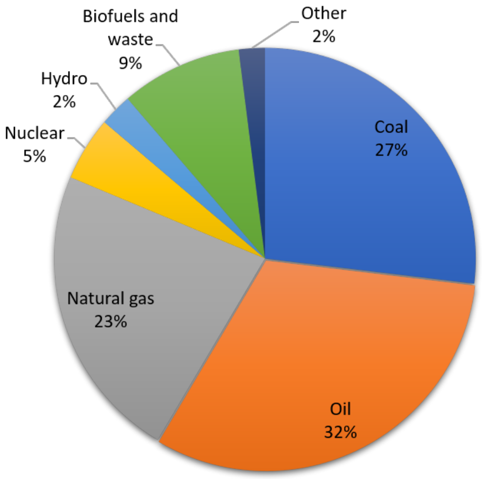

Figure 1.1 – World total energy supply by source in 2018. More than 80% of the total energy is provided by fossil fuels. Source: the International Energy Agency.

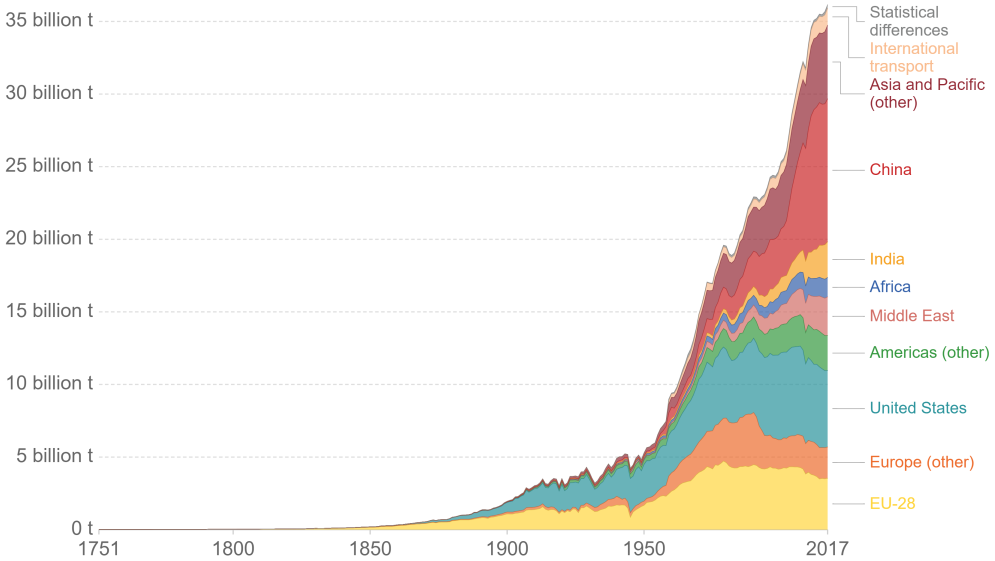

Figure 1.2 – Global annual emission of CO_2 from 1751 to 2017. The global emission of CO_2 doubled in the period 1975-2017. Source: Carbon Dioxide Information Analysis Center (CDIAC).

1.1 Thermonuclear fusion

One of the few alternatives to fossil fuels is provided by nuclear fusion, the energy source of the stars. Thanks to nuclear fusion, two light nuclei fuse together generating heavier elements and releasing energy. The energy released during a fusion reaction, E_f, is proportional to the difference between the total mass of reactants, m_r, and the total mass of products, m_p, i.e. $E_f = c^2(m_r - m_p)$.

Only few nuclear reactions are of interest for energy production on Earth. Among them, the nuclear reaction of deuterium and tritium,

$$ {}^2_1\mathrm{D} + {}^3_1\mathrm{T} \longrightarrow {}^4_2\mathrm{He} + {}^1_0\mathrm{n}\,, \tag{1.1} $$

is particularly appealing for the first generation of fusion power plants [65]. The net energy released by this reaction is 17.6 MeV, which goes into kinetic energy of the α-particle (3.5 MeV) and neutron (14.1 MeV). In fact, the energy density associated with the reaction in Eq. (1.1) is very high and one gram of fuel releases approximately 350 GJ of energy. The reaction in Eq. (1.1) does not emit CO_2. In addition, deuterium can be extracted from sea water and it is practically inexhaustible. On the other hand, being tritium unstable, it is not generally available on Earth. However, it can be bred inside the power plant from the neutrons produced by the nuclear reaction itself and lithium, which is an abundant element in the Earth's crust,

$$ {}^{1}_{0}\mathrm{n} + {}^{6}_{3}\mathrm{Li} \longrightarrow {}^{3}_{1}\mathrm{T} + {}^{4}_{2}\mathrm{He}\,, \tag{1.2} $$

$$ {}^{1}_{0}\mathrm{n} + {}^{7}_{3}\mathrm{Li} \longrightarrow {}^{3}_{1}\mathrm{T} + {}^{4}_{2}\mathrm{He} + {}^{1}_{0}\mathrm{n}\,. \tag{1.3} $$

Since Eq. (1.1) is not based on a chain process, it is intrinsically safe and it can be interrupted in case of emergency. In addition, Eq. (1.1) and, in general, fusion reactions are season, weather and location independent, and for this reason they are in principle accessible by all the countries in the world. On the other hand, fusion poses extreme scientific and technological challenges.

In order to fuse together, two nuclei have to overtake the Coulomb repulsion acting among the involved protons. This repulsive barrier can be overcome only at high temperatures. In particular, D-T reactions require a temperature higher than 1 keV in order to occur. At this temperature, the fuel of the nuclear reactor is fully ionized and in the plasma state. This is a globally neutral gas made of electrically charged particles that interact among each other through long-range electromagnetic interaction. The minimum condition for a fusion power plant to produce energy, known as break-even, is met when the fusion power (power due to α-particles and neutrons) is higher than the input power. Due to the weak interaction between neutrons and plasma, only α-particles contribute to heat fusion plasma. Therefore, self-sustaining fusion reactions are achieved when the power lost from a fusion reactor is compensated by the heating power from the α-particles. This requirement, known as ignition, is summarized by the Lawson's criterion that, for ion temperature T_i in the range of 10-20 keV, can be written as [115, 238]

$$ n_e T_i \tau_E \gtrsim 5 \cdot 10^{21}\mathrm{s\ m^{-3} keV}\,, \tag{1.4} $$

where n_e is the plasma density and τ_E is the energy confinement time, defined as the energy content of the plasma W divided by the power losses P_{loss}, i.e. $\tau_E = W/P_{\mathrm{loss}}$. Fusion power plants will operate between break-even and ignition.

In order to satisfy the inequality in Eq. (1.4), two main approaches are currently pursued. The first approach is based on high density plasma, $n \simeq 10^{30}$ m^{-3}, and low energy confinement time, $\tau_E \simeq 10^{-10}$ s. High density pellets of a deuterium and tritium mixture are hit by several high-power lasers that ablate the pellet surface. As the surface is ablated, the pellet core is compressed towards its center because of the rocket effect, leading to a strong and fast increase of core temperature and density. The largest inertial confinement fusion experiment currently operational is the National Ignition Facility in the USA [146]. The second approach is based on much longer energy confinement times, $\tau_E \simeq 1$ s, and smaller plasma densities, $n \simeq 10^{20}$ m^{-3}. For this purpose, the Lorentz force is used to confine the charged particles inside the reactor. Since the Lorentz force acts only in the direction perpendicular to the magnetic field and because of the drifts charged particles are subject to in a magnetic field [238], confinement is only possible

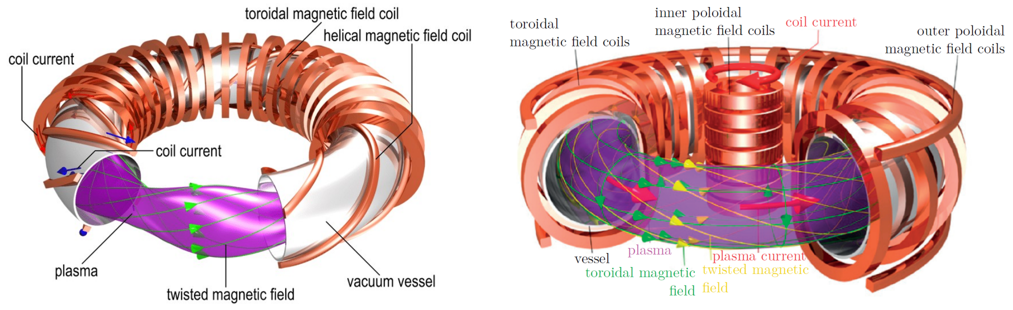
toroidal magnetic field coil
helical magnetic field coil
coil current
coil current
plasma
twisted magnetic field
vacuum vessel
toroidal
magnetic field coils
inner poloidal
magnetic field coils
coil current
outer poloidal
magnetic field coils
vessel
plasma
plasma current
toroidal magnetic
field
twisted magnetic
field

(a) (b)

Figure 1.3 – Schematic representation of a stellarator (a) and tokamak (b). In (a) the twisted magnetic field lines (green lines) are generated by a set of coils of very complex design and production. In (b) the twisted magnetic field lines are obtained by overlapping a toroidal magnetic field (green lines), produced by toroidal field coils, and a poloidal magnetic field, produced by the plasma current (red arrow) induced by the central solenoid. Image source: Eurofusion website.

when the magnetic field lines wind around toroidal surfaces [65]. Depending on how the magnetic field is obtained, we distinguish between stellarators and tokamaks (see Fig. 1.3). In stellarators, the magnetic field is entirely produced by a set of external coils that, in general, have a complex non-planar shape. The two largest stellarators in the world are Wendelstein 7-X [105] in Germany and the Large Helical Device (LHD) [99] in Japan. In tokamaks, the toroidal magnetic field is generated by a set of external toroidal coils and a current driven inside the plasma by means of a central solenoid. Although results from stellarators are encouraging [217], the tokamak is currently the most advanced device for magnetic confinement fusion. The largest tokamak in the world is JET in the UK, which reached the highest fusion energy gain $Q \simeq 0.67$, defined as the ratio of the fusion power to the injected power, with a triple product of $n_e T_i \tau_E \simeq 8 \cdot 10^{20}$ s m^{-3} keV [100].

The international tokamak experiment ITER (The Way) is being built to demonstrate the feasibility of energy from fusion [149]. ITER is among the most ambitious scientific projects in the world. The project started in 1986 as an agreement between European Union (Euratom), Japan, the Soviet Union and the USA. China, Korea and India joined it afterward. The ITER tokamak is currently under construction in Caradache, France, and the first plasma is foreseen by the end of 2025. ITER goal is to show the possibility to produce 500 MW of fusion power with 50 MW of input power ($Q = 10$) while testing steady-state production, by achieving 1 hour discharge with $Q = 5$ [8]. A schematic view of ITER is shown in Fig. 1.4. Although a fundamental step towards fusion energy production, ITER will not be connected to the power grid. The design of future demonstrative fusion power plants connected to the grid, such as DEMO, is ongoing [58, 252].

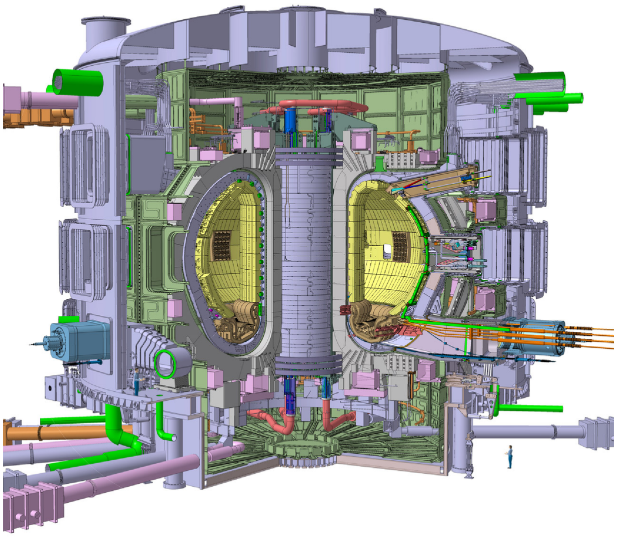

Figure 1.4 – Schematic view of ITER device. Image source: official ITER website.

1.2 The tokamak device

A charged particle in a uniform and constant magnetic field is subject to the Lorentz force. This force constraints the particle motion in the directions orthogonal to a magnetic field line, while the particle moves freely along it. However, because of particle drifts, non-twisted circular magnetic field lines (in practice a tokamak with only toroidal magnetic field) are not sufficient to confine a charged particle [238]. Both toroidal and poloidal magnetic fields are needed. In tokamaks, the toroidal magnetic field is generated by a set of planar toroidal coils, while the poloidal magnetic field is produced by driving a toroidal current in the plasma (see Fig. 1.3 (b)). This current is driven through a central solenoid that induces a loop voltage inside the plasma. Thanks to the ohmic effect, the plasma current is also used to heat up the plasma to a few keV. Since these temperatures are not sufficiently high to start fusion reactions, other external heating systems are used to further increase the temperature [238]. Even if the confinement of a single charged particle is guaranteed by twisted magnetic field lines, the collective behavior of the plasma gives rise to transport across the magnetic surfaces. For instance, this transport is due to Coulomb collisions among charged particles. Even more important, the presence of curvature of magnetic field lines and pressure gradients leads to the onset of plasma instability and turbulence, which cause a much larger radial transport, known as anomalous transport [232].

The plasma volume in a tokamak can be divided in three regions usually denoted as core, edge and scrape-off layer (SOL), as shown in Fig. 1.5. The core is characterized by magnetic field lines that wrap around nested flux surfaces. In the hot and well confined core plasma (~ 10 keV), fusion reactions take place. In the core, the density and

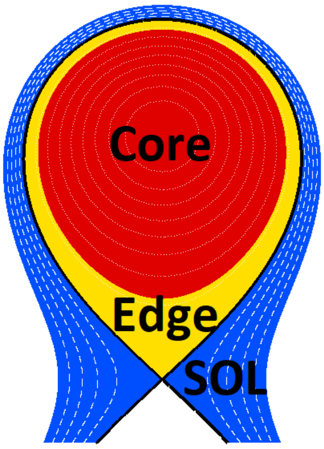

Figure 1.5 – Schematic representation of core (red), edge (yellow), and SOL (blue) on a poloidal plane. The black solid line represents the separatrix of a X-point diverted configuration.

temperature fluctuations are usually very small compared to the equilibrium quantities ($\sim 1\%$).

The SOL is the outer region of the plasma and is characterized by magnetic field lines that intersect the wall. Particles and heat from the confined region are exhausted through the SOL to the vessel wall. To avoid material damage, the plasma in the SOL must be much colder (~ 10 eV) than in the core. The magnetic field lines in the SOL are usually shaped by means of external coils, usually leading to one or more X-points where the poloidal magnetic field vanishes (see Fig. 1.5). This magnetic field configuration directs the plasma flow and it allows most of the heat flux to be exhausted through the target plates, which are complex components able to withstand large heat fluxes (up to 10 MW/m^2). Moreover, the SOL is also characterized by large amplitude density and temperature fluctuations, which are comparable to the equilibrium quantities.

The edge is the thin region between the core and SOL. The edge magnetic field lines also lie on nested flux surfaces. Since the edge connects the hot plasma in the core and the relatively cold plasma in the SOL, it is characterized by very steep pressure gradients, which constitute a source of free energy for plasma instability and turbulence. Although this region has a small radial extension if compared to the core, it plays an essential role in determining the overall performance of a fusion reactor. In fact, a steep pressure gradient in the edge allows for high pressure in the core and therefore a larger fusion power, being this proportional to the square of plasma pressure. The magnetic surface that separates the edge and SOL is denoted as the last closed flux surface (LCFS) or separatrix.

1.3 The plasma boundary

The plasma boundary usually denotes the plasma region that includes the edge and the SOL. Understanding the phenomena taking place in this region is a fundamental step towards the realization of fusion energy. In fact, the plasma dynamics in the boundary controls the overall performance of a fusion reactor, sets the boundary conditions for the core, controls the plasma refueling, heat exhaust and impurity dynamics and regulates the plasma-wall interaction.

The heat exhaust is one of the crucial issue in the design and operation of future fusion power plants. In fact, a large fraction of the heat produced by fusion reactions in the plasma core might be exhausted over a region few millimeters thick, leading to heat fluxes at the limit of material survival [135]. For this reason, the heat flux in the divertor region must be strongly mitigated by inducing radiation before the plasma reaches the target plates. In future fusion power plants, the magnetic geometry designed for ITER may not be sufficient to guarantee that the peak of heat flux remains below the technological limit imposed by the materials and alternative divertor configurations are under investigation by the fusion community [253].

Besides regulating the heat exhaust, phenomena occurring in the tokamak boundary can strongly affect plasma and energy confinement, with important consequence on the overall performance of a magnetic fusion device. In fact, the plasma dynamics in the tokamak boundary is responsible of the L-H transition, which is a transition from a low (L) to high (H) confinement regime [231]. This transition results into a very steep pressure gradient at the plasma edge and an increase of the plasma pressure in the core by, approximately, a factor of two. Experimental observations [51, 61, 79, 92, 112, 197, 226] have also linked the physics of the tokamak boundary to the density limit [79, 80], i.e. the maximum density that can be achieved in a tokamak before causing a plasma disruption.

The dynamics in the plasma boundary is strongly nonlinear and characterized by a wide range of length and time scales, from the ion Larmor radius ($\rho_i \sim 0.3$ mm at $T_e = 10$ eV and $B = 1$ T) to the machine size ($a \sim 1$ m), and from the ion gyro-motion ($\sim 10^{-9}$ s) to the energy confinement time (~ 1 s). In addition, large amplitude turbulent structures do not allow for decoupling between fluctuating and background quantities. Wide range of scales, large amplitude fluctuations, and a non-trivial magnetic geometry make the plasma boundary extremely challenging to model and simulate.

In order to approach the complexity of the plasma boundary, gyrokinetic and fluid models are used. Gyrokinetic models have been originally developed for the simulation of the tokamak core where the collisionality is very low and where unstable modes develop at the ion and electron gyro-radius scales with small amplitude fluctuations. On the other hand, fluid models are usually applied in the SOL, taking advantage of the higher plasma collisionality. The edge region, the border between core and SOL, is characterized by intermediate values of plasma collisionality. Simulating separately core, edge and SOL limits the possibilities to advance the understanding of the plasma dynamics in the plasma boundary since their dynamics are strongly coupled [60, 44, 81]. For this reason, significant effort was recently carried out in order to extend gyrokinetic models towards the edge and the SOL [64, 84, 166] and simulate the plasma boundary by means of gyrokinetic codes, such as COGENT [45], ELMFIRE [35], GENE [157], Gkeyll [202] and XGC1 [31]. However, because of the large computational cost of gyrokinetic simulations and the complexity of gyrokinetic models in the plasma boundary, fluid codes, such as BOUT++ [47], GBS [170], GDB [251], GRILLIX [212], HESEL [154] and TOKAM3X [218], are usually applied to simulate plasma turbulence in this region.

In the present thesis, the GBS code with the domain encompassing the whole tokamak to include core, edge and SOL interplay is used to investigate different turbulent transport regimes in the plasma boundary of diverted configurations, such as the one in ITER, as well as advanced magnetic configurations.

1.4 Scope and outline of the thesis

The main goal of the present thesis is to identify and characterize the turbulent transport regimes in the tokamak boundary as they result from two-fluid turbulence simulations, a stepping stone to the interpretation of future gyrokinetic boundary simulations. Particular focus is dedicated to the study of the transitions among these transport regimes, which are linked to important phenomena such as the L-H transition and the density limit. In addition, scaling laws of relevant quantities for the operation and design of tokamaks, such as the pressure decay length in the SOL and the maximum edge density achievable, are derived and compared to multi-machine databases. The present thesis addresses also the physics at play in alternative exhaust configurations, in particular the snowflake configuration [188]. These are of large interest to the fusion community since extrapolation of the ITER exhaust solution to fusion power plants may not guarantee a heat flux to the wall below the technological limit imposed by the materials [252, 121].

The present thesis is structured as follows. In Ch. 2, we present a new version of the GBS code [73], which significantly extends our simulation capability. In particular, the physical model is extended by adding electromagnetic effects and avoiding the use of the Boussinesq approximation in a diverted geometry. The plasma model is coupled to a single-species kinetic neutral model, leading to the first GBS simulation in a realistic diverted geometry that self-consistently evolves plasma turbulence and neutral dynamics. In addition, the implementation of the Poisson, Ampère and neutral solvers are carefully optimized, allowing us to efficiently simulate plasma turbulence in medium size tokamaks, such as TCV.

The characterization of different turbulent transport regimes in the plasma boundary is presented in Ch. 3 by closely following Ref. [72], where the results of GBS electrostatic simulations are used to identify three electrostatic turbulent transport regimes: a regime of suppressed turbulent transport at low collisionality and high heat source, a regime of fully developed turbulence at intermediate values of collisionality and heat source, and a regime of extremely large turbulent transport at high collisionality and low heat source, which is associated to the crossing of the density limit. Focusing on the edge region, an analytical estimate of the equilibrium pressure gradient length is derived in all the identified regimes.

In Ch. 4, we focus on the fully developed turbulent transport regime that we associate to the L-mode operation of tokamaks. A theory-based scaling laws of the pressure and density decay lengths in the near and far SOL are analytically derived for L-mode diverted plasma, thus extending the results of Ch. 3 to the SOL. Similarly to Ch. 3, the near SOL pressure and density decay lengths are obtained by balancing the power source, perpendicular turbulent transport across the separatrix and parallel losses at the vessel wall. A different approach is followed in the far SOL, where the pressure and density decay lengths are derived by using a model of intermittent transport mediated by filaments. The theoretical scaling laws are then compared to simulation results and experimental data [74].

The effects of electromagnetic perturbations on turbulent transport and equilibrium profiles are analyzed in Ch. 5 by leveraging the results of GBS electromagnetic simulations at different values of collisionality, heat source and β, thus extending the electrostatic investigation performed in Ch. 3. We show that, at high values of density, electromagnetic effects play only a minor role in determining turbulent transport if β is below the ideal ballooning stability limit and that the density limit can be reached independently of the value of β. The key parameters determining turbulent transport are also identified and used to delineate a phase space of edge turbulence, where both the β and density limits are represented. In particular, a theory-based scaling law of the maximum edge density achievable in magnetic fusion devices is derived and successfully validated against a multi-machine database of density limit discharges.

By following Ref. [75], we present in Ch. 6 the first turbulent simulations in snowflake configurations. The parallel heat flux on the target plates is analyzed in these configurations and compared to a standard single-null geometry, pointing out the important role of equilibrium drifts and turbulence in these configurations.

Finally, the conclusions and an outlook of the thesis follow in Ch. 7.

2 The GBS code for plasma boundary turbulence simulations

The present chapter describes a new version of the GBS code. The simulation domain is extended to encompass the whole plasma volume, avoiding an artificial boundary with the core, hence retaining the core-edge-SOL interplay. A new toroidal coordinate system is introduced to increase the code flexibility, allowing for the simulation of arbitrary magnetic configurations (e.g. single-null, double-null and snowflake configurations), which can also be the result of the equilibrium reconstruction of an experimental discharge. The implementation of a new iterative solver for Poisson and Ampère equations is presented, leading to a remarkable speed-up of the code with respect to the use of direct solvers, therefore allowing for efficient electromagnetic simulations that avoid the use of the Boussinesq approximation. A new MPI parallelisation is implemented to evolve the plasma and neutral models in parallel, thus improving the code scalability. The numerical implementation of the plasma and neutral models is verified by means of the method of manufactured solutions. The chapter ends with an example of a TCV discharge simulation in lower-single null geometry, showing the capabilities of this new version of GBS.

2.1 Introduction

The GBS code was initially developed to study plasma turbulence in basic plasma devices. The initial version of GBS evolved the two-dimensional plasma dynamics in the plane perpendicular to the magnetic field [171, 174], mainly studying ideal-interchange turbulence in simple magnetized plasma (SMT) configurations, such as TORPEX [57]. Later, GBS was extended to include the direction parallel to the magnetic field, using a field-aligned coordinate system, and was used to perform global simulations in SMT configurations [116, 172, 175] and linear devices [183], such as LAPD [71]. In 2012, a new version of GBS was developed to simulate plasma turbulence in the SOL of tokamak devices operated with limited magnetic configurations [170]. An electrostatic model in the cold ion limit was considered. Moreover, the Boussinesq approximation was applied to simplify the numerical implementation of the divergence of the polarisation current.

In 2016, a second version of GBS was developed [87]. The physical model was improved by adding the ion temperature dynamics [148] and electromagnetic effects [86]. The plasma model was coupled to a self-consistent kinetic neutral model, leading to the first plasma turbulence simulations of the SOL that self-consistently include the coupling to the neutral dynamics [237]. The Boussinesq approximation was relaxed and the code parallelisation was substantially improved by means of a three-dimensional Cartesian communicator. The implementation of the plasma model was verified by using the method of manufactured solutions (MMS), described in Ref. [178].

Finally, a non-field-aligned coordinate system was introduced in GBS to simulate complex magnetic geometries including one or more X-points and a third version of the code was reported in 2018, leading to the first GBS simulation of a diverted geometry [160]. The second-order numerical scheme was improved to a fourth-order finite difference scheme. Considering a simplified model with respect to the limited configuration, the diverted version of GBS was electrostatic, made use of the Boussinesq approximation, and did not include the neutral dynamics. Despite the use of a domain with a circular poloidal cross section that avoids the core region, limiting the choice of magnetic geometry, the version of GBS described in Ref. [160] was used to investigate plasma turbulence in both single- and double-null magnetic configurations, shading light on the properties of blobs [10, 159].

The goal of the present chapter is to describe in detail a new version of GBS that significantly improves the diverted version of GBS reported in Ref. [160]. First, while keeping the same fourth-order numerical scheme and non-field-aligned coordinate system, a rectangular poloidal cross section is implemented, which encompasses the whole plasma volume avoiding an artificial boundary with the core, hence retaining the core-edge-SOL turbulence interplay that is found to play a key role in determining the plasma dynamics of the tokamak boundary [44, 60, 81]. Although the use of a fluid model to simulate the whole plasma volume results in a description of the plasma dynamics in the core region that lacks some of the fundamental elements, such as kinetic effects, at play in this region, it avoids some unphysical phenomena due to the use of artificial boundary conditions with the core, especially concerning the electrostatic potential and the parallel velocities in the tokamak edge, as discussed in Ref. [160]. Moreover, the density source due to ionization of the neutral atoms can be better described with a domain that encompasses the whole plasma volume since ionization events may also occur in the core region. In addition, including the core region will allow the GBS model to be extended by adding further moments of the electron and ion distribution functions in future, thus retaining kinetic effects and improving the simulation accuracy of plasma turbulence in the core region [64, 102]. The new implemented geometry allows also for more flexibility on the choice of the magnetic configuration, which can also be loaded from an equilibrium reconstruction or a Grad-Shafranov solver. The possibility to simulate a magnetic configuration loaded from an equilibrium reconstruction has recently allowed for a direct comparison between GBS simulations and TCV experiments [155]. Second, the physical model of Ref. [160] is extended by adding electromagnetic effects, and the self-consistent kinetic neutral model, initially developed in the context of the limited version of GBS [87, 237], is ported to the present configuration, with an improved set of boundary conditions. Third, both the plasma and neutral implementations are carefully refactorized and optimized. In particular, the implementation of a new iterative solver for the Poisson and Ampère equations is introduced, leading to a remarkable speed-up of the code, therefore allowing for efficient electromagnetic simulations that avoid the use of the Boussinesq approximation. Fourth, the GBS parallelisation scheme is improved here by allowing the evolution in parallel of the plasma and neutral dynamics, and leading to an improvement of the code scalability. In addition, the relatively simple numerical scheme used in GBS allows for an effective parallelisation of GBS through domain decomposition applied to all three coordinates and implemented with the Message Passing Interface (MPI). The numerical implementation of both the plasma and neutral models is also verified by means of the MMS for the first time. In addition, taking advantage of the improvements of GBS brought to the present version, we present the first GBS electromagnetic simulation of a single-null TCV equilibrium, including the self-consistent evolution of the neutral dynamics.

The present chapter is organized as follows. The kinetic single-species neutral model evolved by GBS is summarized in Sec. 2.2, while the fluid plasma model is reported in Sec. 2.3. The implementation of the physical model in GBS as well as the initial and boundary conditions are described in Sec. 2.4. Sec. 2.5 focuses on the numerical discretization and optimization of the GBS plasma and neutral models. The code verification is reported in Sec. 2.6, while parallelisation scalability tests are described in Sec. 2.7. Convergence properties are presented in Sec. 2.8. The first application of the new version of GBS described herein is then presented in Sec. 2.9. The conclusions follow in Sec. 2.10.

2.2 The neutral model

We consider a single mono-atomic neutral species represented by a distribution function f_n with its dynamics being described by the following kinetic equation,

$$\frac{\partial f_\mathrm{n}}{\partial t} + \mathbf{v} \cdot \nabla f_\mathrm{n} = -\nu_\mathrm{iz} f_\mathrm{n} - \nu_\mathrm{cx}\left(f_\mathrm{n} - \frac{n_\mathrm{n}}{n_i} f_i\right) + \nu_\mathrm{rec} f_i \, , \tag{2.1}$$

where f_i and n_i are the ion distribution function and the ion density, respectively. The ionization, charge-exchange, and recombination processes are described through the use of Krook operators with collision frequencies defined as

$$\nu_\mathrm{iz} = n_e \langle v_e \sigma_\mathrm{iz}(v_e) \rangle_{v_e} \, , \tag{2.2}$$

$$\nu_\mathrm{rec} = n_e \langle v_e \sigma_\mathrm{rec}(v_e) \rangle_{v_e} \, , \tag{2.3}$$

and

$$\nu_{\mathrm{cx}} = n_i \langle v_i \sigma_{\mathrm{cx}}(v_i) \rangle_{v_i} \,, \tag{2.4}$$

where σ_{iz}, σ_{rec} and σ_{cx} are the ionization, recombination and charge-exchange cross-sections, v_e and v_i are the modulus of the electron and ion velocity and $\langle \cdot \rangle_{v_e}$ and $\langle \cdot \rangle_{v_i}$ denote the average in the velocity space over the electron and ion distribution functions, respectively. The effective reaction rates, $\langle v\sigma \rangle$, are taken from the OpenADAS database [215]. The neutral velocity is neglected in Eqs. (2.2)-(2.4) when evaluating the relative velocity between colliding particles [211, 237]. The neutral-neutral collisions, which have a lower reaction rate than the charge-exchange and ionization processes, possibly except in detached conditions, are neglected in Eq. (2.1). The elastic electron-neutral collisions are also neglected in Eq. (2.1) because of the electron-to-neutral mass ratio, but they are retained in the electron dynamics (see Eq. (2.8)).

The boundary conditions for f_{n} at the wall are derived under the assumption that the impacting neutrals and ions are either reflected or absorbed. If absorbed, the neutral particle is immediately released with a velocity that depends on the wall properties and is independent of the impacting particle velocity. The distribution function of the neutrals flowing from wall to the plasma volume (i.e. neutrals with velocity such that $\mathbf{v} \cdot \hat{\mathbf{n}} > 0$, with $\hat{\mathbf{n}}$ the unit vector normal to the wall) is therefore given by

$$f_{\mathrm{n}}(\mathbf{x}_b, \mathbf{v}) = (1-\alpha_{\mathrm{refl}})\Gamma_{\mathrm{out}}(\mathbf{x}_b)\chi_{\mathrm{in}}(\mathbf{x}_b, \mathbf{v}, T_b) + \alpha_{\mathrm{refl}}[f_{\mathrm{n}}(\mathbf{x}_b, \mathbf{v}-2\mathbf{v}_p) + f_i(\mathbf{x}_b, \mathbf{v}-2\mathbf{v}_p)] \,, \tag{2.5}$$

where α_{refl} is the reflection fraction, assumed the same for neutrals and ions, $\mathbf{x}_b$ indicates the boundary position, $\Gamma_{\mathrm{out}} = \Gamma_{\mathrm{out,n}} + \Gamma_{\mathrm{out,i}}$ is the sum of the neutral and ion fluxes to the wall and projected in the direction perpendicular to it, $\mathbf{v}_p = \mathrm{v}_p \hat{\mathbf{n}}$ is the velocity perpendicular to the boundary, with $\mathrm{v}_p = \mathbf{v} \cdot \hat{\mathbf{n}}$, and χ_{in} is the inflowing velocity distribution function given by the Knudsen cosine law,

$$\chi_{\mathrm{in}}(\mathbf{x}_b, \mathbf{v}, T_b) = \frac{3}{4\pi} \frac{m^2}{T_b^2} \cos\theta \exp\left(-\frac{m\mathrm{v}^2}{2T_b}\right) , \tag{2.6}$$

with $\theta = \arccos(\mathrm{v}_p/\mathrm{v})$ and T_b the wall temperature [237].

Further details on the neutral model are reported in Ref. [237], while the implementation of Eqs. (2.1) and (2.5) in GBS is described in Sec. 2.4.

2.3 The plasma model

This section briefly summarizes the derivation of the plasma model evolved by GBS. We first report on the derivation of the Braginskii equations in the presence of neutral-plasma collisions. Then, we consider the drift limit of these equations, which is implemented in the GBS code.

2.3.1 Braginskii equations

The Braginskii equations [23] were developed in the 1960s to describe the dynamics of a highly collisional plasma. The derivation of these equations starts from the description at a kinetic level of the plasma particle species. We consider here a single ion species plasma and we include collision terms in the form of Krook operators to describe the interaction with neutrals. The kinetic Boltzmann equations describing the evolution of the ion distribution function f_i is given by

$$\begin{aligned}\frac{\partial f_i}{\partial t} + \mathbf{v}\cdot\frac{\partial f_i}{\partial \mathbf{x}} + q_i\left(\frac{\mathbf{E}+\mathbf{v}\times\mathbf{B}}{m_i}\right)\cdot\frac{\partial f_i}{\partial \mathbf{v}} =& C_i(f_i, f_e) - \nu_{\mathrm{cx}}\left(\frac{n_{\mathrm{n}}}{n_i}f_i - f_n\right)\\ &+ \nu_{\mathrm{iz}} f_n - \nu_{\mathrm{rec}} f_i + s_i\,, \end{aligned}\tag{2.7}$$

while the kinetic equation for the evolution of the electron distribution function f_e is

$$\begin{aligned}\frac{\partial f_e}{\partial t} + \mathbf{v}\cdot\frac{\partial f_e}{\partial \mathbf{x}} - e\left(\frac{\mathbf{E}+\mathbf{v}\times\mathbf{B}}{m_e}\right)\cdot\frac{\partial f_e}{\partial \mathbf{v}} =& C_e(f_e, f_i) + \nu_{\mathrm{iz}} n_{\mathrm{n}}\left[2\Phi_e(\mathbf{V}_{\mathrm{n}}, T_{e,\mathrm{iz}}) - \frac{f_e}{n_e}\right] - \nu_{\mathrm{rec}} f_e\\ &+ \nu_{\mathrm{en}} n_{\mathrm{n}}\left[\Phi_e(\mathbf{V}_n, T_{e,\mathrm{en}}) - \frac{f_e}{n_e}\right] + s_e\,, \end{aligned}\tag{2.8}$$

where m_i and m_e are the ion and electron masses, q_i is the ion charge, e is the elementary charge, $C_i(f_i, f_e)$ and $C_e(f_e, f_i)$ are the collisional operators, $\mathbf{V}_{\mathrm{n}} = \int \mathbf{v} f_{\mathrm{n}} \mathrm{d}\mathbf{v}/n_{\mathrm{n}}$ is the neutral mean velocity, $\Phi_e(\mathbf{v}, T)$ is a Maxwellian velocity distribution function, $\nu_{\mathrm{en}} = n_e\langle v_e \sigma_{\mathrm{en}}(v_e)\rangle_{v_e}$ is the elastic electron-neutral collision frequency neglected in Eq. (2.1), and s_i and s_e are external sources of particles and heat. In Eq. (2.8), the two electrons resulting from an ionization event are considered emitted with a Maxwellian velocity distribution function, $\Phi_e(\mathbf{V}_{\mathrm{n}}, T_{e,\mathrm{iz}})$, of average velocity $\mathbf{V}_n = \int \mathbf{v} f_{\mathrm{n}} \mathrm{d}\mathbf{v}/n_{\mathrm{n}}$ and temperature $T_{e,\mathrm{iz}} = T_e/2 - E_{\mathrm{iz}}/3 + m_e V_e^2/6 - m_e V_{\mathrm{n}}^2/3$, where T_e and $\mathbf{V}_e$ are the local electron temperature and fluid velocity, respectively, and assuming that the electrons are released isotropically in the neutral reference frame (see Ref. [237] for details). The electron-neutral collisions are described in Eq. (2.8) by a loss term proportional to the electron distribution function and a source term with a Maxwellian distribution function, $\Phi_e(\mathbf{V}_{\mathrm{n}}, T_{e,\mathrm{en}})$, where $T_{e,\mathrm{en}} = T_e + m_e(V_e^2 - V_n^2)/3$ (see Ref. [237]).

The density, mean velocity and temperature of a species a associated with a distribution function f_a are defined as

$$n_a(t, \mathbf{x}) = \int f_a(t, \mathbf{x}, \mathbf{v}) \mathrm{d}\mathbf{v}\,, \tag{2.9}$$

$$\mathbf{V}_a(t, \mathbf{x}) = \frac{1}{n_a}\int \mathbf{v} f_a(t, \mathbf{x}, \mathbf{v}) \mathrm{d}\mathbf{v} = \langle \mathbf{v}\rangle_a\,, \tag{2.10}$$

$$T_a(t, \mathbf{x}) = \frac{1}{n_a}\int \frac{m}{3}(\mathbf{v} - \mathbf{V}_a)^2 f_a(t, \mathbf{x}, \mathbf{v}) \mathrm{d}\mathbf{v} = \frac{m}{3}\langle(\mathbf{v} - \mathbf{V}_a)^2\rangle_a\,. \tag{2.11}$$

The continuity, the momentum, and the temperature equations for a plasma composed of electrons and a single ion species of charge Ze are then derived by taking the first three moments of Eqs. (2.7) and (2.8), that is

$$
\begin{aligned}
\frac{\partial n_e}{\partial t} + \nabla \cdot (n_e \mathbf{V}_e) =& n_\mathrm{n}\nu_\mathrm{iz} - n_i\nu_\mathrm{rec} + s_n\,, && (2.12)\\
\frac{\partial n_i}{\partial t} + \nabla \cdot (n_i \mathbf{V}_i) =& n_\mathrm{n}\nu_\mathrm{iz} - n_i\nu_\mathrm{rec} + s_n\,, && (2.13)\\
m_e n_e \frac{\mathrm{d}_e \mathbf{V}_e}{\mathrm{d}t} =& -\nabla p_e - \nabla \cdot \pi_e - e n_e \Big(\mathbf{E} + \mathbf{V}_e \times \mathbf{B}\Big) + \mathbf{R}_e \\
& + m_e n_\mathrm{n}(\nu_\mathrm{en} + 2\nu_\mathrm{iz})(\mathbf{V}_\mathrm{n} - \mathbf{V}_e)\,, && (2.14)\\
m_i n_i \frac{\mathrm{d}_i \mathbf{V}_i}{\mathrm{d}t} =& -\nabla p_i - \nabla \cdot \pi_i + Zen_i \Big(\mathbf{E} + \mathbf{V}_i \times \mathbf{B}\Big) + \mathbf{R}_i \\
& + m_i n_\mathrm{n}(\nu_\mathrm{iz} + \nu_\mathrm{cx})(\mathbf{V}_\mathrm{n} - \mathbf{V}_i)\,, && (2.15)\\
\frac{3}{2} n_e \frac{\mathrm{d}_e T_e}{\mathrm{d}t} + p_e \nabla \cdot \mathbf{V}_e =& -\nabla \cdot \mathbf{q}_e - \pi_e : \nabla \mathbf{V}_e + Q_e \\
& + n_\mathrm{n}\nu_\mathrm{iz}\left[-E_\mathrm{iz} - \frac{3}{2}T_e + \frac{3}{2} m_e \mathbf{V}_e \cdot \left(\mathbf{V}_e - \frac{4}{3}\mathbf{V}_\mathrm{n}\right)\right] \\
& - n_\mathrm{n}\nu_\mathrm{en} m_e \mathbf{V}_e \cdot (\mathbf{V}_\mathrm{n} - \mathbf{V}_e) + n_e s_{T_e}\,, && (2.16)\\
\frac{3}{2} n_i \frac{\mathrm{d}_i T_i}{\mathrm{d}t} + p_i \nabla \cdot \mathbf{V}_i =& -\nabla \cdot \mathbf{q}_i - \pi_i : \nabla \mathbf{V}_i + Q_i + n_i s_{T_i} \\
& + n_\mathrm{n}(\nu_\mathrm{iz} + \nu_\mathrm{cx})\left[\frac{3}{2}(T_\mathrm{n} - T_i) + \frac{m_i}{2}(\mathbf{V}_n - \mathbf{V}_i)^2\right]\,, && (2.17)
\end{aligned}
$$

where

$$
\begin{aligned}
\frac{\mathrm{d}_e}{\mathrm{d}t} =& \frac{\partial}{\partial t} + \mathbf{V}_e \cdot \nabla\,, && (2.18)\\
\frac{\mathrm{d}_i}{\mathrm{d}t} =& \frac{\partial}{\partial t} + \mathbf{V}_i \cdot \nabla && (2.19)
\end{aligned}
$$

are the total time derivatives for the electrons and the ions, respectively, and $p_e = n_e T_e$, $p_i = n_i T_i$ are the electron and ion plasma pressure, respectively.

The terms on the right-hand side of Eqs. (2.14) and (2.15) represent the change in momentum due to the gradient of the pressure tensor $P_{\alpha\beta} = p_\alpha \delta_{\alpha\beta} + \pi_{\alpha\beta}$, where

$$
\begin{aligned}
p =& nm\langle v'^2 \rangle / 3\,, && (2.20)\\
\pi_{\alpha\beta} =& mn\langle v'_\alpha v'_\beta - v'^2/3\delta_{\alpha\beta}\rangle\,, && (2.21)
\end{aligned}
$$

with $\mathbf{v}' = \mathbf{v} - \mathbf{V}$, while the momentum exchanged per unit time due to electron-ion collisions is expressed in terms of

$$
\mathbf{R} = \int m\mathbf{v}' C \mathrm{d}\mathbf{v}\,. \tag{2.22}
$$

In Eqs. (2.16) and (2.17), $\mathbf{q}$ denotes the heat flux associated with the thermal motion of the particles,

$$\mathbf{q} = nm\left\langle \frac{v'^2}{2}\mathbf{v} \right\rangle \tag{2.23}$$

and Q represents the heat density generated as a consequence of the collisions with the other species in the plasma,

$$Q = \int \frac{mv'^2}{2} C \mathrm{d}\mathbf{v} \,. \tag{2.24}$$

In Eqs. (2.16) and (2.17), the Frobenius inner product, $\pi : \nabla\mathbf{V} = \pi_{\alpha\beta}\partial V_\alpha / \partial x_\beta$, is used. Eqs. (2.12)-(2.17) are coupled to the full set of Maxwell equations to express the electric and magnetic field.

A self-consistent model that describes the evolution of n, $\mathbf{V}$ and T requires that the quantities π, $\mathbf{q}$, $\mathbf{R}$ and Q in Eqs. (2.12)-(2.17) are expressed as a function of n, $\mathbf{V}$ and T. Within the assumption of considering timescales longer than the time interval between collisions and spatial variations occurring on scales longer than the space travelled by a particle between two collisions, the solution of Eqs. (2.7) and (2.8) can be approximated by a perturbed Maxwellian. As a consequence, the quantities π, $\mathbf{q}$, $\mathbf{R}$ and Q are proportional to n, $\mathbf{V}$, T and their gradients. The proportionality coefficients are called transport coefficients. In Ref. [23], the transport coefficients are calculated by assuming a strongly magnetized plane, i.e. $\Omega_{e,i}\tau_{e,i} \gg 1$, where $\Omega_{e,i} = q_{e,i}B/m_{e,i}$ are the electron/ion cyclotron frequencies and

$$\tau_e = \frac{3\sqrt{m_e}}{4\sqrt{2\pi}} \frac{(4\pi\epsilon_0)^2}{Z^2 e^4} \frac{T_e^{3/2}}{n\lambda} \,, \tag{2.25}$$

$$\tau_i = \frac{3\sqrt{m_i}}{4\sqrt{2\pi}} \frac{(4\pi\epsilon_0)^2}{Z^4 e^4} \frac{T_i^{3/2}}{n\lambda} \tag{2.26}$$

are the electron and ion collision times, with λ the Coulomb logarithm [209].

In the considered limit, Ref. [23] shows that the momentum transfer between ions and electrons, $\mathbf{R} = \mathbf{R}_e = -\mathbf{R}_i$, consists of two terms: the friction force, $\mathbf{R}_u$, due to electron/ion collisions, and the thermal force, $\mathbf{R}_T$, due to the coexistence of a temperature gradient in the presence of electron/ion collisions. By neglecting the friction in the direction perpendicular to the magnetic field and terms of order $1/(\Omega_e\tau_e)$, the friction and thermal forces are

$$\mathbf{R}_u = en_e \frac{j_\parallel}{\sigma_\parallel}\mathbf{b} \,, \tag{2.27}$$

$$\mathbf{R}_T = -0.71 n_e \nabla_\parallel T_e \,, \tag{2.28}$$

where $\mathbf{b}$ is the unit vector parallel to the magnetic field, $j_\parallel = en_e(V_{\parallel i} - V_{\parallel e})$ is the current in the direction parallel to $\mathbf{b}$, and $\sigma_\parallel$ is the parallel conductivity,

$$\sigma_\parallel = 1.96\frac{e^2 n_e \tau_e}{m_e}\,. \tag{2.29}$$

Within the same approximations, the electron and ion heat fluxes appearing in Eqs. (2.16) and (2.17) are

$$\mathbf{q}_e = -0.71 n_e T_e \frac{j_\parallel}{e} - \chi_{\parallel e}\mathbf{b}\nabla_\parallel T_e - \frac{5}{2}\frac{n_e T_e}{eB}\mathbf{b}\times\nabla T_e\,, \tag{2.30}$$

$$\mathbf{q}_i = -\chi_{\parallel i}\mathbf{b}\nabla_\parallel T_i + \frac{5}{2}\frac{n_i T_i}{ZeB}\mathbf{b}\times\nabla T_i\,, \tag{2.31}$$

where

$$\chi_{\parallel e} = 3.16\frac{n_e T_e \tau_e}{m_e}\,, \tag{2.32}$$

$$\chi_{\parallel i} = 3.9\frac{n_i T_i \tau_i}{m_i} \tag{2.33}$$

are the parallel thermal conductivities.

The heat generation Q is composed of the Joule heating due to friction between ions and electrons, the electron-ion heat transfer, and the term arising from the thermal force. For the typical timescales of turbulence in the plasma boundary, the first contribution is negligible. The heat generation for electrons is given by

$$Q_e = \frac{0.71}{e} j_\parallel \nabla T_e + 2\frac{m_e}{m_i}\frac{n}{\tau_e}(T_i - T_e)\,, \tag{2.34}$$

while for ions by

$$Q_i = 2\frac{m_e}{m_i}\frac{n}{\tau_e}(T_e - T_i)\,. \tag{2.35}$$

Finally, the components of the stress tensor π, having aligned the z axis along the magnetic field direction, can be written as

$$\pi_{xx} = -\frac{\eta_0}{2}(W_{xx} + W_{yy}) - \eta_3 W_{xy}\,, \tag{2.36}$$

$$\pi_{yy} = -\frac{\eta_0}{2}(W_{xx} + W_{yy}) + \eta_3 W_{xy}\,, \tag{2.37}$$

$$\pi_{xy} = \pi_{yx} = \frac{\eta_3}{2}(W_{xx} - W_{yy})\,, \tag{2.38}$$

$$\pi_{xz} = \pi_{zx} = -2\eta_3 W_{yz}\,, \tag{2.39}$$

$$\pi_{yz} = \pi_{zy} = +2\eta_3 W_{yz}\,, \tag{2.40}$$

$$\pi_{zz} = -\eta_0 W_{zz}\,, \tag{2.41}$$

where the rate-of-strain tensor W is

$$W_{\alpha\beta} = \frac{\partial V_\alpha}{\partial x_\beta} + \frac{\partial V_\beta}{\partial x_\alpha} - \frac{2}{3}\delta_{\alpha\beta}\nabla \cdot \mathbf{V}\,, \tag{2.42}$$

with

$$\eta_{0i} = 0.96 n_i T_i \tau_i\,,\ \eta_{3i} = \frac{n_i T_i}{2\Omega_i}\,, \tag{2.43}$$

$$\eta_{0e} = 0.73 n_e T_e \tau_e\,,\ \eta_{3e} = -\frac{n_e T_e}{2\Omega_e} \tag{2.44}$$

the viscosities.

2.3.2 Drift-reduced Braginskii equations

The Braginskii equations describe the plasma dynamics occurring on a wide range of time and spatial scales, ranging from the electron cyclotron frequency $\Omega_{ce} = eB/m_e \sim 10^{11}$ s^{-1} up to the confinement timescale, which is of order 1 s, and from the electron Larmor radius, which is of the order of 10^{-5} m (for typical values of T_e in the SOL), up to typical machine size, of the order of 1 m. On the other hand, turbulent fluctuations in the plasma boundary occur at timescale of order 10^{-6}s, which is therefore much slower than the fast cyclotron motion, and on spatial scale of the order of the ion sound Larmor radius, $\rho_s = c_s/\Omega_{ci}$, with c_s the sound speed. It follows that simulating the plasma dynamics by means of the Braginskii equations is extremely challenging from a numerical point of view. It is therefore of fundamental importance to eliminate the fast timescales from the Braginskii equations in order to obtain a model that can be addressed numerically. This reduction consists in simplifying Eqs. (2.12)-(2.17) by applying a drift ordering,

$$\frac{\partial}{\partial t} \sim \mathbf{V}_E \cdot \nabla \sim \frac{\rho_s^2}{L_\perp^2}\Omega_{ci} \ll \Omega_{ci}\,, \tag{2.45}$$

being ρ_s much smaller than the typical equilibrium scale length $L_\perp$, and $\mathbf{V}_E = \mathbf{b} \times \nabla\phi/B$ the $\mathbf{E} \times \mathbf{B}$ drift velocity. Moreover, since the plasma turbulence takes place on a spatial scale much larger than the Debye length, we assume the plasma to be quasi-neutral, i.e. $n_i = n_e \equiv n$.

Within the drift-reduced approximation, the particle velocities can be conveniently split into a component parallel to the magnetic field and a component perpendicular to it. In fact, the electron and ion perpendicular velocities can be written as [237, 249]

$$\mathbf{V}_{\perp e} = \mathbf{V}_E + \mathbf{V}_{de}\,, \tag{2.46}$$

$$\mathbf{V}_{\perp i} = \mathbf{V}_E + \mathbf{V}_{di} + \mathbf{V}_{pol} + \mathbf{V}_{in}\,, \tag{2.47}$$

where

$$\mathbf{V}_{de} = -\frac{1}{enB}\mathbf{b} \times \nabla p_e\,, \tag{2.48}$$

$$\mathbf{V}_{di} = \frac{1}{ZenB}\mathbf{b} \times \nabla p_i \tag{2.49}$$

are the electron and ion diamagnetic drift velocities, respectively. The $\mathbf{E} \times \mathbf{B}$ and diamagnetic drift velocities provide the zeroth order approximation to the perpendicular velocity, i.e. $\mathbf{V}_{\perp i} = \mathbf{V}_E + \mathbf{V}_{di}$ and, similarly, $\mathbf{V}_{\perp e} = \mathbf{V}_E + \mathbf{V}_{de}$. The first order corrections to the ion perpendicular velocity are the polarisation drift, $\mathbf{V}_{pol}$, and the drift arising from the ion-neutral friction due to charge exchange, $\mathbf{V}_{in} = (n_{\mathrm{n}}/n)(\nu_{\mathrm{cx}}/\Omega_{ci})(\mathbf{V}_{\perp \mathrm{n}} - \mathbf{V}_{\perp i}) \times \mathbf{b}$. The ion polarization drift can be obtained from Eq. (2.13) by splitting the stress tensor π into two contributions: a viscous part,

$$\pi_{vis} = \left(\mathbf{bb} - \frac{I}{3}G\right), \tag{2.50}$$

$$G = -3\eta_0\left(\nabla_{\|}V_{\|} - \boldsymbol{\kappa}\cdot\mathbf{V} - \frac{1}{3}\nabla\cdot\mathbf{V}\right), \tag{2.51}$$

with G the stress function and $\boldsymbol{\kappa} = \mathbf{b}\cdot\nabla\mathbf{b}$ the field line curvature, and a finite Larmor radius (FLR) part, π_{FLR}, such that

$$\begin{aligned}\nabla\cdot\pi_{FLR} = &-m_i n\mathbf{V}_{di}\cdot\nabla\mathbf{V}_i + p_i\left(\nabla\times\frac{\mathbf{b}}{\Omega_{ci}}\right)\cdot\nabla\mathbf{V}_i\\ &+\nabla_\perp\left(\frac{p_i}{2\Omega_{ci}}\nabla\cdot\mathbf{b}\times\mathbf{V}_i\right) + \mathbf{b}\times\nabla\left(\frac{p_i}{2\Omega_{ci}}\nabla_\perp\cdot\mathbf{V}_i\right).\end{aligned} \tag{2.52}$$

The ion polarization drift can then be written as [249],

$$\begin{aligned}\mathbf{V}_{pol} = &\frac{\mathbf{b}}{\Omega_{ci}}\times\frac{\mathrm{d}}{\mathrm{d}t}\mathbf{V}_{\perp i0} + \frac{1}{nm_i\Omega_{ci}}\left\{\mathbf{b}\times\left[p_i\left(\nabla\times\frac{\mathbf{b}}{\Omega_{ci}}\right)\cdot\nabla\mathbf{V}_{\perp i0}\right]\right.\\ &\left.+\mathbf{b}\times\nabla_\perp\left(\frac{p_i}{2\Omega_{ci}}\nabla\cdot\mathbf{b}\times\mathbf{V}_{\perp i0}\right) - \nabla_\perp\left(\frac{p_i}{2\Omega_{ci}}\nabla_\perp\cdot\mathbf{V}_{\perp i0}\right)\right\}\\ &+\frac{1}{nm_i\Omega_{ci}}\mathbf{b}\times\left(G\boldsymbol{\kappa} - \frac{\nabla G}{3}\right),\end{aligned} \tag{2.53}$$

where $\mathrm{d}/\mathrm{d}t = \partial/\partial t + (\mathbf{V}_E + V_{\|i}\mathbf{b})\cdot\nabla$, being $\mathbf{V}_{pol}$ and $\mathbf{V}_{in}$ dropped because of the drift-ordering. The diamagnetic drift cancels out the first term of Eq. (2.52).

The polarisation drift appears in the continuity equation in a divergence term, $\nabla\cdot(n\mathbf{V}_{pol})$, which can be written as (see Ref. [249] for details)

$$\nabla\cdot(n\mathbf{V}_{pol}) = \nabla_\perp\cdot\frac{nc}{B\Omega_{ci}}\frac{\mathrm{d}}{\mathrm{d}t}\left(\mathbf{E}_\perp - \frac{\nabla_\perp p_i}{en}\right) + \frac{1}{3m_i\Omega_{ci}}\mathbf{b}\times\boldsymbol{\kappa}\cdot\nabla G\,. \tag{2.54}$$

On the other hand, the electron polarization drift is neglected, since $\nabla \cdot (n\mathbf{V}_{pol,e})$ is a factor $\sqrt{m_e/m_i}$ smaller than $\nabla \cdot \mathbf{V}_{pol}$. Similarly, $\mathbf{V}_{en}$ is a factor $\sqrt{m_e/m_i}$ smaller than $\mathbf{V}_{in}$ and it is therefore neglected. We now have the main elements to derive the set of equations that are implemented in the GBS code.

Continuity and vorticity equations

Under the assumption of quasi-neutrality, the drift-reduced continuity equations for ions and electrons are

$$\frac{\partial n}{\partial t} + \nabla \cdot \Big[n\Big(\mathbf{V}_E + \mathbf{V}_{di} + \mathbf{V}_{pol} + V_{\parallel i}\mathbf{b} + \mathbf{V}_{\text{in}}\Big)\Big] = n_{\text{n}}\nu_{\text{iz}} - n\nu_{\text{rec}} + s_n \,, \tag{2.55}$$

$$\frac{\partial n}{\partial t} + \nabla \cdot \Big[n\Big(\mathbf{V}_E + \mathbf{V}_{de} + V_{\parallel e}\mathbf{b}\Big)\Big] = n_{\text{n}}\nu_{\text{iz}} - n\nu_{\text{rec}} + s_n \,, \tag{2.56}$$

By subtracting Eq. (2.55) and Eq. (2.56), we obtain the vorticity equation,

$$\nabla \cdot (n\mathbf{V}_{pol}) + \frac{1}{e}\nabla_\parallel j_\parallel + \nabla \cdot [n(\mathbf{V}_{di} - \mathbf{V}_{de})] + \nabla \cdot (n\mathbf{V}_{\text{in}}) = 0 \,, \tag{2.57}$$

where we assume that the modulus B of the magnetic field varies slowly along $\mathbf{b}$, $\nabla \cdot f\mathbf{b} \simeq \nabla_\parallel f$. Eq. (2.57) is equivalent to $\nabla \cdot \mathbf{j} = 0$. By replacing the term $\nabla \cdot (n\mathbf{V}_{pol})$ in Eq. (2.57), the vorticity equation becomes

$$\nabla_\perp \cdot \left[\frac{n}{B\Omega_{ci}}\frac{\mathrm{d}}{\mathrm{d}t}\left(\mathbf{E}_\perp - \frac{\nabla_\perp p_i}{en}\right)\right] + \frac{1}{3m_i\Omega_{ci}}\mathbf{b} \times \boldsymbol{\kappa} \cdot \nabla G + \frac{1}{e}\nabla_\parallel j_\parallel + \nabla \cdot [n(\mathbf{V}_{di} - \mathbf{V}_{de})] + \frac{n_{\text{n}}}{n}\nu_{\text{cx}}\nabla \cdot \left(n\mathbf{E}_\perp - \frac{1}{e}\nabla_\perp p_i\right) = 0 \,, \tag{2.58}$$

which determines the time evolution of $\mathbf{E}_\perp$.

The semi-electrostatic limit

Since the Braginskii model evaluates the electric and magnetic field as the solution of the complete set of Maxwell equations, both compressional and shear Alfvén waves are included in its description [16]. However, compressional Alfvén waves are several orders of magnitude faster than typical turbulent fluctuations in the plasma boundary. Hence, it is important to remove these fast oscillations from the model, which can be done by neglecting the component of the vector potential perpendicular to the magnetic field. Shear Alfvén waves are instead retained in the model as the associated oscillations are sufficiently slow that they play a role in the turbulent dynamics of the plasma boundary.

Neglecting the displacement current, considering the Ampère's law for the magnetic field and current fluctuations, $\nabla \times \delta\mathbf{B} = \mu_0\delta\mathbf{j}$, and expressing the magnetic field in terms of the potential vector, $\delta\mathbf{B} = \nabla \times \delta\mathbf{A}$, we obtain

$$\nabla^2 \delta\mathbf{A} = -\mu_0 \delta\mathbf{j}\,, \tag{2.59}$$

where $\delta\mathbf{j} = \mathbf{j} - \bar{\mathbf{j}}$ accounts for the small-scale and small-amplitude current perturbations (the contribution of the equilibrium current, $\bar{\mathbf{j}}$, is subtracted to the total current, $\mathbf{j}$). Therefore, Eq. (2.59) does not evolve the externally imposed equilibrium magnetic field, which otherwise would require to couple the plasma model to a Grad-Shafranov solver and to self-consistently simulate the plasma current, and focuses on electromagnetic effects rising from small-scale, small-amplitude magnetic perturbations [249]. By assuming that $\beta = 2\mu_0(p_e + p_i)/B^2 \ll 1$ and observing that the typical turbulent scale lengths in the parallel direction are much larger than the ones in the perpendicular direction, Eq. (2.59) can be written as

$$\nabla_\perp^2 \psi = \mu_0 \delta j_\parallel\,, \tag{2.60}$$

where we define $\psi = -\delta A_\parallel$, with $\delta A_\parallel = \delta\mathbf{A} \cdot \mathbf{b}$. Within the same approximations, the electric field is given by

$$\mathbf{E} = -\nabla\phi + \frac{\partial\psi}{\partial t}\mathbf{b}\,. \tag{2.61}$$

We note that the magnetic fluctuations affect the direction of the magnetic field, and therefore the parallel gradient,

$$\nabla_\parallel = (\mathbf{b} + \delta\mathbf{b}) \cdot \nabla = \mathbf{b} \cdot \nabla - \frac{\nabla \times \psi\mathbf{b}}{B} \cdot \nabla \simeq \mathbf{b} \cdot \nabla + \frac{\mathbf{b}}{B} \times \nabla_\perp \psi \cdot \nabla\,, \tag{2.62}$$

where the second term is the contribution to the parallel derivative due to magnetic fluctuations.

Parallel momentum equations

The parallel force balance equation for electrons, known as generalized Ohm's law, can be derived by projecting Eq. (2.14) along the parallel direction,

$$\begin{aligned} m_e \frac{\mathrm{d}_e V_{\parallel e}}{\mathrm{d}t} =& -\frac{1}{n}\nabla_\parallel p_e + e\nabla_\parallel \phi - e\frac{\partial\psi}{\partial t} + e\frac{j_\parallel}{\sigma_\parallel} - 0.71\nabla_\parallel T_e \\ &+ m_e \frac{n_\mathrm{n}}{n}(\nu_{en} + 2\nu_\mathrm{iz})(V_{\parallel n} - V_{\parallel e})\,, \end{aligned} \tag{2.63}$$

where $\mathbf{b} \cdot (\nabla \cdot \pi_{vis,e}) \simeq 2\nabla_\parallel G_e/3$ and $\mathbf{b} \cdot (\nabla \cdot \pi_{FLR,e}) \simeq -nm_e\mathbf{V}_{de} \cdot \nabla V_{\parallel e}$ (we assume that B varies slowly along $\mathbf{b}$). We note that the term $-nm_e\mathbf{V}_{de} \cdot \nabla V_{\parallel e}$ cancels out the electron diamagnetic convection, leading to $\mathrm{d}_e/\mathrm{d}t = \partial/\partial t + (\mathbf{V}_E + V_{\parallel e}\mathbf{b}) \cdot \nabla$.

Within the same approximations, by projecting Eq. (2.15) onto the parallel direction and neglecting terms of the order m_e/m_i and $\sqrt{m_e/m_i}$, the parallel momentum equation for the ions is given by

$$m_i \frac{\mathrm{d}V_{\parallel i}}{\mathrm{d}t} = -\frac{1}{n}\nabla(p_i + p_e) - \frac{2}{3}\nabla_\parallel G_i + m_i \frac{n_\mathrm{n}}{n}(\nu_\mathrm{iz} + \nu_\mathrm{cx})(V_{\parallel n} - V_{\parallel i})\,. \tag{2.64}$$

Temperature equations

The electron temperature equation is derived from Eq. (2.16) by applying the drift ordering. By neglecting the viscous heat losses, the frictional heating related to $\mathbf{R}_u$ and the electron-ion heat transfer, we obtain

$$\begin{aligned}\frac{3}{2}n\frac{\mathrm{d}_e T_e}{\mathrm{d}t} &+ \frac{3}{2}n\mathbf{V}_{de}\cdot\nabla T_e + p_e\nabla\cdot\Big(\mathbf{V}_E + \mathbf{V}_{de} + V_{\parallel e}\mathbf{b}\Big) - 0.71\frac{T_e}{e}\nabla_\parallel j_\parallel \\ &- \nabla_\parallel(\chi_{\parallel e}\nabla_\parallel T_e) - \frac{5e}{2}\nabla\cdot\left[p_e\left(\frac{\mathbf{b}}{B}\times\nabla T_e\right)\right] + 2\frac{m_e}{m_i}\frac{n}{\tau_e}(T_e - T_i) = s_{T_e} + S^\mathrm{n}_{T_e}\,,\end{aligned} \tag{2.65}$$

where the source term on the right hand side,

$$S^\mathrm{n}_{T_e} = n_\mathrm{n}\nu_\mathrm{iz}\left[-E_\mathrm{iz} - \frac{3}{2}T_e + \frac{3}{2}m_e\mathbf{V}_e\cdot\left(\mathbf{V}_e - \frac{4}{3}\mathbf{V}_\mathrm{n}\right)\right] - n_\mathrm{n}\nu_\mathrm{en}m_e\mathbf{V}_e\cdot(\mathbf{V}_\mathrm{n} - \mathbf{V}_e)\,, \tag{2.66}$$

accounts for the interaction between electron and neutrals.

Analogously, the ion temperature equation is derived from Eq. (2.17),

$$\begin{aligned}\frac{3}{2}n\frac{\mathrm{d}T_i}{\mathrm{d}t} &+ \frac{3}{2}n\mathbf{V}_{di}\nabla T_i + p_i\nabla\cdot(\mathbf{V}_E + \mathbf{V}_{di} + \mathbf{V}_{pol} + V_{\parallel i}\mathbf{b}) \\ &- \nabla_\parallel(\chi_{\parallel i}\nabla_\parallel T_i) + \frac{5e}{2}\nabla\cdot\left[p_i\left(\frac{\mathbf{b}}{B}\times\nabla T_i\right)\right] + 2\frac{m_e}{m_i}\frac{n}{\tau_e}(T_i - T_e) = s_{T_i} + S^\mathrm{n}_{T_i}\,,\end{aligned} \tag{2.67}$$

where

$$S^\mathrm{n}_{T_i} = n_\mathrm{n}(\nu_\mathrm{iz} + \nu_\mathrm{cx})\left[T_\mathrm{n} - T_i + \frac{1}{3}(V_{\parallel\mathrm{n}} - V_{\parallel i})^2\right]. \tag{2.68}$$

The term $\nabla\cdot\mathbf{V}_{pol}$ can be evaluated by using the ion and electron continuity equations,

$$n\nabla\cdot(\mathbf{V}_E + \mathbf{V}_{di} + \mathbf{V}_{pol} + \mathbf{V}_\mathrm{in} + V_{\parallel i}\mathbf{b}) = -\mathbf{V}_{di}\cdot\nabla n - \frac{\mathrm{d}n}{\mathrm{d}t}\,, \tag{2.69}$$

where the terms $\mathbf{V}_{pol}\cdot\nabla n$ and $\mathbf{V}_{in}\cdot\nabla n$ are dropped because of the drift-reduced ordering, and

$$\frac{\mathrm{d}n}{\mathrm{d}t} = \frac{\mathrm{d}_e n}{\mathrm{d}t} + (V_{\parallel i} - V_{\parallel e})\nabla_\parallel n\,. \tag{2.70}$$

By using Eqs. (2.69) and (2.70), Eq. (2.67) can be rewritten as

$$
\begin{aligned}
&\frac{3}{2}n\frac{\mathrm{d}T_i}{\mathrm{d}t} + T_i\nabla\cdot n\mathbf{V}_{de} + p_i\nabla\cdot(\mathbf{V}_E + V_{\parallel e}\mathbf{b}) - T_i\frac{j_\parallel}{en}\nabla_\parallel n \\
&\qquad - \nabla_\parallel(\chi_{\parallel i}\nabla_\parallel T_i) + \frac{5p_i}{2e}\left(\nabla\times\frac{\mathbf{b}}{B}\right)\cdot\nabla T_i + 2\frac{m_e}{m_i}\frac{n}{\tau_e}(T_i - T_e) = s_{T_i} + S^{\mathrm{n}}_{T_i}\,. \qquad (2.71)
\end{aligned}
$$

2.4 Implementation of the physical model in GBS

This section presents the plasma and neutral models in normalized units, as they are implemented in the GBS code. The spatial differential operators used by GBS are derived in the new adopted coordinate system. The section concludes with a summary of the boundary and initial conditions used in GBS. The numerical discretization of the physical model and its optimization follow in Sec. 2.5.

2.4.1 The GBS plasma model

The plasma model implemented in GBS is the drift-reduced Braginskii model described in Sec. 2.3. Namely GBS considers the density continuity equation, Eq. (2.56), the vorticity equation, Eq. (2.58), the electron and ion parallel momentum balance, Eqs. (2.63) and (2.64), and the electron and ion temperature equations, Eqs. (2.65) and (2.71), which take the following form

$$
\begin{aligned}
\frac{\partial n}{\partial t} =& -\frac{1}{B}[\phi, n] + \frac{2}{eB}\Big[C(p_e) - enC(\phi)\Big] - \nabla_\parallel(nV_{\parallel e}) \\
&+ D_n\nabla_\perp^2 n + s_n + \nu_{\mathrm{iz}}n_{\mathrm{n}} - \nu_{\mathrm{rec}}n\,, \qquad (2.72)\\
\frac{\partial \Omega}{\partial t} =& -\frac{1}{B}\nabla\cdot[\phi, \boldsymbol{\omega}] - \nabla\cdot\left(V_{\parallel i}\nabla_\parallel\boldsymbol{\omega}\right) + \frac{B\Omega_{ci}}{e}\nabla_\parallel j_\parallel + \frac{2\Omega_{ci}}{e}C(p_e + p_i) \\
&+ \frac{\Omega_{ci}}{3e}C(G_i) + D_\Omega\nabla_\perp^2\Omega - \frac{n_{\mathrm{n}}}{n}\nu_{\mathrm{cx}}\Omega\,, \qquad (2.73)\\
\frac{\partial U_{\parallel e}}{\partial t} =& -\frac{1}{B}[\phi, V_{\parallel e}] - V_{\parallel e}\nabla_\parallel V_{\parallel e} + \frac{e}{m_e}\left(\frac{j_\parallel}{\sigma_\parallel} + \nabla_\parallel\phi - \frac{1}{en}\nabla_\parallel p_e - \frac{0.71}{e}\nabla_\parallel T_e - \frac{2}{3en}\nabla_\parallel G_e\right) \\
&+ D_{V_{\parallel e}}\nabla_\perp^2 V_{\parallel e} + \frac{n_{\mathrm{n}}}{n}(\nu_{\mathrm{en}} + 2\nu_{\mathrm{iz}})(V_{\parallel n} - V_{\parallel e})\,, \qquad (2.74)\\
\frac{\partial V_{\parallel i}}{\partial t} =& -\frac{1}{B}[\phi, V_{\parallel i}] - V_{\parallel i}\nabla_\parallel V_{\parallel i} - \frac{1}{m_i n}\nabla_\parallel(p_e + p_i) - \frac{2}{3m_i n}\nabla_\parallel G_i \\
&+ D_{V_{\parallel i}}\nabla_\perp^2 V_{\parallel i} + \frac{n_{\mathrm{n}}}{n}(\nu_{\mathrm{iz}} + \nu_{\mathrm{cx}})(V_{\parallel n} - V_{\parallel i})\,, \qquad (2.75)
\end{aligned}
$$

$$
\begin{aligned}
\frac{\partial T_e}{\partial t} =& -\frac{1}{B}[\phi, T_e] - V_{\parallel e}\nabla_\parallel T_e + \frac{2}{3}T_e\left[0.71\frac{\nabla_\parallel j_\parallel}{en} - \nabla_\parallel V_{\parallel e}\right] \\
&+ \frac{4}{3}\frac{T_e}{eB}\left[\frac{7}{2}C(T_e) + \frac{T_e}{n}C(n) - eC(\phi)\right] \\
&+ \nabla_\parallel(\chi_{\parallel e}\nabla_\parallel T_e) + D_{T_e}\nabla_\perp^2 T_e + s_{T_e} - \frac{n_\mathrm{n}}{n}\nu_\mathrm{en} m_e \frac{2}{3}V_{\parallel e}(V_{\parallel n} - V_{\parallel e}) \\
&- \frac{4}{3}\frac{m_e}{m_i}\frac{1}{\tau_e}(T_e - T_i) + \frac{n_\mathrm{n}}{n}\nu_\mathrm{iz}\left[-\frac{2}{3}E_\mathrm{iz} - T_e + m_e V_{\parallel e}\left(V_{\parallel e} - \frac{4}{3}V_{\parallel n}\right)\right],
\end{aligned}
\tag{2.76}
$$

$$
\begin{aligned}
\frac{\partial T_i}{\partial t} =& -\frac{1}{B}[\phi, T_i] - V_{\parallel i}\nabla_\parallel T_i + \frac{4}{3}\frac{T_i}{eB}\left[C(T_e) + \frac{T_e}{n}C(n) - eC(\phi)\right] - \frac{10}{3}\frac{T_i}{eB}C(T_i) \\
&+ \frac{2}{3}T_i\left[(V_{\parallel i} - V_{\parallel e})\frac{\nabla_\parallel n}{n} - \nabla_\parallel V_{\parallel e}\right] + \nabla_\parallel(\chi_{\parallel i}\nabla_\parallel T_i) + D_{T_i}\nabla_\perp^2 T_i + s_{T_i} \\
&+ \frac{4}{3}\frac{m_e}{m_i}\frac{1}{\tau_e}(T_e - T_i) + \frac{n_\mathrm{n}}{n}(\nu_\mathrm{iz} + \nu_\mathrm{cx})\left[T_n - T_i + \frac{1}{3}(V_{\parallel n} - V_{\parallel i})^2\right].
\end{aligned}
\tag{2.77}
$$

Eqs. (2.72)–(2.77) are coupled to the Poisson and Ampère equations introduced in Sec. 2.3, which take the following form

$$
\nabla\cdot\Big(n\nabla_\perp\phi\Big) = \Omega - \frac{\nabla_\perp^2 p_i}{e}\,, \tag{2.78}
$$

$$
\left(\nabla_\perp^2 - \frac{e^2\mu_0}{m_e}n\right)V_{\parallel e} = \nabla_\perp^2 U_{\parallel e} - \frac{e^2\mu_0}{m_e}nV_{\parallel i} + \frac{e^2\mu_0}{m_e}\bar{j}_\parallel\,. \tag{2.79}
$$

In Eqs. (2.72)–(2.79), $\Omega = \nabla\cdot\boldsymbol{\omega} = \nabla\cdot(n\nabla_\perp\phi + \nabla_\perp p_i/e)$ is the scalar vorticity, while $U_{\parallel e} = V_{\parallel e} + e\psi/m_e$ is the sum of the electron inertia and the electromagnetic induction contributions.

The spatial operators appearing in Eqs. (2.72)–(2.79) are the $\mathbf{E}\times\mathbf{B}$ convective term,

$$
[\phi, f] = \mathbf{b}\;\cdot\;\Big(\nabla\phi\times\nabla f\Big)\,, \tag{2.80}
$$

the curvature operator,

$$
C(f) = \frac{B}{2}\left(\nabla\times\frac{\mathbf{b}}{B}\right)\cdot\nabla f\,, \tag{2.81}
$$

the parallel gradient, which includes the electromagnetic flutter contribution,

$$
\nabla_\parallel f = \mathbf{b}\cdot\nabla f + \frac{1}{B}[\psi, f]\,, \tag{2.82}
$$

and the perpendicular Laplacian,

$$
\nabla_\perp^2 f = \nabla\cdot\Big[(\mathbf{b}\times\nabla f)\times\mathbf{b}\Big]\,, \tag{2.83}
$$

where f is a general scalar function.

The terms s_n and s_T are externally imposed sources in the density and temperature equations, which are analytical and toroidally uniform functions of the poloidal magnetic flux $\Psi(R, Z)$,

$$s_n = s_{n0} \exp\left(-\frac{(\psi(R,Z) - \psi_n)^2}{\Delta_n^2} \right), \tag{2.84}$$

$$s_T = \frac{s_{T0}}{2} \left[\tanh\left(-\frac{\psi(R,Z) - \psi_T}{\Delta_T} \right) + 1 \right], \tag{2.85}$$

where ψ_n and ψ_T are flux surfaces located inside the LCFS.

The gyroviscous terms are defined as

$$G_i = -\eta_{0i} \left[2\nabla_\parallel V_{\parallel i} + \frac{1}{B} C(\phi) + \frac{1}{enB} C(p_i) \right], \tag{2.86}$$

$$G_e = -\eta_{0e} \left[2\nabla_\parallel V_{\parallel e} + \frac{1}{B} C(\phi) - \frac{1}{enB} C(p_e) \right], \tag{2.87}$$

where $\eta_{0i} = 0.96 n T_i \tau_i$ and $\eta_{0e} = 0.73 n T_e \tau_e$. The numerical diffusion terms, $D_f \nabla_\perp^2 f$, are added for numerical stability.

Eqs. (2.72)-(2.79) are implemented in GBS in dimensionless form, i.e.

$$\begin{aligned} \frac{\partial n}{\partial t} =& -\frac{\rho_*^{-1}}{B}[\phi, n] + \frac{2}{B}\Big[C(p_e) - nC(\phi)\Big] - \nabla_\parallel(nV_{\parallel e}) + D_n \nabla_\perp^2 n \\ &+ s_n + \nu_{\mathrm{iz}} n_{\mathrm{n}} - \nu_{\mathrm{rec}} n \,, \end{aligned} \tag{2.88}$$

$$\begin{aligned} \frac{\partial \Omega}{\partial t} =& -\frac{\rho_*^{-1}}{B} \nabla \cdot [\phi, \boldsymbol{\omega}] - \nabla \cdot \Big(V_{\parallel i} \nabla_\parallel \boldsymbol{\omega} \Big) + B^2 \nabla_\parallel j_\parallel + 2BC(p_e + \tau p_i) \\ &+ \frac{B}{3} C(G_i) + D_\Omega \nabla_\perp^2 \Omega - \frac{n_{\mathrm{n}}}{n} \nu_{\mathrm{cx}} \Omega \,, \end{aligned} \tag{2.89}$$

$$\begin{aligned} \frac{\partial U_{\parallel e}}{\partial t} =& -\frac{\rho_*^{-1}}{B}[\phi, V_{\parallel e}] - V_{\parallel e} \nabla_\parallel V_{\parallel e} + \frac{m_i}{m_e}\left(\nu j_\parallel + \nabla_\parallel \phi - \frac{1}{n}\nabla_\parallel p_e - 0.71 \nabla_\parallel T_e - \frac{2}{3n}\nabla_\parallel G_e \right) \\ &+ D_{V_{\parallel e}} \nabla_\perp^2 V_{\parallel e} + \frac{n_{\mathrm{n}}}{n}(\nu_{\mathrm{en}} + 2\nu_{\mathrm{iz}})(V_{\parallel n} - V_{\parallel e}) \,, \end{aligned} \tag{2.90}$$

$$\begin{aligned} \frac{\partial V_{\parallel i}}{\partial t} =& -\frac{\rho_*^{-1}}{B}[\phi, V_{\parallel i}] - V_{\parallel i} \nabla_\parallel V_{\parallel i} - \frac{1}{n}\nabla_\parallel(p_e + \tau p_i) - \frac{2}{3n}\nabla_\parallel G_i \\ &+ D_{V_{\parallel i}} \nabla_\perp^2 V_{\parallel i} + \frac{n_{\mathrm{n}}}{n}(\nu_{\mathrm{iz}} + \nu_{\mathrm{cx}})(V_{\parallel n} - V_{\parallel i}) \,, \end{aligned} \tag{2.91}$$

$$\begin{aligned} \frac{\partial T_e}{\partial t} =& -\frac{\rho_*^{-1}}{B}[\phi, T_e] - V_{\parallel e} \nabla_\parallel T_e + \frac{2}{3} T_e \left[0.71 \frac{\nabla_\parallel j_\parallel}{n} - \nabla_\parallel V_{\parallel e} \right] - 2.61 \nu n (T_e - \tau T_i) \\ &+ \frac{4}{3}\frac{T_e}{B}\left[\frac{7}{2} C(T_e) + \frac{T_e}{n} C(n) - C(\phi) \right] + \nabla_\parallel(\chi_{\parallel e} \nabla_\parallel T_e) + D_{T_e} \nabla_\perp^2 T_e \\ &+ s_{T_e} + \frac{n_{\mathrm{n}}}{n} \nu_{\mathrm{iz}} \left[-\frac{2}{3} E_{\mathrm{iz}} - T_e + m_e V_{\parallel e}\left(V_{\parallel e} - \frac{4}{3} V_{\parallel n} \right) \right], \end{aligned} \tag{2.92}$$

$$\begin{aligned}\frac{\partial T_i}{\partial t} =& -\frac{\rho_*^{-1}}{B}[\phi, T_i] - V_{\parallel i}\nabla_\parallel T_i + \frac{4}{3}\frac{T_i}{B}\left[C(T_e) + \frac{T_e}{n}C(n) - C(\phi)\right] - \frac{10}{3}\tau\frac{T_i}{B}C(T_i)\\ &+ \frac{2}{3}T_i\left[(V_{\parallel i} - V_{\parallel e})\frac{\nabla_\parallel n}{n} - \nabla_\parallel V_{\parallel e}\right] + \nabla_\parallel(\chi_{\parallel i}\nabla_\parallel T_i) + D_{T_i}\nabla_\perp^2 T_i + s_{T_i}\\ &+ 2.61\nu n(T_e - \tau T_i) + \frac{n_{\rm n}}{n}(\nu_{\rm iz} + \nu_{\rm cx})\left[T_n - T_i + \frac{1}{3}(V_{\parallel n} - V_{\parallel i})^2\right], \end{aligned} \tag{2.93}$$

and

$$\nabla \cdot \left(n\nabla_\perp\phi\right) = \Omega - \tau\nabla_\perp^2 p_i\,, \tag{2.94}$$

$$\left(\nabla_\perp^2 - \frac{\beta_{e0}}{2}\frac{m_i}{m_e}n\right)V_{\parallel e} = \nabla_\perp^2 U_{\parallel e} - \frac{\beta_{e0}}{2}\frac{m_i}{m_e}nV_{\parallel i} + \frac{\beta_{e0}}{2}\frac{m_i}{m_e}\bar{j}_\parallel\,, \tag{2.95}$$

where the density, n, is normalized to the reference density n_0, the electron and ion temperatures, T_e and T_i, are normalized to the reference values T_{e0} and T_{i0}, respectively, the electron and ion parallel velocities, $V_{\parallel e}$ and $V_{\parallel i}$, are normalized to the reference sound speed $c_{s0} = \sqrt{T_{e0}/m_i}$, the magnetic field is normalized to its modulus B_0 at the tokamak magnetic axis, the electrostatic potential, ϕ, is normalized to T_{e0}/e and ψ is normalized to $\rho_{s0}B_0$, with $\rho_{s0} = c_{s0}/\Omega_{ci}$ the reference ion sound Larmor radius. Perpendicular lengths are normalized to ρ_{s0} and parallel lengths are normalized to the tokamak major radius, R_0. Time is normalized to R_0/c_{s0}. The dimensionless parameters that regulate the system dynamics are the normalized ion sound Larmor radius, $\rho_* = \rho_{s0}/R_0$, the ion to electron reference temperature ratio, $\tau = T_{i0}/T_{e0}$, the normalized electron and ion parallel thermal conductivities,

$$\chi_{\parallel e} = \left(\frac{1.58}{\sqrt{2\pi}}\frac{m_i}{\sqrt{m_e}}\frac{(4\pi\epsilon_0)^2}{e^4}\frac{c_{s0}}{R_0}\frac{T_{e0}^{3/2}}{\lambda n_0}\right)T_e^{5/2} \tag{2.96}$$

and

$$\chi_{\parallel i} = \left(\frac{1.94}{\sqrt{2\pi}}\sqrt{m_i}\frac{(4\pi\epsilon_0)^2}{e^4}\frac{c_{s0}}{R_0}\frac{T_{e0}^{3/2}\tau^{5/2}}{\lambda n_0}\right)T_i^{5/2}\,, \tag{2.97}$$

the reference electron plasma β, $\beta_{e0} = 2\mu_0 n_0 T_{e0}/B_0^2$, and the normalized Spitzer resistivity, $\nu = e^2 n_0 R_0/(m_i c_{s0}\sigma_\parallel) = \nu_0 T_e^{-3/2}$, with

$$\sigma_\parallel = \left(1.96\frac{n_0 e^2\tau_e}{m_e}\right)n = \left(\frac{5.88}{4\sqrt{2\pi}}\frac{(4\pi\epsilon_0)^2}{e^2}\frac{T_{e0}^{3/2}}{\lambda\sqrt{m_e}}\right)T_e^{3/2} \tag{2.98}$$

and

$$\nu_0 = \frac{4\sqrt{2\pi}}{5.88}\frac{e^4}{(4\pi\epsilon_0)^2}\frac{\sqrt{m_e}R_0 n_0\lambda}{m_i c_{s0}T_{e0}^{3/2}}\,, \tag{2.99}$$

where λ is the Coulomb logarithm. Normalized GBS units will be used throughout the present thesis when presenting results from GBS simulations.

When the Boussinesq approximation is considered, the spatial and time dependence of the density in the polarization velocity is neglected, with a substantial simplification in the numerical treatment of the Poisson equation. In fact, in this case Eq. (2.94) becomes

$$\nabla_\perp^2 \phi = \omega - \tau \nabla_\perp^2 T_i \,. \tag{2.100}$$

and the vorticity equation, Eq. (2.89), reduces to

$$\begin{aligned}\frac{\partial \omega}{\partial t} =& -\frac{\rho_*^{-1}}{B}[\phi, \omega] - V_{\parallel i}\nabla_\parallel \omega + \frac{B^2}{n}\nabla_\parallel j_\parallel + \frac{2B}{n}C(p_e + p_i) \\ &+ \frac{B}{3n}C(G_i) + D_\omega \nabla_\perp^2 \omega - \frac{n_\mathrm{n}}{n}\nu_{cx}\omega \,,\end{aligned} \tag{2.101}$$

where ω is defined by Eq. (2.100). Although the Boussinesq approximation is often applied in tokamak boundary turbulence simulations, see e.g. Refs. [10, 17, 160, 170, 245], its validity cannot be taken for granted, especially in the tokamak edge where steep density gradients can form. The effect of this approximation on plasma turbulence and equilibrium profiles is discussed in Ch. 5.

2.4.2 The GBS neutral model

The implementation in GBS of the neutral model described in Sec. 2.2 is detailed in Ref. [237] for limited configurations. Here, this model is extended to the simulation of diverted configurations. The boundary conditions of the neutral model of Ref. [237] are also improved by including the contribution of the $\mathbf{E} \times \mathbf{B}$ and diamagnetic fluxes to the ion flux to the wall.

In the limit where the turbulent timescale is much longer than the typical time of flight of neutrals, $\tau_\mathrm{turb} \gg \tau_n$, the neutral adiabatic approximation can be applied. This corresponds to imposing $\partial_t f_\mathrm{n} = 0$ in Eq. (2.1). Moreover, we assume that the neutral mean free path is shorter than the typical parallel scale lengths of the plasma structures. Under these assumptions, the formal solution of Eq. (2.1) can be obtained by using the method of characteristics [237],

$$\begin{aligned}f_\mathrm{n}(\mathbf{x}_\perp, x_\parallel, \mathbf{v}, t) = \int_0^{r_{\perp b}} &\left[\frac{S(\mathbf{x}'_\perp, x_\parallel, \mathbf{v}, t)}{v_\perp} + \delta(r'_\perp - r_{\perp b}) f_\mathrm{n}(\mathbf{x}'_{\perp b}, x_\parallel, \mathbf{v}, t)\right] \\ &\times \exp\left[-\frac{1}{v_\perp}\int_0^{r'_\perp} \nu_\mathrm{eff}(\mathbf{x}''_\perp, x_\parallel, t)\mathrm{d}r''_\perp\right]\mathrm{d}r'_\perp \,,\end{aligned} \tag{2.102}$$

where we express a position $\mathbf{x}$ in terms of $\mathbf{x}_\perp$, the coordinate on the plane perpendicular to $\mathbf{B}$, and $x_\parallel$, the coordinate parallel to $\mathbf{B}$, $r'_\perp$ is the coordinate along the neutral characteristic defined by $\mathbf{x}'_\perp = \mathbf{x}_\perp - r'_\perp \mathbf{v}_\perp / \mathrm{v}_\perp$, $r_{\perp b}$ denotes the distance along the characteristic from the position $\mathbf{x}$ and the wall, $\mathbf{v}_\perp$ is the component of the velocity perpendicular to $\mathbf{B}$, and $\nu_\mathrm{eff} = \nu_\mathrm{iz} + \nu_\mathrm{cx}$ is the effective collision frequency for neutral loss. In the following, we drop the parametric dependencies on t and $x_\parallel$ to simplify the notation.

The volumetric source term in Eq. (2.102) results from charge-exchange and recombination processes and is given by [237]

$$S(\mathbf{x}'_\perp, \mathbf{v}) = \nu_{\mathrm{cx}}(\mathbf{x}'_\perp) n_{\mathrm{n}}(\mathbf{x}'_\perp) \Phi_i(\mathbf{x}'_\perp, \mathbf{v}) + \nu_{\mathrm{rec}}(\mathbf{x}'_\perp) f_i(\mathbf{x}'_\perp, \mathbf{v}) \,, \tag{2.103}$$

where $\Phi_i = [m_i/(2\pi T_i)]^{3/2} \exp[-m_i \mathrm{v}^2/(2T_i)]$ is the ion velocity distribution. The source of neutrals at the wall, $\delta(r'_\perp - r_{\perp b}) f_{\mathrm{n}}(\mathbf{x}'_{\perp b}, x_\parallel, \mathbf{v}, t)$, is given by the boundary conditions in Eq. (2.5).

The ion recycling term present in the boundary conditions and the recombination term appearing in $S(\mathbf{x}'_\perp, \mathbf{v})$ (see Eqs. (2.5) and (2.103)) do not depend on the neutral distribution function and can be computed directly from the plasma quantities. On the other hand, the charge-exchange term in $S(\mathbf{x}'_\perp, \mathbf{v})$, as well as the reflected and re-emitted neutrals in the boundary conditions (see Eqs. (2.5) and (2.103)), depend on $n_{\mathrm{n}}(\mathbf{x}_\perp) = \int f_{\mathrm{n}} \mathrm{d}\mathbf{v}$. This suggests to integrate Eq. (2.102). In fact, Ref. [237] shows that, by integrating Eq. (2.102), a linear integral equation for $n_{\mathrm{n}}(\mathbf{x}_\perp)$ is obtained,

$$\begin{aligned} n_{\mathrm{n}}(\mathbf{x}_\perp) = & \int_D n_{\mathrm{n}}(\mathbf{x}'_\perp) \nu_{\mathrm{cx}}(\mathbf{x}'_\perp) K_{p\to p}(\mathbf{x}_\perp, \mathbf{x}'_\perp) \mathrm{d}A' \\ & + \int_{\partial D} (1 - \alpha_{\mathrm{refl}}) \Gamma_{\mathrm{out,n}}(\mathbf{x}'_{\perp b}) K_{b\to p}(\mathbf{x}_\perp, \mathbf{x}'_{\perp b}, T_b) \mathrm{d}a'_b \\ & + n_{\mathrm{n[out,i]}}(\mathbf{x}_\perp) + n_{\mathrm{n[rec]}}(\mathbf{x}_\perp) \,, \end{aligned} \tag{2.104}$$

where $\mathrm{d}A'$ is the infinitesimal area in the poloidal plane D, $\mathrm{d}a'_b$ is the infinitesimal length along the boundary ∂D, and $\Gamma_{\mathrm{out,n}}(\mathbf{x}_{\perp b})$ is the neutral flux towards the wall,

$$\begin{aligned} \Gamma_{\mathrm{out,n}}(\mathbf{x}_{\perp b}) = & \int_D n_{\mathrm{n}}(\mathbf{x}'_\perp) \nu_{\mathrm{cx}}(\mathbf{x}'_\perp) K_{p\to b}(\mathbf{x}_{\perp b}, \mathbf{x}'_\perp) \mathrm{d}A' \\ & + \int_{\partial D} (1 - \alpha_{\mathrm{refl}}) \Gamma_{\mathrm{out,n}}(\mathbf{x}'_{\perp b}) K_{b\to b}(\mathbf{x}_{\perp b}, \mathbf{x}'_{\perp b}, T_b) \mathrm{d}a'_b \\ & + \Gamma_{\mathrm{out,n[out,i]}}(\mathbf{x}_{\perp b}) + \Gamma_{\mathrm{out,n[rec]}}(\mathbf{x}_{\perp b}) \,. \end{aligned} \tag{2.105}$$

The contribution to the neutral density due to the ion recycling at the wall and recombination events in Eq. (2.104), $n_{\mathrm{n[out,i]}}$ and $n_{\mathrm{n[rec]}}$, as well as the corresponding contribution to the neutral flux in Eq. (2.105), $\Gamma_{\mathrm{out,n[out,i]}}$ and $\Gamma_{\mathrm{out,n[rec]}}$, are defined as

$$\begin{aligned} n_{\mathrm{n[out,i]}}(\mathbf{x}_\perp) = & \int_{\partial D} \Gamma_{\mathrm{out,i}}(\mathbf{x}'_{\perp b}) \Big[(1 - \alpha_{\mathrm{refl}}) K_{b\to p}(\mathbf{x}_\perp, \mathbf{x}'_{\perp b}, T_b) \\ & + \alpha_{\mathrm{refl}} K_{b\to p}(\mathbf{x}_\perp, \mathbf{x}'_{\perp b}, T_i) \Big] \mathrm{d}a'_b \,, \end{aligned} \tag{2.106}$$

$$n_{\mathrm{n[rec]}}(\mathbf{x}_\perp) = \int_D n_i(\mathbf{x}'_\perp) \nu_{\mathrm{rec}}(\mathbf{x}'_\perp) K_{p\to p}(\mathbf{x}_\perp, \mathbf{x}'_\perp) \mathrm{d}A' \,, \tag{2.107}$$

$$\begin{aligned}\Gamma_{\text{out,n[out,i]}}(\mathbf{x}_{\perp b}) = \int_{\partial D} \Gamma_{\text{out,i}}(\mathbf{x}'_{\perp b})\Big[&(1-\alpha_{\text{refl}})K_{b\to b}(\mathbf{x}_{\perp b},\mathbf{x}'_{\perp b},T_b) \\ &+\alpha_{\text{refl}}K_{b\to b}(\mathbf{x}_{\perp b},\mathbf{x}'_{\perp b},T_i)\Big]\mathrm{d}a'_b\,, \qquad (2.108)\end{aligned}$$

$$\Gamma_{\text{out,n[rec]}}(\mathbf{x}_{\perp b}) = \int_D n_i(\mathbf{x}'_\perp)\nu_{\text{rec}}(\mathbf{x}'_\perp)K_{p\to b}(\mathbf{x}_{\perp b},\mathbf{x}'_\perp)\mathrm{d}A'\,. \qquad (2.109)$$

Generalizing Ref. [237], the ion flux projected in the direction perpendicular to the wall, $\Gamma_{\text{out,i}}$, is evaluated by considering the ion parallel flux and the perpendicular fluxes due to the $\mathbf{E}\times\mathbf{B}$ and the diamagnetic drifts, that is

$$\Gamma_{\text{out,i}}(\mathbf{x}_{\perp b}) = -n_i(\mathbf{x}_{\perp b})\Big[V_{\parallel i}(\mathbf{x}_{\perp b})\mathbf{b}+\mathbf{V}_E(\mathbf{x}_{\perp b})+\mathbf{V}_{di}(\mathbf{x}_{\perp b})\Big]\cdot\hat{\mathbf{n}}\,. \qquad (2.110)$$

The kernel functions, appearing in Eqs. (2.104) and (2.105), involve integrals in the velocity space, and can be developed as

$$\begin{aligned}K_{p\to p}(\mathbf{x}_\perp,\mathbf{x}'_\perp) &= K^{\text{dir}}_{p\to p}(\mathbf{x}_\perp,\mathbf{x}'_\perp)+\alpha_{\text{refl}}K^{\text{refl}}_{p\to p}(\mathbf{x}_\perp,\mathbf{x}'_\perp)\,, &(2.111)\\ K_{b\to p}(\mathbf{x}_\perp,\mathbf{x}'_{\perp b},T) &= K^{\text{dir}}_{b\to p}(\mathbf{x}_\perp,\mathbf{x}'_{\perp b},T)+\alpha_{\text{refl}}K^{\text{refl}}_{b\to p}(\mathbf{x}_\perp,\mathbf{x}'_{\perp b},T)\,, &(2.112)\\ K_{p\to b}(\mathbf{x}_{\perp b},\mathbf{x}'_\perp) &= K^{\text{dir}}_{p\to b}(\mathbf{x}_{\perp b},\mathbf{x}'_\perp)+\alpha_{\text{refl}}K^{\text{refl}}_{p\to b}(\mathbf{x}_{\perp b},\mathbf{x}'_\perp)\,, &(2.113)\\ K_{b\to b}(\mathbf{x}_{\perp b},\mathbf{x}'_{\perp b},T) &= K^{\text{dir}}_{b\to b}(\mathbf{x}_{\perp b},\mathbf{x}'_{\perp b},T)+\alpha_{\text{refl}}K^{\text{refl}}_{b\to b}(\mathbf{x}_{\perp b},\mathbf{x}'_{\perp b},T)\,, &(2.114)\end{aligned}$$

where we consider the direct path between two points as well as the paths that include one reflection at the wall (we neglect paths with multiple reflections as $\lambda_n/L<1$, with λ_n the averaged neutral mean free path and L the typical machine size in poloidal plane). We define, for path = {dir, refl},

$$K^{\text{path}}_{p\to p}(\mathbf{x}_\perp,\mathbf{x}'_\perp) = \int_0^\infty \frac{1}{r'_\perp}\Phi_{\perp i}(\mathbf{x}'_\perp,\mathbf{v}_\perp)\exp\left[-\frac{1}{v_\perp}\int_0^{r'_\perp}\nu_{\text{eff}}(\mathbf{x}''_\perp)\mathrm{d}r''_\perp\right]\mathrm{d}v_\perp\,, \qquad (2.115)$$

$$K^{\text{path}}_{b\to p}(\mathbf{x}_\perp,\mathbf{x}'_{\perp b},T) = \int_0^\infty \frac{v_\perp}{r'_\perp}\cos\theta'\chi_{\perp\text{in}}(\mathbf{x}'_{\perp b},\mathbf{v}_\perp,T)\exp\left[-\frac{1}{v_\perp}\int_0^{r'_\perp}\nu_{\text{eff}}(\mathbf{x}''_\perp)\mathrm{d}r''_\perp\right]\mathrm{d}v_\perp\,, \qquad (2.116)$$

$$K^{\text{path}}_{p\to b}(\mathbf{x}_{\perp b},\mathbf{x}'_\perp) = \int_0^\infty \frac{v_\perp}{r'_\perp}\cos\theta\Phi_{\perp i}(\mathbf{x}'_\perp,\mathbf{v}_\perp)\exp\left[-\frac{1}{v_\perp}\int_0^{r'_\perp}\nu_{\text{eff}}(\mathbf{x}''_\perp)\mathrm{d}r''_\perp\right]\mathrm{d}v_\perp\,, \qquad (2.117)$$

$$K^{\text{path}}_{b\to b}(\mathbf{x}_{\perp b},\mathbf{x}'_{\perp b},T) = \int_0^\infty \frac{v_\perp^2}{r'_\perp}\cos\theta\cos\theta'\chi_{\perp\text{in}}(\mathbf{x}'_b,\mathbf{v}_\perp,T)\exp\left[-\frac{1}{v_\perp}\int_0^{r'_\perp}\nu_{\text{eff}}(\mathbf{x}''_\perp)\mathrm{d}r''_\perp\right]\mathrm{d}v_\perp\,, \qquad (2.118)$$

with $\Phi_{\perp i}(\mathbf{x}_\perp,\mathbf{v}_\perp)=\int\Phi_i(\mathbf{x}_\perp,\mathbf{v})\mathrm{d}v_\parallel = m_i/(2\pi T_i)\exp[-m_iv_\perp^2/(2T_i)]$ and $\chi_{\perp\text{in}}(\mathbf{x}_\perp,\mathbf{v}_\perp)=\int\chi_{\text{in}}(\mathbf{x}_\perp,\mathbf{v})\mathrm{d}v_\parallel = 3m_i^2/(4\pi T_i^2)v_\perp\cos\theta\exp[-m_iv_\perp^2/(4T_i)]\mathcal{K}_0[m_iv_\perp^2/(4T_i)]$, being $\mathcal{K}_0(x)$ the modified Bessel function of the second kind. The vector $\mathbf{x}''_\perp$ indicates a position along the path from the source to the target points. The four kernels represent the

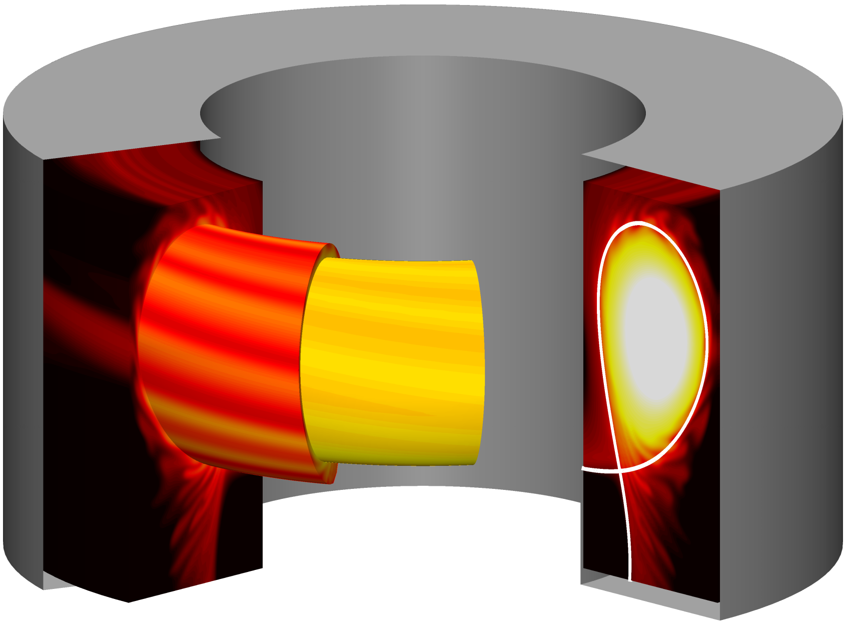

Figure 2.1 – Representation of a three dimensional time snapshot of the plasma electron pressure, $p_e = nT_e$, from a GBS simulation. The domain encompasses the whole tokamak volume, and develops over the complete toroidal angle and poloidal cross section. The white line denotes the separatrix. The magnetic equilibrium is given by the equilibrium reconstruction of the TCV discharge #65402 at time 1.0 s.

four possibilities for neutral particles of being generated within the plasma, p, or at the boundary, b, and reach a point also in the plasma or in the boundary.

We note that a neutral flux can be externally imposed by means of a gas puff that introduces a localized source of neutrals [237]. Similarly, a pumping region on the wall can also be considered. This can be simply implemented by multiplying the kernel functions, $K_{b\to p}$ and $K_{b\to b}$, by a recycling coefficient smaller than one [129].

2.4.3 Differential operators

The differential operators in Eqs. (2.80)–(2.83) are written in the (R, φ, Z) cylindrical non-field-aligned coordinate system, where R is the distance from the axis of symmetry of the torus, Z is the vertical coordinate, and φ is the toroidal angle. The poloidal cross section has a rectangular shape, particularly suitable for the simulation of the TCV tokamak, and the domain encompasses the whole plasma volume. A representation of the GBS domain is shown in Fig. 2.1.

The toroidally symmetric equilibrium magnetic field, used to compute the GBS differential operators, is written in terms of the poloidal magnetic flux Ψ, as

$$\mathbf{B} = RB_\varphi \nabla\varphi + \nabla\varphi \times \nabla\Psi \,. \tag{2.119}$$

The poloidal magnetic flux is a function of R and Z, and can be provided as an analytical function, an equilibrium reconstruction, or as the result of a Grad-Shafranov solver. As an example, the magnetic separatrix of a TCV equilibrium reconstruction is shown in Fig. 2.1.

The spatial differential operators in Eqs. (2.72)–(2.79) are written in (R, φ, Z) coordinates. They are expanded in the large aspect ratio limit, $\epsilon \sim r/R_0 \ll 1$, assuming the poloidal component of the magnetic field smaller than the toroidal one, $\delta \sim B_p/B_\varphi \ll 1$, with a safety factor at the midplane $q \sim \epsilon/\delta$ of order unity. Only the leading order terms in ϵ and δ are retained.

In the following, we derive the expression of the operators as they are implemented in GBS. As a first step, we note that, at zeroth-order in ϵ and δ, the modulus of the magnetic field is constant,

$$\frac{B^2}{B_0^2} = \frac{B_R^2}{B_0^2} + \frac{B_Z^2}{B_0^2} + \frac{B_\varphi^2}{B_0^2} = \frac{B_\varphi^2}{B_0^2} + O(\delta^2) = 1 + O(\epsilon, \delta^2) \,, \tag{2.120}$$

where the magnetic field is written as

$$\mathbf{B} = B_R \mathbf{e}_R + B_Z \mathbf{e}_Z + B_\varphi \mathbf{e}_\varphi \,, \tag{2.121}$$

with $\mathbf{e}_R$, $\mathbf{e}_Z$ and $\mathbf{e}_\varphi$ the basis vectors. Hence, the Poisson brackets, Eq. (2.80), can be written as

$$\begin{aligned}
[\phi, f] &= \mathbf{b} \cdot \nabla\phi \times \nabla f \\
&= \mathbf{b} \cdot \left[\left(\partial_R \phi \, \mathbf{e}_R + \partial_Z \phi \, \mathbf{e}_Z + \frac{1}{R} \partial_\varphi \phi \, \mathbf{e}_\varphi \right) \times \left(\partial_R f \, \mathbf{e}_R + \partial_Z f \, \mathbf{e}_Z + \frac{1}{R} \partial_\varphi f \, \mathbf{e}_\varphi \right) \right] \\
&= \frac{1}{R} \frac{B_R}{B} (\partial_\varphi \phi \, \partial_Z f - \partial_Z \phi \, \partial_\varphi f) + \frac{1}{R} \frac{B_Z}{B} (\partial_R \phi \, \partial_\varphi f - \partial_\varphi \phi \, \partial_R f) + \frac{B_\varphi}{B} (\partial_Z \phi \, \partial_R f - \partial_R \phi \, \partial_Z f) \,,
\end{aligned} \tag{2.122}$$

which, in dimensionless units, leads to

$$\begin{aligned}
[\phi, f] &= \frac{\rho_{s0}}{R} \frac{B_R}{B} (\partial_\varphi \phi \, \partial_Z f - \partial_Z \phi \, \partial_\varphi f) + \frac{\rho_{s0}}{R} \frac{B_Z}{B} (\partial_R \phi \, \partial_\varphi f - \partial_\varphi \phi \, \partial_R f) + \frac{B_\varphi}{B} (\partial_Z \phi \, \partial_R f - \partial_R \phi \, \partial_Z f) \\
&= \frac{B_\varphi}{B} (\partial_Z \phi \, \partial_R f - \partial_R \phi \, \partial_Z f) + O(\epsilon, \delta) \,,
\end{aligned} \tag{2.123}$$

since $B_Z/B \sim B_R/B \sim \delta$ and $\rho_{s0}/R \sim \rho_* \ll \epsilon$.

Neglecting local current and therefore assuming $\nabla \times \mathbf{B} = 0$, the curvature operator, Eq. (2.81), is expanded in ϵ and δ as

$$C(f) = \frac{1}{2B}\left(\frac{B_\varphi}{B^2}\partial_Z B^2 \partial_R f - \frac{B_\varphi}{B^2}\partial_R B^2 \partial_Z f\right) + O(\epsilon, \delta)\,. \tag{2.124}$$

The spatial derivatives $\partial_Z B^2$ and $\partial_R B^2$ can be determined by using Eq. (2.120),

$$\frac{\partial_Z B^2}{B_0^2} = \frac{\partial}{\partial Z}\left(\frac{R_0}{R}\right)^2 + O(\delta^2) = 0 + O(\delta^2) \tag{2.125}$$

$$\frac{\partial_R B^2}{B_0^2} = \frac{\partial}{\partial R}\left(\frac{R_0}{R}\right)^2 + O(\delta^2) = -2\frac{R_0^2}{R^3} + O(\delta^2) = -\frac{2}{R} + O(\epsilon, \delta^2)\,, \tag{2.126}$$

where we use $B_\varphi^2/B_0^2 = R_0^2/R^2 = 1 + O(\epsilon)$. Finally, by keeping only the leading order terms in ϵ and δ, the curvature operator, normalized to $1/(R_0\rho_{s0})$, becomes

$$C(f) = \frac{B_\varphi}{B_0}\partial_Z f + O(\epsilon, \delta)\,. \tag{2.127}$$

The parallel gradient, Eq. (2.82), is normalized to $1/R_0$ and, in dimensionless units, is given by

$$\begin{aligned}\nabla_\parallel f = \frac{\mathbf{B}}{B}\cdot\nabla f &= \rho_*^{-1}\left(\frac{B_R}{B}\partial_R f + \frac{B_Z}{B}\partial_Z f + \frac{B_\varphi}{B}\frac{\rho_{s0}}{R}\partial_\varphi f\right)\\ &= \partial_Z\Psi\,\partial_R f - \partial_R\Psi\,\partial_Z f + \frac{B_\varphi}{B_0}\partial_\varphi f + O(\epsilon, \delta)\,,\end{aligned} \tag{2.128}$$

where $B_R = \partial_Z\Psi/R$, $B_Z = -\partial_R\Psi/R$.

The perpendicular laplacian, Eq. (2.83), can be developed as

$$\nabla_\perp^2 f = \nabla\cdot\left[\frac{1}{B^2}(\mathbf{B}\times\nabla f)\times\mathbf{B}\right] = \frac{1}{B^2}\nabla\cdot\Big[(\mathbf{B}\times\nabla f)\times\mathbf{B}\Big] - \frac{\nabla B^2}{B^4}\cdot\Big[(\mathbf{B}\times\nabla f)\times\mathbf{B}\Big]\,. \tag{2.129}$$

The second term on the right-hand side of Eq. (2.129) is one order ϵ smaller than the first one, which can be written in cylindrical coordinates as

$$\begin{aligned}(\mathbf{B}\times\nabla f)\times\mathbf{B} = &\left(B_Z^2\partial_R f - B_Z B_R \partial_Z f - \frac{B_R B_\varphi}{R}\partial_\varphi f + B_\varphi^2\partial_R f\right)\mathbf{e}_R\\ &+\left(B_\varphi^2\partial_Z f - \frac{B_Z B_\varphi}{R}\partial_\varphi f - B_Z B_R\partial_R f + B_R^2\partial_Z f\right)\mathbf{e}_Z\\ &+\left(\frac{B_R^2}{R}\partial_\varphi f - B_\varphi B_R\partial_R f - B_\varphi B_Z\partial_Z f + \frac{B_Z^2}{R}\partial_\varphi f\right)\mathbf{e}_\varphi\,,\end{aligned} \tag{2.130}$$

and expanded in ϵ and δ,

$$(\mathbf{B}\times\nabla f)\times\mathbf{B}\simeq\frac{B_\varphi^2}{B^2}\partial_R f\,\mathbf{e}_R+\frac{B_\varphi^2}{B^2}\partial_Z f\,\mathbf{e}_Z+O(\epsilon,\delta)\,. \tag{2.131}$$

Thus, the leading order terms of Eq. (2.131) can be expressed as

$$\nabla_\perp^2 f=\partial_{RR}^2 f+\partial_{ZZ}^2 f+O(\epsilon,\delta)\,. \tag{2.132}$$

In addition to the differential operators given by Eqs. (2.80)–(2.83), there are three operators appearing in Eqs. (2.72)–(2.77) that can be derived from Eqs. (2.80)–(2.83) by applying the same ordering in ϵ and δ: the parallel laplacian, $\nabla_\parallel^2 f$, the curvature of the parallel gradient, $C(\nabla_\parallel f)$, and the parallel gradient of the curvature, $\nabla_\parallel[C(f)]$. In dimensionless units, the parallel laplacian is given by

$$\begin{aligned}\nabla_\parallel^2 f=&\Big(\partial_Z\Psi\partial_{RZ}^2\Psi-\partial_R\Psi\partial_{ZZ}^2\Psi\Big)\partial_R f+\Big(\partial_R\Psi\partial_{RZ}^2\Psi-\partial_Z\Psi\partial_{RR}^2\Psi\Big)\partial_Z f\\&+\Big[(\partial_Z\Psi)^2\partial_{RR}^2 f+(\partial_R\Psi)^2\partial_{ZZ}^2 f-2\partial_Z\Psi\partial_R\Psi\partial_{RZ}^2 f\Big]\\&+2\frac{B_\varphi}{B}\partial_Z\Psi\partial_{\varphi R}^2 f-2\frac{B_\varphi}{B}\partial_R\Psi\partial_{\varphi Z}^2 f+\partial_{\varphi\varphi}^2 f+O(\epsilon,\delta)\,,\end{aligned} \tag{2.133}$$

the curvature of the parallel gradient by

$$C(\nabla_\parallel f)=\frac{B_\varphi}{B}\Big(\partial_{ZZ}\Psi\partial_R f+\partial_Z\Psi\partial_{RZ}f-\partial_{RZ}\Psi\partial_Z f-\partial_R\Psi\partial_{ZZ}f\Big)+\partial_{Z\varphi}f+O(\epsilon,\delta)\,, \tag{2.134}$$

and the parallel gradient of the curvature by

$$\nabla_\parallel[C(f)]=\frac{B_\varphi}{B}\partial_Z\Psi\partial_{RZ}f-\frac{B_\varphi}{B}\partial_R\Psi\partial_{ZZ}f+\partial_{Z\varphi}f+O(\epsilon,\delta)\,. \tag{2.135}$$

In summary, the differential operators implemented in GBS (in normalized units) are

$$[\phi,f]=\frac{B_\varphi}{B}(\partial_Z\phi\partial_R f-\partial_R\phi\partial_Z f)\,, \tag{2.136}$$

$$C(f)=\frac{B_\varphi}{B}\partial_Z f\,, \tag{2.137}$$

$$\nabla_\parallel f=\partial_Z\Psi\partial_R f-\partial_R\Psi\partial_Z f+\frac{B_\varphi}{B}\partial_\varphi f \tag{2.138}$$

and

$$\nabla_\perp^2 f=\partial_{RR}^2 f+\partial_{ZZ}^2 f\,. \tag{2.139}$$

2.4.4 Boundary and initial conditions

The large electric field established on the ρ_s scale in the magnetic pre-sheath violates the hypothesis behind the drift-approximation. Consequently, the boundary conditions are applied at the magnetic pre-sheath entrance in the GBS code. The set of generalized Bohm-Chodura sheath boundary conditions implemented in GBS was originally derived in Ref. [123] in the cold ion limit and extended in Ref. [148] to include warm ions. In this version of GBS, we neglect the correction terms arising from the variation of the density and electrostatic potential in the direction tangent to the wall, and we apply the magnetic pre-sheath boundary conditions at the walls containing the strike points, i.e. the walls where the divertor legs terminate. For instance, in the case of the TCV magnetic equilibrium shown in Fig. 2.1, magnetic pre-sheath boundary conditions are applied at the bottom and inner walls. The boundary conditions assume the following form:

$$V_{\parallel i} = \pm\, c_s\sqrt{1+\frac{T_i}{T_e}}\,, \tag{2.140}$$

$$V_{\parallel e} = \pm\, c_s\ \exp\left(\Lambda_0 - \frac{e\phi}{T_e}\right), \tag{2.141}$$

$$\partial_s n = \mp\,\frac{n}{c_s\sqrt{1+\frac{T_i}{T_e}}}\partial_s V_{\parallel i}\,, \tag{2.142}$$

$$\partial_s T_e = \partial_s T_i = \ 0\,, \tag{2.143}$$

$$\Omega = \mp\,\frac{m_i n}{e}c_s\sqrt{1+\frac{T_i}{T_e}}\partial^2_{ss} V_{\parallel i}\,, \tag{2.144}$$

$$\partial_s \phi = \mp\,\frac{m_i c_s}{e\sqrt{1+\frac{T_i}{T_e}}}\partial_s V_{\parallel i}\,, \tag{2.145}$$

where $\Lambda_0 = \log\sqrt{m_i/(2\pi m_e)} \simeq 3$ for hydrogen plasmas, and s denotes the derivative in the direction perpendicular to the wall ($s = Z$ for the top and bottom walls, and $s = R$ for the inner and outer walls). The top (bottom) sign refers to the magnetic field pointing towards (away from) the target plate. In addition to the boundary conditions in Eqs. (2.140)–(2.145), we simply consider $\psi = 0$ at the magnetic pre-sheath entrance. In order to avoid the discontinuity of the parallel velocities at the location where the magnetic field is tangent to the wall, a smoothing function from $+c_s$ to $-c_s$ is applied to guarantee that $V_{\parallel i}$ and $V_{\parallel e}$ vary without strong discontinuities. In these smoothing regions, we also impose $\partial_s|V_{\parallel i}| = 0$ and $\partial^2_{ss}|V_{\parallel i}| = 0$ in Eqs. (2.140)-(2.145), since the derivative normal to the wall of $|V_{\parallel i}|$ can become negative, leading to unphysical boundary conditions for n, ϕ and Ω. We highlight that the smoothing affects less than 2% of the wall surface and is at certain distance from the strike points, therefore it has a negligible effect on the overall dynamics.

The boundary conditions in Eqs. (2.140)-(2.144) are also applied at the walls that do not contain strike points, while the Dirichlet boundary condition $\phi = \Lambda T_e/e$ is used for ϕ, with $\Lambda = \Lambda_0 - \log\sqrt{1+T_i/T_e}$. In fact, Poisson equation is ill-defined if a Neumann boundary condition for the electrostatic potential is applied at the four walls of the domain.

In our analysis, we focus on the quasi-steady state that is established after a transient when sources, parallel and perpendicular transport, as well as losses at the vessel balance each other. As long as this quasi-steady state is statistically independent of the initial conditions, these do not present physical interest. Therefore, as initial condition for our simulations, we impose $\phi = \Lambda T_e/e$, with T_e the initial electron temperature, which is uniform over the entire GBS domain. Also Ω, n, and T_i have initial uniform profiles. The electron and ion parallel velocities are properly designed functions to satisfy the boundary conditions $V_{\|e,i} = \pm c_s\sqrt{1+T_i/T_e}$ with $\partial_s V_{\|e,i} = 0$ at the wall, being s the coordinate perpendicular to it. The constraint $\partial_s V_{\|i} = 0$ at the wall guarantees vanishing Neumann boundary conditions for n, ϕ, ω, in agreement with the uniform initial profiles of these quantities. Random noise is added to all fields to trigger the turbulent dynamics.

2.5 Numerical implementation and optimization of the GBS model

While the time evolution is provided by a fourth-order Runge-Kutta algorithm and the spatial discretization by a fourth-order centered finite differences scheme, similarly to the GBS diverted version of Ref. [160], GBS now relies on an optimized iterative solver for the Poisson and Ampère equations. In addition, the kinetic neutral model, initially developed in the limited version of GBS [87, 237] and ported here to the diverted geometry, is significantly optimized.

The workflow of GBS is shown in Fig. 2.2. Following the initialization of the simulation, plasma and neutral modules are run simultaneously. Each Runge-Kutta substep, used to advance the GBS plasma equations, performs three tasks (see the grey area of Fig. 2.2). First, the boundary conditions are applied to every plasma quantity and the necessary spatial operators are applied to the plasma fields. Then, the right-hand side of the drift-reduced Braginskii equations is evaluated and Eqs. (2.72)–(2.77) are advanced, updating the values of n, T_e, T_i, Ω, $U_{\|e}$ and $V_{\|i}$. Finally, the Poisson and Ampère equations, Eqs. (2.78) and (2.79), are numerically solved to update ϕ and ψ. After every Runge-Kutta time step (see the blue area of Fig. 2.2), the plasma module checks if the neutral calculation is completed and updates the value of the neutral-related terms in Eqs. (2.72)–(2.77) with the result of the new neutral calculation, if available. In parallel to the plasma evolution, the neutral density, temperature and velocity are computed by the neutral module (red area in Fig. 2.2). At the beginning of each neutral calculation, GBS computes the reaction rates, Eqs. (2.2)–(2.4), by using the current plasma quantities. Then, it evaluates the kernel functions, Eqs. (2.111)–(2.114), and finally it computes the neutral density, temperature and velocity by solving Eq. (2.104). After every neutral

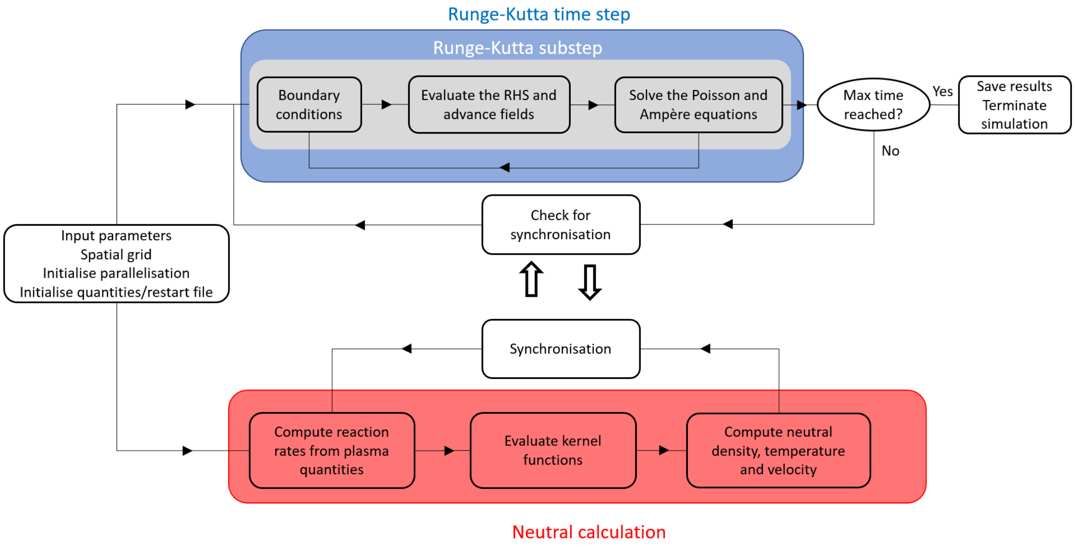
Runge-Kutta time step
Runge-Kutta substep
Boundary conditions
Evaluate the RHS and advance fields
Solve the Poisson and Ampère equations
Max time reached?
Yes
Save results
Terminate simulation
No
Check for synchronisation
Input parameters
Spatial grid
Initialise parallelisation
Initialise quantities/restart file
Synchronisation
Compute reaction rates from plasma quantities
Evaluate kernel functions
Compute neutral density, temperature and velocity
Neutral calculation

Figure 2.2 – Workflow of the GBS code. The grey and blue areas highlight a Runge-Kutta substep and step, respectively, for the solution of the plasma equations. After every Runge-Kutta time step the plasma module checks if updated values of the neutral quantities are available. The workflow of a neutral calculation is highlighted by the red area. The synchronization is performed at the end of each neutral calculation.

calculation, the plasma and neutral modules synchronize, and the values of the plasma density, electron and ion temperatures used to compute the reaction rates is updated. The minimum neutral calculation frequency can be imposed in order to guarantee a good convergence of the simulation results, as detailed in Sec. 2.8.

The remainder of this section is structured as follows. First, we describe the spatial discretization of the plasma equations. Then, we focus on the implementation and optimization of the Poisson and Ampère laws. Finally, we report on the implementation and optimization of the neutral model.

2.5.1 Spatial discretization of the plasma equations

All plasma quantities are evaluated on a uniform Cartesian grid, which discretizes the R, Z and φ coordinates, with a size $N_R \times N_Z \times N_\varphi$, where N_R, N_Z and N_φ are the number of grid points in the radial, vertical and toroidal direction, respectively. The grid spacing is denoted as ΔR, ΔZ and $\Delta\varphi$. The grid for n, T_e, T_i, Ω, and ϕ, denoted as ϕ-grid, is staggered in the vertical and toroidal directions with respect to the grid for $V_{\|e}$, $V_{\|i}$ and ψ, which is denoted as v-grid. More precisely, the ϕ-grid is shifted by $\Delta Z/2$ and $\Delta\varphi/2$, along the vertical and toroidal directions, respectively, with respect to the v-grid. The use of staggered grids prevents the formation of checkerboard patterns that can appear when treating an advection problem with a finite centered difference scheme, as shown in Ref. [161]. In the following, we denote a quantity at the position (R_i, φ_j, Z_k) in the v-grid as $f_{i,j,k}$ and a quantity at the position $(R_i, \varphi_{j+\frac{1}{2}}, Z_{k+\frac{1}{2}})$ in the ϕ-grid as $f_{i,j+\frac{1}{2},k+\frac{1}{2}}$. The neutral quantities are also discretized on a uniform grid in the (R, φ, Z) cylindrical coordinate system, $N'_R \times N'_Z \times N'_\varphi$, that is in general coarser than the plasma grid in the poloidal plane ($N'_R < N_R$ and $N'_Z < N_Z$), while the neutral and plasma grid resolutions along the toroidal direction are the same ($N'_\varphi = N_\varphi$). The neutral grid is located at the toroidal position of the ϕ-grid.

The differential operators in Eqs. (2.81)–(2.83) are computed as a linear combination of first and second derivatives along R, Z and φ, with subsequent interpolation between staggered grids, if needed. For instance, the first derivative along Z is discretized at the fourth-order by means of a 5-point stencil as

$$(\partial_Z f)_{i,j,k} = \frac{1}{\Delta Z}\left(\frac{1}{12}f_{i,j,k-2} - \frac{2}{3}f_{i,j,k-1} + \frac{2}{3}f_{i,j,k+1} - \frac{1}{12}f_{i,j,k+2}\right), \tag{2.146}$$

if both the field and its derivative are evaluated on the v-grid. On the other hand, we have

$$(\partial_Z f)_{i,j+\frac{1}{2},k+\frac{1}{2}} = \frac{1}{\Delta Z}\left(\frac{1}{24}f_{i,j,k-1} - \frac{9}{8}f_{i,j,k} + \frac{9}{8}f_{i,j,k+1} - \frac{1}{24}f_{i,j,k+2}\right), \tag{2.147}$$

if the field is evaluated on the v-grid and its derivative on the ϕ-grid. Analogous expressions to Eqs. (2.146) and (2.147) hold for fields evaluated on the ϕ-grid, if their derivatives are evaluated on the ϕ-grid or v-grid, respectively. A quantity evaluated on the v-grid is interpolated to the ϕ-grid by using a fourth-order interpolation,

$$(I_Z f)_{i,j+\frac{1}{2},k+\frac{1}{2}} = -\frac{1}{16}f_{i,j,k-1} + \frac{9}{16}f_{i,j,k} + \frac{9}{16}f_{i,j,k+1} - \frac{1}{16}f_{i,j,k+2}\,, \tag{2.148}$$

and an analogous expression is used to interpolate from the ϕ-grid to the v-grid. The second derivative along Z is discretized by

$$(\partial_{ZZ} f)_{i,j,k} = \frac{1}{\Delta Z^2}\left(-\frac{1}{12}f_{i,j,k-2} + \frac{4}{3}f_{i,j,k-1} - \frac{5}{2}f_{i,j,k} + \frac{4}{3}f_{i,j,k+1} - \frac{1}{12}f_{i,j,k+2}\right), \tag{2.149}$$

if both the field and its derivative are evaluated on the v-grid. Analogous expression holds if both the field and its derivative are evaluated on the ϕ-grid. The Poisson brackets, Eq. (2.80), are discretized by means of a fourth-order Arakawa scheme [162]. We note that the discretization at fourth-order of the curvature-related contributions in the gyroviscous terms, Eqs. (2.86) and (2.87), requires a 7-point stencil because of the presence of second derivatives on the ϕ-grid of a quantity evaluated on the v-grid and vice versa. In order to use a 5-point stencil for all GBS operators, these derivatives are implemented at the second-order. For example, the second derivative on the ϕ-grid of a field evaluated on the

v-grid is given by

$$(\partial_{ZZ} f)_{i,j+\frac{1}{2},k+\frac{1}{2}} = \frac{1}{\Delta Z^2}\left(\frac{1}{2} f_{i,j,k-1} - \frac{1}{2} f_{i,j,k} - \frac{1}{2} f_{i,j,k+1} + \frac{1}{2} f_{i,j,k+2}\right). \tag{2.150}$$

2.5.2 Implementation and optimization of the Poisson and Ampère equations

In Ref. [160], the Boussinesq approximation is applied, thus considerably simplifying the implementation of the Poisson equation, and the electrostatic potential is computed by a direct inversion of the perpendicular laplacian operator, Eq. (2.83), through LU factorization using the external MUMPS library [2]. Despite being computationally demanding, the LU factorization is carried out once for all at the beginning of a simulation and therefore does not significantly impact the cost of a simulation.

In the version of GBS described here, the Boussinesq approximation is avoided, requiring the implementation at fourth-order of the $\nabla \cdot (n\nabla_\perp \phi) = \partial_R(n\partial_R\phi) + \partial_Z(n\partial_Z\phi)$ operator, i.e.

$$\begin{aligned}\Big[\partial_R(n\partial_R\phi)\Big]_{i,j,k} =& \frac{1}{\Delta R^2}\Big(\delta_{i-2,j,k}\phi_{i-2,j,k} + \delta_{i-1,j,k}\phi_{i-1,j,k} + \delta_{i,j,k}\phi_{i,j,k} \\ &+ \delta_{i+1,j,k}\phi_{i+1,j,k} + \delta_{i+2,j,k}\phi_{i+2,j,k}\Big),\end{aligned} \tag{2.151}$$

with

$$\begin{aligned}\delta_{i-2,j,k} =& \frac{n_{i-2,j,k}}{144} - \frac{n_{i-1,j,k}}{18} - \frac{n_{i,j,k}}{12} + \frac{n_{i+1,j,k}}{18} - \frac{n_{i+2,j,k}}{144}, \\ \delta_{i-1,j,k} =& -\frac{n_{i-2,j,k}}{18} + \frac{4n_{i-1,j,k}}{9} + \frac{4n_{i,j,k}}{3} - \frac{4n_{i+1,j,k}}{9} + \frac{n_{i+2,j,k}}{18}, \\ \delta_{i,j,k} =& -\frac{5n_{i,j,k}}{2},\end{aligned} \tag{2.152}$$

$$\begin{aligned}\delta_{i+1,j,k} =& \frac{n_{i-2,j,k}}{18} - \frac{4n_{i-1,j,k}}{9} + \frac{4n_{i,j,k}}{3} + \frac{4n_{i+1,j,k}}{9} - \frac{n_{i+2,j,k}}{18}, \\ \delta_{i+2,j,k} =& -\frac{n_{i-2,j,k}}{144} + \frac{n_{i-1,j,k}}{18} - \frac{n_{i,j,k}}{12} - \frac{n_{i+1,j,k}}{18} + \frac{n_{i+2,j,k}}{144},\end{aligned}$$

and similarly for $\Big[\partial_Z(n\partial_Z\phi)\Big]_{i,j,k}$. Since n depends on time, the δ coefficients vary in time, therefore the matrix that discretizes the Laplacian operator has to be assembled and factorized every time step, leading to a dramatic increase of the computational effort, which becomes prohibitively large already for a medium size grid, such as the one used to simulate a medium size tokamak as TCV, if a LU factorization is used to solve Poisson equation. In fact, an initial profiling of GBS, carried out on a TCV poloidal grid ($N_R \times N_Z = 300 \times 600$), shows that, if the MUMPS direct solver is used, more than

50% of the time used to advance the plasma equations is spent in the factorization of the matrix that discretizes Poisson equation. We note that a similar matrix needs to be assembled and inverted every time step to solve the Ampère equation (see Eq. (2.79)). However, the factorization of the Poisson matrix is computationally more expensive than the factorization of the matrix that discretizes Ampère equation.

In order to avoid the LU factorization and improve GBS performance, an iterative solver is used. We rely on the Data Management for Structured Grids (DMDA) of the PETSc library [9] that provides a flexible framework to implement a large number of solvers and preconditioners. By carrying out a scan on different solvers and preconditioners, analysing more than 2000 combinations, we find that the best performance is achieved with the algebraic multigrid preconditioner `boomerAMG` provided by the external package HYPRE [56] and the deflated `GMRES` solver [233]. In order to fine tune the preconditioner parameters, we focus on the main options of `boomerAMG`, i.e. the strong threshold, the maximum number of levels, the coarsen type, and the interpolation type (see Ref. [56] for details). The best performance is achieved by using a strong threshold of 0.25, a maximum of levels of 30, the `Falgout` coarsen type, and the `ext+i` interpolation type.

In order to evaluate the performance gain arising from the iterative solver implemented with the PETSc library with this set of optimized parameters, we run a set of GBS simulations considering the $N_R \times N_Z = 150 \times 300$, $N_R \times N_Z = 300 \times 600$ and $N_R \times N_Z = 600 \times 1200$ grids. We refer to these grids as the half-TCV, TCV and double-TCV grids, since $N_R \times N_Z = 300 \times 600$ is the typical poloidal grid used for a simulation of a TCV discharge with toroidal magnetic field of 0.9 T [155]. The time to solution per time step is shown in Fig. 2.3 for the different grid sizes. Across all sizes considered here, we observe a speed-up of, approximately, a factor of 40 when the iterative solver is used, with respect to a direct solver, reducing considerably the cost of our simulations and making the simulation at the TCV scales possible, otherwise prohibitively expensive. As an aside, we also note that the solution of the Poisson and Ampère equations using the iterative solver and the evaluation of the right-hand side of Eqs. (2.88)-(2.93) have approximately the same computational cost in the half-TCV and TCV simulations. On the other hand, more than half of the computational time is spent to solve the Poisson equation in the double-TCV simulation, even using the iterative solver (see Fig. 2.3). Simulations at scales larger than TCV require therefore further optimization.

2.5.3 Implementation and optimization of neutral model in diverted geometry

By discretizing the kernel functions, Eqs. (2.111)–(2.114), the equations for the neutral density, Eq. (2.104), and neutral flux to the wall, Eq. (2.105), can be written as a linear

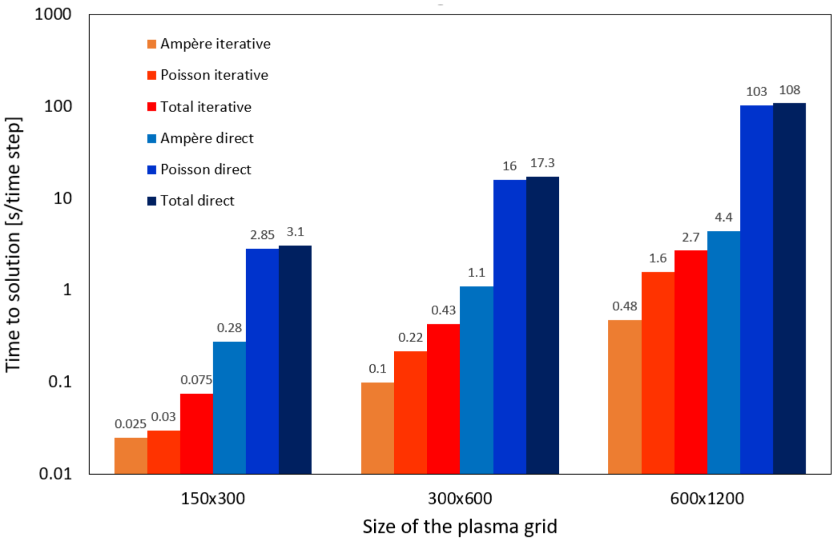

Figure 2.3 – Time to solution per time step averaged from simulations of 10 time steps that consider different poloidal grid sizes. No coupling to neutral dynamics is considered here. The simulations are carried out on one node (36 cores) of the multi-core partition of Piz Daint (Cray XC40 equipped with two 18-core Intel Xeon E5-2695 v4 CPUs at 2.10GHz) and are performed taking as initial conditions the results of a simulation in turbulent state. This allows us to compare the solvers in typical working conditions. The iterative and direct solvers are based on the PETSc and MUMPS libraries, respectively. The time of MUMPS includes the factorization.

system,

$$\begin{bmatrix} n_\mathrm{n} \\ \Gamma_\mathrm{out,n} \end{bmatrix} = \begin{bmatrix} \nu_\mathrm{cx} K_{p\to p} & (1-\alpha_\mathrm{refl}) K_{b\to p} \\ \nu_\mathrm{cx} K_{p\to b} & (1-\alpha_\mathrm{refl}) K_{b\to b} \end{bmatrix} \begin{bmatrix} n_\mathrm{n} \\ \Gamma_\mathrm{out,n} \end{bmatrix} + \begin{bmatrix} n_\mathrm{n[rec]} + n_\mathrm{n[out,i]} \\ \Gamma_\mathrm{out,n[rec]} + \Gamma_\mathrm{out,n[out,i]} \end{bmatrix} . \quad (2.153)$$

The linear system of Eq. (2.153) can then be solved by inverting the kernel matrix,

$$K = \begin{bmatrix} \nu_\mathrm{cx} K_{p\to p} & (1-\alpha_\mathrm{refl}) K_{b\to p} \\ \nu_\mathrm{cx} K_{p\to b} & (1-\alpha_\mathrm{refl}) K_{b\to b} \end{bmatrix} , \quad (2.154)$$

which, in the limit of large aspect ratio considered here, has $[N_R' N_z' + 2(N_R' + N_Z')]^2$ elements and is inverted for each poloidal plane at every neutral calculation. Since our simulation domain encompasses the whole plasma volume, contrary to the previous neutral version of GBS, the K matrix is a dense matrix with, in principle, all its elements strictly positive. However, since the value of the matrix elements decays exponentially with the distance between the two connected points, becoming negligible when their distance is several neutral mean free paths, we introduce a threshold value below which the matrix element is considered as vanishing. Since the evolution of the neutral dynamics is computationally more expensive than the evolution of the plasma dynamics, we recalculate the neutral quantities over a time interval longer than the time step used to evolve the plasma equation, but still smaller than the turbulence timescale.

The solution of the kinetic equation is a two-step process. First, the elements of the K matrix are computed, requiring the evaluation of the kernel functions, Eqs. (2.111)–(2.114). In the present version of GBS, the evaluation of K is optimized by improving the code vectorisation and avoiding unnecessary computation. Then, the K matrix is inverted to compute the neutral density by using Eq. (2.153). The matrix inversion is improved by avoiding an expensive LU factorization.

We first focus on the evaluation of the K matrix. This requires to compute $[N'_R N'_Z + 2(N'_R + N'_Z)]^2$ elements, all of them involving the evaluation of one of the four kernel functions defined in Eqs. (2.111)–(2.114), a computationally expensive evaluation. In fact, approximately 65% of a neutral step is spent in the computation of the K matrix elements (the remaining time is spent in the solution of the associated linear system). In the version of GBS presented in Ref. [237], each element of the K matrix was evaluated by using the same routine that included logic conditions used to identify points belonging to the plasma volume or the wall. Here, the logic conditions are moved outside the routine that evaluates the elements of K, which is split into four specialized routines, each of them computing one of the kernel functions in Eqs. (2.111)-(2.114). Therefore, points belonging to the plasma and the wall are separated at the beginning of the simulation and a whole subset of K is evaluated instead of computing each single element. In addition, the modified Bessel function of second kind involved in the $K_{b\to p}$ and $K_{b\to p}$ kernels is pre-computed at the beginning of the simulation and later re-used at the cost of a memory access. Finally, the computation of the integral $\int_0^{r'_\perp} \nu_{\mathrm{eff}}(\mathbf{x}''_\perp)\mathrm{d}r''_\perp$ appearing in the four kernel functions, Eqs. (2.111)–(2.114), is improved. This requires first the interpolation of the plasma quantities necessary to compute ν_{eff} along the neutral trajectory and then the numerical evaluation of the integral. The interpolation is performed by using a second-order method that is carefully implemented to enable the compiler auto-vectorisation. In contrast to Ref. [237], here we use the same routine to integrate along the neutral trajectory and over the velocity space. Moreover, integrals can be evaluated by either the (left) rectangular or midpoint rules.

We focus now on the inversion of the K matrix in Eq. (2.153). We note that the K matrix evolves in time, similarly to the matrix associated with the Poisson and Ampère equations. While a direct solver based on the MUMPS library was used in Ref. [237], requiring an expensive LU factorization, here we implement an iterative solver. Also in this case, we choose to use the framework provided by the PETSc library, opting for the use of the `GMRES` solver without preconditioner.

In order to evaluate the improvement of performance arising from the new implementation, we analyze the time to carry out one neutral step with various neutral grid sizes. We consider a coarse neutral grid of size $N'_R \times N'_Z = 25 \times 50$, a medium neutral grid of size $N'_R \times N'_Z = 50 \times 100$, and a fine neutral grid of size $N'_R \times N'_Z = 100 \times 200$, which is

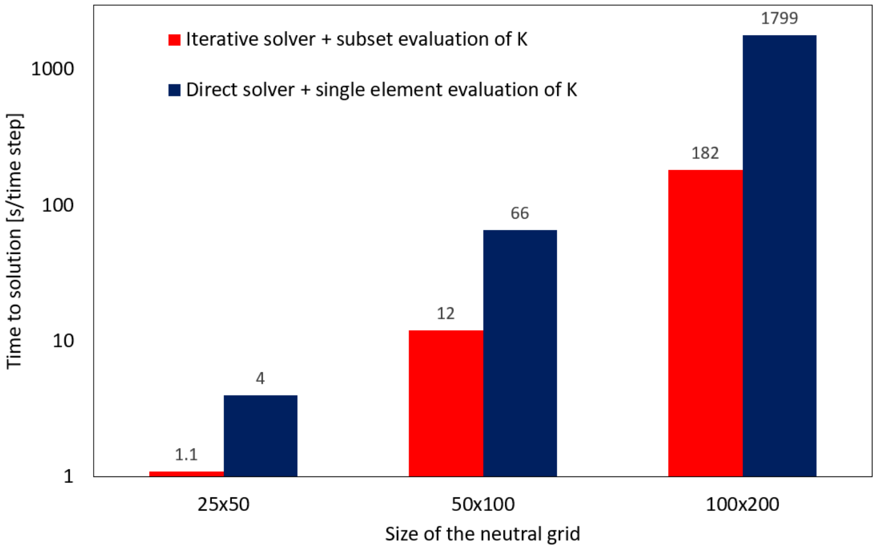

Figure 2.4 – Time to solution per neutral calculation of the implementation based on an iterative solver and the evaluation of a subset of the K matrix, compared to the implementation based on a direct solver and the evaluation of single elements of the K matrix. Tests are carried out for different neutral grid sizes (one poloidal plane) on one computing node of the multi-core partition of Piz Daint (Cray XC40 equipped with two 18-core Intel Xeon E5-2695 v4 CPUs at 2.10 GHz). The implementation of the iterative and direct solvers are based on the PETSc and MUMPS libraries, respectively.

typical of a simulation of a TCV discharge. In Fig. 2.4, the time to solution per neutral time step of the implementation that evaluates single elements of the K matrix and uses the direct solver is compared to the one of the implementation that evaluates a whole subset of the K matrix and uses the iterative solver. We note that the speed-up arising from the new implementation increases with the size of the system, ranging from a factor of four to a factor of ten.

2.6 Verification of GBS implementation

The validation of GBS results has been addressed in several works and carried out with a state of art methodology (see, e.g., Refs. [68, 155, 179]) and it is not discussed here. In this section, we report on the verification of the plasma and neutral implementation, i.e. on the assessment that the model equations are correctly implemented in the GBS code.

2.6.1 Verification of the plasma model

Similarly to the past versions, we verify the plasma model implementation in the present version of GBS by using the MMS. Here, we briefly describe the MMS. A detailed description can be found in Ref. [178] where the MMS was applied for the first time to verify a plasma turbulence code.

In order to verify the numerical implementation of a model M, the analytical solution s of the model M, which satisfies $M(s) = 0$, is compared to the numerical solution s_h of the discretized model M_h, where h is the discretization parameter. The code is successfully verified if the discretization error $e_h = ||s - s_h|| \to h^p$ as $h \to 0$, with p the order of the adopted discretization scheme. Since the analytical solution of a model equations is in general unknown, the main idea behind the MMS is to manufacture an arbitrary analytical function, u, and evaluate $S = M(u)$. We remark that, in general, $S \neq 0$, since u is not the solution of M. On the other hand, the arbitrary function u is solution of the model N, defined as $N(u) = M(u) - S = 0$. Since S can be analytically evaluated, N_h and M_h are affected by the same discretization error. Therefore, verifying N_h is equivalent to verify M_h, with the discretization error given by $e_h = ||u - u_h||$.

In the following, we report for the first time the verification of the implementation in GBS of the plasma model that avoids the Boussinesq approximation and includes electromagnetic effects. We consider a simulation domain with a rectangular poloidal cross section of size $L_R = 37.5\,\rho_{s0}$ and $L_Z = 50\,\rho_{s0}$, in the radial and vertical directions, respectively. The verification is carried out with $\rho_*^{-1} = 100$, $\nu = 1$, $\beta_{e0} = 10^{-4}$, $\tau = 1$ and $m_i/m_e = 1$. The dimensionless parameters are chosen so that the terms on the right-hand side of Eqs. (2.88)–(2.93) are all of the same order of magnitude.

The magnetic field considered for the verification is analytically obtained by solving the Biot-Savart law in the infinite aspect ratio limit for a current density with a Gaussian distribution inside the simulation domain, which guarantees continuity and derivability of the magnetic field, and an additional current filament outside the simulation domain, which produces the X-point. This leads to

$$\begin{aligned}\Psi(R,Z) = \frac{I_0}{2}\Bigg\{\log\left[\frac{(R-R_1)^2+(Z-Z_1)^2}{\rho_{s0}^2}\right] + \mathrm{EI}\left[\frac{(R-R_1)^2+(Z-Z_1)^2}{\sigma_0^2}\right] \\ + \log\left[\frac{(R-R_1)^2+(Z-Z_2)^2}{\rho_{s0}^2}\right]\Bigg\},\end{aligned} \tag{2.155}$$

where $\mathrm{EI}(x)$ is the exponential integral function, with $I_0 = 40\,\rho_{s0}^2 B_0$, $\sigma_0 = 6.25\,\rho_{s0}$, $R_1 = 100\,\rho_{s0}$, $Z_1 = 0$, and $Z_2 = -40\,\rho_{s0}$. The manufactured solutions for the evolved scalar quantities $u = n, T_e, T_e, V_{\|e}, V_{\|i}, \Omega, \phi, \psi$ are chosen as

$$u_M(R,Z,\varphi,t) = A_u\Big[B_u + \sin(C_u Z + \alpha_u)\sin(D_u\varphi + \beta_u)\sin(E_u t + F_u R + \gamma_u)\Big], \tag{2.156}$$

where A_u, B_u, C_u, D_u, E_u, F_u, α_u, β_u, and γ_u are arbitrary constants whose value is chosen to excite all terms in the right-hand side of Eqs. (2.88)–(2.95), ensuring that none of them provides a dominating contribution to the numerical error. The source terms can be computed by substituting Eq. (2.156) into Eqs. (2.88)–(2.95). This process is carried out by using the symbolic calculation offered by the Mathematica software package [241] and the analytical expressions of the source terms are directly converted to the Fortran language of the GBS code.

In order to decouple the tolerance error associated with the iterative solver from the discretization error, we first consider the verification of GBS where Poisson and Ampère equations are solved with a direct method. As a second step, we discuss the verification of the iterative solver. We do not include the curvature-related contributions appearing in the gyroviscous terms, Eqs. (2.86) and (2.87), since they are implemented at second-order. These terms are verified independently.

Figs. 2.5 (a) and (b) show the L_2 and L_∞ norms of the discretization errors at $t = 0.01$. We consider various grid refinements as a function of the discretization parameter $h = \Delta R/\Delta R_0 = \Delta Z/\Delta Z_0 = \Delta\varphi/\Delta\varphi_0 = \Delta t/\Delta t_0$, where ΔR_0, ΔZ_0, and $\Delta\varphi_0$ is the spacing of the $N_R \times N_Z \times N_\varphi = 256 \times 256 \times 256$ grid, with time step $\Delta t_0 = 6.25 \times 10^{-6}$. The coarsest grid considered for the verification is $N_R \times N_Z \times N_\varphi = 8 \times 8 \times 8$ with $\Delta t = 2 \times 10^{-4}$. The order of accuracy,

$$p = \frac{\log(e_{rh}/e_h)}{\log r}, \tag{2.157}$$

with rh indicating the coarsening of the temporal and spatial grids by a factor of r, is shown in Figs. 2.5 (c) and (d). Since a fourth-order numerical scheme is used to discretize both space and time, we expect the discretization error to decrease as h^4 when $h \to 0$, in good agreement with the result of Fig. 2.5 that shows the convergence to $p = 4$ for both the L_2 and L_∞ norms as h decreases.

We discuss now the verification of the iterative solver. The error affecting the solution of an iterative solver is the combination of the discretization error and the tolerance error, the last depending on the tolerance threshold. We consider the solution of Poisson and Ampère equations and we compare the results of the direct and iterative solvers based on the MUMPS and PETSc libraries. Fig. 2.6 shows the global and local errors of ϕ, for Poisson equation, and ψ, for Ampère equation, as a function of the relative tolerance of the iterative solver. We note that the errors decrease with the relative tolerance until a value of 10^{-7}. Below this value, the discretization error dominates, independently of the solver tolerance.

2.6.2 Verification of the neutral model

We verify here, for the first time, the implementation of the neutral model. We proceed in two steps. First, we verify the correct implementation of the routine used to perform integrals over a neutral trajectory and over the velocity space, which appear in the kernel functions, Eqs. (2.111)–(2.114). Second, we focus on the construction and inversion of

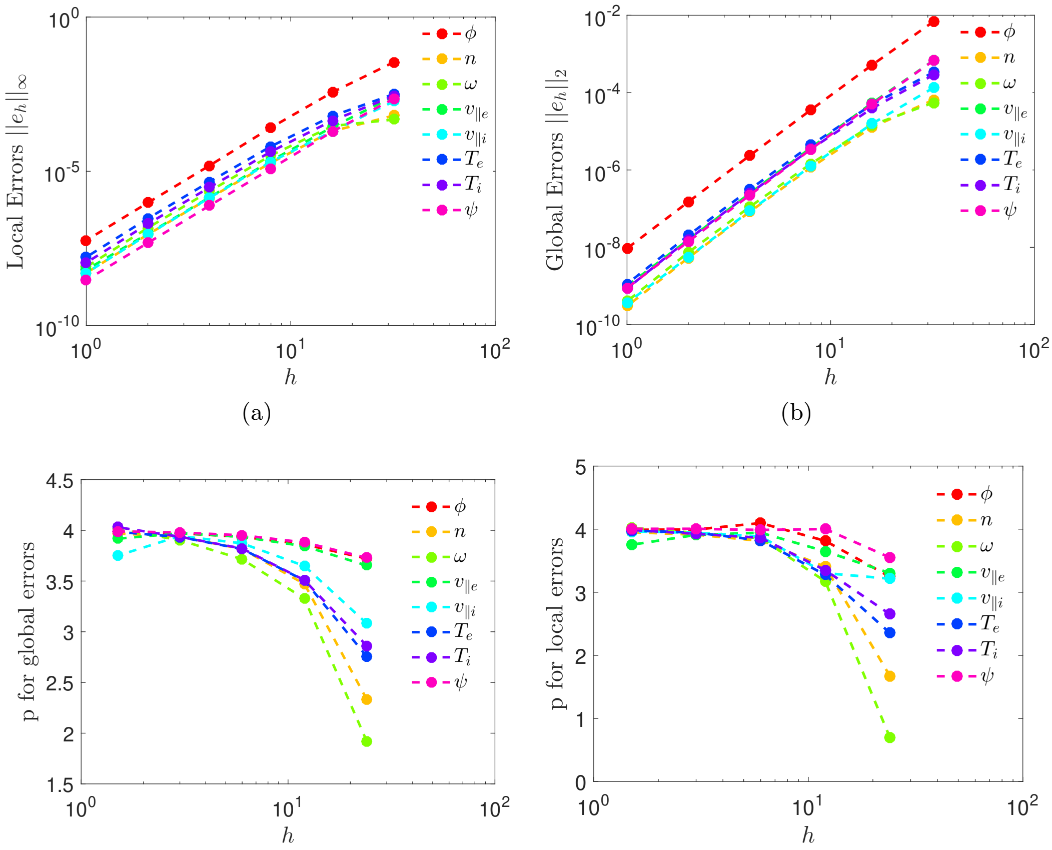

(a) (b)

(c) (d)

Figure 2.5 – Local, L_∞, (a) and global, L_2, (b) norms of the discretization error as a function of the grid resolution parameter $h = \Delta R/\Delta R_0 = \Delta Z/\Delta Z_0 = \Delta\varphi/\Delta\varphi_0 = \Delta t/\Delta t_0$, where ΔR_0, ΔZ_0, and $\Delta\varphi_0$ is the grid spacing for the $N_R \times N_Z \times N_\varphi = 256 \times 256 \times 256$ grid with time step $\Delta t_0 = 6.25 \times 10^{-6}$. The order of convergence p is also shown for the local (c) and the global (d) norms of the discretization errors. As expected from the order of convergence of the numerical scheme, p tends to 4 as h decreases. Results are shown in dimensionless units.

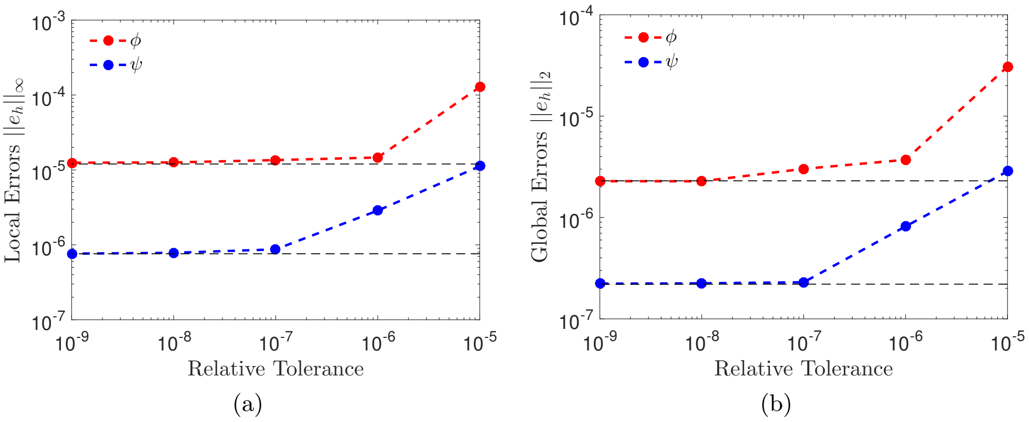

Figure 2.6 – Local (a) and global (b) errors of ϕ and ψ as a function of the relative tolerance of the iterative solver based on the PETSc library for the grid $N_R \times N_Z \times N_\varphi = 64 \times 64 \times 64$, and $L_R = 37.5\,\rho_{s0}$ and $L_Z = 50\,\rho_{s0}$. The horizontal dashed lines represent the discretization error when the direct solver based on the MUMPS library is used. Convergence is achieved for values of the relative tolerance below 10^{-7}. Results are show in dimensionless units.

the matrix K, Eq. (2.154), used to evaluate the neutral density.

To carry out the first verification step, we perform unit tests that allow us to verify individually the routines used to numerically integrate and to interpolate along a neutral trajectory. The interpolating routine is tested on an analytical function f, considering various resolutions. Fig. 2.7 shows the typical discretization error in a point of f domain as a function of the grid resolution. The order of convergence is correctly retrieved as h decreases. The integration routine is tested by comparing the numerical and analytical result of the integral of an analytical function f over an arbitrary interval. The discretization error as well as the order of convergence is shown in Fig. 2.8. The results of the unit tests point out the correct implementation of the routines used to evaluate integrals along a neutral trajectory.

We focus now on the verification of the correct construction and inversion of the matrix K. For this purpose, we compare the numerical solution of the neutral density, n_n, to the analytical manufactured solution,

$$n_{\mathrm{n},M} = A_\mathrm{n} + B_\mathrm{n} \sin(\alpha_\mathrm{n} R) \cos(\beta_\mathrm{n} Z)\,, \tag{2.158}$$

where A_n, B_n, α_n, and β_n are arbitrary constants. In addition, we consider the manufactured neutral flux as vanishing, i.e. $\Gamma_{\mathrm{out,n},M} = 0$. The analytical source term required by the MMS is directly computed by substituting $n_{\mathrm{n},M}$ and $\Gamma_{\mathrm{out,n},M}$ in Eq. (2.104),

$$S_M(\mathbf{x}_\perp) = n_{\mathrm{n},M}(\mathbf{x}_\perp) - \int_D n_{\mathrm{n},M}(\mathbf{x}'_\perp)\nu_\mathrm{cx}(\mathbf{x}'_\perp) K_{p\to p}(\mathbf{x}_\perp, \mathbf{x}'_\perp)\mathrm{d}A'\,, \tag{2.159}$$

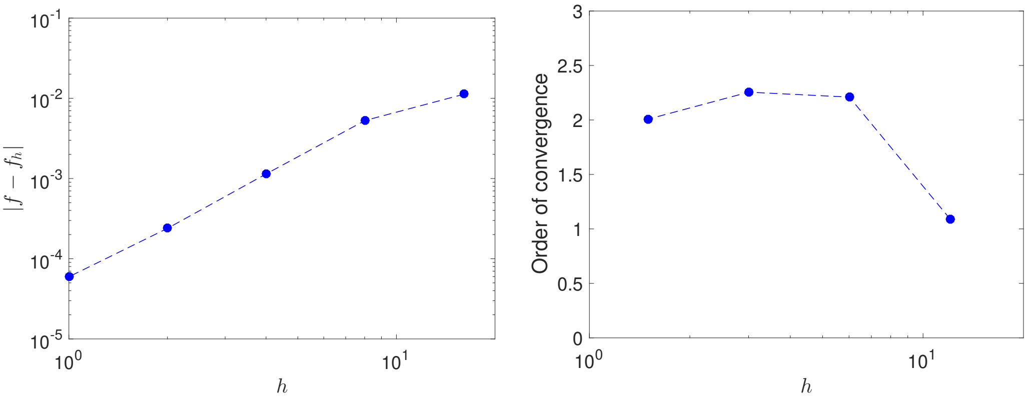

(a) (b)

Figure 2.7 – Discretization error of the interpolated test function $f(x) = 2x^2 + 4y^2$, discretized on an arbitrary domain $x \in [x_0, x_1]$ and $y \in [y_0, y_1]$, as a function of the discretization parameter $h = \mathrm{d}x/\mathrm{d}x_0 = \mathrm{d}y/\mathrm{d}y_0$ at the position $x_0 = -10$, $x_1 = 10$, $y_0 = -7$ and $y_1 = 7$ (a), and the corresponding order of convergence (b). The expected order of convergence to the analytical result is correctly retrieved.

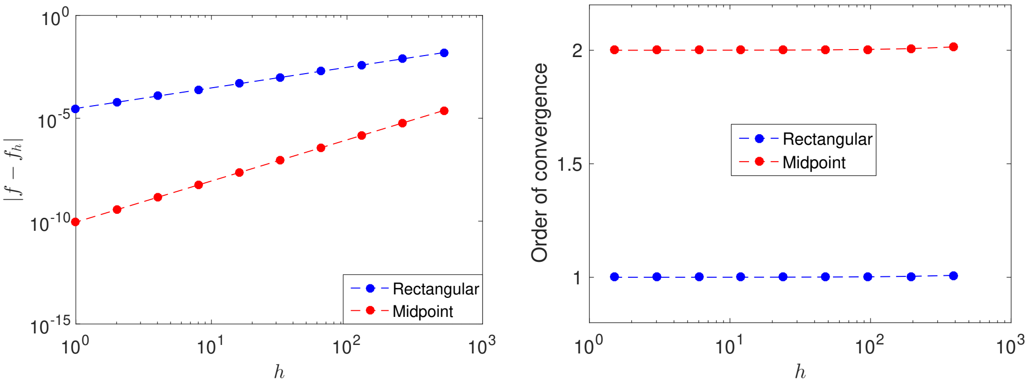

(a) (b)

Figure 2.8 – Result of the unit test to verify the numerical integration routine used in GBS. The discretization error resulting from the numerical integration of the test function $f(x) = \cos x$ (a) and the corresponding order of convergence (b) are shown as a function of the discretization parameter $h = \mathrm{d}x/\mathrm{d}x_0$. The integral is performed between $x = 1$ and $x = 3$. The expected order of convergence to the analytical result is correctly retrieved for both the rectangular and the midpoint rules.

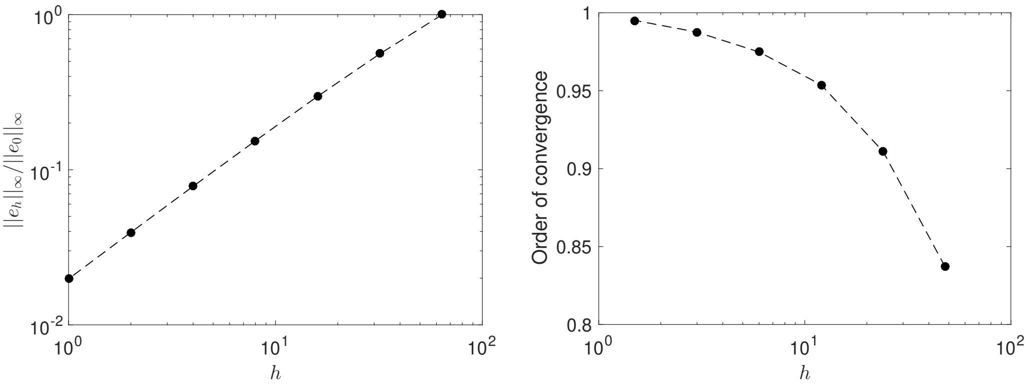

(a) (b)

Figure 2.9 – Local discretization error of the neutral density as a function of the discretization parameters $h = \mathrm{d}v/\mathrm{d}v_0$ (a) and the corresponding order of convergence (b). The poloidal neutral spatial grid considered here is $N'_R \times N'_Z = 10 \times 10$. The expected order of convergence of n_n to the analytical solution $n_{\mathrm{n},M}$ is correctly retrieved as h decreases.

where the contribution from the ion flux is not included to decouple the neutral and plasma modules. We note that Eq. (2.159) requires the analytical evaluation of the kernel function $K_{p\to p}(\mathbf{x}_\perp, \mathbf{x}'_\perp)$, Eq. (2.111). For simplicity, we choose $\nu_{\mathrm{iz}}(\mathbf{x}_\perp) = 0$, $\chi_{\perp\mathrm{in}}(\mathbf{x}_\perp, \mathbf{v}_\perp) = 0$, $\nu_{\mathrm{cx}}(\mathbf{x}_\perp) = \mathrm{const}$, and

$$\Phi_\perp(\mathbf{x}_\perp, \mathbf{v}_\perp) = \frac{2m_i}{\sqrt{\pi}T_{i0}} r_\perp \exp\left(\frac{\nu_{cx} r_\perp}{v_\perp} - \frac{m_i v_\perp^2}{T_{i0}}\right). \tag{2.160}$$

The choice of these functions allows for the straightforward analytical evaluation of $K_{p\to p}(\mathbf{x}_\perp, \mathbf{x}'_\perp)$, resulting in $K_{p\to p}(\mathbf{x}_\perp, \mathbf{x}'_\perp) = \mathrm{const}$. As a consequence, all the elements of the matrix associated to $K_{p\to p}$ arising from the discretization are equal. The integral over the poloidal plane in Eq. (2.104), evaluated through the matrix inversion (see Eq. (2.153)), is discretized using the rectangular integration rule. Therefore, the numerical solution of the neutral density is expected to converge to the manufactured solution with the order of convergence $p = 1$ as h decreases. The local discretization error of the neutral density and the corresponding order of convergence are shown in Fig. 2.9 as a function of h. The expected order of convergence of the neutral density to the analytical solution is retrieved, hence verifying the correct implementation in GBS of Eq. (2.153).

2.7 Parallelisation scalability tests

The use of finite differences on a uniform (R, φ, Z) grid allows for an effective implementation of GBS on parallel high-performance computers. Domain decomposition is applied to all three spatial dimensions and implemented with the Message Passing Interface (MPI) for both the plasma and neutral equations. Communication between different processors is carried out by means of ghost cell passing, using standard MPI functions. In addition, the global MPI communicator is split into two independent ones in order to evolve the plasma and neutral equations in parallel. After every neutrals calculation, the neutral and the plasma modules synchronize, i.e. the neutral terms appearing in the plasma equations and the plasma quantities in the neutral module are updated (see Fig. 2.2). The splitting of the MPI communicators has some important advantages with respect to the serial approach: (i) the neutral density is evolved continuously, updating the neutral sources in the plasma equations at the desired frequency by choosing the number of MPI tasks for the plasma and neutral modules, (ii) the time to solution is reduced, and (iii) the code scalability is improved allowing us to run on a larger number of computing nodes, which is essential on large systems due to the large amount of memory required by the neutral module. We show here that this approach leads to a very efficient strong and weak scalability.

Being independent, the parallelization properties of the plasma and neutral modules are analyzed separately. Focusing, first, on the plasma module, we consider a typical grid size of a TCV simulation, with n_{pR}, n_{pZ} and $n_{p\varphi}$ the number of MPI tasks in the R, Z and φ direction, respectively. To avoid the demanding communications on poloidal planes required by the Poisson and Ampère equations, the strong scalability test is carried out by only increasing the MPI resources allocated to the φ dimension, i.e. by solving whole RZ-planes on a computing node. As shown in Fig. 2.10 (a), GBS scales with an almost perfect efficiency up to $n_{p\varphi} = 32$, while efficiency decreases to 0.75 at $n_{p\varphi} = 64$ (two toroidal planes per computing node), pointing out the high scalability of GBS especially on the toroidal direction, mainly thanks to the fact that the Poisson and Ampère equations are solved independently on each poloidal plane. The weak scalability of the plasma module is carried out on grids of size $N_R \times N_Z \times N_\varphi = 300 \times 600 \times 2n_{p\varphi}$, where $n_{p\varphi}$ is the number of MPI tasks in the toroidal direction. The results are shown in Fig. 2.10 (b), confirming the good scalability properties of the plasma module in GBS.

The strong scalability of the neutral module is carried out on a neutral grid typical of medium size simulations such as TCV. Similarly to the plasma scalability, we consider one computing node in the RZ-plane, while increasing $n_{p\varphi}$, starting from the minimum number of nodes allowed by memory requirements. In fact, the solution of the neutral system, Eq. (2.153), requires the allocation of matrices of sizes $[N'_R \times N'_Z + 2(N'_R + N'_Z)]^2$ in each poloidal plane, thus being highly memory consuming. As shown in Fig. 2.11 (a), the speed-up is almost ideal up to $n_{p\varphi} = 128$. The weak scalability is performed on neutral grids of size $N'_R \times N'_Z \times N'_\varphi = 300 \times 600 \times 2n_{p\varphi}$. Fig. 2.11 (b) shows an almost perfect efficiency as the system size increases.

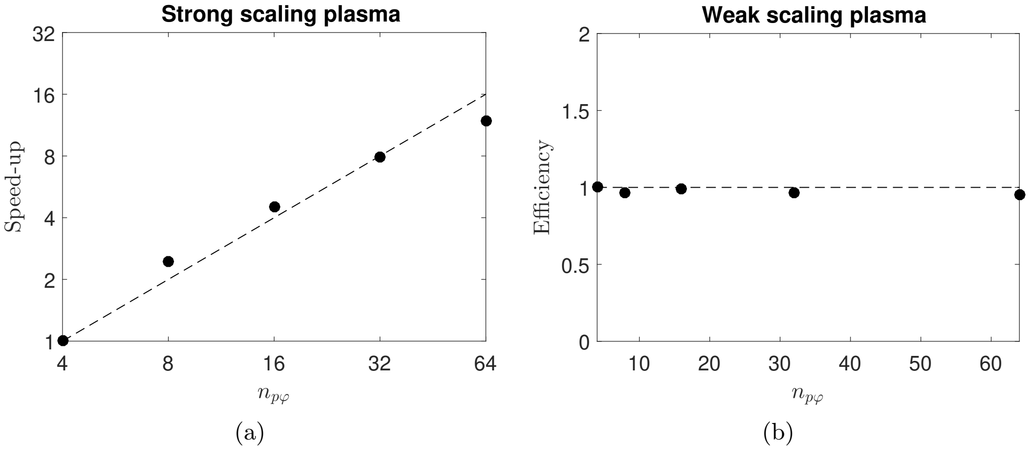

(a) (b)

Figure 2.10 – Strong (a) and weak (b) scalability tests performed on the multi-core partition of Piz Daint (Cray XC40 equipped with two 18-core Intel Xeon E5-2695 v4 CPUs at 2.10GHz). The strong scalability is carried out on a grid of size $N_R \times N_Z \times N_\varphi = 300 \times 600 \times 128$, with one node (36 cores) on the RZ-plane. GBS scales with an almost perfect efficiency up to $n_{p\varphi} = 32$, while efficiency decreases to 0.75 at $n_{p\varphi} = 64$, corresponding to $n_{pR} \times n_{pZ} \times n_{p\varphi} = 2304$ cores (64 nodes). The weak scalability test is carried out on grids of size $N_R \times N_Z \times N_\varphi = 300 \times 600 \times 2n_{p\varphi}$, where $n_{p\varphi}$ is the number of MPI tasks in the φ direction.

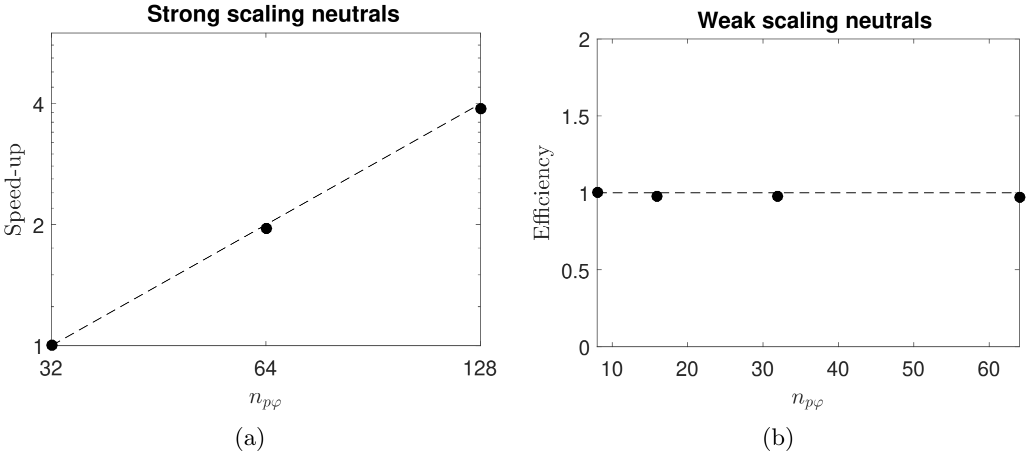

(a) (b)

Figure 2.11 – Strong (a) and weak (b) scalability tests of the neutral module performed on the multi-core partition of Piz Daint (Cray XC40 equipped with two 18-core Intel Xeon E5-2695 v4 CPUs at 2.10GHz). The strong scalability is carried out on a neutral grid of size $N'_R \times N'_Z \times N'_\varphi = 100 \times 200 \times 128$, with one node (36 cores) on the RZ-plane, and is tested starting from 32 nodes, which is the minimum number of nodes required by memory constraints. The speed-up is almost ideal up to $n_{p\varphi} = 128$, corresponding to a total of 4608 cores (128 nodes). The weak scalability is carried out on neutral grids of size $N'_R \times N'_Z \times N'_\varphi = 300 \times 600 \times 2n_{p\varphi}$, where $n_{p\varphi}$ is the number of MPI tasks along φ.

2.8 Convergence properties

We test here the convergence of GBS results with respect to the plasma and neutral grid refinement. We consider the magnetic field given by the analytical flux function in Eq. (2.155) and we compare the results of three simulations with increasing plasma grid resolution and no coupling with neutrals, and of three simulations with increasing neutral grid resolution and same plasma grid resolution. The results are analyzed when the simulations reach a quasi-steady state, resulting from the balance between the plasma and heat sources and losses at the wall. We also study the convergence with respect to the frequency of the neutral computation.

The simulations considered for studying the convergence with respect to the plasma grid are performed with a coarse ($\Delta R = \Delta Z = 3.75\ \rho_{s0}$ and $R_0\Delta\varphi = 65.4\ \rho_{s0}$), a medium ($\Delta R = \Delta Z = 2.50\ \rho_{s0}$ and $R_0\Delta\varphi = 49.1\ \rho_{s0}$) and a fine ($\Delta R = \Delta Z = 1.67\ \rho_{s0}$ and $R_0\Delta\varphi = 32.7\ \rho_{s0}$) resolution grid. In order to investigate the convergence, we consider the time and toroidally averaged radial profiles at the outer midplane of n, T_e, T_i and ϕ. As shown in Fig. 2.12, the radial profiles clearly converge to the ones obtained from the simulation with the finest resolution. Assuming that ρ_{s0} is the characteristic spatial length along the direction perpendicular to the magnetic field for phenomena occurring in our simulations, we conclude that $\Delta R = \Delta Z \simeq 2.50\ \rho_{s0}$ is the minimum spatial resolution of the plasma grid on the poloidal plane that guarantees convergence of simulation results. In order to guarantee stability of the simulations, the resolution along φ is chosen according to the ratio of the poloidal to the toroidal component of the magnetic field, $R_0\Delta\varphi \lesssim B_0\Delta Z/B_Z \sim B_0\Delta R/B_R$.

The convergence with respect to the neutral grid refinement is tested by comparing the results of three simulations with the same plasma resolution, $\Delta R = \Delta Z = 1.67\ \rho_{s0}$ and $R_0\Delta\varphi = 32.7\ \rho_{s0}$, and different neutral grid resolutions: coarse ($\Delta R' = \Delta Z' = 0.15\ \lambda_n$), medium ($\Delta R' = \Delta Z' = 0.075\ \lambda_n$), and fine ($\Delta R' = \Delta Z' = 0.038\ \lambda_n$) resolutions, where λ_n is the mean free path of neutrals for ionization, evaluated by considering a value of T_e and n in the simulations near the separatrix ($T_e \simeq 20$ eV and $n \simeq 4 \times 10^{19}$ m^{-3}). The resolution along φ is given by the plasma grid. The neutral density is evaluated every $\Delta t = 0.08\ R_0/c_{s0}$. The time traces of the spatially averaged neutral density, neutral temperature and neutral parallel velocity show a clear convergence to the results of the finest neutral grid (see Fig. 2.13). We also analyze the time and the toroidal averages of the neutral density and ionization source, S_{iz}, at the bottom wall, where the two strike points are located. Fig. 2.14 shows that there is no noticeable difference in the neutral density and ionization source profiles between simulations with different neutral grid resolutions, pointing out that the resolution $\Delta R' = \Delta Z' \simeq 0.075\ \lambda_n$ is sufficient to guarantee the convergence of the simulation results.

Finally, we study the convergence of GBS results with respect to the frequency of the neutral calculation. We consider three simulations with a plasma grid resolution

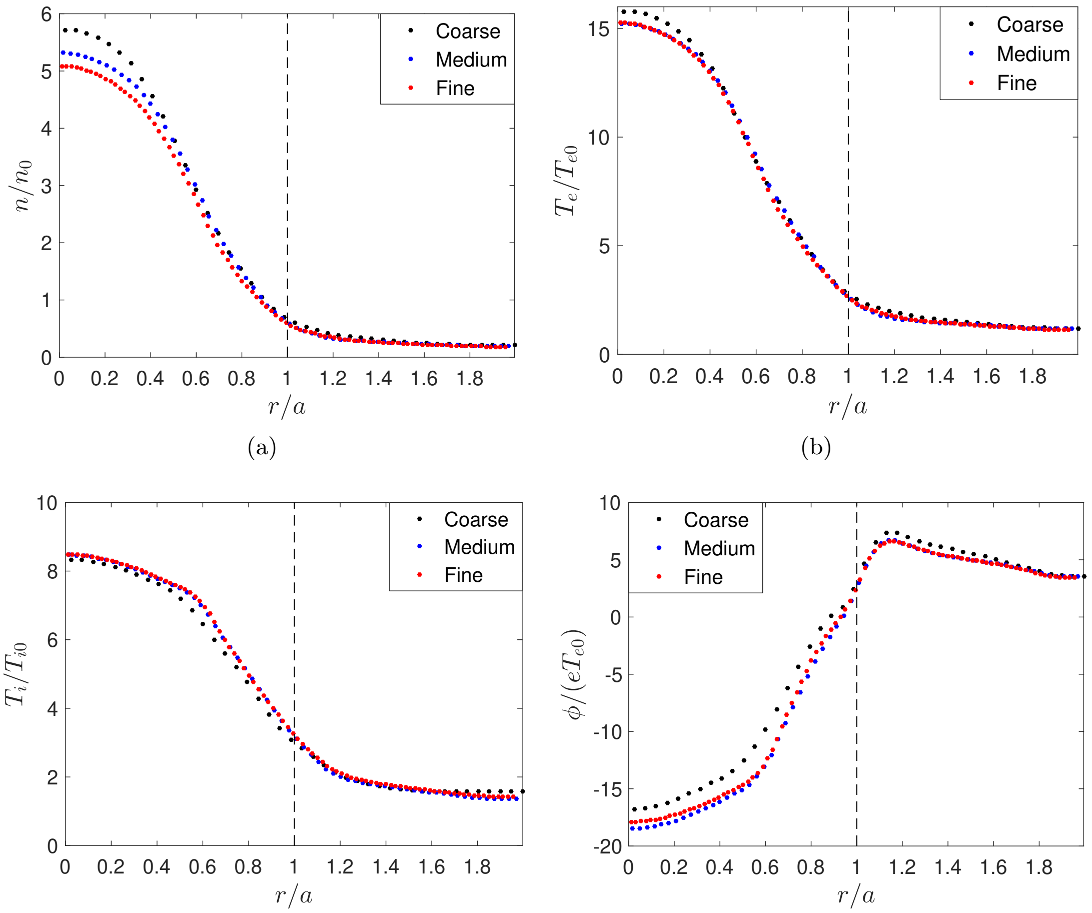

(a) (b)

(c) (d)

Figure 2.12 – Time and toroidally averaged radial profiles of density (a), electron temperature (b), ion temperature (c), and electrostatic potential (d) at the outer midplane of GBS simulations at different plasma grid resolutions ($N_R \times N_Z \times N_\varphi = 80 \times 110 \times 24$, coarse grid; $N_R \times N_Z \times N_\varphi = 120 \times 160 \times 32$, medium grid; $N_R \times N_Z \times N_\varphi = 180 \times 240 \times 48$, fine grid). The dashed vertical line represents the position of the separatrix.

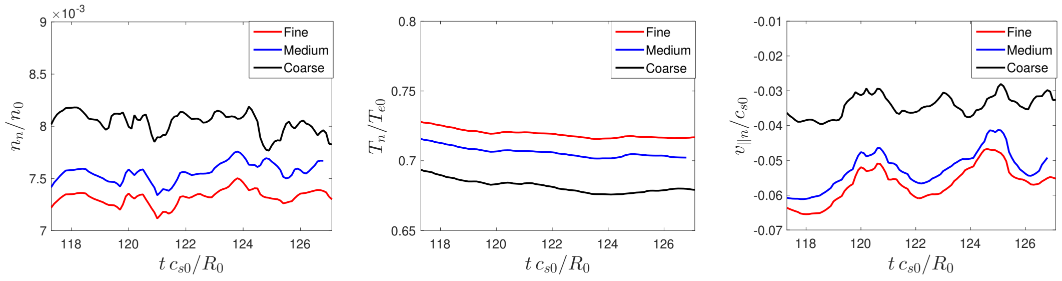

(a) (b) (c)

Figure 2.13 – Time traces of the spatially averaged neutral density (a), neutral temperature (b) and neutral parallel velocity (c) at different neutral grid resolutions ($N'_R \times N'_Z = 24 \times 28$, coarse; $N'_R \times N'_Z = 42 \times 56$, medium; $N'_R \times N'_Z = 84 \times 112$, fine).

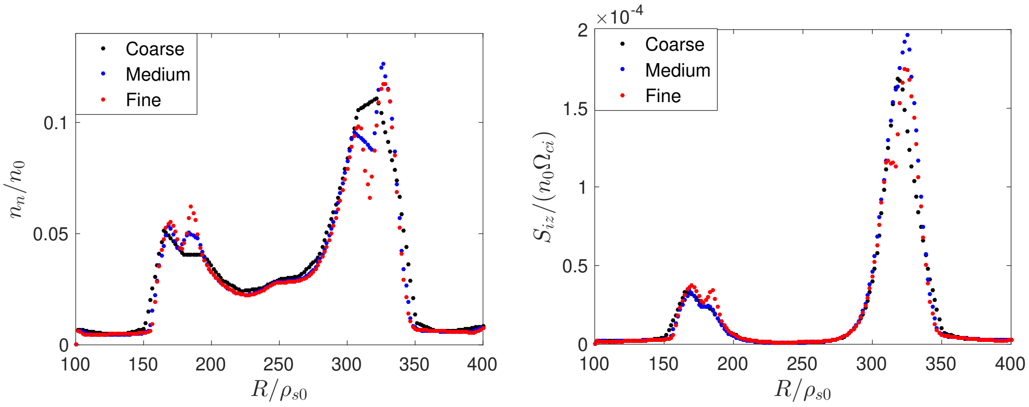

(a) (b)

Figure 2.14 – Time and toroidal average of the neutral density (a) and ionization source (b) at the bottom wall at different neutral grid resolutions ($N'_R \times N'_Z = 24 \times 28$, coarse; $N'_R \times N'_Z = 42 \times 56$, medium; $N'_R \times N'_Z = 84 \times 112$, fine).

of $\Delta R = \Delta Z = 1.67\ \rho_{s0}$ and $R_0 \Delta\varphi = 32.7\ \rho_{s0}$, and a neutral grid resolution of $\Delta R' = \Delta Z' = 0.075\ \lambda_n$. The neutral density is evaluated every $\Delta t = 0.04\ R_0/c_{s0}$, $\Delta t = 0.08\ R_0/c_{s0}$ and $\Delta t = 0.16\ R_0/c_{s0}$, respectively. Fig. 2.15 shows that the time and toroidally averaged radial density profile at the outer midplane and neutral density at the bottom wall do not display any significant difference among the three simulations considered here. We conclude that evaluating the neutral density every $\Delta t \simeq 0.1\ R_0/c_{s0}$ guarantees the correct convergence of the results. We note that, since in our simulations turbulence is typically driven by ballooning modes with a maximum growth rate of $\gamma_B = \sqrt{2}c_s/\sqrt{L_p R_0}$ [147], with $L_p = |p_e/\partial_R p_e|$ the equilibrium pressure gradient length at the separatrix on the outer midplane, the minimum neutral calculation frequency that guarantees the convergence of the simulation results is $\gamma_B \Delta t \simeq 0.7$. Since the neutral and the plasma models can be evolved simultaneously, the number of MPI tasks for the plasma and neutral modules can be chosen to guarantee this neutral calculation frequency.

2.9 First simulation results in an experimentally-relevant scenario

As an example of application of the new version of GBS presented here, we report on the results of the first GBS electromagnetic simulation that includes the coupling with neutral dynamics of a lower single-null discharge performed in the TCV tokamak (tokamak major radius $R_0 = 0.9$ m and minor radius measured from the tokamak magnetic axis to the separatrix at the outer midplane $a = 0.20$ m). The magnetic equilibrium considered in the simulation is given by the equilibrium reconstruction of the TCV discharge #65402 at 1 s (plasma elongation and triangularity at the separatrix $\kappa = 1.71$ and $\delta = 0.35$, respectively,

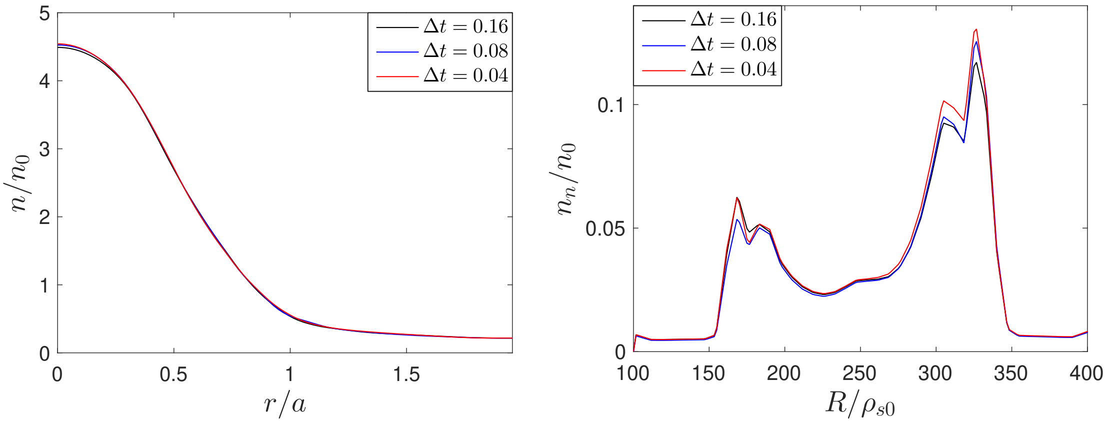

(a) (b)

Figure 2.15 – Time and toroidally averaged radial density profile at the outer midplane (a) and neutral density at the bottom wall (b) of GBS simulations with the neutral density evaluated every $\Delta t = 0.04\ R_0/c_{s0}$, $\Delta t = 0.08\ R_0/c_{s0}$ and $\Delta t = 0.16\ R_0/c_{s0}$.

toroidal magnetic field at the tokamak magnetic axis $B_0 = 0.9$ T, plasma current I_p=146 kA). The discharge considered here is in forward field (ion-∇B drift direction pointing toward the active X-point). The upstream density and electron temperature at the separatrix, taken as reference density and temperature in the simulation, are $n_0 = 0.6 \times 10^{19}$ m^{-3} and $T_{e0} = 35$ eV, respectively. With these reference values, the ion sound Larmor radius is $\rho_{s0} \simeq 1$ mm, the sound speed is $c_{s0} \simeq 4.1 \times 10^4$ m/s, and the reference time is $t_0 = R_0/c_{s0} \simeq 0.02$ ms. In order to reduce the computational cost of the simulation, we consider here a domain corresponding to half size of TCV, i.e. $L_R = 300\,\rho_{s0}$ and $L_Z = 600\,\rho_{s0}$. We note that full size TCV simulations have been recently performed and validated against TCV data, as shown in Ref. [155]. The dimensionless simulation parameters are $\rho_*^{-1} = 450$, $\tau = 1$, $\eta_{0e} = 3 \times 10^{-4}$, $\eta_{0i} = 1$, $\chi_{\parallel e} = 20$, $\chi_{\parallel i} = 1$, $D_f = 7$ for $f = \{n, T_e, T_i, \Omega, U_{\parallel e}, V_{\parallel i}\}$, $m_i/m_e = 3000$, $\beta_{e0} = 2 \times 10^{-6}$, and $\nu_0 = 0.05$. The amplitude of the electron temperature source is chosen so that $T_e/T_{e0} \simeq 1$ at the separatrix. This leads to a power source with an intensity, in physical units, of approximately 150 kW, which is close to the experimental estimated value of the power crossing the separatrix, $P_{\text{sep}} = 120$ kW. No external ion temperature source is used in the simulation and the ion heating is provided by the equipartition term in Eq. (2.77). The value of neutral reflection coefficient is $\alpha_{\text{refl}} = 0.2$. Although we consider a discrete gas puff in the private flux region, most of the neutral particles are generated from the ion recycling at the wall. A discrete pump at the bottom wall in the region $R > 500\rho_{s0}$ is also considered.

The plasma spatial grid is $N_R \times N_Z \times N_\varphi = 150 \times 300 \times 64$ and the neutral spatial grid is $N_R' \times N_Z' \times N_\varphi' = 50 \times 100 \times 64$. The time step is $\mathrm{d}t = 10^{-5} R_0/c_{s0}$ and the neutral kinetic equation is solved every $\Delta t = 0.04\ R_0/c_{s0}$. The simulation reaches the turbulent quasi-steady state after approximately 80 R_0/c_{s0}, starting from flat initial profiles of

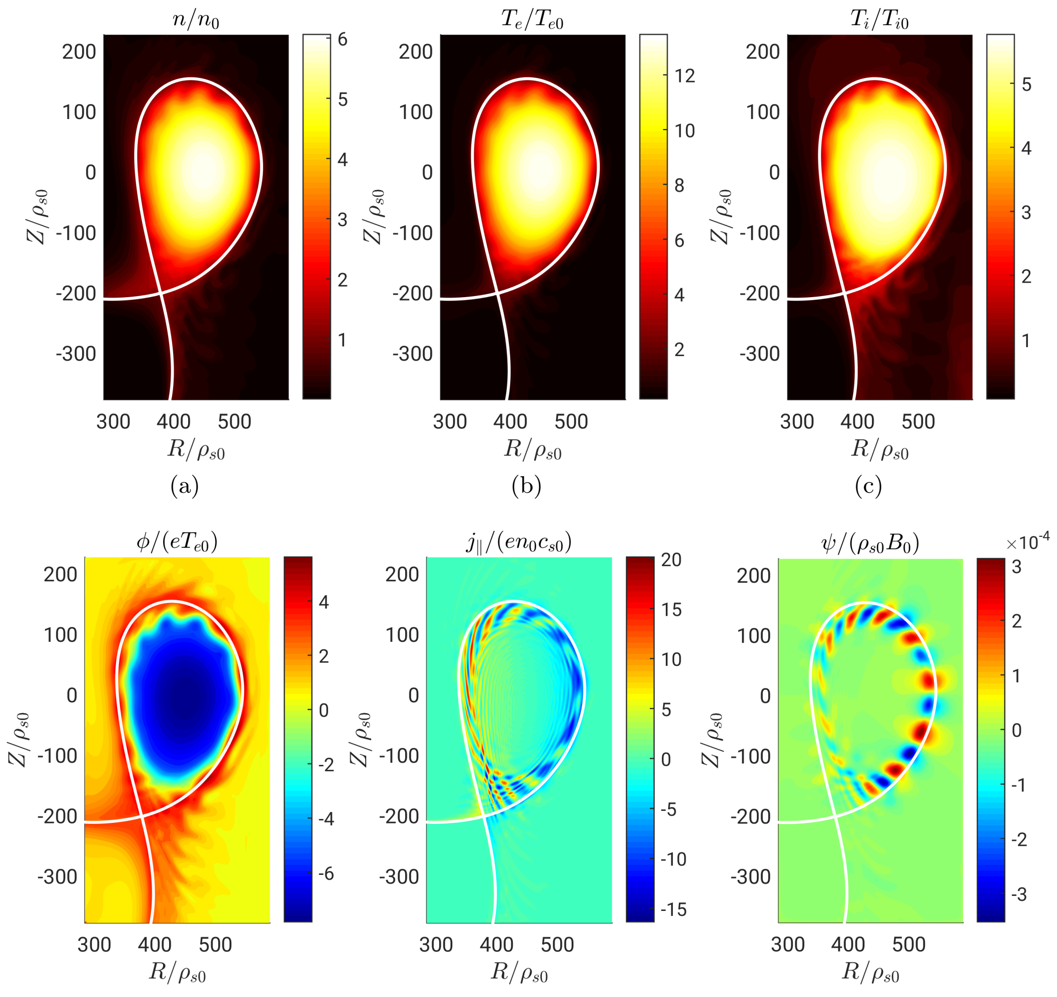

(a) (b) (c)

(d) (e) (f)

Figure 2.16 – Typical snapshots of the density (a), electron temperature (b), ion temperature (c), electrostatic potential (d), parallel current (e) and fluctuating vector potential (f) for the TCV simulation described in Sec. 2.9.

density and temperature.

We briefly discuss here the simulation results, showing that they are in agreement with typical experimental observations. Typical snapshots on a poloidal plane of n, T_e, T_i, ϕ, $j_\parallel$ and ψ are presented in Fig. 2.16. As experimentally observed (see, e.g., Refs. [38, 63]), the tokamak core is characterized by low-amplitude density and temperature fluctuations, which increase from the core to the edge. A wave-like turbulent dynamics, experimentally observed [67, 243], is clearly visible in the edge (see Fig. 2.16). When crossing the separatrix, the turbulent eddies experience a strong $\mathbf{E}\times\mathbf{B}$ shear and detach from the main plasma, forming filaments that propagate radially in the SOL, in agreement with experimental observations described, e.g., in Refs. [67, 243]. In addition, as it is also

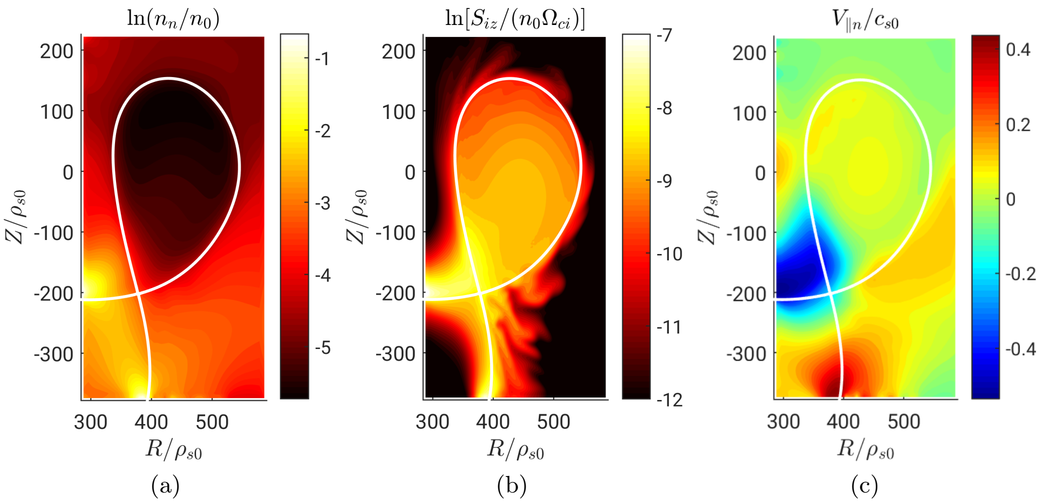

Figure 2.17 – Typical snapshots of the neutral density (a), ionization source (b) and neutral parallel velocity (c) for the TCV simulation described in Sec. 2.9.

experimentally observed [78, 219, 223, 236], turbulence in the far SOL is characterized by intermittent events due to coherent plasma filaments [48].

The strong electric field gradient observed across the separatrix also reflects experimental observations [138, 196]. Because of the ambipolarity of the plasma flow at the sheath, the electrostatic potential in the SOL is positive and proportional to the electron temperature [211]. Therefore, the electrostatic potential increases from the far SOL to the separatrix. On the other hand, the electrostatic potential inside the separatrix is negative with an electric field proportional to the ion pressure gradient. As a consequence, a strong electric field gradient and an associated poloidal $\mathbf{E} \times \mathbf{B}$ shear form in the region across the separatrix. The $\mathbf{E} \times \mathbf{B}$ shear can play an important role in suppressing turbulence at the tokamak edge, as discussed in Ch. 3 where GBS simulations are used to investigate the turbulent transport regimes in this region.

Typical snapshots of n_{n}, S_{iz} and $V_{\|\mathrm{n}}$ are shown in Fig. 2.17. As expected, the neutral density is larger in the proximity of the target plates, where most of the recycling takes place, although a non-negligible fraction of neutrals can be found in the core, mainly in the region close to the X-point. In fact, a significant fraction of neutral particles reaches the separatrix from the target on the high-field side before being ionized (see Fig. 2.17 (b)). In our simulation, core ionization accounts for approximately 25% of the total ionization source, which is in agreement with the fact that the TCV discharge considered here is in the low-density and low-recycling regime. We note that $V_{\|\mathrm{n}}$ is positive in the outer strike point region and negative in the inner strike point region (see Fig. 2.17 (c)). Since the direction of the magnetic field points towards (away from) the outer (inner) target, the parallel neutral flux is directed towards the wall at both targets.

2.10 Conclusions

The present chapter describes a new version of GBS, where the simulation domain is extended to encompass the whole plasma volume, avoiding an artificial boundary with the tokamak core and retaining the core-edge-SOL turbulence interplay. Both the plasma and neutral implementations are carefully optimized leading to a significant speed-up of the code. In particular, a new iterative solver based on the PETSc library is implemented and optimized for the solution of Poisson and Ampère equations, allowing us to efficiently carry out electromagnetic simulations, while avoiding the use of the Boussinesq approximation. Moreover, the neutral module is refactored and optimized by implementing an iterative solver based on the PETSc library.

The implementation of the plasma and neutral models is then carefully verified by means of the MMS, including, for the first time, the verification of the electromagnetic terms and of the kinetic neutral model. The verification of the neutral model is completed by a set of unit tests to verify the routines used to compute the integrals over the neutral trajectories.

Our tests show the efficient scalability of GBS on parallel high-performance computers, mainly thanks to the numerical scheme used to discretize the differential operators. The uniform Cartesian grid allows for a massive parallelisation through MPI domain decomposition. The splitting of the plasma and neutral communicators improves the parallelisation of GBS.

The convergence properties with respect to the plasma and neutral grid refinement are tested in typical turbulence simulations, showing that convergence of the simulation results is achieved with a plasma and neutral grid spacing of approximately 2.5 ρ_{s0} and 0.075 λ_n, respectively. The convergence with respect to the neutral calculation frequency is also studied, showing that evaluating the neutral density every $\Delta t = 0.1 R_0/c_{s0}$ is sufficient to guarantee the convergence of the simulation results.

Finally, the results of the first GBS electromagnetic simulation of a TCV lower single-null discharge, which include the self-consistent evolution of neutral dynamics, are presented.

3 Turbulent transport regimes in the tokamak edge

The goal of this chapter is to present an overview of the turbulent transport regimes that can be identified in the tokamak edge from the results of three-dimensional, flux-driven, two-fluid electrostatic simulations in single-null configuration carried out by using the GBS code. In particular, three turbulent transport regimes are identified: (i) a developed transport regime with turbulence driven by an interchange instability, which shares a number of features with the standard L-mode of tokamak operation; (ii) a suppressed transport regime, characterized by a higher value of the energy confinement time, low relative amplitude fluctuations driven by a Kelvin-Helmholtz (KH) instability, a strong $\mathbf{E} \times \mathbf{B}$ sheared flow, and the formation of a transport barrier, which recalls the H-mode; (iii) a degraded confinement regime, characterized by a catastrophically large interchange-driven turbulent transport, which reminds the crossing of the Greenwald density limit. For each transport regime, an analytical scaling of the edge pressure gradient length is derived and compared to simulation results, showing a good agreement. We also discuss the transitions between the developed and suppressed transport regime.

The main results of this chapter have been recently published in Ref. [72].

3.1 Introduction

The turbulent plasma dynamics in the tokamak edge plays a key role in determining the overall performances of a tokamak. In fact, fundamental phenomena, such as the L-H transition [231] and the density limit [79, 80], strongly depend on the plasma dynamics in this region and have been associated to the transition between different turbulent regimes. Understanding the physical mechanisms behind these phenomena, identifying the edge turbulent regimes and their transition while improving our predictive capability, is therefore of fundamental importance in the design and operation of future magnetic fusion devices.

Focusing on the L-H transition, an empirical scaling law of the power threshold for

H-mode access, P_{LH}, has been proposed in Ref. [134] based on an international H-mode threshold power database:

$$P_{\text{LH}} \propto n_e^{0.78\pm0.04} B_0^{0.77\pm0.03} a^{0.98\pm0.08} R^{1.0\pm0.1}, \tag{3.1}$$

where n_e is the line-averaged electron density. In addition, it has been experimentally observed in a single-null geometry that P_{LH} is lower when the ion-∇B drift direction is towards the X-point, rather than away from it [6]. Moreover, experimental results show that P_{LH} depends inversely on m_i/m_e [128, 176]. Experimental observations in Alcator C-Mod [205] and DIII-D [222] tokamaks have pointed out the presence of hysteresis in the L-H transition, although this is not a feature universally observed [187]. Furthermore, just before the L-H transition, it has been experimentally observed the formation at the tokamak edge of a clear well in the radial electric field profile that induces a strong $\mathbf{E} \times \mathbf{B}$ shear flow, which, in turn, suppresses plasma turbulence [25, 82, 186].

In the present chapter, we consider a set of GBS simulation to explore the edge turbulent regimes. The simulations are carried out by using the drift-reduced two-fluid model described in Ch. 2, simplified here by taking the electrostatic limit, making use of the Boussinesq approximation and neglecting the coupling with neutrals. The importance of the electromagnetic effects and of the Boussinesq approximation is discussed in Ch. 5. While using a fluid model in the SOL is well justified by the high plasma collisionality, its application to the tokamak edge, especially in H-mode, depends on machine size and density. For instance, if we consider typical values of density and temperature at the top of the pedestal for neutral beam heated discharges of a medium size tokamak such as TCV, $\lambda_e/L_\parallel$ ranges from 0.05 ($T_e \simeq 100$ eV and $n \simeq 5 \times 10^{19}$ m^{-3}) to 0.4 ($T_e \simeq 200$ eV and $n \simeq 3 \times 10^{19}$ m^{-3}), depending on the external gas injection rate [201], thus providing a justification to the use of a fluid model. On the other hand, in the case of JET tokamak, typical values of density and temperature at the top of the pedestal [14] ($T_e \simeq 900$ eV and $n \simeq 7 \times 10^{19}$ m^{-3}) lead to $\lambda_e/L_\parallel \simeq 2$. Focusing on the drift approximation that, contrary to more advanced fluid models (see e.g. Ref. [240]), does not allow us to describe finite-Larmor radius effects, we observe that the dominant modes in our simulations satisfy $k_\perp \rho_i \ll 1$, consistently with our model hypothesis, although turbulence in the tokamak edge can also be driven by unstable modes with $k_\perp \rho_i \sim 1$ [43, 101].

GBS simulations point out the presence of various turbulent transport regimes in the tokamak edge, which we identify according to the value of the edge collisionality and heat source. In particular, we identify a regime of developed transport with turbulence driven by a resistive interchange instability, a regime of suppressed transport with turbulence driven by a KH instability, and a regime of extremely large turbulent transport. The transition between the developed and the suppressed transport regime is carefully analyzed, leading to an analytical estimate of the power threshold to access the suppressed transport regime. The analysis presented in this chapter is focused mainly on the tokamak edge. The extension of this analysis to the SOL is reported in Ch. 4, where analytical scaling laws of the near and far SOL widths are derived in the developed transport regime and compared to experimental data taken from a multi-machine database of L-mode discharges. The transition to the degraded confinement regime is instead treated in Ch. 5, where a theoretical scaling law of the maximum density achievable in magnetic fusion devices is derived and successfully validated against a multi-machine database of density limit discharges.

The present chapter is structured as follows. An overview of the simulation results is presented in Sec. 3.2. The mechanisms that regulate the electrostatic potential in the tokamak boundary are described in Sec. 3.3. The developed transport regime is presented in Sec. 3.4, the suppressed transport regime in Sec. 3.5, while the degraded confinement regime in Sec. 3.6. The transition from the developed to the suppressed transport regime is studied in Sec. 3.7, where an analytical estimate of the heat source threshold to access the suppressed transport regime is derived. The conclusions follow in Sec. 3.8.

3.2 Overview of simulation results

We consider a set of GBS simulations carried out with the following parameters: $\rho_*^{-1} = 500$, $a/R_0 \simeq 0.3$, $\tau = 1$, $\eta_{0e} = 5\times10^{-3}$, $\eta_{0i} = 1$, $\chi_{\parallel e} = \chi_{\parallel i} = 1$, $L_R = 600$, $L_Z = 800$, $s_{n0} = 0.3$, $\Delta_n = 800$, $\Delta_T = 720$, and $D_f = 6$. The simulations have been run at different values of heat source, s_{T0} (see Eq. (2.85)), and resistivity, ν_0 (see Eq. (2.99)), at both ion-∇B drift directions (see Tab. 3.1), considering the same values of temperature source for both the ion and electron species. Regarding the numerical parameters, the grid used is $N_R \times N_Z \times N_\varphi = 240 \times 320 \times 80$ and the time-step is 2×10^{-5}.

The single-null magnetic configuration considered for this set of simulations is analytically obtained by solving the Biot-Savart law for a straight current filament, which is located outside the domain, and a current density with Gaussian profile, which is centered at the tokamak magnetic axis, i.e. at the position (R_0,Z_0), and mimics the plasma current (see Fig. 3.1). The current filament and the plasma current are centered at the same radial position. The amplitude and the width of the current density is chosen to have a safety factor $q_0 \simeq 1$ at the tokamak axis and $q \simeq 4$ at the tokamak edge. The plasma current is parallel to the toroidal magnetic field when the ion-∇B drift points upwards and anti-parallel when it points downwards. The value of the current in the filament is chosen to be equal to the plasma current. Contour lines of the poloidal flux function are displayed in Fig. 3.1. The radial and vertical components of the dimensionless poloidal magnetic field as well as its norm are shown in Fig. 3.2.

After an initial transient, the simulations reach a global turbulent quasi-steady state, resulting from the interplay between the sources in the closed flux surface region, the turbulence that transports plasma and heat from the core to the SOL, and the losses at the vessel. The analysis is carried out in the quasi-steady state conditions.

s_{T0}	ν_0	**ion-∇B drift**
0.6	0.9	upwards
0.3	2.0	upwards
0.3	0.9	upwards
0.3	0.9	downwards
0.3	0.6	upwards
0.3	0.2	upwards
0.15	2.0	upwards
0.15	0.9	upwards
0.15	0.9	downwards
0.15	0.6	upwards
0.15	0.2	upwards
0.075	2.0	upwards
0.075	0.9	upwards
0.075	0.2	upwards
0.075	0.2	downwards

Table 3.1 – Temperature source strength, normalized resistivity, and ion-∇B drift direction for the set of GBS simulations considered in the present chapter.

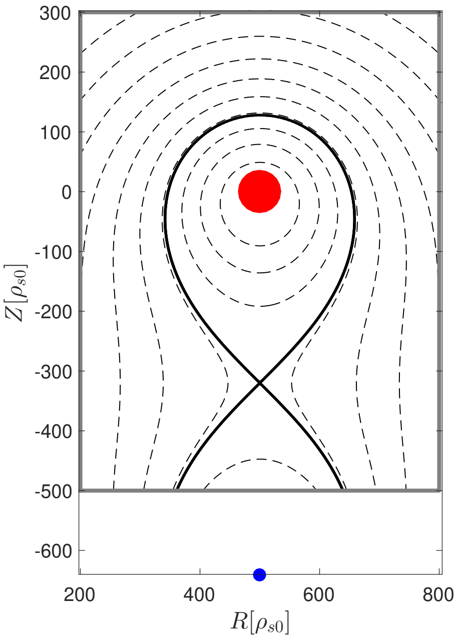

Figure 3.1 – Contour plot of the poloidal flux function ψ (black dashed lines). The separatrix is shown as a solid black line. The boundary domain is indicated by a solid grey line. The red circle represents the plasma current, while the blue point, located outside the domain, represents the current filament used to generate the X-point.

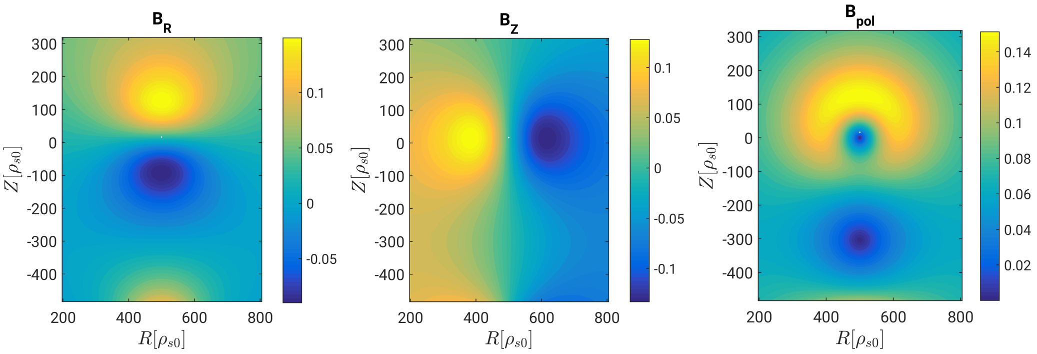

(a) (b) (c)

Figure 3.2 – Radial component (a), vertical component (b), and norm (c) of the dimensionless poloidal magnetic field considered in the present chapter.

In the following, we refer to the equilibrium of any quantity f as its time and toroidal average, $\bar{f} = \langle f \rangle_{\varphi,t}$, and to its fluctuating component as $\tilde{f} = f - \bar{f}$. In addition, we consider the $(\nabla\psi, \nabla\chi, \nabla\varphi)$ flux-aligned coordinate system, where $\nabla\psi$ denotes the direction orthogonal to flux surfaces, $\nabla\varphi$ is the toroidal direction, and $\nabla\chi = \nabla\varphi \times \nabla\psi$.

We define S_n and S_T as the total density and temperature source integrated over the area inside the separatrix,

$$S_n = \int_{A_{\mathrm{LCFS}}} \rho_* s_n(R, Z)\, \mathrm{d}R\mathrm{d}Z \tag{3.2}$$

and

$$S_T = \int_{A_{\mathrm{LCFS}}} \rho_* s_T(R, Z)\, \mathrm{d}R\mathrm{d}Z\,, \tag{3.3}$$

where the factor ρ_* appears from the normalization. Analogously, we define the electron power source $S_p = \int_{A_{\mathrm{LCFS}}} \rho_* s_p\, \mathrm{d}R\mathrm{d}Z$, with $s_p = n s_{T_e} + T_e s_n$ and s_{T_e} the electron temperature source.

An example of typical simulation results is shown in Fig. 3.3, where the equilibrium density, electrostatic potential, electron temperature, ion temperature, vorticity, and parallel current is from the simulation with s_{T0}=0.15 and ν_0=0.2. We note that $\bar{n}$ is approximately a factor of 20 larger in the core than in the near SOL and a factor of 100 larger than in the far SOL. Similar profiles are observed for $\bar{T}_e$ and $\bar{T}_i$. The equilibrium electrostatic potential $\bar{\phi}$ is positive in the SOL and increases from the far SOL towards the separatrix, while it drops and becomes negative inside the LCFS. The change in slope of the electrostatic potential across the separatrix, associated with a change of sign in the equilibrium vorticity, generates a region of very strong $\mathbf{E} \times \mathbf{B}$ shear, which is the main element responsible of the transition between the developed and suppressed transport regimes. The equilibrium parallel current inside the LCFS is mainly regulated by the pressure profile. In fact, by taking the time and toroidal average of Eq. (2.89) and retaining only the dominant terms, we obtain

$$B\nabla_{\parallel}\bar{j}_{\parallel} \simeq -2C(\bar{p}_e + \tau\bar{p}_i)\,. \tag{3.4}$$

The equilibrium parallel current in the SOL close to the target plates is imposed by the boundary conditions through the electrostatic potential (see Eqs. (2.140) and (2.141)) and has been the subject of Ref. [122].

Typical radial profiles at the low-field side (LFS) midplane of the equilibrium electron pressure, electrostatic potential and $\mathbf{E} \times \mathbf{B}$ shear are shown in Fig. 3.4 for three different values of ν_0 corresponding to the three turbulent transport regimes revealed by our simulations. In particular, we consider the simulations with $s_{T0} = 0.15$, ion-∇B drift pointing upwards, and $\nu_0 = 0.2$ (suppressed transport regime), $\nu_0 = 0.6$ (developed transport regime), and $\nu_0 = 2.0$ (degraded confinement regime). In the suppressed transport regime, the electrostatic potential drops significantly inside the separatrix, generating a strong $\mathbf{E} \times \mathbf{B}$ shear across it. This is associated to a steep gradient in the density, electron and ion temperatures. With respect to the suppressed transport regime, the electrostatic potential across the separatrix is flatter in the developed transport regime. In addition, the equilibrium $\mathbf{E} \times \mathbf{B}$ shear is reduced, transport due to turbulence is larger and, consequently, the density and temperature gradient at the tokamak edge is significantly lower. In the degraded confinement regime, turbulent transport is extremely large, leading to a flat profile of density, temperature and electrostatic potential. We note that analogous transitions can be observed by varying the heat source while keeping ν_0 constant. We also observe that the transition from the developed to the suppressed transport regime is rather sharp. The transition from the developed transport regime to the degraded confinement regime is instead gradual.

Typical snapshots of plasma turbulence in the three transport regimes can be seen in Fig. 3.5, where the relative density fluctuations and the corresponding normalized standard deviation are shown for the three simulations we are considering. In the case of $\nu_0 = 0.2$, turbulence is localized near the separatrix and, as a consequence of being sheared apart by the strongly varying $\mathbf{E} \times \mathbf{B}$ radial profile, turbulent structures are elongated along the $\nabla\chi$ direction, effectively reducing the cross-field transport. While the value of the normalized standard deviation of density fluctuations is comparable in the three simulations, the radial extension of turbulent structures is larger for $\nu_0 = 0.6$ and $\nu_0 = 2.0$. In particular, at $\nu_0 = 2.0$, turbulent structures penetrate into the core region, leading to a larger normalized standard deviation of density fluctuations inside the separatrix. This is in agreement with experimental observations of density fluctuations when the density limit is approached [111]. In addition, in the case of $\nu_0 = 0.2$, density fluctuations are generated both at the LFS and high-field side, while, in the other two cases, turbulence mainly develops at the LFS.

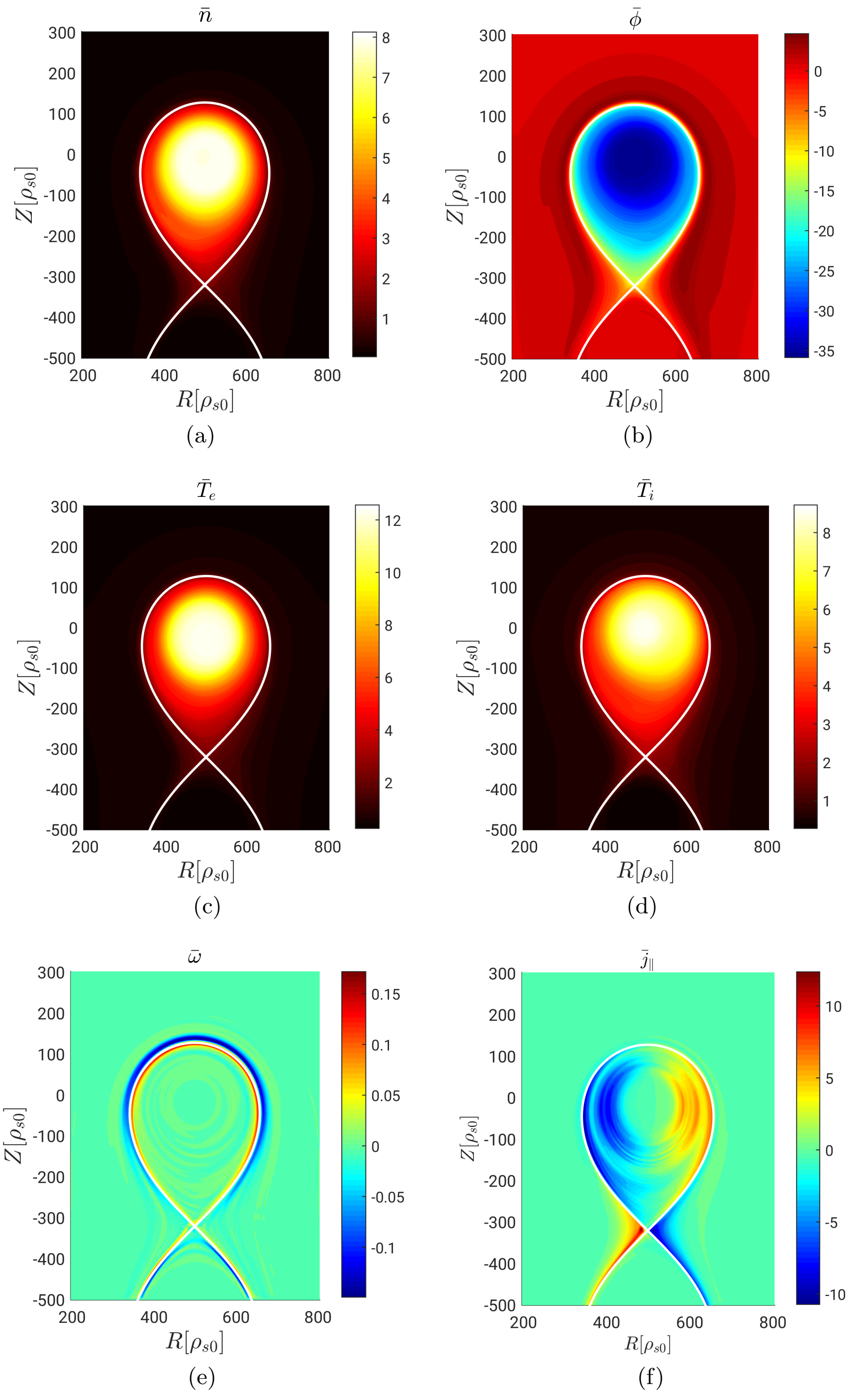

(a) (b) (c) (d) (e) (f)

Figure 3.3 – Equilibrium density (a), equilibrium electrostatic potential (b), equilibrium electron temperature (c), equilibrium ion temperature (d), equilibrium vorticity (e), and equilibrium parallel current (f) in the simulation with $s_{T0} = 0.15$ and $\nu_0 = 0.2$. The white line represents the separatrix.

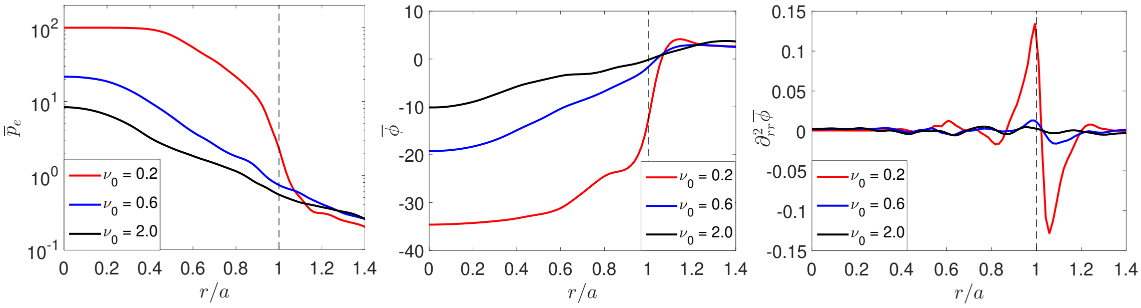

(a) (b) (c)

Figure 3.4 – Radial profiles at the LFS midplane of the equilibrium pressure (a), equilibrium electrostatic potential (b) and equilibrium $\mathbf{E}\times\mathbf{B}$ shear (c) for the simulation with $s_{T0} = 0.15$ and $\nu_0 = 0.2$ (suppressed transport regime), $\nu_0 = 0.6$ (developed transport regime) and $\nu_0 = 2.0$ (degraded confinement regime). The radial coordinate is normalized to the radial position a of the separatrix at the midplane.

In order to highlight the difference on the confinement properties between the different regimes, we compute the electron energy confinement time,

$$\tau_E = \frac{\frac{3}{2}\int_{A_{\mathrm{LCFS}}} \bar{p}_e \,\mathrm{d}R\mathrm{d}Z}{\int_{A_{\mathrm{LCFS}}} s_p \,\mathrm{d}R\mathrm{d}Z}\,, \tag{3.5}$$

for the set of simulations considered in the present chapter, at different values of S_T and ν_0 (see Fig. 3.6). At a given ν_0 or S_T, we note that the simulations in the suppressed transport regime have a higher energy confinement time than the simulations in the developed transport regime. For this reason, we also refer to the developed transport regime as the L-mode and to the suppressed transport regime as the H-mode. The energy confinement time increases by a factor of two from the L-mode to the H-mode, as observed in the experiments.

3.3 Mechanisms regulating the equilibrium electrostatic potential

The equilibrium electrostatic potential plays a key role in suppressing turbulent transport through the poloidal equilibrium $\mathbf{E}\times\mathbf{B}$ shear. It is therefore important to understand the mechanisms that regulate its equilibrium radial profile.

In the SOL, ambipolarity of the plasma flow at the sheath imposes that the electrostatic potential is proportional to the electron temperature, $\bar{\phi} \sim \Lambda \bar{T}_e$ [124, 211]. In fact, the dominant terms of the equilibrium generalized Ohm's law (see Eq. (2.74)), as identified

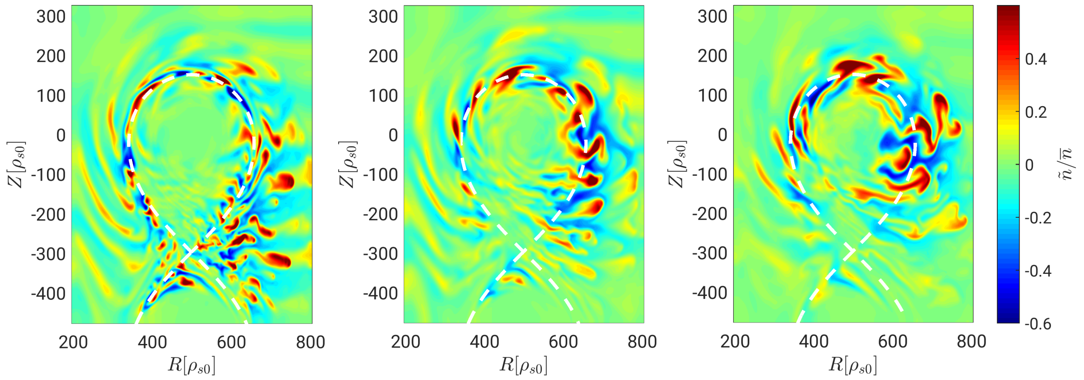

(a) Suppressed transport (b) Developed transport (c) Degraded confinement

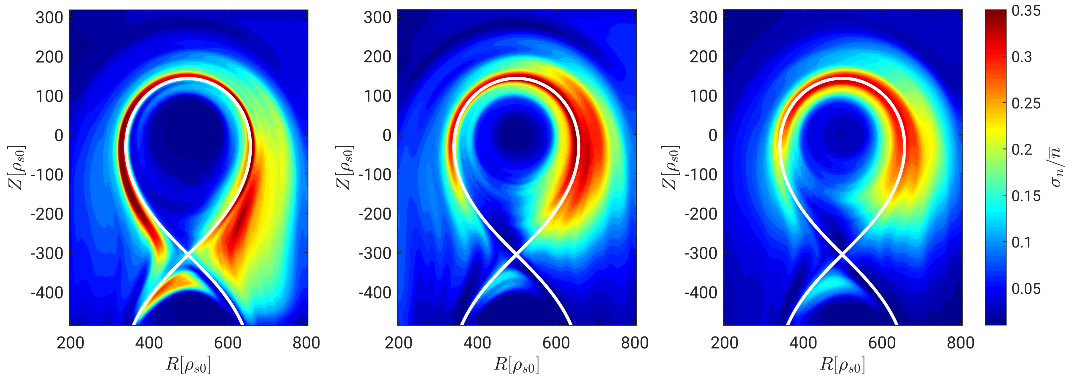

(d) Suppressed transport (e) Developed transport (f) Degraded confinement

Figure 3.5 – Typical snapshot of the relative density fluctuations (top raw) and normalized standard deviation of the density fluctuations (bottom raw) for three simulations with $s_{T0} = 0.15$ in the suppressed transport regime, $\nu_0 = 0.2$ [(a) and (d)], developed transport regime, $\nu_0 = 0.6$ [(b) and (e)], and degraded confinement regime, $\nu_0 = 2.0$ [(c) and (f)].

from GBS simulations, lead to

$$\nabla_\parallel \bar{\phi} \sim \frac{\nabla_\parallel \bar{p}_e}{\bar{n}} + 0.71 \nabla_\parallel \bar{T}_e \,, \tag{3.6}$$

since the contribution of the parallel current can be neglected. By assuming that the density variation along magnetic field lines is weaker than the electron temperature one, Eq. (3.6) can be easily integrated [124],

$$\bar{\phi} \sim \frac{1}{2}(\phi_{t1} + \phi_{t2}) + 1.71 \left[\bar{T}_e - \frac{1}{2}(T_{e,t1} + T_{e,t2}) \right] , \tag{3.7}$$

where ϕ_{t1}, ϕ_{t2} and $T_{e,t1}$, $T_{e,t2}$ are the values of the electrostatic potential and electron temperature at the two magnetic pre-sheath entrances on the target plates. If we neglect the temperature variation along magnetic field lines and assume $T_{e,t1} = T_{e,t2}$, Eq. (3.7) can be further simplified, and the sheath ambipolarity condition $\phi_{t1} \simeq \phi_{t2} \simeq \Lambda \bar{T}_e$ leads

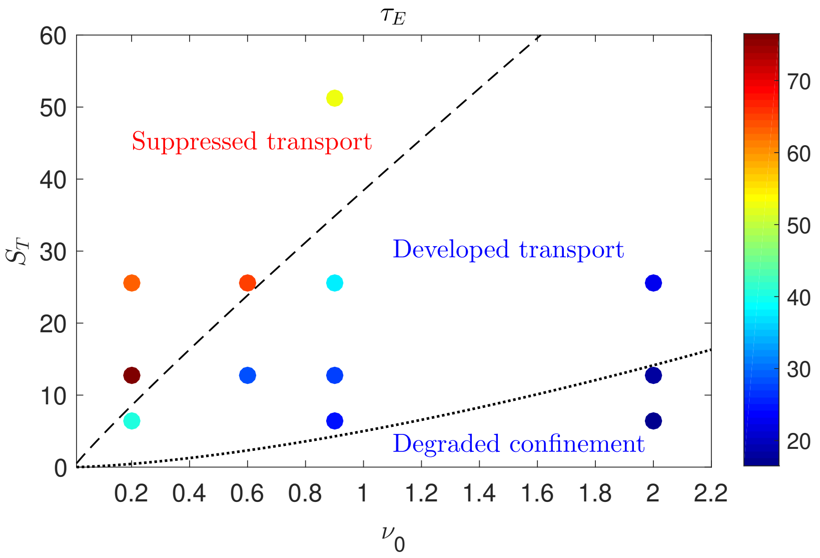

Figure 3.6 – Electron energy confinement time for the set of simulations with ion-∇B drift pointing upwards. The dashed black line represents the heat source threshold to access the suppressed transport regime (derived in Sec. 3.7). The transition between the developed transport and the degraded confinement regimes (dotted black line) is discussed in Ch. 5.

to

$$\bar{\phi} \sim \Lambda \bar{T}_e \,. \tag{3.8}$$

A comparison between the analytical estimate of Eq. (3.8) and the equilibrium electrostatic potential obtained from the simulation is shown in Fig. 3.7 for the simulation with $s_{T0} = 0.3$ and $\nu_0 = 0.9$. The analytical theory reproduces well the equilibrium electrostatic potential in the SOL, while failing when approaching the separatrix, where the electrostatic potential drops and the sheath ambipolarity condition is not satisfied.

In contrast to the SOL, where the dynamics of $\bar{\phi}$ is mainly imposed by the sheath, in the tokamak core the equilibrium radial electric field is proportional to the ion pressure gradient, $\partial_\psi \bar{\phi} \sim -\partial_\psi \bar{p}_i/\bar{n}$, as experimentally observed (e.g., see Refs. [196] and [138]). The relation between $\bar{\phi}$ and $\bar{T}_i$ can be derived from the drift-reduced Braginskii equations by following a procedure similar to the one outlined in Ref. [250]. We consider the leading order terms of the equilibrium density and vorticity equations (see Eqs. (2.88) and (2.89)),

$$-\rho_*^{-1}\overline{[\phi, n]} - 2\bar{n}C(\bar{\phi}) + 2C(\bar{p}_e) - \nabla_\parallel(\bar{n}\bar{V}_{\parallel e}) \simeq 0 \,, \tag{3.9}$$

$$\nabla_\parallel \bar{j}_\parallel + 2C(\bar{p}) \simeq 0 \,. \tag{3.10}$$

We then subtract Eq. (3.10) to Eq. (3.9) and approximate $\nabla_\parallel(\bar{n}\bar{V}_{\parallel e}) \simeq -\nabla \bar{j}_\parallel$, obtaining

$$\rho_*^{-1}\overline{[\phi, n]} + 2\bar{n}C(\bar{\phi}) + 2C(\bar{p}_i) \simeq 0 \,. \tag{3.11}$$

The Poisson bracket in Eq. (3.11) can be decomposed in an equilibrium and a fluctuating component, leading to

$$\overline{[\phi, n]} = \left(\partial_\chi \bar{\phi} \partial_\psi \bar{n} - \partial_\psi \bar{\phi} \partial_\chi \bar{n}\right) + \overline{\partial_\chi \tilde{\phi} \partial_\psi \tilde{n} - \partial_\psi \tilde{\phi} \partial_\chi \tilde{n}}\,. \tag{3.12}$$

If we restrict our analysis to the tokamak core, the fluctuating component is negligible with respect to the equilibrium one. Since equilibrium quantities are approximately flux functions, they can be expanded in Fourier series retaining only the first order contribution, leading to

$$\begin{aligned} \bar{\phi} &\sim \phi_0(\psi) + \phi_1(\psi)\cos(\chi + \vartheta_\phi)\,, && (3.13)\\ \bar{n} &\sim n_0(\psi) + n_1(\psi)\cos(\chi + \vartheta_n)\,, && (3.14)\\ \bar{p_i} &\sim p_{i0}(\psi) + p_{i1}(\psi)\cos(\chi + \vartheta_p)\,, && (3.15)\\ & && (3.16) \end{aligned}$$

where $\phi_1 \ll \phi_0$, $n_1 \ll n_0$ and $p_{i1} \ll p_{i0}$, with χ denoting the poloidal angle[I]. Simulation results show that the phase difference between ϕ_1, n_1 and p_{i1} is negligible, i.e. $\vartheta_\phi \simeq \vartheta_n \simeq \vartheta_p \simeq 0$. By expanding $\bar{n}$, $\bar{\phi}$ and $\bar{p_i}$ in Eq. (3.11), we obtain

$$-\rho_*^{-1}(\phi_1 \partial_\psi n_0 - n_1 \partial_\psi \phi_0) + 2n_0 \partial_\psi \phi_0 + 2\partial_\psi p_{i0} \simeq 0\,. \tag{3.17}$$

The quantity ϕ_1 can be estimated from the leading order terms in Eq. (2.74),

$$\partial_\chi \phi_1 \simeq \frac{\partial_\chi p_{e1}}{n} + 0.71 \partial_\chi T_{e1} \sim 2.71 \partial_\chi n_1\,. \tag{3.18}$$

By approximating $\partial_\chi T_{e1} \sim \partial_\chi n_1$ and substituting ϕ_1 in Eq. (3.17), the radial electric field is given by

$$\partial_\psi \phi_0 \sim \frac{-2\partial_\psi p_{i0} + 2.71 \rho_*^{-1} n_1 \partial_\psi n_0}{2n_0 + \rho_*^{-1} n_1}\,. \tag{3.19}$$

We highlight that, although generally small, poloidal variations of density and temperature contribute to the radial electric field through the terms proportional to $\rho_*^{-1} n_1$. However, neglecting any poloidal variation in Eqs. (3.13)-(3.15), leads to

$$\partial_\psi \bar{\phi} \sim -\frac{\partial_\psi \bar{p_i}}{\bar{n}}\,, \tag{3.20}$$

which is in agreement with the theoretical result derived in Ref. [250]. A comparison between the numerical result and the analytical estimate of $\partial_\psi \bar{\phi}$ (see Eq. (3.20)) is shown in Fig. 3.7 for the simulation with $s_{T0} = 0.3$ and $\nu_0 = 0.9$. The agreement is good throughout the entire core, while it breaks close to the separatrix where the assumption of small fluctuations in the Poisson brackets of Eq. (3.11) breaks down, being the fluctuating

---

[I] The analysis is carried out in the confined region where the coordinate $\chi \in [0, 2\pi]$, associated with the $(\nabla\psi, \nabla\chi, \nabla\varphi)$ flux coordinate system, corresponds to the poloidal angle.

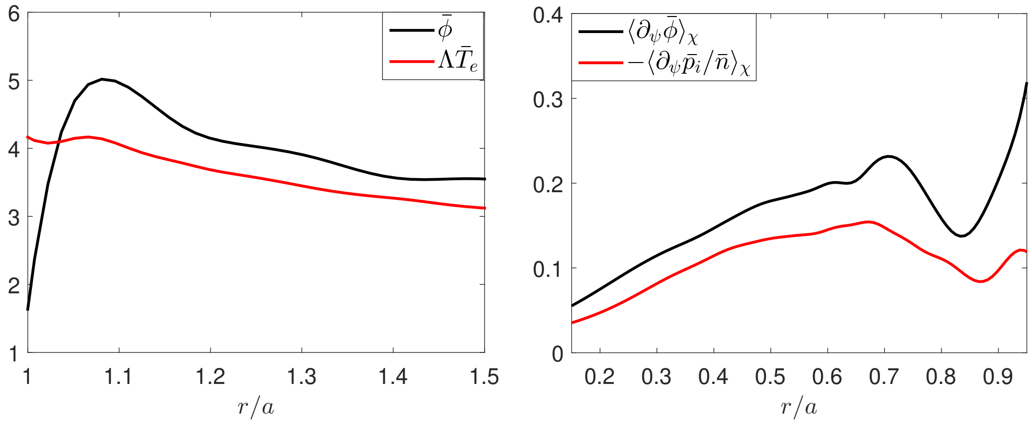

(a) (b)

Figure 3.7 – Comparison between the equilibrium radial electrostatic potential profile (black line) and the equilibrium radial electron temperature profile (red line) in the SOL at the outboard midplane for the simulation with $s_{T0} = 0.3$ and $\nu_0 = 0.9$ (a). Flux-surface average of the equilibrium radial electric field (black line) and ion pressure gradient (red line) inside the LCFS for the same simulation (b).

component in Eq. (3.12) comparable to the equilibrium one. Moreover, in the proximity of the separatrix, the contribution of the polarization current, associated to the presence of zonal flows, has to be included in Eq. (3.10), making it very challenging to proceed analytically.

3.4 Developed transport regime

The developed transport regime, shown by GBS simulations at intermediate values of heat source and collisionality, is characterized by turbulent transport driven by nonlinear development of interchange-driven electrostatic ballooning modes [147] with a negligible effect of the shear flow. This can be verified by removing the interchange drive from the simulations, i.e. by toroidally averaging the term proportional to $C(p_e + \tau p_i)$ in Eq. (2.73). The result of this test is displayed in Fig. 3.8, where a snapshot of the electron temperature, with and without the interchange drive, is shown for a simulation in the developed transport regime ($s_{T0} = 0.075$ and $\nu_0 = 0.9$). Plasma turbulence is strongly suppressed when the term $C(p_e + \tau p_i)$ is toroidally averaged and, as a consequence, an increase of the equilibrium temperature and pressure gradients is observed. On the other hand, turbulent structures and plasma profiles do not change significantly when the Reynolds stress, i.e. the term $\rho_*^{-1}[\phi, \omega]/B$ appearing in Eq. (2.73), is toroidally averaged (see Fig. 3.8). This shows that the $\mathbf{E} \times \mathbf{B}$ shear and the KH instability do not play a major role in the developed transport regime.

We provide now an analytical estimate of the pressure gradient length across the separatrix

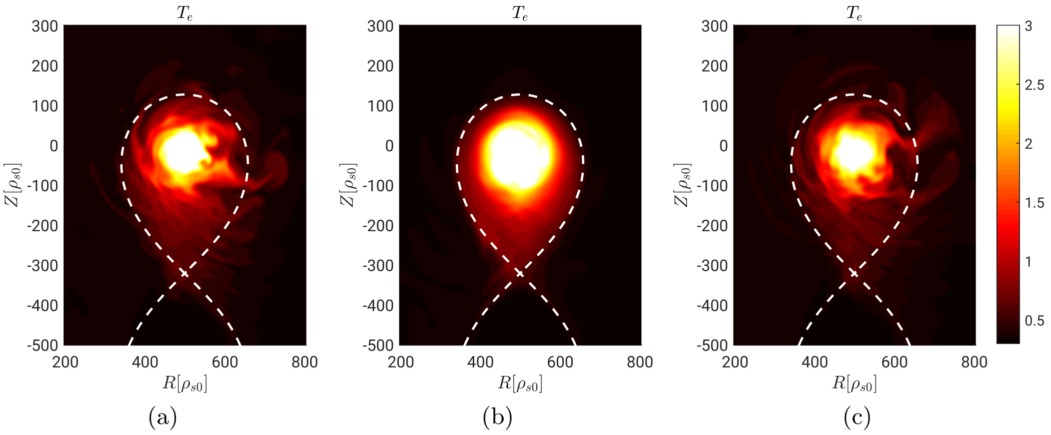

(a) (b) (c)

Figure 3.8 – A typical snapshot of the electron temperature for the simulation with $s_{T0} = 0.075$ and $\nu_0 = 0.9$ (a). Snapshots of simulations with the same parameters but the interchange drive $C(p_e + \tau p_i)$ term in Eq. (2.73) toroidally averaged (b), and with the KH drive term $\rho_*^{-1}[\phi, \omega]/B$ in Eq. (2.73) toroidally averaged (c).

in the developed transport regime by balancing the perpendicular heat flux crossing the separatrix with the heat source integrated over the volume inside the LCFS. As shown in Fig. 3.9, the equilibrium cross-field heat flux near the separatrix is negligible with respect to the turbulent one, $\overline{\bar{p}_e \partial_\chi \bar{\phi}} \ll \overline{\tilde{p}_e \partial_\chi \tilde{\phi}}$, and therefore we focus on the perpendicular turbulent transport, $q_\psi \simeq \overline{\tilde{p}_e \partial_\chi \tilde{\phi}}$, at the LCFS. The quantity $\partial_\chi \tilde{\phi}$ is estimated from the leading terms of the linearized electron pressure equation, which is obtained by linearizing and summing Eqs. (2.88) and (2.92),

$$\partial_t \tilde{p}_e \sim \rho_*^{-1} \partial_\psi \bar{p}_e \partial_\chi \tilde{\phi} \,, \tag{3.21}$$

where the curvature and parallel gradient terms are significantly smaller than the terms we retain. In Eq. (3.21), we estimate the time derivative as the growth rate of the ballooning instability driving the transport, $\gamma_i = \sqrt{2\bar{T}_e/(\rho_* L_p)}$. We also approximate $|\partial_\psi \bar{p}_e| \sim \bar{p}_e/L_p$ being L_p the equilibrium pressure gradient length. The resulting expression of $\partial_\chi \tilde{\phi}$ can then be used to evaluate the cross-field interchange-induced heat flux as

$$q_{\psi,i} \sim \rho_* \gamma_i \frac{\tilde{p}_e^2}{\bar{p}_e} L_p \,. \tag{3.22}$$

The amplitude of the pressure fluctuations appearing in Eq. (3.22) can be estimated by observing that the growth of the linearly unstable modes saturates when the instability drive is removed from the system, i.e. $k_\psi \tilde{p}_e \sim \bar{p}_e/L_p$ [173, 174]. The perpendicular heat flux is then written as

$$q_{\psi,i} \sim \rho_* \frac{\gamma_i}{k_{\psi,i}^2} \frac{\bar{p}_e}{L_p} \,, \tag{3.23}$$

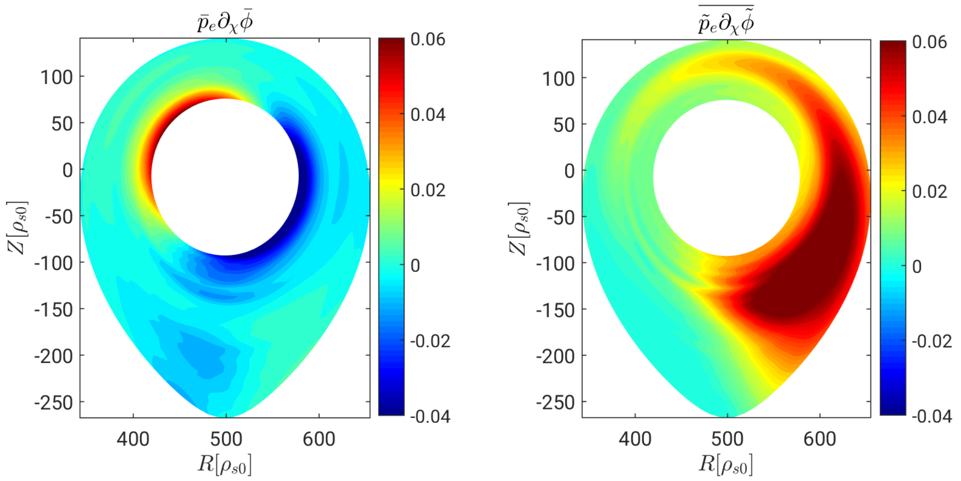

(a) (b)

Figure 3.9 – Equilibrium (a) and turbulent (b) cross-field heat flux inside the LCFS for the simulation with $s_{T0} = 0.015$ and $\nu_0 = 0.6$.

where $k_{\psi,i}$ can be derived from non-local linear calculations, as show in Ref. [174], which lead to $k_{\psi,i} \simeq \sqrt{k_{\chi,i}/L_p}$. The poloidal wavenumber of the ballooning instability $k_{\chi,i}$ can then be obtained by balancing the interchange drive and the parallel current terms in Eq. (2.73). Since turbulence in this regime is driven by resistive ballooning modes [147], the parallel current is limited by the resistivity [89, 88], from which it follows that $k_{\chi,i} = (\bar{n}\nu q^2\gamma_i)^{-1/2}$. As a consequence, Eq. (3.23) becomes

$$q_{\psi,i} \sim \rho_*^{1/4}\sqrt{\bar{n}\nu q^2}\left(\frac{2\bar{T}_e}{L_p}\right)^{3/4}\bar{p}_e\,. \tag{3.24}$$

We observe that the heat source integrated over the poloidal plane inside the LCFS corresponds, approximately, to the perpendicular turbulent heat flux crossing the LCFS on a poloidal plane:

$$S_p(R,Z) \simeq \oint_{\mathrm{LCFS}} q_{\psi,i}(R,Z)\,\mathrm{d}l\,. \tag{3.25}$$

The integral on the right-hand side of Eq. (3.25) can be computed by noting that turbulent transport is driven by ballooning modes that develop in the bad-curvature region (see Fig. 3.8). As a consequence, we assume that $q_{\psi,i}(R,Z)$ has a constant value at the LCFS on the LFS and vanishes at the high-field side, i.e.

$$S_p \sim \frac{L_\chi}{2}q_{\psi,i}\,, \tag{3.26}$$

where $L_\chi = \oint_{\mathrm{LCFS}}\mathrm{d}l$ is the length of the LCFS poloidal circumference. The equilibrium pressure gradient length across the separatrix is obtained by using Eqs. (3.24) and (3.26),

$$L_{p,i} \sim \left[\frac{\rho_*}{2} (\nu q^2 \bar{n})^2 \left(\frac{L_\chi}{S_p} \bar{p}_e \right)^4 \right]^{1/3} \bar{T}_e \,, \tag{3.27}$$

where $\bar{n}$, $\bar{T}_e$, and $\bar{p}_e$ are evaluated at the LCFS.

We highlight that $\bar{T}_e$ at the LCFS appearing in Eq. (3.27) depends on S_p. The relation between $\bar{T}_e$ at the LCFS and S_p can be obtained by balancing S_p with the parallel losses to the vessel walls. As an order of magnitude estimate, this balance can be expressed by integrating the heat flux over the SOL width, Δ_{SOL}, as

$$\int_{\Delta_{\mathrm{SOL}}} \bar{p}_e \bar{c}_s \, \mathrm{d}l \sim S_p \,, \tag{3.28}$$

where we assume to be in the sheath limited-regime (i.e. no temperature drop in the divertor region) and that the plasma outflows at the divertor plate with the sound speed. This assumption restricts the applicability of the L_p scaling derived here to the low-density and low-recycling regime. An extension of this scaling to high density regimes is discussed in Ch. 5. By assuming that the electron pressure and electron temperature decay exponentially in the SOL on the scale L_p and L_T, respectively, with $L_T \simeq (1+\eta_e)L_p/\eta_e$ and $\eta_e \simeq 0.77$ given by Ref. [174], $\bar{T}_e$ at the LCFS is derived by integrating Eq. (3.28), leading to

$$\bar{T}_e \sim \left[\left(1 + \frac{\eta_e}{2(1+\eta_e)} \right) \frac{S_p}{\bar{n} L_p} \right]^{2/3} . \tag{3.29}$$

The final expression of $L_{p,i}$ is derived by replacing $\bar{T}_e$, Eq. (3.29), in Eq. (3.27),

$$L_{p,i} \sim \left[\frac{1}{8} \left(1 + \frac{\eta_e}{2(1+\eta_e)} \right)^8 \rho_*^3 \nu_0^6 q^{12} L_\chi^{12} \bar{n}^{10} S_p^{-4} \right]^{1/17} . \tag{3.30}$$

We show in Fig. 3.10 the ratio of L_p, the equilibrium pressure gradient length directly obtained from the simulations, to $L_{p,i}$, the interchange estimate in Eq. (3.30), for the different values of S_T and ν_0 considered in the present chapter. At low values of S_T and high values of ν_0, we note that $L_p/L_{p,i} \simeq 1$, thus revealing a good agreement between the analytical estimate of Eq. (3.30) and the simulation results. Hence, in the developed transport regime (as well as in the degraded confinement regime), turbulence is driven by the interchange instability with a negligible effect of the shear flow. On the other hand, for high values of the heat source and low ν_0, the pressure gradient length of the simulations is larger than the value predicted by Eq. (3.30), $L_p/L_{p,i} > 1$, meaning that a mechanism different than the interchange instability is responsible for driving turbulent transport and setting the equilibrium pressure gradient length.

It should be noted that, despite being still described as the result of the development of

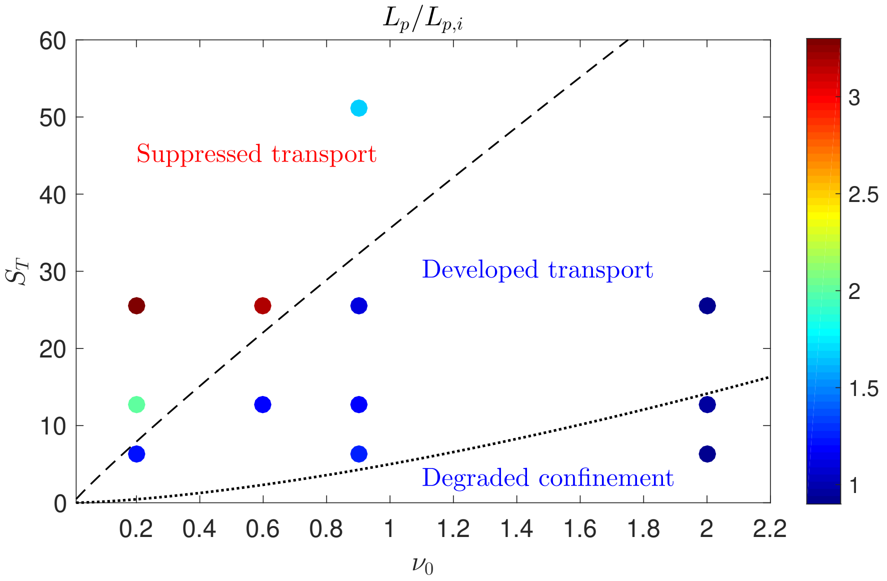

Figure 3.10 – Ratio of L_p, the equilibrium pressure gradient length directly obtained from the simulations, to $L_{p,i}$, the estimate in Eq. (3.30) based on the assumption that transport is driven by the interchange instability, for all the simulations considered in the present study. The dashed black line represents the heat source threshold to access the suppressed transport regime (derived in Sec. 3.7). The transition between the developed transport and the degraded confinement regimes (dotted black line) is discussed in Ch. 5.

the interchange instability, turbulent transport becomes catastrophically large at high values of ν_0 and low heat source values, with turbulent eddies that extend from the edge towards the tokamak core, a behaviour that we associate to the crossing of the density limit (discussed in Ch. 5).

3.5 Suppressed transport regime

As shown in Fig. 3.4, the equilibrium electrostatic potential profile inside the LCFS in the suppressed transport regime is significantly different from the one in the developed transport regime. As detailed in Sec. 3.3, $\bar{\phi}$ radially increases as one moves from the magnetic axis towards the LCFS ($-\partial_r \bar{p}_i/\bar{n} > 0$) and then decreases from the LCFS towards the far SOL ($\partial_r \bar{T}_e < 0$). It follows that $\bar{\phi}$ peaks near the separatrix (see Fig. 3.4 (b)). As s_{T0} increases or ν_0 decreases, both T_e and T_i increase and, as a consequence, also the $\mathbf{E} \times \mathbf{B}$ shear flow across the LCFS increases (see Fig. 3.4 (c)). Because of the $\mathbf{E} \times \mathbf{B}$ shear, the turbulent eddies in the edge resulting from the interchange instability are sheared along the $\nabla\chi$ direction. Furthermore, when the shearing rate, $\rho_*^{-1}\partial_\psi^2\bar{\phi}$, is comparable to γ_i, ballooning turbulence is nonlinearly suppressed [25, 220]. At the same time, the $\mathbf{E} \times \mathbf{B}$ shear provides the drive of the KH instability through the Reynolds stress [150]. In fact, as shown in Fig. 3.11 for the simulation with $s_{T0} = 0.15$ and $\nu_0 = 0.2$, at sufficiently

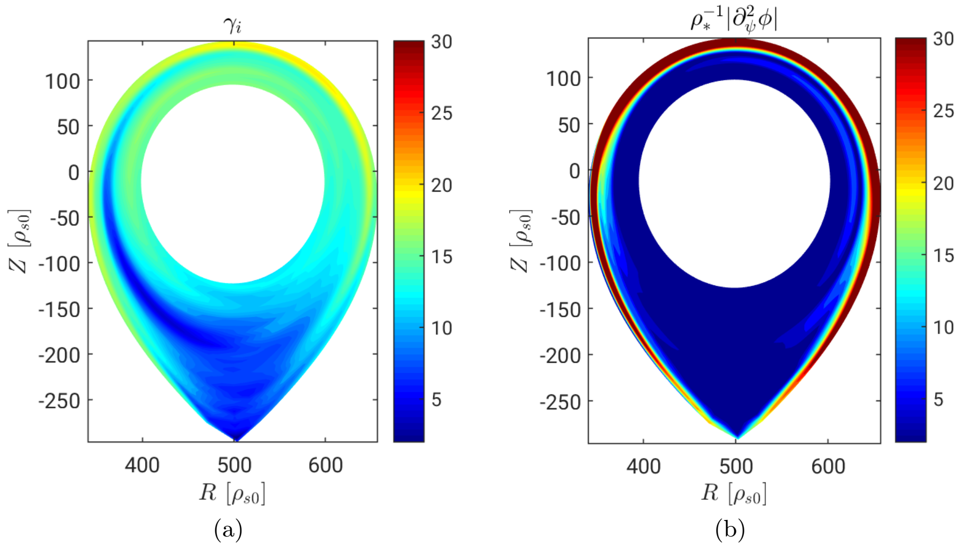

(a) (b)

Figure 3.11 – Maximum growth rate of the interchange instability (a) and $\mathbf{E}\times\mathbf{B}$ shear rate (b).

high values of the heat source or low values of resistivity, $\rho_*^{-1}\partial_\psi^2\bar{\phi}$ is larger than γ_i in the proximity of the LCFS and, as a consequence, the interchange instability is suppressed in the edge, with the KH instability that becomes the primary instability driving turbulent transport [150, 180].

A typical snapshot of the electron temperature for a simulation in the suppressed transport regime ($s_{T0} = 0.6$ and $\nu_0 = 0.9$) is shown in Fig. 3.12 and compares to two simulations having the same parameters, but with the KH and ballooning drives removed. Turbulence is strongly suppressed when the Reynolds stress is toroidally averaged. On the other hand, no significant effect on turbulence is noticed when the interchange drive is removed. This shows that the KH instability is the main drive of turbulent transport and, consequently, regulates the equilibrium pressure gradient in the suppressed transport regime.

An analytical estimate of the equilibrium pressure gradient length in the edge when turbulence is driven by the KH instability can be derived by following a procedure similar to the one detailed in the previous section and discussed for a linear device in Ref. [183]. The growth rate of the KH instability is proportional to the $\mathbf{E}\times\mathbf{B}$ shear [150], $\gamma_{\mathrm{KH}} \sim \rho_*^{-1}\partial_{rr}^2\bar{\phi} \sim \rho_*^{-1}\bar{T}_e/L_p^2$, where we assume that $L_\phi \sim L_p$. Since the KH instability leads to a global mode, the size of the turbulent eddies that it generates is comparable to the pressure gradient length, $k_{\psi,\mathrm{KH}} \sim 1/L_p$. Therefore, similarly to Eq. (3.23), the KH-driven heat flux can be expressed as

$$q_{\psi,\mathrm{KH}} \sim \frac{\bar{T}_e\bar{p}_e}{L_p}\,. \tag{3.31}$$

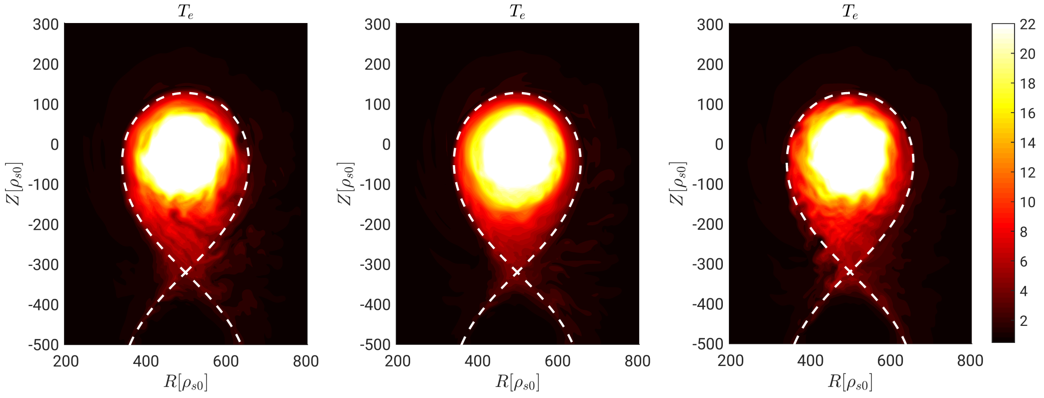

(a) (b) (c)

Figure 3.12 – A typical snapshot of the electron temperature for the simulation with $s_{T0} = 0.6$ and $\nu_0 = 0.9$ (a). Snapshots of simulations with the same parameters but the KH drive term $\rho_*^{-1}\Big[\phi, \omega\Big]/B$ in Eq. (2.73) toroidally averaged (b), and with the interchange drive term $C(p_e + \tau p_i)$ in Eq. (2.73) toroidally averaged (c).

By balancing the heat source integrated over the region inside the LCFS and the perpendicular turbulent heat flux crossing the LCFS, similarly to Eq. (3.25), but assuming that $q_{\psi,\mathrm{KH}}$ is approximately uniform along the LCFS, we obtain

$$L_{p,\mathrm{KH}} \sim \frac{\bar{p}_e \bar{T}_e}{4 S_p} L_\chi \,, \tag{3.32}$$

where $\bar{T}_e$ and $\bar{p}_e$ are evaluated at the LCFS. By replacing $\bar{T}_e$ at the LCFS given by Eq. (3.29) in Eq. (3.32), we obtain the final expression for $L_{p,\mathrm{KH}}$:

$$L_{p,\mathrm{KH}} \sim 2^{-6/7} \left(1 + \frac{\eta_e}{2(1+\eta_e)}\right)^{4/7} \frac{S_p^{1/7} L_\chi^{3/7}}{\bar{n}^{1/7}} \,. \tag{3.33}$$

The ratio of L_p, the equilibrium pressure gradient length directly obtained from the simulations, to $L_{p,\mathrm{KH}}$ is displayed in Fig. 3.13 for the simulations considered in the present chapter. At large values of S_T and small ν_0, $L_{p,\mathrm{KH}}$ well reproduces the simulation results. In fact, the results of Figs. 3.10 and 3.13 show that turbulent transport is driven by the KH instability in the suppressed transport regime, otherwise the interchange instability regulates the equilibrium pressure gradient length. Furthermore, we note that $L_p > L_{p,\mathrm{KH}}$ in the ballooning-driven parameter region, while $L_p > L_{p,i}$ in the suppressed transport regime, as expected from the fact that the mode driving turbulence minimises the pressure gradient.

The suppressed transport regime shows some of the main key aspects observed experimentally in H-mode discharges, such as the presence of a strong sheared flow (see Fig. 3.4

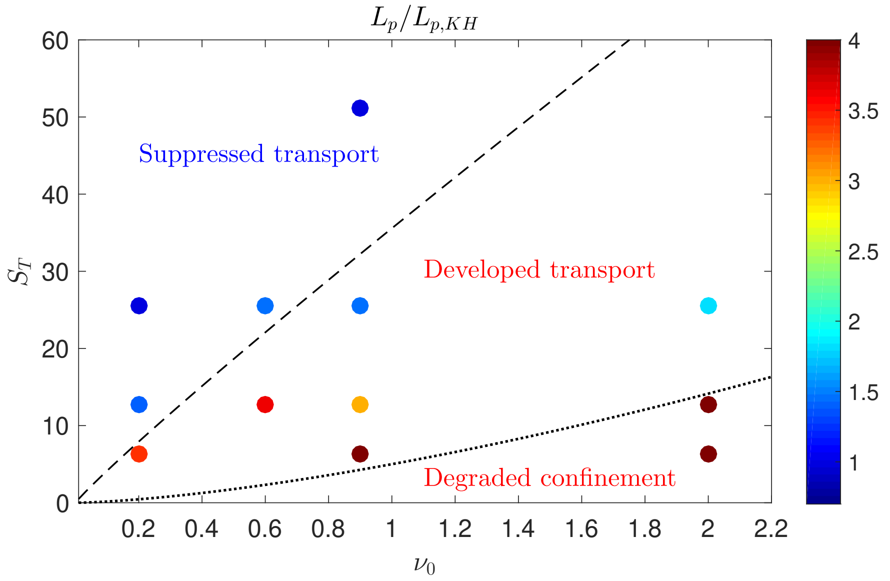

Figure 3.13 – Ratio of L_p, the equilibrium pressure gradient length directly obtained from the simulations, to $L_{p,\mathrm{KH}}$, the estimate in Eq. (3.33) based on the assumption that the transport is driven by the KH instability. The dashed black line represents the heat source threshold to access the suppressed transport regime (derived in Sec. 3.7). The transition between the developed transport and the degraded confinement regimes (dotted black line) is discussed in Ch. 5.

(c)), the reduction of the turbulence level with respect to the L-mode that leads to the formation of a transport barrier near the separatrix (see Fig. 3.4 (a)), and the increase of the energy confinement time (see Fig. 3.6). All this occurs when a power threshold is exceeded, as detailed in Sec. 3.7. We conclude this section by remarking that the KH instability, which characterizes the suppressed transport regime described here, is weakly affected by the value of the viscosity, even at large viscosity when the KH instability is expected to be suppressed [97]. Moreover, as detailed in Ch. 5, this is a consequence of the use of the Boussinesq approximation.

3.6 Degraded confinement regime

At high values of ν_0 and low values of s_{T0}, poor confinement properties and a catastrophically large turbulent transport are observed. In fact, in this parameter regime, despite being described as the non-linear development of a ballooning mode, turbulence results into high level fluctuations, with amplitude comparable to the equilibrium quantity, that propagate from the edge to the core region, as shown in Fig. 3.5. This is due to the fact that, since $k_{\chi,i} \propto \nu_0^{-1/2}$ and $k_{\psi,i} \simeq \sqrt{k_{\chi,i}/L_{p,i}} \propto \nu_0^{-7/12}$, the radial size of the turbulent structures increases with ν_0. The radial extension of turbulent eddies normalized to the tokamak minor radius are shown in Fig. 3.14 for the various simulations considered in

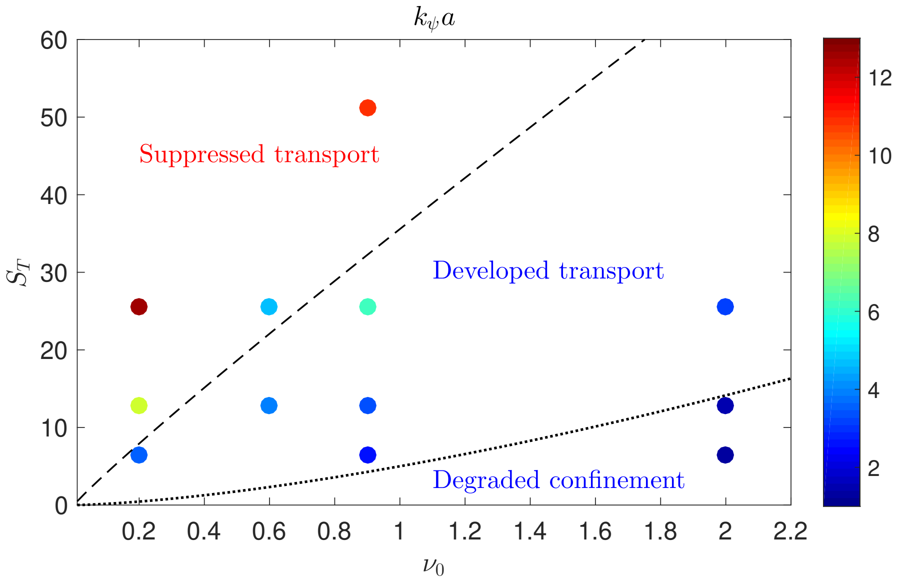

Figure 3.14 – Radial wavenumber computed from the correlation length of turbulent eddies, normalized to the tokamak minor radius, for the simulations with ion-∇B drift pointing upwards. The dashed black line represents the heat source threshold to access the suppressed transport regime (derived in Sec. 3.7), while the dotted black line the threshold to access the degraded confinement regime (see Ch. 5).

the present study. In particular, if the value of ν_0 is sufficiently large and s_{T0} sufficiently small, turbulent eddies appear to have a size comparable to the tokamak minor radius, i.e. $k_\psi a \sim 1$. As a consequence, they extend towards the core region leading to a very large cross-field turbulent transport throughout the closed field line region. In these conditions, the core temperature can significantly drop and MHD modes, which are beyond the description provided by our model, can lead to a plasma disruption [70]. The degraded confinement regime is linked to high values of the density. For this reason, we associate it to the crossing of the density limit, in agreement with the result of Ref. [85]. Experimental evidences that the density limit is due to an increase of edge collisionality, proportional to ν_0 in our model, are reported in Refs. [51, 50, 61, 92, 112, 197, 226] for both tokamaks and stellarators.

Three main effects are observed when crossing the density limit. First, the $\mathbf{E} \times \mathbf{B}$ shear near the separatrix in the degraded confinement regime is weaker than in the developed transport regime, as shown in Fig. 3.4 (c). This is in agreement with recent experiments that show how the edge shear flow collapses when the density limit is approached [92]. The $\mathbf{E} \times \mathbf{B}$ shear turns out to be an important quantity not only to explain the transition from the developed transport regime to the suppressed transport regime, but also to recognize the crossing of the density limit. Second, the degraded confinement regime is characterized by a flatter equilibrium density profile in the SOL with respect to the developed and suppressed transport regimes (see Fig. 3.15). In fact, the blob size increases

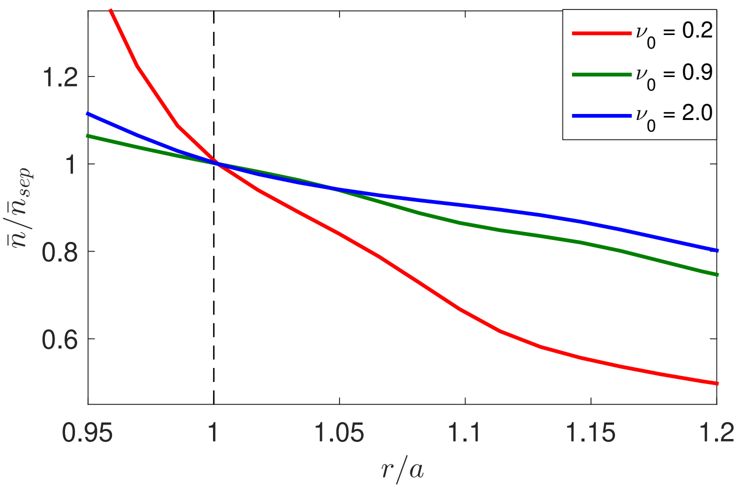

Figure 3.15 – Equilibrium density radial profile at the outboard midplane for simulations at $s_{T0} = 0.075$ and various values of ν_0.

with the collisionality [48, 152, 10], leading to an enhancement of the cross-field turbulent transport in the far SOL (a detailed analysis of the far SOL and blob dynamics is reported in Ch. 4). The density profile becomes flatter with no clear distinction between the edge, near SOL and far SOL. Experimental observations of the flattening of the density profiles as the density increases towards the density limit are reported in Ref. [111]. Third, the large amplitude fluctuations that extend towards the core region lead to a strong enhancement of cross-field turbulent transport and the loss of confinement. This regime is discussed in details in Ch. 5.

3.7 Heat source threshold to access the suppressed transport regime

In this section, we provide an analytical estimate of the heat source threshold to access the suppressed transport regime, while the transition to the degraded confinement regime is discussed in Ch. 5. The transition from the developed transport regime to the suppressed transport regime occurs when $L_{p,i} \simeq L_{p,\mathrm{KH}}$, namely when the turbulent transport due to the interchange instability equals the one due to the KH instability. By equating Eqs. (3.30) and (3.33), we obtain

$$S_p^{\mathrm{LH}} \sim 2^{9/5}\left(1+\frac{\eta_e}{2(1+\eta_e)}\right)^{-4/15}\rho_*^{14/15}\nu_0^{14/15}q^{28/15}L_\chi^{11/15}\bar{n}^{29/15}\,. \tag{3.34}$$

In order to compare the theoretical heat source threshold to access the suppressed transport regime to the simulation results, we express Eq. (3.34) in terms of S_T by using

$S_p \simeq S_T/\bar{n}$,

$$S_T^{\mathrm{LH}} \sim 2^{9/5}\left(1+\frac{\eta_e}{2(1+\eta_e)}\right)^{-4/15} \rho_*^{14/15}\nu_0^{14/15}q^{28/15}L_\chi^{11/15}\bar{n}^{14/15}\,. \tag{3.35}$$

The analytical estimate of the threshold S_T^{LH} as a function of ν_0 is displayed in Fig. 3.13, showing a very good agreement between the analytical prediction of Eq. (3.35) and the simulation results.

We also link the transition from the developed to the suppressed transport regime with experimental observations of the L-H transition. In order to identify the scaling of S_p^{LH} with the main experimental parameters, we write the power threshold in Eq. (3.34) in physical units

$$\begin{aligned} P_{\mathrm{LH}} = 2\pi R_0 S_p^{\mathrm{LH}} &\simeq 0.01 A^{-3/5} n^{29/15} R_0^{22/15} q^{28/15} a^{11/15} (1+\kappa^2)^{11/30} B_T^{-11/15} \\ &\simeq 0.01 A^{-0.6} n^{1.9} R_0^{1.5} q^{1.9} a^{0.7} (1+\kappa^2)^{0.4} B_T^{-0.7}, \end{aligned} \tag{3.36}$$

where the factor $2\pi R_0$ takes into account the integration along the toroidal direction, P_{LH} is the power crossing the separatrix in units of MW, A is the mass number of the main plasma ions, n is the density at the LCFS in units of 10^{19} m^{-3}, R_0 is the tokamak major radius in units of m, $L_\chi \simeq 2\pi a\sqrt{(1+\kappa^2)/2}$ is written in terms of the tokamak minor radius a (in m) and of the plasma elongation κ, and B_T is the toroidal magnetic field at the magnetic axis.

The scaling law in Eq. (3.36) correctly reproduces the isotope effect observed in the experiments [128, 176] and also found in previous theoretical investigations [42]. The dependence on a and R_0 shows a good agreement with the experimental scaling law in Eq. (3.1). The exponent of the density in Eq. (3.36) is approximately a factor 2.7 larger than the one predicted by the experimental scaling law in Eq. (3.1), although we remark that the density in Eq. (3.36) is evaluated at the LCFS, while the density in Eq. (3.1) denotes the line-averaged density. The power threshold in Eq. (3.36) depends inversely on the toroidal magnetic field, while the experimental scaling law in Eq. (3.1) shows a direct dependence on B_T. Moreover, in contrast to the experimental scaling law in Eq. (3.1), the power threshold in Eq. (3.36) depends on the safety factor. We remind that the power threshold in Eq. (3.36) is derived by considering that turbulence in the suppressed transport regime is driven by the KH instability. On the other hand, we show in Ch. 5 that the KH instability observed in this turbulent transport regime is a consequence of the use of the Boussinesq approximation. In fact, as shown in Ch. 5, GBS simulations that avoid the use of the Boussinesq approximation point out that turbulence in the suppressed transport regime is instead driven by the drift-wave instability. The different linear instability at play in the suppressed transport regime could possibly explain the inverse dependence of P_{LH} on B_T in Eq. (3.36).

As an example of the evaluation of Eq. (3.36) in experimental conditions, we consider

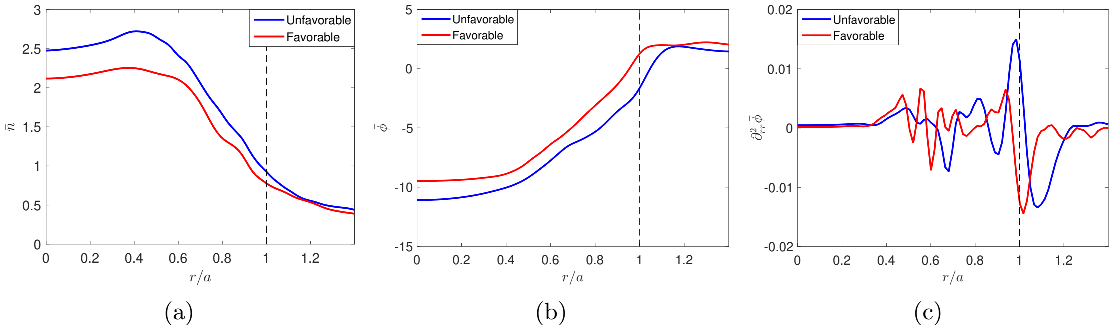

(a) (b) (c)

Figure 3.16 – Radial profiles at the LFS midplane of the equilibrium density (a), equilibrium electrostatic potential (b) and equilibrium $\mathbf{E}\times\mathbf{B}$ shear (c) for the simulation with $s_{T0} = 0.075$, $\nu_0 = 0.2$ and both favorable and unfavorable magnetic field directions.

the value of the power threshold predicted for typical parameters of the TCV tokamak ($a = 0.25$ m, $R_0 = 0.88$ m, line-averaged density $n_e \simeq 4 \times 10^{19}$ m^{-3}, density at the LCFS $n \simeq 2\times10^{19}$ m^{-3}, $B_T \simeq 1.4$ T, and $q \simeq 4$). The estimate in Eq. (3.36) gives $P_{\rm LH} \simeq 142$ kW, a power threshold that has the same order of magnitude as the experimental TCV power threshold, $P_{\rm LH} \simeq 260$ kW (see, e.g., Refs. [192, 133]).

We investigate now the dependence of the heat source threshold in our simulations on the ion-∇B drift direction. In fact, experimental measurements show that the power to access the H-mode is lower when the ion-∇B drift direction is towards the X-point, rather than away from it [6]. We consider a pair of simulations with parameters $s_{T0} = 0.075$ and $\nu_0 = 0.2$ close to the transition when the ion-∇B drift direction points upwards (unfavorable for H-mode access). As shown in Fig. 3.16, the equilibrium density, electrostatic potential and $\mathbf{E}\times\mathbf{B}$ shear profiles at the LFS midplane do not show significant differences between the simulations with favorable and unfavorable ion-∇B drift direction, both simulations belonging to the developed transport regime. Similar observations hold for the simulations with parameters $s_{T0} = 0.3$, $\nu_0 = 0.9$ and opposite ion-∇B drift direction. Therefore, at least in the cases analysed here, the power threshold to access the H-mode is independent of the toroidal magnetic field direction in our simulations. The discrepancy between experimental and simulation observations may be due to the absence of kinetic effects involving passing and trapped particles. Among these, we mention the effects of ion orbit loss that can be important in establishing the dependence of the L-H transition on the ion-∇B drift direction [214, 20], as also pointed out by XGC1 simulations [106].

Experimental observations [205, 222] and theoretical models [46, 90] point out the presence of hysteresis on the power threshold for the L-H transition, i.e. once in H-mode, the hysteresis allows for a decrease of the power below the threshold for H-mode access without inducing the H-L transition. The presence of hysteresis in our simulations is investigated by performing a set of simulations at $\nu_0 = 0.2$ and different values of s_{T0} in the proximity

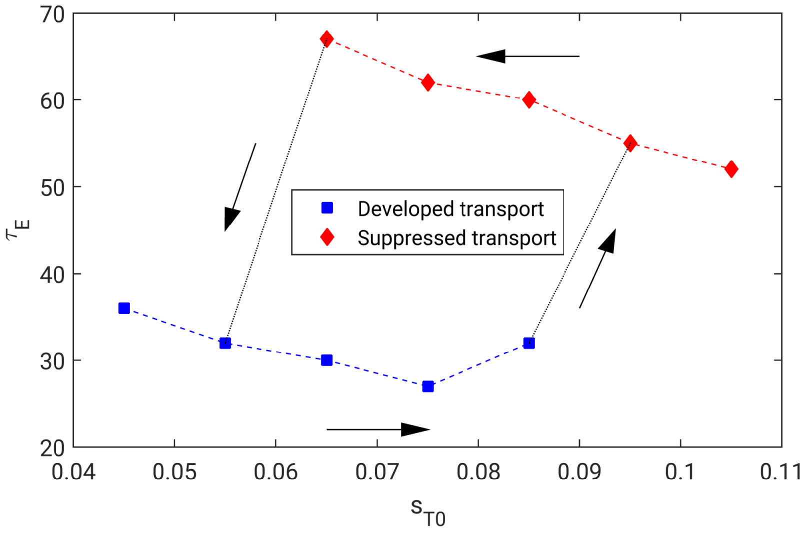

Figure 3.17 – Energy confinement time for simulations with $\nu_0 = 0.2$ and different values of s_{T0}. Simulations in the developed transport regime are denoted by blue squares and in the suppressed transport regime by red diamonds. Starting from a simulation in the developed transport regime, s_{T0} is progressively increased from 0.045 to 0.105. The transition to the suppressed transport regime occurs approximately at $s_{T0} \simeq 0.085$. The heat source is then progressively reduced until the reverse transition occurs, approximately at $s_{T0} \simeq 0.065$. The transitions are represented as dotted black lines.

of the threshold to access the suppressed transport regime (more precisely we consider $s_{T0} = 0.045, 0.055, 0.065, 0.075, 0.085, 0.095, 0.105$). Starting from a simulation in the developed transport regime, s_{T0} is progressively increased from 0.045 to 0.105 where the transition to the suppressed transport regime occurs. Then, by using the simulation at $s_{T0} = 0.105$ in the suppressed transport regime as initial condition, we perform a second set of simulations where s_{T0} is progressively reduced, observing the H-L transition at $s_{T0} \simeq 0.065$ (see Fig. 3.17). Therefore, the transition from the developed transport regime to the suppressed transport regime occurs at a higher value of the heat source than the reverse transition, thus pointing out the presence of hysteresis in the considered model.

The presence of hysteresis can be explained as follows. In the suppressed transport regime, the $\mathbf{E} \times \mathbf{B}$ shear is strong near the separatrix and the turbulent transport is mainly driven by the KH instability. As the heat source decreases, the $\mathbf{E} \times \mathbf{B}$ shear near the separatrix decreases, but it remains sufficiently strong to stabilize ballooning modes, thus allowing for a decrease of the heat source below the L-H transition threshold with no collapse of the $\mathbf{E} \times \mathbf{B}$ shear. This collapse is suddenly followed by the onset of the interchange instability, with the developed transport regime eventually reached.

As an aside observation of Fig. 3.17, we note that, within the same transport regime, the energy confinement time decreases as the heat source increases, the only exception being the simulation at $s_{T0} = 0.085$ in the developed transport regime, which is in proximity of the transition. The decrease of the energy confinement time following the increase of the heat source is also observed in many experiments [40, 246].

3.8 Conclusions

In the present chapter, results of GBS simulations are used to study the important role of the heat source and edge collisionality in driving turbulence in the tokamak edge, showing the presence of three turbulent transport regimes: a regime of developed turbulent transport, which is linked to the L-mode observed in the experiments, a regime of suppressed turbulent transport, with similarities to the H-mode, and a regime of degraded confinement, which is associated to the crossing of the density limit. The developed transport and degraded confinement regimes appear at low values of heat source and large values of collisionality, with turbulent transport driven by the interchange instability, while the suppressed transport regime appears at large values of heat source and low values of collisionality, with turbulent transport driven by the KH instability. An analytical estimate of the equilibrium pressure gradient length in the tokamak edge is derived for all the transport regimes.

The transition from the developed to the suppressed transport regime shows many features in common with the L-H transition observed experimentally, such as the presence of a strong sheared flow, the reduction of the turbulence level, the formation of a transport barrier near the separatrix and the presence of a power threshold. This transition is subject to hysteresis as it occurs at a higher value of the heat source with respect to the inverse transition. However, at least in the case analyzed here, no dependence of the power threshold to access the suppressed transport regime on the ion-∇B direction is observed in GBS simulations.

The transition to the degraded confinement regime is associated to the crossing of the density limit. This transition is extensively discussed in Ch. 5, where a theory-based scaling of the density limit is derived and validated against experimental data of a multi-machine database of density limit discharges.

Besides the use of the Boussinesq approximation and the electrostatic limit, we remark that the model considered in this chapter neglects coupling with neutrals dynamics, neoclassical and kinetic effects. These terms can definitely have an impact on the edge turbulent regimes. In fact, neutral dynamics may affect the L-H transition dynamics, as shown in Ref. [29, 156, 199]. Neoclassical terms may play an important role on the radial electric field responsible for the onset of a transport barrier [33, 34, 229]. In addition, kinetic effects are also expected to be important [20, 214].

4 Theory-based scaling of the L-mode near and far SOL decay lengths

The aim of this chapter is to derive theoretical scaling laws of the near and far SOL density and pressure decay length in the developed transport regime described in Ch. 3 and corresponding to the L-mode tokamak operation. We show herein that the pressure profile is characterized by one decay length across the separatrix, thus linking the equilibrium pressure gradient length in the tokamak edge to the one in the near SOL. Therefore, we extend the analysis of Ch. 3, carried out in the tokamak edge, to the near SOL. We derive a theory-based scaling law for the pressure and density decay length in the near SOL that is written in terms of engineering parameters and successfully validated against experimental measurements taken from a multi-machine database of divertor heat flux profiles at the outer target.

In addition, turbulent transport in the far SOL is analyzed and a theory-based scaling of the density and pressure decay length in this region is derived. The theoretical predictions of the far SOL pressure decay length are then compared to simulation results and to experimental measurements in TCV L-mode discharges.

The main results of this chapter have been recently published in Ref. [74].

4.1 Introduction

Understanding the mechanisms that regulate turbulent transport in the SOL and predicting the SOL power decay length is of fundamental importance to determine the operational window for a divertor solution compatible with a good core confinement. This is true for ITER where the limit of 10 $\mathrm{MW/m^2}$ on the peak heat flux at the target plate imposed by materials [121, 164] is expected to be exceeded without high volumetric power radiation in the SOL and partial divertor detachment [32, 52, 49, 117, 135] and, even more, for all future high-performance fusion devices.

As observed experimentally (see, e.g., Refs. [21, 28, 107, 111, 184]), the SOL presents two density and power decay lengths; a shorter one in the near SOL and a longer one in the far SOL, which is the result of different turbulence dynamics in these two regions. Indeed, as experimentally shown, e.g. in Refs. [67, 243], turbulence dynamics is wave-like in the near SOL and intermittent in the far SOL.

Significant experimental efforts were made in the past few years to derive experimental scaling laws of the power fall-off length in the near SOL at the divertor plates in L-mode diverted plasmas (see, e.g., Refs. [1, 93, 120, 193, 203]). Recently, a nonlinear regression has been carried out on a set of power fall-off length measurements from a multi-machine database including the Alcator C-Mod, COMPASS, EAST, JET and MAST tokamaks [93]. By combining five hundred L-mode outer and inner divertor heat flux profiles obtained by Langmuir probes or IR camera, thirteen credible scaling laws were derived. A scaling law in good agreement with the experimental data (describing $R^2 = 92\%$ of data variation) obtained by considering only outer divertor measurements is [93]

$$\lambda_q = 2800\left(\frac{a}{R_0}\right)^{1.03} f_{GW}^{0.48} j_p^{-0.35}\,, \tag{4.1}$$

where λ_q is the power fall-off length in units of mm, f_{GW} is the Greenwald fraction, a is the tokamak minor radius in m, R_0 is the tokamak major radius in m, and j_p is the plasma current density in units of $\mathrm{MA/m^2}$.

In parallel to the experimental effort, recent theoretical and numerical studies based on two-fluid models, justified by the high plasma collisionality in the plasma boundary, have investigated the mechanisms that regulate the near SOL width in L-mode, leading to analytical and numerical scaling laws of the SOL density and pressure gradient lengths in both limited [59, 87, 88, 89] and diverted [10, 72, 143, 150] geometries. A direct comparison of theoretical scaling laws to experimental data has been carried out in limited geometry [89, 96, 87, 153], showing a good agreement with experimental measurements. However, no in-depth comparison between first-principles theory-based scaling laws and experimental data taken from a multi-machine database has been carried out in L-mode diverted geometry.

While turbulence in the near SOL is characterized by a wave-like dynamics, turbulent transport in the far SOL is dominated by intermittent events due to coherent plasma filaments, also known as blobs [48]. Filaments extend along the parallel direction with a cross section spatially localized on the poloidal plane and their associated density fluctuations have an amplitude even larger than the background density. Filaments originate near the LCFS as the result of the nonlinear saturation of interchange-like instabilities, with the density fluctuations sheared apart by the $\mathbf{E}\times\mathbf{B}$ velocity and detached from the main plasma [67, 48]. Then, the vertical charge separation inside the filaments, caused by magnetic gradients and curvature drifts, generates a vertical electric field that, in turns, gives rise to a radial $\mathbf{E}\times\mathbf{B}$ drift that transports filaments outwards, contributing significantly to the perpendicular transport in the far SOL, flattening the density and pressure profile, and increasing the plasma-wall contact, as experimentally observed in Ref. [22]. Plasma filaments have been experimentally studied in tokamaks [12, 78, 108, 219, 223, 236], stellarators [190], reversed field pinch [210], and basic plasma devices [3, 30, 67, 103].

An analytical theory, referred to as two-region model, based on considering separately the divertor region and the upstream SOL region, has been proposed to describe the propagation of filaments in the SOL. Four regimes of filament motion have been identified, depending on the mechanism responsible for balancing the charge separation driven by the magnetic curvature and gradient drifts [151]: the sheath connected regime (C_s), where the curvature drive is balanced by the current flowing to the sheath; the ideal interchange mode regime (C_i), where the ion polarization current due to fanning of the flux surfaces in the divertor region damps the charge separation; the resistive ballooning regime (RB), where the damping of upstream ion polarization current dominates; and the resistive X-point regime (RX), where the parallel current flowing between the upstream and divertor regions is the key damping mechanism. Each damping mechanism results into a different dependence of filament velocity on filament size. The two key parameters that determine the filament regime are the collisionality parameter,

$$\Lambda = \frac{\nu_{ei} L_{\parallel 1}^2}{\rho_s \Omega_{ce} L_{\parallel 2}}, \tag{4.2}$$

and the size parameter [151],

$$\Theta = \left(\frac{a_b}{a_*}\right)^{5/2}, \tag{4.3}$$

where ν_{ei} is the electron to ion collision frequency, $\rho_s = c_s/\Omega_{ci}$ is the ion sound Larmor radius, with $c_s = \sqrt{T_e/m_i}$ the sound speed and $\Omega_{ci} = eB/m_i$ the ion cyclotron frequency, $L_{\parallel 1}$ is the parallel connection length from upstream to the divertor region entrance, $L_{\parallel 2}$ is the parallel connection length from the divertor region entrance to the target plate, $\Omega_{ce} = eB/m_e$ is the electron cyclotron frequency, a_b is the filament size in the poloidal plane, and a_* is the reference filament size introduced in Ref. [244] and then redefined in Ref. [159] taking into account effects described by the two-region model,

$$a_* = \rho_s \left(\frac{2L_{\parallel 2}^2}{\rho_s R_0} \frac{n_b}{n'}\right)^{1/5}, \tag{4.4}$$

with n_b the average of the filament density and n' the density at the near-to-far SOL interface. The two-region model for filament motion has been extensively validated against experimental results (see, e.g., [7, 221, 223]) and verified through numerical simulations. These include recent numerical nonlinear two-dimensional [15, 142], three-dimensional single-seed filament [47, 200], as well as three-dimensional self-consistently generated filament simulations in realistic geometry [10, 152, 159], which have shown a good agreement with the two-region model, also in H-mode plasmas [37]. Moreover, the work carried out in Ref. [10] in double-null geometry has shown that the far SOL density decay length can be described as the result of the transport associated to filaments, whose velocity is described by using the two-region model.

The considerations reported in the present chapter are based on the physical model considered in Ch. 3, namely we consider the GBS model described in Ch. 2 in the electrostatic limit, we neglect the coupling to the neutral dynamics and we make use of the Boussinesq approximation. Following an overview of the simulation results in Sec. 4.2, the analysis described in Ch. 3 for the tokamak edge is extended to the SOL. A theory-based scaling law of the pressure and density decay length in the near and far SOL, written in terms of engineering parameters, are derived in Sec. 4.3. In Sec. 4.4, the theoretical predictions from the pressure decay length scaling in the near SOL are then compared to experimental measurements of the power decay length at the outer divertor plate taken from a multi-machine database of L-mode discharges in attached conditions and the pressure decay length in the far SOL is compared to experimental measurements from TCV L-mode discharges. The conclusions follow in Sec. 4.5.

4.2 Simulation results: turbulence in the near and far SOL

We focus here on the set of simulations in the L-mode turbulent transport regime described in Ch. 3. These simulations are carried out with the following parameters: $\rho_*^{-1} = 500$, $a/R_0 \simeq 0.3$, $\tau = 1$, $\eta_{0e} = 5 \times 10^{-3}$, $\eta_{0i} = 1$, $\chi_{\parallel e} = \chi_{\parallel i} = 1$, $D_f = 6$ for all fields, $L_R = 600$, $L_Z = 800$, $s_{n0} = 0.3$, $\Delta_n = 800$, $\Delta_T = 720$, and different values of s_{T0} (see Eq. (2.85)) and ν_0 (see Eq. (2.99)), with both favorable and unfavorable ion-∇B drift directions being considered. The magnetic equilibrium, described in Ch. 3, is analytically obtained by solving the Biot-Savart law in the infinite aspect-ratio limit for a current density with a Gaussian distribution centered at the tokamak magnetic axis, which mimics the plasma current, and an additional current filament outside the simulation domain to produce the X-point. The value of the plasma current and the width of its Gaussian distribution are chosen to have a safety factor $q_0 \simeq 1$ at the tokamak axis and $q_{95} \simeq 4$ at the tokamak edge. The simulation results are analyzed when they reach a global turbulent quasi-steady state resulting from the interplay between the sources in the closed flux surface region, turbulence, which transports plasma and heat from the core to the SOL, and the losses at the vessel. Similarly to Ch. 3, we refer to the equilibrium of any quantity f as its time and toroidal average during the quasi-steady state, $\bar{f} = \langle f \rangle_{\varphi,t}$, and to its fluctuating component as $\tilde{f} = f - \bar{f}$.

An example of typical simulation results is shown in Fig. 3.3, where the equilibrium density, the normalized standard deviation and the skewness of density fluctuations in the plasma boundary is shown for the simulation with s_{T0}=0.15 and ν_0=0.6. Since in this chapter we focus on the SOL turbulence, the core region in Fig. 3.3 is not shown. The

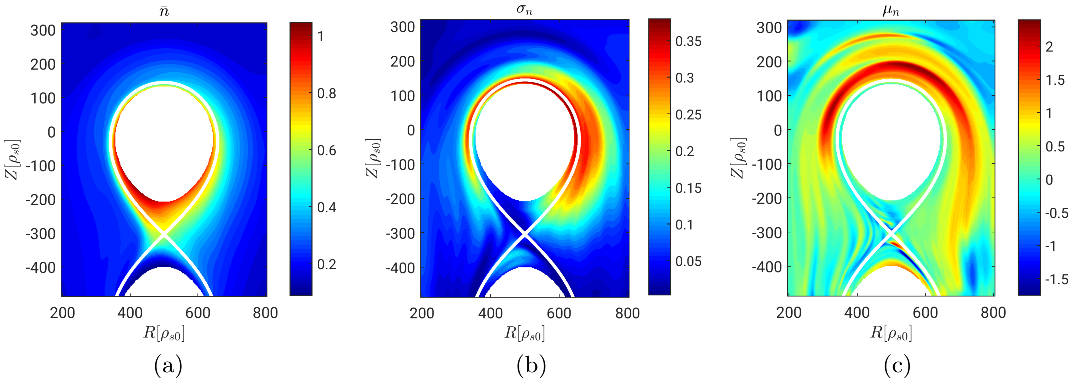

(a) (b) (c)

Figure 4.1 – Equilibrium density, $\bar{n}$, (a), normalized standard deviation, σ_n, (b) and skewness, μ_n, (c) of density fluctuations at the plasma boundary for the simulation with s_{T0}=0.15 and ν_0=0.6. In order to improve the visualisation in the plasma boundary, avoiding the saturation of the colorbar, the core region is not shown. The white line represents the separatrix.

normalized standard deviation of the density fluctuations peaks on the LFS and remains relatively large throughout the entire LFS SOL, as expected from turbulent transport being driven by ballooning modes. The near and far SOL is characterized by large fluctuations with amplitude comparable to the equilibrium quantity, as experimentally observed in Refs. [18, 95, 109, 111]. The skewness is small in the LFS of the near SOL, suggesting wave-like turbulence, and increases in the far SOL, hinting at the presence of intermittent turbulent events. A snapshot of the normalized density fluctuations for the same simulation (see Fig. 4.2 (a)) shows that density fluctuations mainly develop across the separatrix, forming eddies that extend in the radial direction and detach from the main plasma. Detached eddies give rise to filaments that radially propagate in the far SOL and are ultimately responsible for its intermittent nature. Therefore, turbulence in the far SOL arises from the steep pressure and density gradients across the separatrix and not from the local equilibrium pressure and density profiles. The different nature of plasma turbulence in the near and far SOL, namely the highly intermittent and non-local character of turbulence in the far SOL in contrast to wave-like turbulence dynamics in the near SOL, is highlighted in Fig. 4.2 (b), where two typical time traces of the density in the near and far SOL are shown.

As a consequence of the different transport mechanisms taking place in the near and far SOL, density and pressure show a different decay length in these two regions. Two distinct exponential decay lengths have been observed also in experiments (see, e.g., Refs. [28, 107]) as well as in other fluid simulations (see, e.g., Refs. [10, 62]). An example from one of our simulations is shown in Fig. 4.3, where the equilibrium pressure and density radial profiles at the outer midplane are fitted by assuming only one or two distinct exponential decay lengths. One exponential overestimates the decay length in the near SOL and underestimates the one in the far SOL. On the other hand, the fit

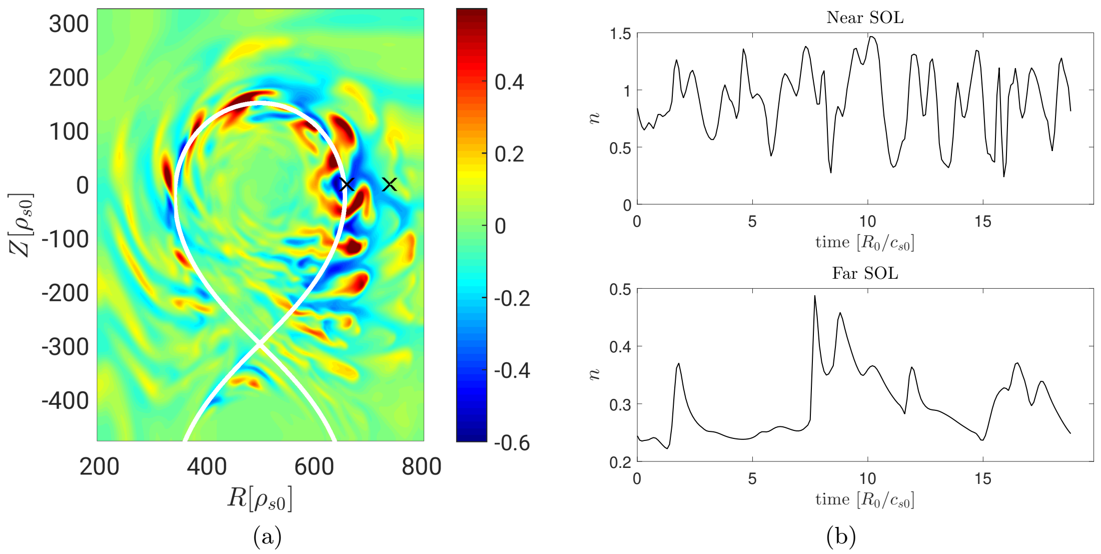

(a) (b)

Figure 4.2 – Typical snapshot of normalized density fluctuations on a poloidal plane (a) and typical time traces of the density in the near and far SOL (b) for the simulation with s_{T0}=0.15 and ν_0=0.6. The position where the time traces are extracted is indicated by a black cross.

based on two distinct exponential decay lengths agrees well with the equilibrium pressure and density radial profiles on the entire plasma boundary. We note that, as revealed by the fit based on two exponential functions, the decay lengths of density and pressure in the near SOL match the ones in the tokamak edge inside the LCFS, in agreement with experimental observations that show the presence of one characteristic pressure decay length across the separatrix [216]. Since the position of the near-to-far SOL interface depends on ν_0, in agreement with experimental observations [111, 145, 109], the fitting regions in Fig. 4.3 are properly chosen by identifying the near and far SOL in all the simulations and excluding the transition between these.

Fig. 4.4 shows the near and far SOL pressure (density) decay lengths, denoted as $L_{p,\mathrm{GBS}}$ ($L_{n,\mathrm{GBS}}$) and $L'_{p,\mathrm{GBS}}$ ($L'_{n,\mathrm{GBS}}$), respectively, for the set of GBS simulations considered here. The near SOL pressure gradient length increases as the collisionality increases or the heat source decreases. In fact, as outlined in Ch. 3, the effective turbulent diffusion coefficient associated to resistive ballooning turbulent transport increases with collisionality and, therefore, for the same value of the input power (i.e. s_{T0}), the pressure gradient decreases as ν_0 increases. The far SOL pressure decay length shows a weak dependence on the heat source and collisionality, especially for high values of collisionality and heat source where L'_p seems to saturate. Similar conclusions can be drawn for the near and far SOL density decay lengths.

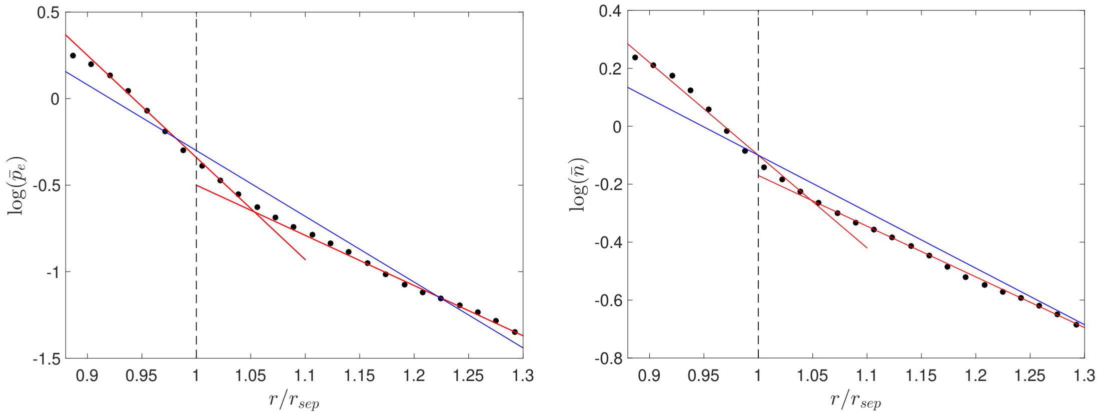

(a) (b)

Figure 4.3 – Radial profile of the equilibrium electron pressure, $\bar{p}_e$, (a) and density, $\bar{n}$, (b) at the outer midplane (black dots) for the simulation with $s_{T0} = 0.075$ and $\nu_0 = 0.2$, and overposed the exponential fits based on one (blue line) or two (red lines) exponential decay lengths. The vertical dashed black line denotes the position of the separatrix.

4.3 Theoretical derivation of the near and far SOL decay lengths

We now estimate the near and far SOL pressure and density decay lengths and we express them in terms of engineering parameters. Since density and pressure scale lengths in the near SOL correspond to the ones in the edge, we rely on the results of Ch. 3. In addition, turbulent transport in the far SOL is studied by means of a pattern-recognition algorithm for filament detection/tracking that is applied to the results of GBS simulations. Based on a balance between perpendicular transport due to filament motion and parallel transport in the far SOL, theoretical estimates of the density and pressure decay lengths are derived in this region and compared to simulation results.

4.3.1 Near SOL decay length

Fig. 4.3 shows that the equilibrium pressure profile exhibits one decay length across the separatrix. Therefore, the estimate of L_p in the developed transport regime of Ch. 3 (see Eq. (3.30)) can be applied to the near SOL. This is confirmed by Fig. 4.5 that shows a good agreement between the analytical estimate of L_p, given by Eq. (3.30), and the pressure decay length in the near SOL obtained from GBS simulations. A strong connection between confined edge and near SOL physics has been also experimentally observed in Refs. [24, 54, 204] across various confinement regimes. The equilibrium density gradient length in the near SOL can be directly obtained from Eq. (3.30) and the relation

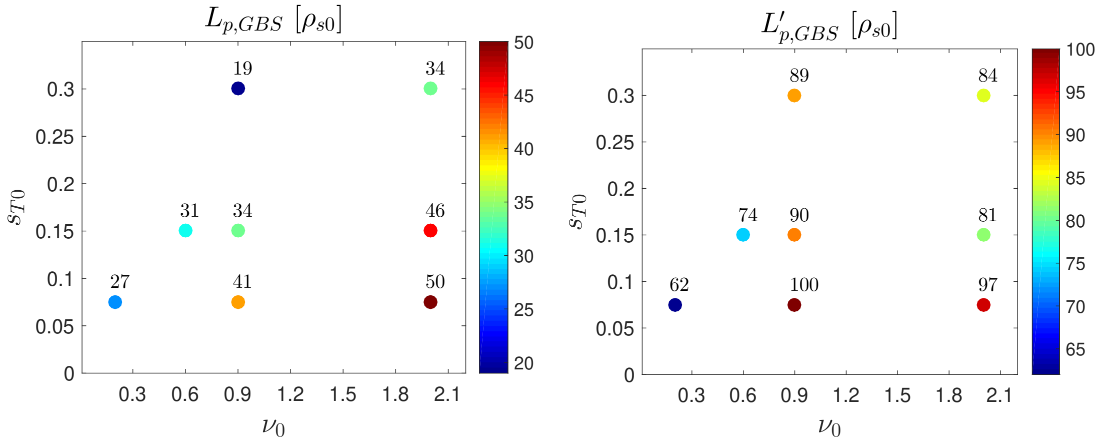

(a) Pressure decay length in the near SOL.

(b) Pressure decay length in the far SOL.

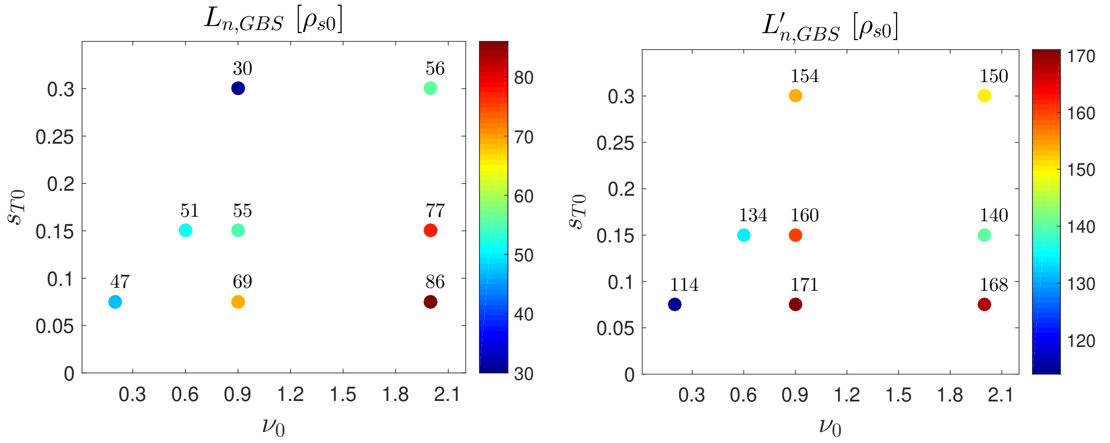

(c) Density decay length in the near SOL.

(d) Density decay length in the far SOL.

Figure 4.4 – Near and far SOL pressure ((a) and (b)) and density ((c) and (d)) decay lengths, normalised to ρ_{s0}, obtained from GBS simulations at the various values of s_{T0} and ν_0 considered in this work with the ion-∇B drift pointing upwards. Comparable values are obtained for the simulations with downwards ion-∇B drift direction. The numerical value of the equilibrium gradient length is reported next to the data points.

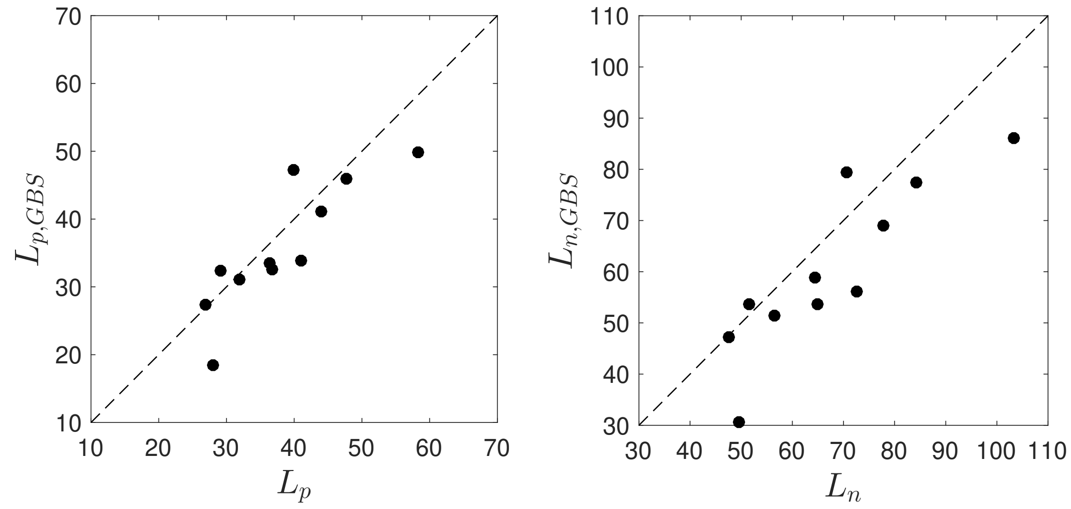

(a) (b)

Figure 4.5 – Comparison between the analytical estimates of the near SOL pressure (a) and density (b) decay lengths and the corresponding ones obtained from GBS simulations.

$L_n \simeq (1+\eta_e)L_p$, leading to

$$L_n \sim (1+\eta_e)\left[\frac{1}{8}\left(1+\frac{\eta_e}{2(1+\eta_e)}\right)^8 \rho_*^3\nu_0^6 q^{12} L_\chi^{12}\bar{n}^{10}S_p^{-4}\right]^{1/17}, \tag{4.5}$$

where $\eta_e = L_n/L_{T_e} \simeq 0.77$ [174].

We now extend the results of Ch. 3 by expressing L_p in terms of engineering parameters, such as the power entering into the SOL, P_{SOL}, the tokamak major and minor radius, R_0 and a, and the toroidal magnetic field, B_T. This facilitates the comparison to experimental results and the applicability of Eq. (3.30) to tokamak operation. Therefore, we substitute $S_p \simeq P_{\mathrm{SOL}}/(2\pi R_0)$, $L_\chi \simeq 2\pi a\sqrt{(1+\kappa^2)/2}$ and ν_0, Eq. (2.99), into Eq. (3.30) and we express all the quantities in physical units. This leads to

$$L_p \simeq 5.6\, A^{1/17} q^{12/17} R_0^{7/17} P_{\mathrm{SOL}}^{-4/17} a^{12/17} (1+\kappa^2)^{6/17} n^{10/17} B_T^{-12/17}, \tag{4.6}$$

where L_p is in units of mm, A is the mass number of the main plasma ions, R_0 and a are in units of m, P_{SOL} is in units of MW, n_e is the density at the LCFS in units of 10^{19} m^{-3}, and B_T is in units of T.

We note that the theoretical scaling in Eq. (4.6) depends on q, P_{SOL} and B_T with exponents that are comparable to the ones of the experimental scaling law derived in Ref. [203] from a nonlinear regression performed on λ_q measurements of L-mode ASDEX discharges. This nonlinear regression has been carried out by considering the same fitting quantities as the ones considered in the H-mode scaling of Ref. [52], providing a link between the L-mode and the H-mode scaling laws. In particular, we note that, combining the dependence on q and B_T, the theoretical scaling law of Eq. (4.6) inversely depends on the poloidal magnetic field, a feature shared with the heuristic drift-based H-mode scaling law derived in Ref. [77].

It is also interesting to analyze the analogies and differences between the theoretical scaling law of Eq. (4.6) to the empirical scaling in Eq. (4.1), which is derived from a nonlinear regression of experimental results. For this purpose, Eq. (4.6) is written in terms of the Greenwald fraction f_{GW} and of the current density j_p,

$$L_p \simeq 8.2 A^{0.06} \left(\frac{n}{\langle n \rangle}\right)^{0.59} R_0^{-0.06} \left(\frac{a}{R_0}\right)^{0.47} (1+\kappa^2)^{0.98} \kappa^{-0.12} j_p^{-0.12} \left(\frac{P_{\mathrm{SOL}}}{S_{\mathrm{LCFS}}}\right)^{-0.24} f_{GW}^{0.59} , \tag{4.7}$$

where $n/\langle n \rangle$ is the ratio of the edge density to the line-averaged density that appears from the definition of f_{GW} and $S_{\mathrm{LCFS}} \simeq 4\pi^2 a R_0 \sqrt{(1+\kappa^2)/2}$ is the area of the LCFS. We note that the theoretical L_p increases with the aspect ratio and the Greenwald fraction and decreases with the plasma current density, with exponents that are comparable to the experimental ones (see Eq. (4.1)). According to the theoretical scaling, L_p decreases with $P_{\mathrm{SOL}}/S_{\mathrm{LCFS}}$, a dependence that is not present in the experimental scaling of Eq. (4.1), although a similar dependence on $P_{\mathrm{SOL}}/S_{\mathrm{LCFS}}$ has been retrieved in other credible experimental scaling laws derived from the same database in Ref. [93]. No dependence on A is found in the experimental scaling of Eq. (4.1), in agreement with our theoretical scaling that, in fact, depends very weakly on A.

4.3.2 Far SOL decay length

In order to characterize the turbulence dynamics in the far SOL of our simulations, a pattern-recognition algorithm for filament detection/tracking, described in Refs. [152, 159], is applied to the GBS simulations considered in the present chapter. This allows us to determine the filament size, velocity and the collisionality parameter as well as to identify the filament regime according to these parameters. A typical dispersion plot of the averaged collisionality parameter Λ, Eq. (4.2), and size parameter Θ, Eq. (4.3), of each detected filament in the simulation with $s_{T0} = 0.15$ and $\nu_0 = 0.6$ is shown in Fig. 4.6 (a). The dashed lines delimit the four regimes of filament motion [151]. We note that filaments belong to the RX and RB regimes, a feature in common with all the simulations considered here. We restrict therefore our analysis to the RX and RB regimes. In Fig. 4.6 (b), the averaged normalized velocity $\hat{v} = v_b/v_*$ of each filament, with

$$v_* = c_s \left[2 \left(\frac{\pi a_\psi}{a_\chi} \right)^2 \frac{n_b}{\bar{n}'} \rho_s^2 L_{\parallel 2} \rho_*^2 \right]^{1/5} \tag{4.8}$$

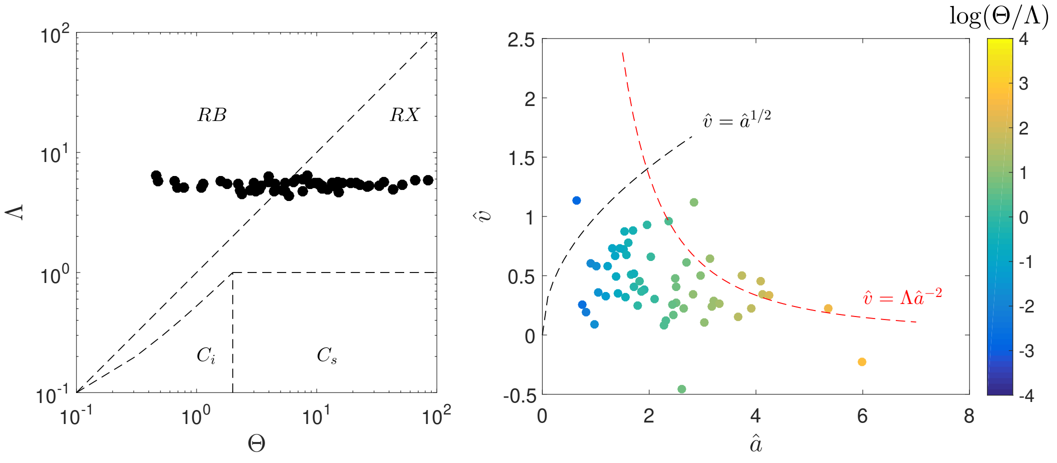

(a) (b)

Figure 4.6 – Dispersion plot in the phase space (Λ, Θ) of detected filaments in the simulation with $s_{T0} = 0.15$ and $\nu_0 = 0.6$ (a). Black dashed lines are used to delimit the four regimes. Normalized filament velocity as a function of filament size of each detected filament in the same simulation (b). The dashed black line represents the velocity scaling predicted by the two-region model in the RB regime $(\Theta < \Lambda)$, while the dashed red line the one in the RX regime $(\Theta > \Lambda)$ [151]. All quantities are obtained by averaging over the filament life.

being the reference filament velocity (see Ref. [159]), is displayed for the same simulation as a function of the normalized size, $\hat{a} = a_b/a_*$. In Eq. (4.8), a_ψ and a_χ denote the average size of filaments along the $\nabla\psi$ and $\nabla\chi$ direction, respectively. The normalized filament velocities are mainly scattered between zero and a maximum velocity that varies as a function of size and collisionality, in agreement with the analytical normalized velocity predicted by the two-region model [151]. This numerical result agrees with experimental observations that show that the theoretical predictions constitute an upper bound for the filament velocities [223]. Indeed, some mechanisms responsible for decreasing the radial filament velocity, such as the filament-filament interaction and the filament rotation, are not included in the two-region model of Ref. [151].

Since filament dynamics is responsible of the far SOL pressure and density transport, as shown in Ref. [10], we derive an analytical estimate of the equilibrium pressure decay length in the far SOL by balancing the perpendicular transport due to filament motion with parallel heat transport. For this purpose, we take the sum of Eq. (2.88), multiplied by T_e, and Eq. (2.92), multiplied by n. Then, by time and toroidal averaging the resulting equation, we obtain

$$\rho_*^{-1}\partial_\psi \bar{q}_{b,\psi} + \nabla_\parallel(\bar{p}_e \bar{v}_{\parallel e}) + \frac{2}{3}1.71\bar{p}_e \nabla_\parallel \bar{v}_{\parallel e} + \frac{2}{3}0.71\bar{T}_e \bar{v}_{\parallel e} \nabla_\parallel \bar{n} \simeq 0\,. \tag{4.9}$$

In Eq. (4.9), we identify the perpendicular heat transport with the one mediated by filaments, $\bar{q}_{b,\psi}$. By assuming that the electron parallel velocity is of the order of c_s, and approximating $\partial_\psi \sim 1/L_p'$ and $\nabla_\parallel \sim 1/L_\parallel$, Eq. (4.9) yields

$$\rho_*^{-1} \frac{\bar{q}_{b,\psi}'}{L_p'} \simeq C \frac{\bar{p}_e' \bar{c}_s'}{L_\parallel} \,, \tag{4.10}$$

where $C = 1 + 1.71\,(2/3) + 0.71\,(2/3) \simeq 2.6$. In Eq. (4.10), the prime symbol appearing in $\bar{p}_e'$, $\bar{c}_s'$, and $\bar{q}_{b,\psi}'$ denotes that these quantities are evaluated at the near-far SOL interface [10, 159]. We note that Eq. (4.10) only holds in case of negligible variation of electron temperature along the magnetic field lines, which is the case of the low-recycling regime considered here. The far SOL pressure decay length can then be obtained from Eq. (4.10),

$$L_p' \sim \frac{\rho_*^{-1}}{C} \frac{\bar{q}_{b,\psi}' L_\parallel}{\bar{p}_e' \bar{c}_s'} \,, \tag{4.11}$$

which relates L_p' to the perpendicular heat flux associated to the filament motion.

In order to estimate $\bar{q}_{b,\psi}'$, we assume that a filament can be described on the poloidal plane as a coherent structure with Gaussian peak pressure $p_{b,i}$ and half width at half maximum $a_{\psi,i}$, along the $\nabla\psi$ direction, and $a_{\chi,i}$, along the $\nabla\chi$ direction (i is the index identifying the i-th filament). The heat flux associated to the filament motion can be estimated by multiplying the pressure associated with a filament and the filament center of mass radial velocity, $v_{b,i}$, and summing over all the filaments. We obtain

$$q_{b,\psi}'(\psi, \chi) \sim \sum_i p_{b,i} v_{b,i} \exp\left(-\frac{(\psi - \psi_{b,i})^2}{(2a_{\psi,i})^2} - \frac{(\chi - \chi_{b,i})^2}{(2a_{\chi,i})^2} \right) , \tag{4.12}$$

where ψ and χ denote coordinate variations along $\nabla\psi$ and $\nabla\chi$, and $(\psi_{b,i}, \chi_{b,i})$ are the i-th filament center of mass coordinates. An estimate of the heat flux due to filament transport is then obtained by averaging $q_{b,i}$ over time and over the LFS SOL area [185],

$$\bar{q}_{b,\psi}' = \left\langle \frac{1}{A_{\mathrm{SOL}}} \int_{A_{\mathrm{SOL}}} q_b(\psi, \chi) \mathrm{d}\psi \mathrm{d}\chi \right\rangle_t = \frac{2\pi}{A_{\mathrm{SOL}} \log 2} \sum_i \langle a_{\psi,i} a_{\chi,i} p_{b,i} v_{b,i} \rangle_t \,, \tag{4.13}$$

where A_{SOL} represents the total far SOL area. We note that poloidal variations of the filament size and velocity are present in our simulations, in agreement with experimental observations [165, 113]. By neglecting possible correlation between filaments [144] and defining N_b as the average number of filaments such that the averaged peak pressure is given by $p_b \sim \sum_i \langle p_{b,i} \rangle_t / N_b$, Eq. (4.13) can be approximated as

$$\bar{q}_{b,\psi}' \sim \frac{2}{\log 2} f_b p_b v_b \,, \tag{4.14}$$

where $f_b = N_b \pi a_\psi a_\chi / A_{\mathrm{SOL}}$ is the blob packing fraction.

In order to make further progress, since filament and background pressure are both progressively drained by the parallel heat flow as moving radially through the far SOL, we assume that the filament peak-to-background pressure ratio remains constant. In Ref. [10], the density fluctuations in the far SOL were assumed to be three times larger than in the near SOL to account for turbulent transport being mainly due to large filaments. Here, as an order of magnitude estimate, we consider that pressure fluctuations in the near and far SOL have similar values, leading to

$$\frac{p_b}{\bar{p}_e'} \sim \frac{\tilde{p}_e}{\bar{p}_e} \sim \frac{1}{L_p k_\psi} \, . \tag{4.15}$$

The peak filament pressure at the near-far SOL interface can then be obtained,

$$p_b \sim \frac{\bar{p}_e'}{L_p k_\psi} \, . \tag{4.16}$$

The blob packing fraction is estimated from the average filament number by balancing the filament generation and loss rates. As filaments are generated by the nonlinear development of the ballooning instability appearing across the LCFS, the filament generation rate $R_{b,\mathrm{gen}}$ is given by the ballooning mode wavenumber along the LCFS, $L_\chi k_\chi/(2\pi)$, divided by the filament generation time, which can be approximated by the time that a streamer takes to travel its own extension, i.e. $4a_\psi/v_b$. We obtain

$$R_{b,\mathrm{gen}} \sim \frac{L_\chi k_\chi k_\psi v_b}{4\pi^2} \, . \tag{4.17}$$

The filament loss rate $R_{b,\mathrm{loss}}$ is given by the average filament number on a poloidal plane divided by the time that a filament takes to cross the radial domain,

$$R_{b,\mathrm{loss}} \sim \frac{N_b v_b}{L_\psi} \, . \tag{4.18}$$

The average filament number is then obtained by equating Eqs. (4.17) and (4.18),

$$N_b \sim \frac{A_{\mathrm{SOL}} k_\chi k_\psi}{4\pi^2} \, , \tag{4.19}$$

where $A_{\mathrm{SOL}} \simeq L_\chi L_\psi$. By using Eq. (4.19), the blob packing fraction becomes

$$f_b \sim \pi/16 \, , \tag{4.20}$$

where we consider $a_\psi \sim \pi/(2k_\psi)$ and $a_\chi \sim \pi/(2k_\chi)$. In all the simulations considered here, the value of f_b is of the order of 0.1 and approximately constant, in agreement with Eq. (4.20) which predicts that f_b is independent of SOL parameters, a feature also observed in experiments [27]. We note that the same estimate for f_b is derived in double-null geometry in Ref. [10].

The last quantity to estimate in Eq. (4.14) is the filament velocity, $v_b = \hat{v} v_*$, where the normalized filament velocity $\hat{v}$ depends on the filament motion regime. From the two-region model (see Refs. [151, 159] for details), we estimate

$$\hat{v}_{\mathrm{RB}} \sim \hat{a}^{1/2} \tag{4.21}$$

in the RB regime, and

$$\hat{v}_{\mathrm{RX}} \sim \Lambda \hat{a}^{-2} \tag{4.22}$$

in the RX regime, with

$$a_b \simeq \left(\frac{2}{\pi} a_\chi\right)^{4/5} a_\psi^{1/5} \tag{4.23}$$

and

$$\Lambda = \nu \bar{n}' \frac{L_{\|1}}{c_s L_{\|2}} \,. \tag{4.24}$$

By replacing the analytical estimates of p_b, v_b, and L_p in Eq. (4.14), the far SOL pressure decay length of Eq. (4.11) becomes

$$L'_{p,\mathrm{RX}} \sim \frac{2^{148/85}}{C \log 2} \left(1 + \frac{\eta_e}{2(1+\eta_e)}\right)^{-32/85} (1+\eta_e)^{-3/5} \frac{f_b \bar{n}^{9/17} \nu_0^{27/85} L_\| L_{\|1}^2}{q^{116/85} L_\chi^{14/85} S_p^{18/85} \rho_*^{63/85}} \tag{4.25}$$

in the RX regime and

$$L'_{p,\mathrm{RB}} \sim \frac{2^{211/170}\sqrt{\pi}}{C \log 2} \left(1 + \frac{\eta_e}{2(1+\eta_e)}\right)^{-32/85} (1+\eta_e)^{-1/10} \frac{f_b \bar{n}^{9/17} q^{54/85} \nu_0^{27/85} L_\|}{S_p^{18/85} L_\chi^{14/85} \rho_*^{63/85}} \tag{4.26}$$

in the RB regime, where we approximate $\bar{n}'$ and $\bar{T}_e'$ with $\bar{n}$ and $\bar{T}_e$ at the LCFS, with $\bar{T}_e$ being given by Eq. (3.29). This approximation is justified by the weak dependence of the ratio $\bar{q}_{b,\psi}'/(\bar{p}_e' \bar{c}_s') \propto v_b/\bar{c}_s'$, appearing in Eq. (4.11), on the radial position of the near-to-far SOL interface.

The equilibrium density decay length in the far SOL can be obtained by following the same procedure described above for the pressure decay length. The perpendicular particle flux due to filament motion, $\Gamma_{b,\psi}$, is balanced to the parallel particle transport and, considering the leading order terms in Eq. (2.88), this leads to

$$\rho_*^{-1} \partial_\psi \bar{\Gamma}_{b,\psi} + \nabla_\| (\bar{n} \bar{v}_{\|e}) \simeq 0 \,, \tag{4.27}$$

and we obtain

$$L_n' \sim \rho_*^{-1} \frac{\bar{\Gamma}_{b,\psi}' L_\|}{\bar{n}' \bar{c}_s'} \,, \tag{4.28}$$

where

$$\bar{\Gamma}_{b,\psi}' \sim \frac{2}{\log 2} n_b f_b v_b \,, \tag{4.29}$$

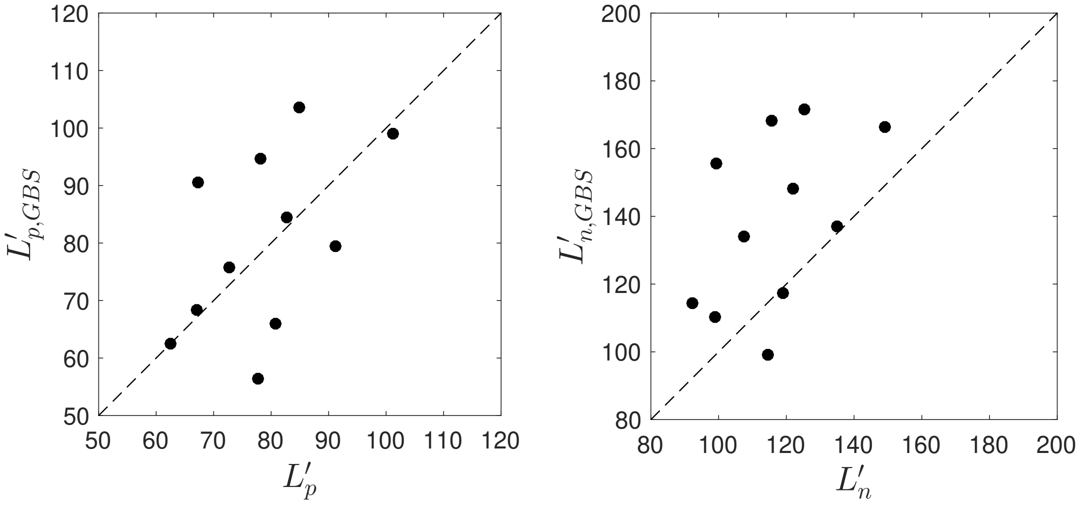

(a) (b)

Figure 4.7 – Comparison between the analytical estimates of the far SOL pressure (a) and density (b) decay lengths and the corresponding ones obtained from GBS simulations. The comparison is carried out by numerically solving a filament dispersion relation that links the filament velocity to the filament size (see Ref. [159] for details), without considering the limit $\Lambda \gg \Theta$ or $\Lambda \ll \Theta$.

with $n_b \sim \bar{n}'/(L_n k_\psi)$. The far SOL density decay length is then obtained by replacing in Eq. (4.29) the analytical estimates of n_b, v_b, L_p and L_n, leading to

$$L'_{n,\mathrm{RX}} \sim \frac{2^{148/85}}{\log 2}\left(1+\frac{\eta_e}{2(1+\eta_e)}\right)^{-32/85}(1+\eta_e)^{-8/5}\frac{f_b \bar{n}^{9/17}\nu_0^{27/85}L_\parallel L_{\parallel 1}^2}{q^{116/85}L_\chi^{14/85}S_p^{18/85}\rho_*^{81/85}}, \quad (4.30)$$

in the RX regime, and to

$$L'_{n,\mathrm{RB}} \sim \frac{2^{211/170}\sqrt{\pi}}{\log 2}\left(1+\frac{\eta_e}{2(1+\eta_e)}\right)^{-32/85}(1+\eta_e)^{-11/10}\frac{f_b \bar{n}^{9/17}q^{54/85}\nu_0^{27/85}L_\parallel}{S_p^{18/85}L_\chi^{14/85}\rho_*^{81/85}}, \quad (4.31)$$

in the RB regime.

Fig. 4.7 shows a comparison between the analytical prediction of the far SOL pressure and density decay lengths and the numerical results obtained from GBS simulations. This comparison is carried out by numerically solving a filament dispersion relation that links the filament velocity to the filament size (see Ref. [159] for details), without considering the limit $\Lambda \gg \Theta$ or $\Lambda \ll \Theta$. The agreement is good for the pressure and density decay lengths, with differences between theoretical and simulation results of the order of 20% for the pressure decay length, while the difference can be of 40% for the density decay length.

Similarly to the near SOL decay length, the far SOL pressure decay lengths for the RB and RX regimes can be written in terms of engineering parameters by replacing $S_p \sim P_{\mathrm{SOL}}/(2\pi R_0)$, $L_\chi \simeq 2\pi a\sqrt{(1+\kappa^2)/2}$ and ν_0, Eq. (2.99), into Eqs. (4.25) and (4.26). In physical units, this leads to

$$L'_{p,\mathrm{RX}} \simeq 3.5 f_b q^{-1.36} R_0^{-1.73} L_\parallel L_{\parallel 1}^2 P_{\mathrm{SOL}}^{-0.21} a^{-0.16} (1+\kappa^2)^{-0.08} n^{0.52} A^{0.05} B_T^{-0.64} \tag{4.32}$$

and

$$L'_{p,\mathrm{RB}} \simeq 6.1 f_b q^{0.64} R_0^{0.27} L_\parallel P_{\mathrm{SOL}}^{-0.21} a^{-0.16} (1+\kappa^2)^{-0.08} n^{0.52} A^{0.05} B_T^{-0.64}\,, \tag{4.33}$$

where $L'_{p,RX}$ and $L'_{p,RB}$ are here in units of mm, R_0 and a are the tokamak major and minor radii in units of m, $L_\parallel$ is the parallel connection length from upstream to the outer target plate in units of m, $L_{\parallel 1}$ is the parallel connection length from upstream to the divertor region entrance in units of m, n is the density at LCFS in units of 10^{19} m^{-3}, P_{SOL} is the power entering into the SOL in units of MW, and B_T is the toroidal magnetic field at the magnetic axis in units of T.

4.4 Validation of the theoretical scaling laws

We present here the validation of the near and far SOL pressure decay length scaling laws derived in Sec. 4.3. The experimental results used for the validation are taken from a multi-machine database of discharges carried out in Alcator C-Mod, COMPASS, JET, MAST and TCV tokamaks.

4.4.1 Near SOL validation

In order to validate the near SOL pressure decay length derived in Sec. 4.3 against experimental data, we consider the multi-machine database of Ref. [93] that contains a set of power fall-off lengths obtained from a nonlinear regression of measurements of divertor heat flux profiles in attached conditions with probes or infrared (IR) cameras on different tokamaks. Both favorable and unfavorable ion-∇B drift directions are considered. We restrict our comparison to the outer target, considering data from Alcator C-Mod, COMPASS, JET and MAST tokamaks. We extend this database by including the TCV λ_q measurements in attached conditions presented in Ref. [136]. These values are obtained from heat flux profile measurements at the TCV outer target by using an IR camera.

In order to relate the analytical scaling of L_p at the outboard midplane with λ_q experimentally measured at the outer target, we first report λ_q upstream accounting for the flux expansion. We also assume that, being the considered discharges in attached conditions, the pressure gradient along the magnetic field lines can be neglected. This allows for a direct comparison between L_p in Eq. (4.6) and the experimental λ_q, i.e. $\lambda_q \propto L_p$, where

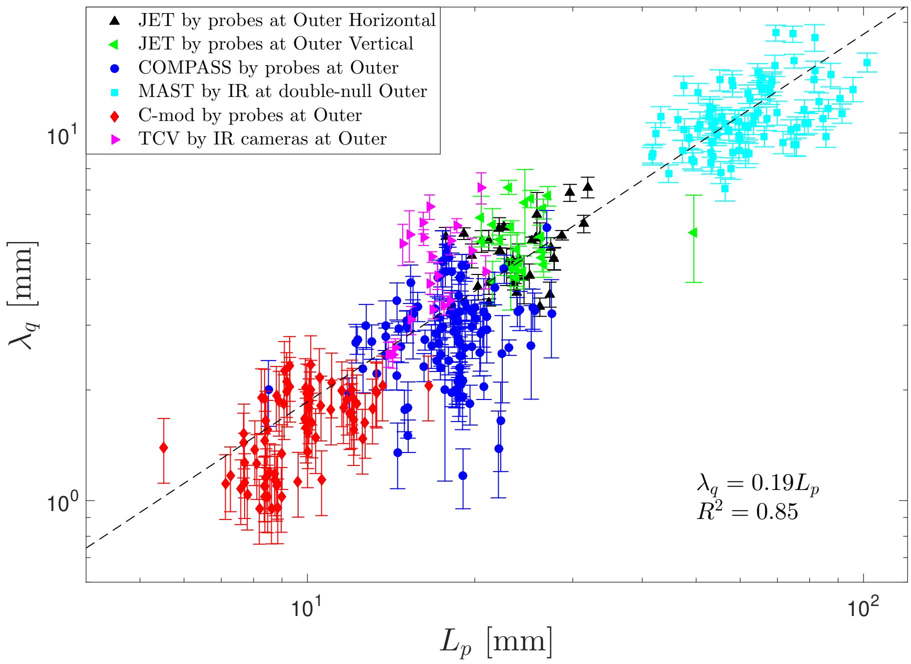

Figure 4.8 – Comparison of the theoretical scaling law of Eq. (4.6) to experimental values of λ_q taken from the multi-machine database of Ref. [93] extended including TCV data from Ref. [136]. The dashed black line represents the best fit $\lambda_q = \alpha L_p$ with α the unique fitting parameter.

the proportionality factor is determined from the best fit of experimental and theoretical results, similarly to the procedure outlined in Ref. [87]. Since only the line-averaged density $\langle n\rangle$ is available in the considered database, we assume the edge density contained in the analytical scaling to be proportional to the line-averaged density, $n \propto \langle n\rangle$, where the proportionality factor is included in the unique fitting parameter. This assumption is supported by experimental observations that show the presence of an almost linear proportionality between n and $\langle n\rangle$ in low-density discharges (see, e.g., Ref. [1]). The quality of the fit is then expressed through the R^2 parameter.

The result of the fitting procedure is shown in Fig. 4.8. The theoretical scaling reproduces experimental data with a very high goodness parameter, $\mathrm{R}^2 \simeq 0.85$. We highlight that the value of R^2 obtained from the comparison between the theoretical scaling and experimental data is even higher than some of the most credible scaling laws derived in Ref. [93] from a direct nonlinear regression of experimental results. In fact, as extensively discussed in Refs. [93, 94], the number of parameters that can be included in a scaling based on the direct nonlinear regression of experimental measurements is limited by their mutual correlation. For instance, a very strong correlation is found between R_0 and P_{SOL}/V [94], with the consequence that including both of them in the nonlinear regression leads to an ambiguity on their exponent. The mutual correlation between experimental input parameters limits the use of nonlinear regressions to find scaling laws directly from experimental databases, a limitation that is overcome by theory-based first-principles scaling laws, such as the one derived in the present work.

The proportionality constant returned by the fit is approximately 0.2. We note that this constant includes both the proportionality factor between λ_q and λ_p (we use here λ_p to refer to the experimental value of the pressure decay length, while L_p is used for the theoretical prediction of Eq. (4.6)) and the one between n and $\langle n\rangle$. By assuming that p_e and T_e decay exponentially in the SOL on the λ_p and $\lambda_T \sim 2\lambda_p$ scales, respectively, the power fall-off length can be written as

$$\lambda_q \sim \left(\frac{1}{\lambda_p} + \frac{1}{2\lambda_T}\right)^{-1} \sim \frac{4}{5}\lambda_p\,. \tag{4.34}$$

Moreover, from the experimental results shown in Ref. [1], we assume $\bar{n} \sim 4\langle n\rangle$, thus leading to

$$\frac{\lambda_q}{L_p} \sim \frac{\lambda_q}{\lambda_p}\left(\frac{n_e}{\bar{n}_e}\right)^{10/17} \sim \frac{4}{5}\left(\frac{1}{4}\right)^{10/17} \sim 0.3\,, \tag{4.35}$$

which is close to the proportionality factor returned by the best fit.

Despite the very high value of R^2, we note a dispersion of the experimental measurements around the best fit in Fig. 4.5. This may suggest incomplete or missing dependencies in the theoretical scaling law of Eq. (4.6). In particular, our theoretical scaling law does not include the effect of plasma triangularity, which has been studied with GBS in Refs. [177, 179] for a limited configuration, showing that the near SOL width is enhanced (reduced) by positive (negative) values of triangularity, in agreement with experimental observations [55]. In addition, interchange-like turbulence, which can develop along the divertor leg, can increase the power fall-off length at the target plate [69]. This may be especially the case in TCV, where magnetic configurations with a long outer divertor leg are considered. This effect is not included in the present model.

The theoretical scaling of Eq. (4.6) with the proportionality constant given by the fitting procedure can be used to predict the SOL width for future tokamaks, such as ITER, COMPASS Upgrade, JT-60SA, and DTT. Considering the baseline scenario just before the L-H transition, we obtain $\lambda_{q,\mathrm{th}} \simeq 3.5$ mm for ITER ($R_0 = 6.2$ m, $a = 2$ m, $q = 2$, $P_{\mathrm{SOL}} = 18$ MW, $\kappa = 1.4$, $\bar{n}_e = 4 \cdot 10^{19}$ m^{-3}, and $B_T = 5.3$ T [4]), $\lambda_{q,\mathrm{th}} \simeq 1.8$ mm for COMPASS Upgrade ($R_0 = 0.89$ m, $a = 0.27$ m, $q = 2.6$, $P_{\mathrm{SOL}} = 3.7$ MW, $\kappa = 1.8$, $\bar{n}_e = 2 \cdot 10^{20}$ m^{-3}, and $B_T = 5.0$ T [158]), $\lambda_{q,\mathrm{th}} \simeq 7.1$ mm for JT-60SA ($R_0 = 2.9$ m, $a = 1.2$ m, $q = 3$, $P_{\mathrm{SOL}} = 10$ MW, $\kappa = 1.9$, $\bar{n}_e = 6.3 \cdot 10^{19}$ m^{-3}, and $B_T = 2.3$ T [76]), and $\lambda_{q,\mathrm{th}} \simeq 3.0$ mm for DTT ($R_0 = 2.1$ m, $a = 0.6$ m, $q = 3$, $P_{\mathrm{SOL}} = 15$ MW, $\kappa = 1.7$, $\bar{n}_e = 1.8 \cdot 10^{20}$ m^{-3}, and $B_T = 6.0$ T [39]). The theoretical value of λ_q for ITER L-mode is within the range of values predicted by the experimental scaling laws derived in Ref. [93].

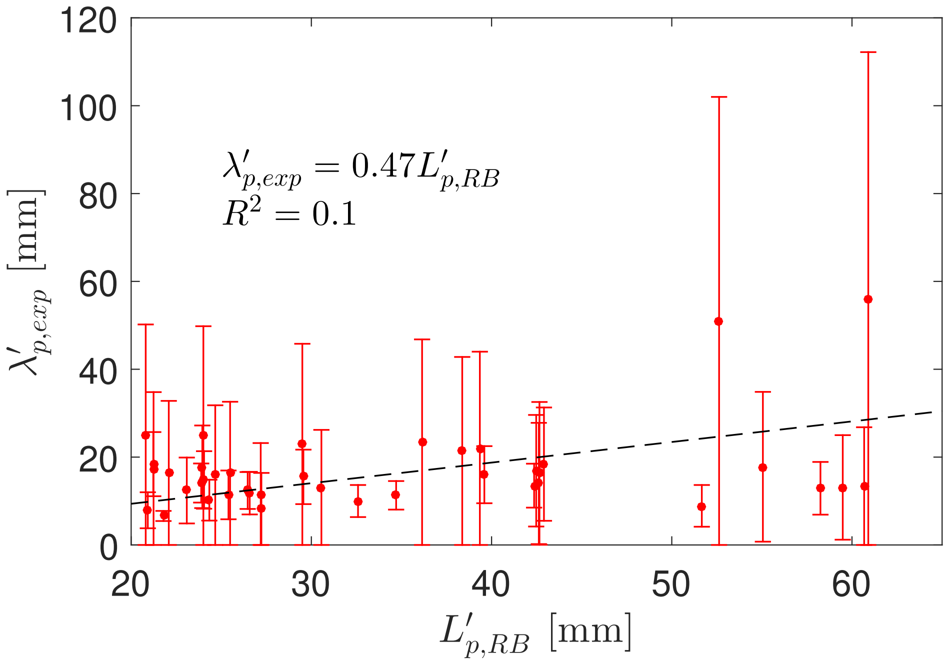

Figure 4.9 – Comparison of the theoretical scaling law of Eq. (4.33) to experimental values of pressure decay length measured with a fast reciprocating probe at the outboard midplane of TCV L-mode discharges in conduction regime. Experimental data are taken from Ref. [223]. The dashed black line represents the best fit $\lambda'_{p,\mathrm{exp}} = \alpha L'_{p,\mathrm{RB}}$ with α the unique fitting parameter.

4.4.2 Far SOL validation

The absence of a multi-machine database or experimental scaling laws for the pressure decay length in the far SOL strongly limits the possibility to carry out a complete validation of our theoretical scaling. As a preliminary comparison with experimental data, we consider a set of measurements of the far SOL decay length taken at the outboard midplane of TCV L-mode discharges in lower single-null configuration by using a fast reciprocating probe [19]. Experimental far SOL decay lengths are measured at fixed $B_T = 1.4$ T, in both reversed and forward magnetic field direction, at various values of density, plasma current, and connection length. A detailed description of the considered database as well as of the experimental setup are reported in Refs. [223, 228]. The result of the comparison is shown in Fig. 4.9.

There are two main difficulties that affect the fitting of the experimental pressure profiles to derive the far SOL experimental pressure decay length. First, in low-density discharges, the transition between the near and far SOL appears to be very close to the LFS tokamak wall, thus making it difficult to clearly distinguish its position and reducing the numbers of data points available for the fit of the far SOL pressure profile. In fact, as shown in Refs. [109, 111, 145], the position of the near-far SOL interface depends on the density and moves towards the first wall as the density decreases. Therefore, an exponential function with a value of decay length close to the one in the near SOL is able to fit the entire experimental profile and the fit with two exponential functions returns near and far decay lengths that are very similar. The discharges that allow a more precise analysis of the far SOL decay length are at high density, in the conduction regime with the presence of significant electron temperature variation along the parallel direction, which questions the applicability of the present model, in particular for the absence of the neutral-plasma interaction processes that might affect the far SOL, as experimentally observed in Refs. [227, 242]. For the comparison of the far SOL decay length presented in Fig. 4.9, we choose to exclude the discharges that do not allow a clear identification of the near and far SOL and consider high-density discharges, despite the questions on the applicability of this model.

The second difficulty emerges when fitting experimental data at high value of λ'_q. In fact, a small variation of the fitting range produces a large variation of λ'_q. This is reflected on large experimental uncertainties that prevent us from an accurate comparison with the theoretical prediction and potentially hide some dependencies. In fact, as shown by the error propagation, the relative uncertainties of $\lambda'_{p,\mathrm{exp}}$ inversely depend on the radial derivative of the pressure profile, meaning that a particularly flat radial pressure profile leads to large uncertainties of $\lambda'_{p,\mathrm{exp}}$.

The subset of the database considered for this comparison includes discharges that are mainly in the RB regime [223] and hence we fit experimental data by using the theoretical RB scaling law in Eq. (4.33) with the unique fitting parameter being the proportionality constant between experimental measurements and $L_{p,\mathrm{RB}}$. The quality of the fit is then expressed through the R^2 parameter. As shown in Fig. 4.9, there is a very weak correlation between theoretical predictions and experimental data, being R^2 only slightly positive.

This preliminary analysis prompts for the need for further investigations in high-recycling conditions, possibly including data from multiple tokamaks and diagnostics. In fact, recent GBS simulations with the self-consistent evolution of the plasma and neutral dynamics in diverted geometry have shown that the neutral dynamics can significantly affect the far SOL parallel transport by decreasing [129], an effect that should be taken into account in the derivation of the far SOL pressure decay length.

4.5 Conclusions

In the present chapter, a theoretical scaling of the pressure and density decay lengths in the near SOL of L-mode diverted plasma discharges valid in low-recycling conditions is analytically derived by balancing the heat source in the core region, the perpendicular heat flux crossing the separatrix, and the parallel losses at the vessel walls. Similarly, by balancing the perpendicular turbulent transport due to plasma filament motion and the parallel flow, an analytical scaling for the far SOL pressure and density exponential decay lengths is analytically derived in the RB and RX filament regimes.

The theoretical scaling laws for pressure and density decay lengths in the near and far SOL are then compared to GBS results. In the near SOL, there is a good agreement between theoretical and numerical results, with a difference between simulation results and theoretical predictions below 20%. The theoretical estimates of the far SOL pressure and density decay lengths in RB and RX regimes agree with simulation results within an error of 20 % for the pressure and 40 % for the density, pointing out that the model considered here contains the main physics, although the dispersion of simulation results around the analytical prediction suggests the need of future investigations with a more accurate model for the filament velocity, which accounts for the filament-filament interaction and filament rotation.

The theoretical predictions of the near SOL pressure decay length are compared to experimental measurements of the power fall-off length taken from a multi-machine database, showing a remarkable good agreement that is reflected on the high value of $R^2 \simeq 0.85$. The theoretical scaling predicts a near SOL width for ITER L-mode plasma of 3.5 mm, a value close to the one predicted by the empirical scaling laws derived in Ref. [93].

Analogously, the theoretical scaling law of the far SOL pressure decay length in the RB regime is compared to experimental measurements obtained from a fast reciprocating probe located at the outboard midplane in TCV L-mode lower single-null discharges. This preliminary comparison shows a very weak correlation between theoretical predictions and experimental results ($R^2 \simeq 0.1$). However, the presence of significant temperature variation along the magnetic field lines in the far SOL observed experimentally for the considered discharges and not included in the present work, the experimental difficulty in identifying at low density the interface between near and far SOL, and the large experimental uncertainties affecting measurements of long pressure decay lengths make the present comparison not conclusive and call for further investigations in high-recycling conditions and possibly including data from multiple tokamaks and diagnostics.

5 Electromagnetic phase space of edge turbulence and the density limit

In Ch. 3, a phase space of edge turbulence is presented based on electrostatic turbulence simulations that make use of the Boussinesq approximation. These simulations reveal the presence of a turbulent regime that can be associated to the crossing of the density limit. However, the importance of electromagnetic effects in the density limit has been pointed out in the past [50, 181, 182, 198]. This motivates the present chapter where the transition to the regime associated to the crossing of the density limit is revisited extending the results presented in Ch. 3 through the investigation of the effects of electromagnetic perturbations and of the Boussinesq approximation on turbulence and equilibrium profiles. The main parameters controlling turbulent transport in the tokamak boundary are identified and used to delineate a phase space of edge turbulence, where both the density and the β limits are reported. We show that the density limit can be explained as the result of an enhanced turbulent transport in the tokamak boundary due to a resistive electrostatic mode with negligible impact of the electromagnetic fluctuations. This leads to the derivation of a theory-based scaling law of the maximum achievable edge density in tokamaks. The theoretical predictions provided by this scaling agree well with density limit measurements carried out in the ASDEX Upgrade (AUG), JET and TCV tokamaks.

5.1 Introduction

The density limit imposes a maximum value of the plasma density that can be achieved in magnetic fusion devices before the onset of MHD modes that lead to strong performance degradation or even a plasma disruption. A widely used empirical scaling law of the maximum density achievable in tokamaks has been proposed in 1988 by Greenwald [80],

$$n_{GW}[10^{20}\mathrm{m}^{-3}] = \frac{I_p[\mathrm{MA}]}{\pi a[\mathrm{m}]^2}, \tag{5.1}$$

where n_{GW}, known as Greenwald density, is the line-averaged density, I_p is the plasma current and a is the tokamak minor radius.

Experimental observations indicate that the plasma cooling in the tokamak boundary and the subsequent increase of the plasma edge collisionality is a strong factor limiting the maximum achievable density in tokamaks, providing a strong link between density limit and the edge collisionality [51, 61, 79, 92, 112, 197, 226]. Moreover, a Multifaceted Asymmetric Radiation From the Edge (MARFE) is commonly observed when crossing the density limit [66, 118, 119, 139]. Experiments also reveal that the Greenwald limit can be significantly exceeded through pellet injection that mainly affects the core, and only weakly, the edge density [11, 83], again underlining a key role played by the edge physics. Experimental observations show that the density limit is in general preceded by a collapse in the edge temperature that is followed by a temperature profile decrease in the core region, leading to changes in the q profile and internal inductance [104, 191]. The change in internal inductance indicates a modified plasma current profile that is susceptible to tearing modes and, finally, plasma disruption [70].

The density limit is often studied experimentally by increasing the gas flux and thus plasma density until causing an intentional disruption, as shown in Fig. 5.1 for the JET discharge #80823. The density increases until the onset of a MARFE, as identified by a strong increase in the radiation intensity in the region above the X-point (see Fig. 5.1), which is followed by an MHD mode and plasma disruption. Fig. 5.2 shows the radial profiles of the electron density, electron temperature and electron pressure at three times before the onset of the MARFE. The density increase is accompanied by a cooling of the electron temperature at the tokamak edge and an increase of the edge collisionality. This increase of plasma collisionality, while approaching the density limit, is expected to enhance turbulent transport, as experimentally shown in Ref. [111]. The enhancement of turbulent transport further decreases the edge temperature and thus pressure gradients until they collapse (see Fig. 5.2). Finally, the collapse of the edge temperature and pressure gradients, that occurs at the MARFE onset, leads to a reduced plasma current channel and then to a change on the q profile that triggers MHD modes.

The relation between density limit and edge turbulent transport was initially studied in Ref. [198] and further developed in Refs. [181, 182]. These theoretical works have associated the crossing of the density limit to a regime of catastrophically large turbulent transport in the tokamak edge, which was explained as due to a nonlinear effect of electromagnetic perturbations on turbulence. The phase space of edge turbulence derived in Ref. [182] claims that no density limit can be retrieved in the electrostatic case. More recently, Ref. [50] has linked the crossing of the density limit to a transition from an electrostatic to an electromagnetic ballooning regime, once again underlining the important role played by electromagnetic fluctuations in the density limit. On the other hand, Ref. [85] argues that turbulent transport in the tokamak boundary is mainly controlled by the plasma collisionality, with only a minor role played by β. Namely,

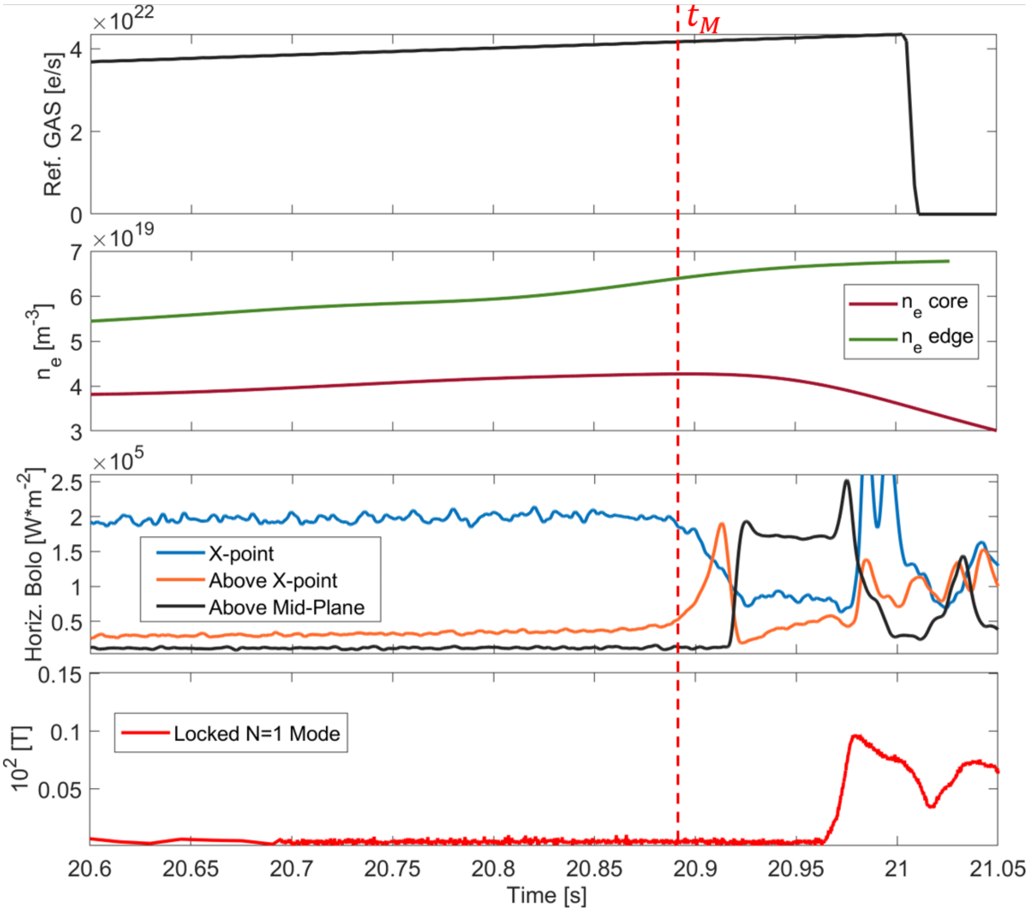

Figure 5.1 – Time trace of the gas flux, electron density from Thomson scattering, radiation intensity and magnetic perturbations in the JET discharge #80823. The MARFE event is identified by the strong increase of the radiation measured above the X-point. The MARFE onset precedes the appearance of a locked mode, which eventually leads to the plasma disruption. The red dashed vertical line represents the time of the MARFE onset, $t_M \simeq 20.9$ s. The onset of the locked $N = 1$ mode occurs at 21.95 s, while the disruption time is at 21.1 s.

Ref. [85] suggests that a regime of enhanced turbulent transport compatible to the crossing of the density limit can be retrieved at high collisionality and low β.

In contrast to the aforementioned theoretical works, a different approach is followed in Ref. [70] where the density limit is explained as the onset criterion for radiation driven islands, with a normalized internal inductance derived by fitting experimental data at the density limit in the JET tokamak [239]. The radiation at the density limit is also the key element of a recent explanation of the origin of the density limit [247, 248]. This is based on a thermal balance between the heating power, the radiative emission and the radial transport evaluated by using an effective perpendicular heat diffusivity coefficient. A reduced scaling law for the edge density limit, which improves the Greenwald empirical

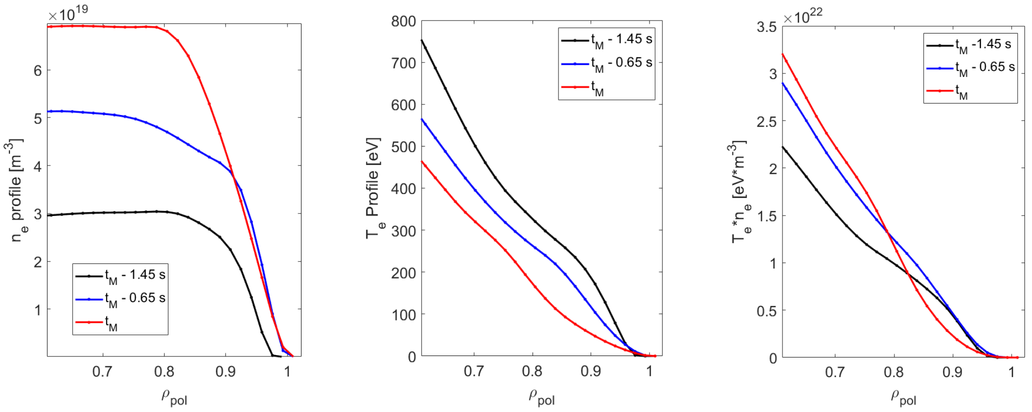

(a) (b) (c)

Figure 5.2 – Radial profile fitted from Thomson scattering of the electron density (a), electron temperature (b) and electron pressure (c) as a function of the normalized radial coordinate ρ_{pol} at three different times of the JET discharge #80823. The time of the MARFE onset is denoted as t_M (see Fig. 5.1).

scaling, is derived in Ref. [247],

$$n_*[10^{20}\text{m}^{-3}] = 0.3\frac{Z_{\text{eff}}^{4/9}}{(f_0 + Z_{\text{eff}} - Z_i)^{5/9}}\frac{P[\text{MW}]^{4/9}I_p[\text{MA}]^{4/9}}{\pi^{8/9}a[\text{m}]^{16/9}}, \tag{5.2}$$

where n_* is the maximum density achievable at the position of the edge radiative layer, P is the total heating power, f_0 is the effective concentration parameter and Z_{eff} is the plasma effective charge [247].

Herein, we extend the results of Ch. 3, which linked the density limit to an electrostatic regime of enhanced turbulent transport, by performing a new set of GBS simulations that include electromagnetic fluctuations and avoid the use of the Boussinesq approximation. The effects of electromagnetic perturbations on turbulence and equilibrium profiles are investigated by considering a wide range of β values, from the electrostatic limit to the high-β limit. Special focus is dedicated to the study of the density limit, in particular with the aim of disentangling the role played by electrostatic and electromagnetic turbulence. The effect of the Boussinesq approximation on turbulent transport is also addressed, pointing out a different turbulent transport regime at low collisionality than the one described in Ch. 3.

The present chapter is organized as follows. An overview of the simulation results is presented in Sec. 5.2, where the effects of electromagnetic perturbations on turbulence and equilibrium profiles are investigated. In Sec. 5.3, the main parameters controlling turbulent transport in the plasma boundary are identified and used to delineate the electromagnetic phase space of edge turbulence. In Sec. 5.4, the theoretical scaling law of

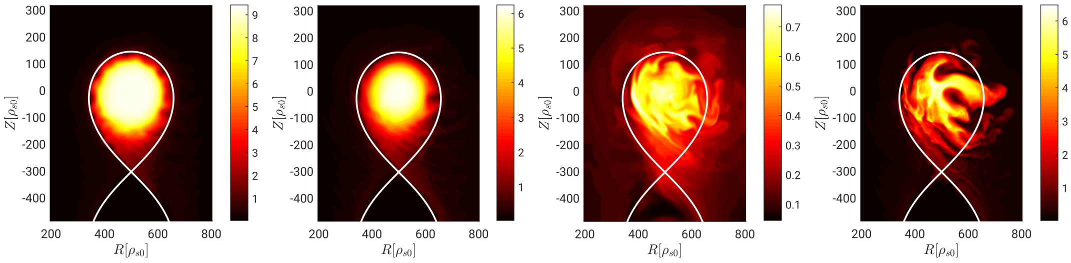

(a) (b) (c) (d)

Figure 5.3 – Typical snapshots of density for a simulation in the suppressed transport regime, $\nu_0 = 0.05$ and $\beta_{e0} = 10^{-6}$ (a), in the developed transport regime, $\nu_0 = 0.2$ and $\beta_{e0} = 10^{-4}$ (b), above the density limit, $\nu_0 = 10$ and $\beta_{e0} = 10^{-4}$ (c), and above the β limit, $\nu_0 = 0.2$ and $\beta_{e0} = 4 \times 10^{-4}$ (d). The same value of $s_{T0} = 0.3$ is considered for these simulations. The white line represents the separatrix.

the density limit is written in terms of engineering parameters and compared to density limit measurements of the AUG, JET and TCV tokamaks. The conclusions follow in Sec. 5.5.

5.2 Overview of the simulation results

The GBS simulations considered here have been carried out with the following dimensionless parameters: $\rho_*^{-1} = 500$, $a/R_0 \simeq 0.3$, $s_{n0} = 0.3$, $\Delta_n = 800$, $\Delta_T = 720$, $\chi_{e0} = 10$, $\chi_{i0} = 1$, upward ion-∇B drift direction, $s_{T0} = \{0.15, 0.3\}$, $\nu_0 = \{0.05, 0.1, 0.2, 0.6, 10\}$, and various values of β_{e0} ranging from 10^{-6} to 5×10^{-3}. The magnetic equilibrium corresponds to the one used in Ch. 3, and it is analytically obtained in the infinite aspect-ratio limit by solving the Biot-Savart law for a current density with a Gaussian distribution centered at the tokamak axis, mimicking the plasma current, and an additional current filament outside the simulation domain to produce the X-point. The value of the plasma current and the width of its Gaussian distribution are chosen to have a safety factor $q_0 \simeq 1$ at the tokamak axis and $q_{95} \simeq 4$ at the tokamak edge. We note that the value of χ_{e0} considered here is larger than the one considered in Ch. 3, although it remains a factor 20 smaller than typical values in the tokamak boundary. This is due to the very large computational cost required to run simulations at realistic values of χ_{e0}. While no major difference in turbulence and equilibrium profiles is observed when comparing simulations at different χ_{e0} in the range allowed by our numerical algorithm, with the parallel heat convection in the SOL dominating over the parallel heat conduction in all the considered simulations, we expect the parallel heat conduction to dominate over the parallel heat convection at realistic values of χ_{e0}. As in the past chapters, the analysis described here is carried out when the simulations are in a global turbulent quasi-steady state resulting from the balance among the sources in the closed flux surface region, turbulence that transports plasma and heat from the core to the SOL, and the losses at the vessel.

In Fig. 5.3, typical snapshots of the plasma density for the electromagnetic simulations that avoid the Boussinesq approximation are shown at various values of ν_0 and β_{e0}, corresponding to the different turbulent transport regimes observed in our simulations. In contrast to Ch. 3, four different turbulent regimes can be identified.

At very low values of collisionality, a regime of suppressed turbulence is observed. In contrast to Ch. 3, here turbulence is mainly driven by drift-waves with the presence of a strong $\mathbf{E} \times \mathbf{B}$ shear flow near the separatrix, which reduces turbulence and, consequently, leads to a steep edge pressure gradient. The main instability driving turbulence is identified by performing a test similar to the ones described in Ch. 3. Namely, for the simulation with $\nu_0 = 0.05$, $s_{T0} = 0.3$ and $\beta_{e0} = 10^{-6}$, drift-waves are removed from the system, i.e. the term $\nabla_\parallel p_e/n + 0.71\nabla T_e$ in Eq. (2.90) is zeroed out. Fig. 5.4 shows that density fluctuations vanish when this term is removed from the dynamics, clearly indicating that in the low collisionality and high heat source regime turbulence is mainly generated by drift-waves. On the other hand, only a weak effect on density fluctuations is observed when the drive of KH instability (the term $\nabla \cdot [\phi, \boldsymbol{\omega}]$ in Eq. (2.89)) is removed from the system, thus excluding KH from being the primary instability in these simulations (Fig. 5.4 (c)). This contrasts with the findings in Ch. 3, where the suppressed transport regime found at low collisionality and large values of heat source is characterized by turbulence being driven by the KH instability, with much larger values of the $\mathbf{E} \times \mathbf{B}$ shear than typical values observed in the electromagnetic simulations.

We note that the differences between the present simulations and the ones of Ch. 3 persist also at low β values. In fact, they are due to the use of the Boussinesq approximation in Ch. 3, $\nabla \cdot (n\nabla_\perp \phi + \tau \nabla_\perp p_i) \simeq n(\nabla_\perp^2 \phi + \tau \nabla_\perp^2 T_i)$, which is avoided here. In fact, although the Boussinesq approximation has usually a weak effect on plasma turbulence and equilibrium profiles in the SOL [17, 245], its validity becomes questionable in the tokamak edge [213], where steep density gradients can form, especially in the regime of suppressed turbulent transport. The results of GBS simulations presented here show that the use of the Boussinesq approximation at low collisionality leads to a change of the primary instability driving turbulent transport, with a non-negligible effect on edge turbulence, equilibrium profiles and shear flows. On the other hand, a regime of suppressed turbulent transport, qualitatively similar to the one presented in Ch. 3, is still observed even when the Boussinesq approximation is relaxed. A regime dominated by drift-wave turbulence has been recently found also in gyro-fluid simulations and associated to the I-mode regime observed in tokamaks [131]. In addition, the theoretical study of Ref. [182] associates the transition to the H-mode to a transition to a regime where turbulence in the tokamak boundary is mostly driven by the drift-wave instability. The detailed investigation of the properties of the suppressed turbulent regime identified in GBS simulations is left as future work.

At intermediate values of collisionality and β, the resistive ballooning instability dominates over the drift-wave instability, the $\mathbf{E} \times \mathbf{B}$ shear plays only a minor role, and no transport

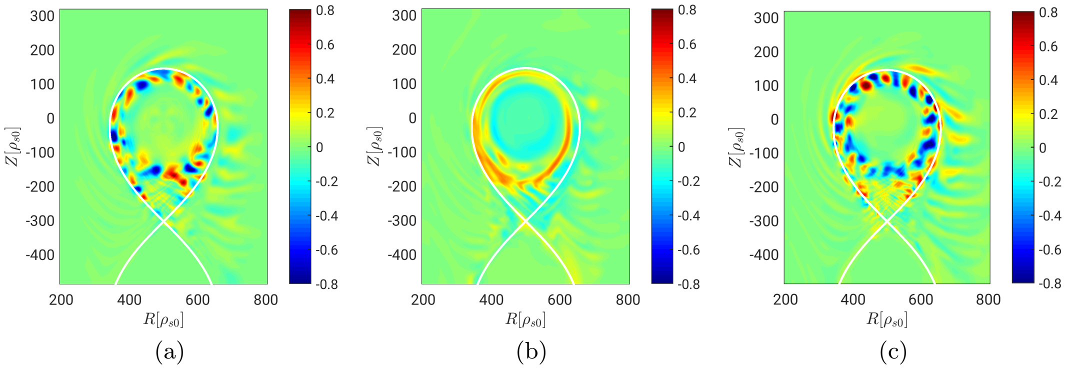

(a) (b) (c)

Figure 5.4 – Typical density fluctuations for the simulation with $\nu_0 = 0.05$, $s_{T0} = 0.3$ and $\beta_{e0} = 10^{-6}$ (a). The panels (b) and (c) show density fluctuations in the case where the drive of the drift-wave instability (the term $\nabla_{\|} p_e/n + 0.71\nabla T_e$ in Eq. (2.74)) or of the Kelvin-Helmholtz instability (the term $\nabla \cdot [\phi, \boldsymbol{\omega}]$ in Eq. (2.73)) is removed from the system.

barrier forms across the separatrix. Similarly to Ch. 3, this regime can be associated to the standard L-mode of tokamak operation. In contrast to the suppressed turbulent transport regime, the use of the Boussinesq approximation in the resistive ballooning regime has a weak effect on turbulence and equilibrium profiles.

The effect of electromagnetic fluctuations on the developed transport regime is investigated in Fig. 5.5, where the equilibrium radial profiles of density, electrostatic potential and $\mathbf{E} \times \mathbf{B}$ shear at the midplane are shown for the simulations at $\nu_0 = 0.2$, $s_{T0} = 0.3$ and three different values of β_{e0}, covering a range of two orders of magnitude values. The radial profiles show a very weak dependence on β_{e0}, suggesting that turbulent transport is weakly affected by this parameter for realistic values of β_{e0}. Therefore, we conclude that electromagnetic effects play only a minor role on turbulent transport in the tokamak boundary in the developed transport regime.

At large values of ν_0, turbulent eddies extend throughout the entire closed field lines region (see Fig. 5.3 (c)) and turbulent transport is extremely large. Consequently, the equilibrium pressure and temperature gradients near the separatrix collapse. This regime of very large turbulent transport and flat pressure and temperature profiles, which is retrieved at high density, is linked to a regime beyond the density limit, in agreement with the result of electrostatic simulations presented in Ch. 3. At these large values of collisionality, the Boussinesq approximation and the electromagnetic perturbations have no effect on turbulence and equilibrium profiles.

Finally, at large values of β_{e0}, the ideal branch of the ballooning instability overcomes the resistive one [147]. Consequently, ideal ballooning modes become the main mechanism driving turbulence. The onset of the ideal ballooning instability generates global modes

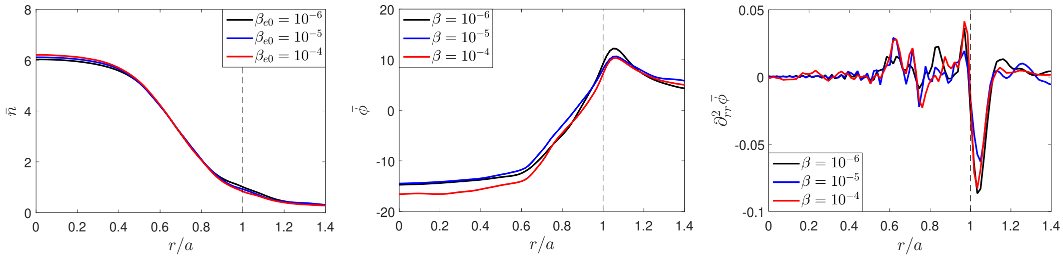

(a) (b) (c)

Figure 5.5 – Equilibrium radial profiles at the midplane of density (a), electrostatic potential (b) and $\mathbf{E} \times \mathbf{B}$ shear (c) for simulations at various values of β_{e0} with $s_{T0} = 0.3$ and $\nu_0 = 0.2$. The vertical dashed line represents the position of the separatrix.

that affect the entire confined region, as shown in Fig. 5.3 (d), eventually leading to a loss of confinement that corresponds to a plasma disruption. This regime, characterized by global modes and large values of β, is associated to a regime beyond the β limit.

In the theoretical study proposed in Refs. [181, 182], the crossing of the density limit is described as the result of the presence of electromagnetic fluctuations that inhibit the formation of sheared flows, which provide a saturation mechanism for resistive ballooning modes. In our simulations, however, the density limit is observed even at very low values of β_{e0} or in the electrostatic limit. In fact, at high values of edge collisionality, simulations show negligible sheared flows near the separatrix at any value of β_{e0}, while nonlinear saturation of the growing modes is provided by the gradient removal mechanism described in Ch. 3, rather than the presence of electromagnetic effects. On the other hand, the presence of a density limit at low values of β_{e0} observed in the simulations presented here is in agreement with the theoretical investigations of Ref. [85], arguing that the edge collisionality is the main key parameter that controls turbulent transport and density limit crossing, independently of the β value. We note that an almost negligible dependence of turbulent transport and equilibrium profiles on β has been observed also in recent gyrokinetic electromagnetic simulations in the open field lines region [130]. Similarly, an increase of turbulent transport with β_{e0} is reported in Ref. [86] only for values of β that are above the β limit.

5.3 Electromagnetic phase space of edge turbulence

By leveraging the results of GBS simulations presented in the previous section and having identified the key parameters that control turbulent transport in the tokamak boundary, we now outline a phase space of edge turbulence that takes into account electromagnetic effects. The result of this analysis is summarized in the phase space of Fig. 5.6, where the time and toroidal average of the radial extension of the turbulent eddies is shown for all the simulations considered in the present chapter. Four main regions can be identified in this

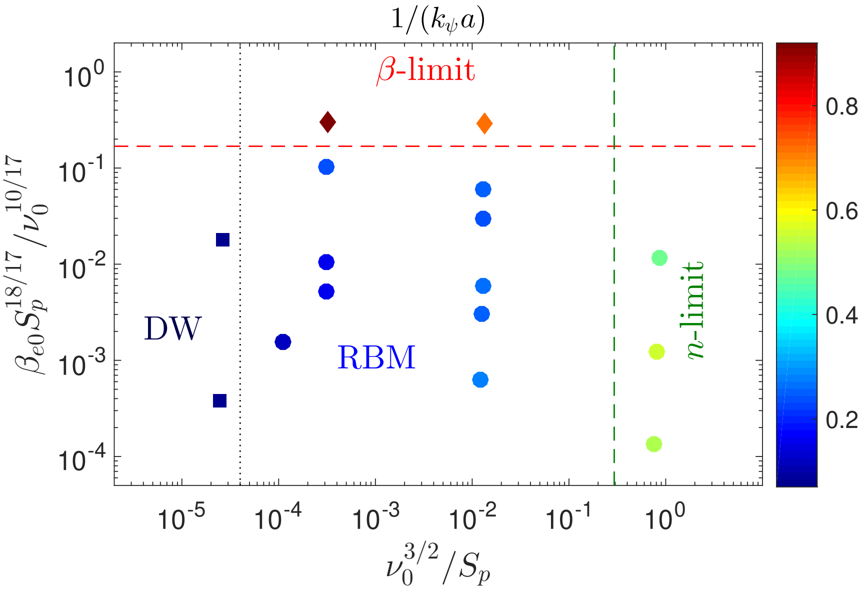

Figure 5.6 – Time and toroidal average of radial extension of the largest turbulent eddies normalized to the tokamak minor radius, $1/(k_\psi a)$, for all the simulations considered in the present work, as a function of the parameters $\beta_{e0}S_p^{18/17}/\nu_0^{10/17}$ and $\nu_0^{3/2}/S_p$, which define our edge turbulence phase space. The green (see Eq. (5.3)) and red (see Eq. (5.6)) dashed lines correspond to the density and β limits, respectively, and delimit the parameter space where the plasma is confined. Square, circle and diamonds markers correspond to simulations where turbulence is mainly driven by drift-wave (DW), resistive ballooning (RBM) and ideal ballooning instabilities, respectively. The dotted vertical line separates the simulations in the resistive ballooning and in the drift-wave regimes.

parameter space: (i) a region where the radial extension of turbulent eddies is significantly smaller than the tokamak minor radius, $1/(k_\psi a) \ll 1$, and turbulence is mainly driven by the drift-wave instability; (ii) a region where $1/(k_\psi a) \simeq 0.1$ and turbulence is mainly driven by resistive ballooning modes; (iii) a region at high collisionality that is characterized by very large turbulent transport, poor plasma confinement and $1/(k_\psi a) \simeq 0.5$, associated to the crossing of a density limit; and (iv) a region at large values of β_{e0} that is characterized by large scale modes affecting the whole confined region, $1/(k_\psi a) \simeq 1$, associated to a regime beyond the β limit. The regime of operation of a tokamak is bounded by the density and β limits represented in the phase space of Fig. 5.6. This region includes simulations with turbulence being driven either by resistive ballooning modes or drift-waves. In the following, we do not consider the transition between the drift-wave and the resistive ballooning regime. The resistive ballooning regime is described in Ch. 3, while the analysis of the drift-wave regime will be performed in a future work. We focus instead on the boundaries that delimit the region in Fig. 5.6 where the plasma is confined.

Starting with the density limit (green line in Fig. 5.6), experimental observations (see Fig. 5.2) show that this limit is overcome when the edge pressure gradient collapses.

This collapse is estimated by L_p becoming comparable to the tokamak minor radius, i.e. $L_p \sim a$. By imposing this condition in Eq. (3.30), we obtain

$$\frac{\nu_0^{3/2}}{S_p} \sim \frac{2^{13/4}}{25\pi^3} \frac{a^{5/4}}{\rho_*^{3/4} q^3 \bar{n}^{5/2} (1+\kappa^2)^{3/2}} \,. \tag{5.3}$$

The left-hand side of Eq. (5.3) depends on the parameters ν_0 and S_p, which vary across the simulation set, while the right-hand side is approximately constant in all the simulations considered here and is approximately equal to 0.5. As shown in Fig. 5.6, the theoretical limit provided by Eq. (5.3) agrees well with the results of GBS simulations. In fact, turbulent eddies in the simulations with $\nu_0^{3/2}/S_p \gtrsim 0.5$ have a radial extension comparable to the tokamak minor radius, $1/k_\psi \sim a$, which leads to a very large cross-field turbulent transport and, consequently, to a flat pressure profile.

The transition at high β is associated to the onset of the ideal ballooning instability, which becomes unstable when the parameter

$$\alpha_{\mathrm{MHD}} \sim \frac{q^2}{\rho_*} \beta_{e0} \frac{\bar{n}\bar{T}_e}{L_p} \tag{5.4}$$

exceeds a value of the order of unity [125, 249]. By substituting the analytical estimates of $\bar{T}_e$ and L_p given by Eq. (3.29) and Eq. (3.30), respectively, into Eq. (5.4), α_{MHD} can be written as

$$\alpha_{\mathrm{MHD}} \sim \frac{\beta_{e0}}{2^{1/17} 5^{2/17} \pi^{20/17}} \left(\frac{q^{14} S_p^{18}}{\rho_*^{22} a^{20} (1+\kappa^2)^{10} \nu_0^{10} \bar{n}^{11}} \right)^{1/17} \,. \tag{5.5}$$

The condition $\alpha_{\mathrm{MHD}} \gtrsim 1$ in Eq. (5.5) leads to

$$\frac{\beta_{e0} S_p^{18/17}}{\nu_0^{10/17}} \gtrsim 2^{1/17} 5^{2/17} \pi^{20/17} \left(\frac{\rho_*^{22} a^{20} (1+\kappa^2)^{10} \bar{n}^{11}}{q^{14}} \right)^{1/17} \,, \tag{5.6}$$

where the left-hand side in Eq. (5.6) depends on the parameters β_{e0}, ν_0 and S_p, which vary across the simulation scan, while the right-hand side is approximately equal to 0.2 in all the simulations. As shown in Fig. 5.6, the radial extension of the turbulent eddies in simulations with $\frac{\beta_{e0} S_p^{18/17}}{\nu_0^{10/17}} \gtrsim 0.2$ is approximately equal to the tokamak minor radius. The whole confined region is therefore affected by large scale and large amplitude fluctuations, thus leading to a total loss of plasma and heat (see Fig. 5.3 (d)).

Although turbulence simulation above the density and β limits can be performed (see Fig. 5.3), these regimes of extremely large turbulent transport are experimentally inaccessible, since the resulting equilibrium profiles lead to a global MHD instability and the subsequent plasma disruption.

We conclude this section by analysing the main analogies and differences between the edge phase space outlined in Fig 5.6 and the one derived in Ref. [182] based on the results of flux-tube simulations. The first important difference is on the choice of the edge parameters used to delineate the phase space. The parameters chosen in Ref. [182] are α_{MHD}, defined here in Eq. (5.4), and the diamagnetic parameter

$$\alpha_d = \sqrt{\frac{m_i c_s \tau_e}{0.51 m_e 4\pi^2 q^2 R_0}} \left(\frac{R_0}{L_p}\right)^{1/4} \propto \nu^{-1/2} \, . \tag{5.7}$$

Both the α_{MHD} and α_d parameters depend on L_p. In turn, L_p depends on turbulent transport and a constant value of L_p is considered in Ref. [182]. We note that in Ref. [50] the parameter α_d is replaced by $\alpha_t = (L_p/R_0)^{1/2}/(\pi\alpha_d)^2 \propto \nu$, which retains the key dependence on the plasma collisionality and removes the dependence on L_p.

In agreement with the phase space of Ref. [182], Fig. 5.6 shows the presence of a regime of reduced turbulent transport at low collisionality, i.e. high value of α_d, where the drift-wave instability dominates over the resistive ballooning instability. In Ref. [182], this regime of reduced transport is associated to the H-mode of tokamak operation. On the other hand, a more recent work based on gyro-fluid simulations has linked the regime where turbulence is driven by drift-waves to the I-mode regime observed in experiments [131]. The β limit derived here is also in agreement with the one described in Ref. [182]. On the other hand, the density limit presented here significantly differs from the one derived in Ref. [182]. In fact, in the phase space of Ref. [182], the density limit can be achieved only for values of α_{MHD} larger than 0.1 and is fundamentally linked to electromagnetic effects. Similarly, a recent work has associated the density limit to a transition from the electrostatic to the electromagnetic resistive ballooning regime, again underlining the need of electromagnetic effects to describe the density limit [50]. However, the simulations presented here show that the density limit can be exceeded at any values of β_{e0} (below the β limit), and even in the electrostatic limit, with turbulent transport that becomes extremely large also without the presence of electromagnetic modes.

The increase of the size of turbulent eddies with resistivity, and therefore as the density limit is crossed, can be estimated by balancing the interchange drive term, $2C(p)$, and the parallel current term, $\nabla_\parallel j_\parallel$, in Eq. (2.89). The term $C(p)$ is estimated from the linearized pressure equation, Eq. (3.21), leading to

$$C(\tilde{p}) \sim -\frac{\bar{p}}{\gamma \rho_* L_p} k_\chi^2 \tilde{\phi} \, . \tag{5.8}$$

The term $\nabla_\parallel j_\parallel$ is estimated from the electron parallel momentum balance, Eq. (2.90), which leads to

$$\frac{\partial \psi}{\partial t} \sim \nu \tilde{j}_\parallel + \nabla_\parallel \tilde{\phi} \, , \tag{5.9}$$

where the electron inertia is neglected. The term on the left-hand side of Eq. (5.9) is estimated by using Eq. (2.95), which leads to $\partial\psi/\partial t \sim \gamma\beta_{e0}/(2k_\perp^2)\tilde{j}_\|$. For typical values of electron density and electron temperature at the edge of a JET discharge in the proximity of the density limit, $n_e \simeq 5 \times 10^{19}$ m^{-3} and $T_e \simeq 20$ eV (see Fig. 5.2), and considering γ as the growth rate of the interchange instability, $\gamma \simeq \sqrt{2T_e/(\rho_* L_p)}$, the ratio of ν to $\gamma\beta_{e0}/(2k_\perp^2)$ is of the order of 10. Consequently, in Eq. (5.9) the term $\nu j_\|$ dominates over the term $\partial\psi/\partial t$, and the resistive and the parallel electric field terms balance. In fact, taking its parallel divergence, Eq. (5.9) can be written as

$$\nabla_\| \tilde{j}_\| \sim \frac{\nabla_\|^2 \tilde{\phi}}{\nu}\,. \tag{5.10}$$

The balance between Eq. (5.8) and Eq. (5.10) leads to $k_\chi \propto \nu^{-1/2}$. Namely, the size of turbulent eddies increases with resistivity, becoming very large even in absence of electromagnetic modes, and can be ascribed to a change of the linear properties of the driving resistive ballooning modes.

Dedicated experimental investigations have been carried out in the past with the aim of validating the phase space derived in Ref. [182] (see, e.g., Refs. [51, 112]). In particular, experimental observations show that turbulent transport in the tokamak boundary strongly depends on α_d, especially at high density, pointing out the important role played by the edge collisionality in the density limit [51, 111, 112]. In addition, the boundary of the density limit experimentally found in Ref. [112] shows also a dependence on the α_{MHD} parameter, a result that may suggest a role of electromagnetic fluctuations. However, we remind that α_{MHD} depends on the edge pressure gradient and, therefore, on turbulent transport, independently of its electrostatic or electromagnetic nature, i.e. the dependence of the density limit on the α_{MHD} parameter is not sufficient to conclude that the density limit is caused by electromagnetic rather than electrostatic turbulent transport. In addition, due to the pressure gradient dependence in α_{MHD} and α_d, these two parameters are correlated and, therefore, cannot be varied independently in the experiments, thus making it challenging to decouple the effects due to collisionality and the ones due to β.

5.4 Theory-based scaling of the density limit

The aim of this section is to provide a theory-based scaling of the density limit written in terms of engineering parameters, which can be directly compared to experimental data. In contrast to the simulations considered in Sec. 5.2 and Sec. 5.3, where a reduced value of parallel heat conductivity is used for numerical reason, in experiments the parallel heat conduction in the SOL is expected to dominate over the convection. Therefore, in order to describe typical experimental conditions, the theoretical scaling of L_p derived in Ch. 3 (see Eq. (3.30)) in the heat convection limit is extended here to the conduction limit. This new scaling of L_p is then used to derive a theory-based scaling of the density limit that can be compared to experimental data.

5.4.1 Pressure decay length in the conduction regime and theory-based scaling for the density limit

In contrast to Ch. 3, where $\bar{T}_e$ at the LCFS is estimated in the sheath-limited regime assuming that the heat parallel transport in the SOL is mainly convective, we consider here parallel conduction to dominate over the parallel convection. In the heat conduction limit, the global balance of Eq. (3.28) becomes

$$S_p \simeq \int_{\mathrm{SOL}} q_{\|}\, \mathbf{b} \cdot \frac{\nabla \chi}{||\nabla \chi||}\, \mathrm{d}l\,, \tag{5.11}$$

where the parallel heat flux in the SOL is given by

$$q_{\|} = \chi_{\| e} \nabla_{\|} \bar{T}_e = \frac{2}{7} \chi_{\| e0} \nabla_{\|} \bar{T}_e^{7/2}\,. \tag{5.12}$$

An analytical estimate of the electron temperature at the LCFS can be obtained from Eq. (5.11) by assuming $\nabla_{\|} \sim 1/L_{\|}$, with $L_{\|}$ the parallel connection length in the SOL. This leads to [211]

$$\bar{T}_e \sim \left(\frac{7}{2} \frac{S_p L_{\|}}{\chi_{\| e0} L_p} \frac{q}{a \rho_*} \right)^{2/7}, \tag{5.13}$$

where we approximate $\mathbf{b} \cdot \nabla \chi / ||\nabla \chi|| \sim q/(\rho_* a)$.

Finally, an analytical estimate of L_p is obtained by substituting $\bar{T}_e$ into Eq. (3.27), leading to

$$L_p \sim \frac{7^{8/29} \pi^{28/29}}{2^{1/29}} \rho_*^{-1/29} (1+\kappa^2)^{14/29} a^{20/29} \nu_0^{14/29} q^{36/29} \bar{n}^{42/29} S_p^{-20/29} \chi_{\| e0}^{-8/29} L_{\|}^{8/29}\,. \tag{5.14}$$

The scaling in Eq. (5.14) describes the equilibrium pressure gradient length near the separatrix at intermediate and high density, where parallel heat conduction in the SOL dominates over parallel heat convection. This estimate of L_p extends the one derived in Ch. 3 assuming no temperature gradient along magnetic field lines in the SOL. We note that the scaling in Eq. (5.14) shares with the scaling in Eq. (3.30) a similar dependence on a, ν_0 and q, while it shows a stronger dependence on $\bar{n}$ and S_p. In fact, while parallel heat transport in the sheath-limited regime depends linearly on density, $q_{\|} \simeq n T_e c_s$, there is no density dependence on the parallel heat conduction, $q_{\|} \simeq \nabla_{\|}(\chi_{\| e} \nabla_{\|} T_e)$. Consequently, in the sheath-limited regime, the increase of density is accompanied by an increase of parallel heat transport that partially compensates for the increase of turbulent transport and, therefore, of L_p (see Eq. (3.24)). On the other hand, in the conduction regime, parallel heat transport is not affected by the increase of the density, while cross-field turbulent heat transport increases with it, leading to an increase of L_p. This change on the parallel heat transport mechanism in the SOL further reduces L_p, thus suggesting an important link between parallel heat transport in the SOL and density limit, as also observed in experiments [98, 111].

A theoretical estimate of the maximum achievable edge density is derived from Eq. (5.14) by imposing $L_p \sim a$, i.e. by noticing that, at the crossing of the density limit, turbulence relaxes the edge pressure gradient that becomes comparable to a fraction of the tokamak minor radius. This leads to

$$n_{\mathrm{lim}} \sim \frac{2^{1/42}}{7^{4/21}\pi^{2/3}} \rho_*^{1/42} a^{3/14} (1+\kappa^2)^{-1/3} q^{-6/7} \nu_0^{-1/3} S_p^{10/21} \chi_{\parallel e0}^{4/21} L_\parallel^{-4/21} \,. \tag{5.15}$$

By substituting the expression for $S_p \simeq P_{\mathrm{SOL}}/(2\pi R_0)$, $\chi_{\parallel e0}$ (see Eq. (2.96)) and ν_0 (see Eq. (2.99)) in Eq. (5.15) and writing all the quantities in physical units, we obtain

$$n_{\mathrm{lim}} \sim A^{1/6} a^{3/14} P_{\mathrm{SOL}}^{10/21} R_0^{-5/6} q^{-6/7} (1+\kappa^2)^{-1/3} B_T^{2/3} L_\parallel^{-4/21} \,, \tag{5.16}$$

where n_{lim} is in units of 10^{20} m^{-3}, A is the mass number of the main plasma ions, a and R_0 are the tokamak minor and major radii in units of m, P_{SOL} is the power crossing the separatrix in units of MW, B_T is the toroidal magnetic field in units of T and $L_\parallel$ is the SOL parallel connection length in units of m.

We note that, given the weak dependence on $L_\parallel$, Eq. (5.16) can be simplified by approximating $L_\parallel \simeq qR_0$, leading to

$$n_{\mathrm{lim}} = \alpha A^{1/6} a^{3/14} P_{\mathrm{SOL}}^{10/21} R_0^{-43/42} q^{-22/21} (1+\kappa^2)^{-1/3} B_T^{2/3} \,, \tag{5.17}$$

where the parameter α is a numerical coefficient, of order unity, that accounts for all the numerical constants and approximations from order of magnitude estimates. In principle, this proportionality constant could depend on the plasma shape, divertor geometry and wall type. However, as shown later, a unique value of α is sufficient, at first order, to describe the maximum density achievable for all the tokamaks and discharges considered here.

In order to compare the theoretical scaling in Eq. (5.17) to the empirical scaling in Eq. (5.1), Eq. (5.17) is written in terms of the plasma current,

$$n_{\mathrm{lim}} \sim A^{1/6} P_{\mathrm{SOL}}^{10/21} R_0^{1/42} B_T^{-8/21} (1+\kappa^2)^{-1/3} \frac{I_p^{22/21}}{a^{79/42}} \,, \tag{5.18}$$

where I_p is the plasma current. We note that Eq. (5.18) and the empirical scaling law in Eq. (5.1) share a main dependence on I_p and a. On the other hand, the density limit in Eq. (5.18) depends also on P_{SOL}, in agreement with experimental observations [13, 53, 98, 140, 167]. The theoretical scaling in Eq. (5.18) shows also a weak dependence on B_T and a negligible dependence on A and R_0.

	$\mathbf{I_p}$ **[MA]**	$\mathbf{P_{SOL}}$ **[MW]**	$\mathbf{n_{avg}}$ $\mathbf{[10^{20}m^{-3}]}$
AUG	0.6 – 1.0	0.8 – 6.0	0.3 – 1.1
JET	1.5 – 2.5	0.3 – 8.7	0.4 – 0.8
TCV	0.1 – 0.2	0.1 – 0.7	0.5 – 0.9

Table 5.1 – Range of plasma current, power crossing the separatrix and line-averaged electron density values in the multi-machine database considered here.

5.4.2 Comparison with experimental data

The theoretical predictions provided by Eq. (5.17) are now compared to the experimental measurements of edge density at the onset of the MARFE in density limit discharges of the AUG, JET and TCV tokamaks[I]. Two different scenarios are considered: (i) a standard scenario where the density limit is reached in L-mode (i.e. no H-mode phase), where the plasma density is increased up to the density limit, and (ii) an ITER-relevant scenario where the density limit is preceded by an H-mode phase [13, 98, 132, 114, 230]. More precisely, in the second scenario, the plasma undergoes first an L-H transition, then, as the density is increased, plasma confinement degrades until an H-L transition occurs and, once in L-mode, a density limit is attained. The pre-disruption L-mode phase shows dynamics similar to those described in the first scenario and shown in Fig. 5.1. The multi-machine database considered here for the comparison covers a wide range of values of the density, plasma current and heating power with several external heating systems, such as Neutral Beam Injection (NBI), Electron Cyclotron Resonance Heating (ECRH) and Ion Cyclotron Resonance Heating (ICRH). In particular, the plasma current ranges from 0.1 MA to 2.5 MA, the toroidal magnetic field from 1.4 T to 3 T and the power crossing the separatrix from 0.1 MW to 9 MW, yielding line-averaged electron density ranging between 2×10^{19} m^{-3} and 1.1×10^{20} m^{-3} (see Tab. 5.1).

The comparison is carried out by fitting the experimental edge density at the MARFE onset with the theoretical scaling in Eq. (5.17), with the numerical factor α treated as the only fitting parameter, which is the same for all discharges and all tokamaks. The experimental value of the density at the MARFE onset is obtained by averaging the edge density, measured by means of Thomson scattering, in the region between $\rho_{\mathrm{pol}} = 0.85$ and $\rho_{\mathrm{pol}} = 0.95$ in all the discharges and tokamaks. This radial interval is chosen to reduce uncertainties of the experimental density. We note that, while choosing the interval

---

[I] The following discharges are considered in the database. AUG: 29244, 29244, 29866, 26346, 26592, 26694, 26901, 26902, 28137, 28330, 28331, 28726, 28727, 28728, 28729, 29809, 29810, 29811, 29812, 29816, 32424, 32447, 32449, 32450, 33626, 33629, 33675, 33676, 33678, 33679, 33680, 33681, 33682, 36098, 36100, 36107, 36112, 36113, 36114, 36298, 36312, 36316, 36317, 36319, 37243, 37245, 37537. JET: 80331, 80821, 80823, 80824, 80962, 80976, 81197, 81200, 81203, 81228, 81469, 81540, 81542, 81543, 81544, 81545, 81547, 81548, 81549, 81550, 81637, 81640, 81643, 81929, 81930, 82502, 82932, 82956, 82960, 82963, 82976, 82980, 82981, 84161, 85106, 85210, 85727, 85774, 85861, 85944, 85964. TCV: 45180, 45180, 46796, 46813, 46842, 46845, 63847, 64855, 64858, 64859, 64914, 64915, 64916, 64917, 64918, 64924, 65253, 65281, 65282, 65336, 65469, 65474, 65488, 65527, 68643, 68699, 68919, 68984, 68987, 69133.

between $\rho_{\text{pol}} = 0.9$ and $\rho_{\text{pol}} = 1.0$ does not affect the overall results presented here, it adds significant uncertainties on the experimental values of density. The choice of the MARFE onset as the reference time is motivated by considering the MARFE as a precursor of the density limit. In fact, the MARFE occurs when the pressure gradient at the tokamak edge collapses, which precedes a locked mode that engenders a plasma disruption.

The result of the comparison between the experimental edge density at the MARFE onset and the theoretical predictions provided by Eq. (5.17) is shown in Fig. 5.7. The theoretical scaling well reproduces the measured edge density at MARFE onset, as indicated by the high fitting quality parameter, $R^2 \simeq 0.8$, with $\alpha \simeq 3.7 \pm 0.3$. Fitting separately the three tokamaks leads to differences of α that are below 10 %, showing the robustness of this approach with respect to machine specificities. We underline that both the L-mode and the ITER baseline scenarios follow the theoretical scaling. The density limit for both scenarios is thus described with the same plasma dynamics, independently of discharge history and/or wall type (TCV has a carbon wall whereas the other machines feature metal walls).

The uncertainty on the theoretical predictions is mainly due to the experimental measurement of the power crossing the separatrix, which is estimated from the total power coupled to the plasma, having subtracting the core radiated power. The later is inferred by line integrated measurements of the bolometer cameras looking at the main plasma (typically by a tomographic inversion) and is affected by an experimental uncertainty that can be up to 50 %. In order to reduce the experimental uncertainty, the power crossing the separatrix is averaged on a time window of 20 ms before the MARFE onset, excluding the values close to the MARFE event where this quantity drops significantly because of the strong increase of the core radiated power. As indicative value, we estimate a 20 % uncertainty for the experimental values of the edge density as well as for its theoretical prediction.

Fig. 5.8 (a) shows a comparison between the maximum line-averaged density of the discharges considered here to the empirical scaling law predictions from Eq. (5.1) (red line in Fig. 5.8 (a)). The quality of the agreement is also evaluated through the parameter R^2 and a proportionality constant is also used for the empirical scaling (black line in Fig. 5.8 (a)). Although the empirical scaling is able to reproduce the overall experimental trend, there is a significant scatter in experimental data, which indicates missing dependencies in Eq. (5.1) and leads to low R^2. Similarly, a comparison between the maximum edge density and the predictions provided by the reduced scaling in Eq. (5.2) is shown in Fig. 5.8 (b), where the quality of the agreement is again evaluated through the R^2 parameter and a proportionality constant is used for the reduced scaling (black line in Fig. 5.8 (b)). We note that the predictions of Eq. (5.2) agree well with the experimental density limit of JET discharges, while Eq. (5.2) overestimates the maximum edge density for both TCV and AUG discharges, leading to a low value of R^2. The misalignment between discharges of different tokamaks in Fig. 5.8 (b) is mainly due to the weaker

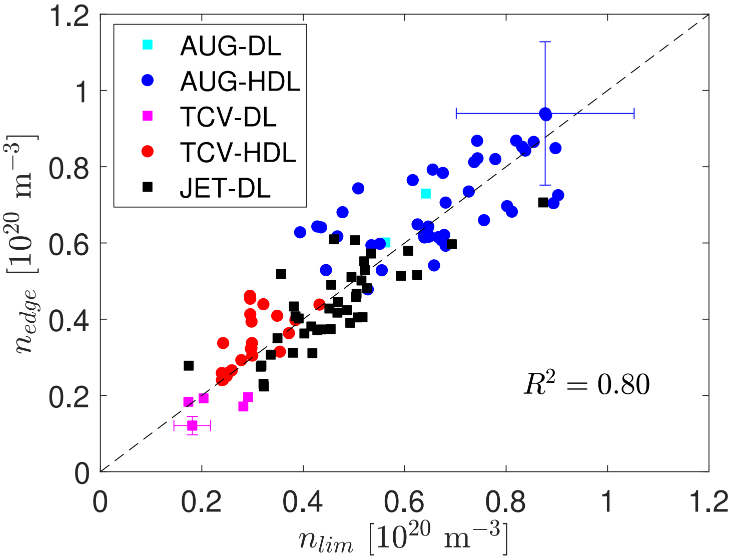

Figure 5.7 – Experimental edge density measured by means of Thomson scattering at the onset of the MARFE compared to the theoretical prediction n_{lim} provided by Eq. (5.17) with $\alpha = 3.7 \pm 0.3$. Different marker shapes and colors are used to distinguish between the standard density limit (DL) and the density limit of discharges with an H-mode phase (HDL). As examples, the errorbars are shown for the discharge with the lowest and highest density.

dependence on the plasma current of the density limit in Eq. (5.2) than the one present in Eqs. (5.1) and (5.17).

5.5 Conclusions

Results of GBS simulations that include electromagnetic effects and avoid the Boussinesq approximation are used to identify various turbulent transport regimes as well as the key parameters that control turbulent transport in the tokamak boundary, extending the work presented in Ch. 3. Based on these parameters, a phase space of edge turbulence simulations is derived, where both the density and the β limits are represented, showing a good agreement between simulation results and theoretical predictions.

Our simulation scan allows us to identify four different regimes. A regime at low collisionality where turbulence is mainly driven by the drift-wave instability, a regime at intermediate values of collisionality and β where turbulence is driven by resistive ballooning modes, a regime at high β where turbulence is driven by the ideal ballooning instability, and a regime at high collisionality where turbulent transport, driven by resistive ballooning modes, is extremely large. In contrast to Ref. [182], the simulations considered in the present chapter show that this regime of extremely large turbulent transport can be retrieved independently of the β value. More in general, a weak effect of

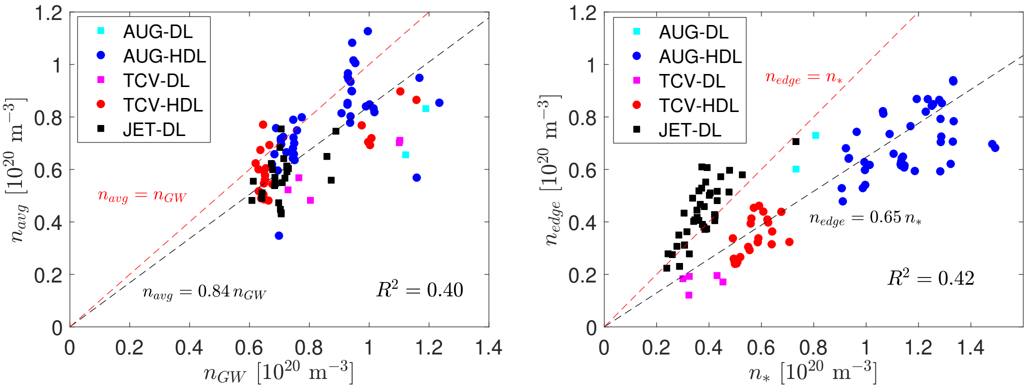

(a) Empirical scaling in Eq. (5.1)

(b) Reduced scaling in Eq. (5.2)

Figure 5.8 – (a) Experimental measured maximum line-averaged density (n_{avg}) compared to the prediction provided by the empirical scaling law in Eq. (5.1) (red dashed line). (b) Experimental maximum edge density measured by means of Thomson scattering compared to the reduced scaling provided by Eq. (5.2) (red dashed line), with $f_0 = 0.5$, $Z_{\text{eff}} = 2$ for TCV, and $Z_{\text{eff}} = 1.2$ for AUG and JET [247]. For comparison purpose, a proportionality factor is also considered in both scaling laws when evaluating the R^2 parameter. Different marker shapes and colors are used to distinguish between the standard density limit (DL) and the density limit of discharges with an H-mode phase (HDL).

electromagnetic perturbations on turbulence and equilibrium profiles is found at realistic values of β_{e0}.

By leveraging experimental observations that show a collapse of the edge pressure gradient when crossing the density limit, we derive a theory-based scaling of the density limit from a balance among heat source, cross-field turbulent heat transport near the separatrix and parallel heat losses at the vessel wall due to parallel heat conduction. This theoretical scaling is in better agreement with density limit measurements in the AUG, JET and TCV tokamaks than the widely used Greenwald empirical scaling.

We conclude with a prediction of the density limit for ITER. The theoretical scaling in Eq. (5.17) with ITER parameters ($R_0 = 6.2$ m, $a = 2$ m, $B_T = 5.3$ T, $q = 3$ and $\kappa = 1.5$) yields to $n_{\text{lim}}^{\text{ITER}} \simeq 0.4\, P_{\text{SOL}}^{10/21}$. We compare two values of P_{SOL}, below and above the power threshold to access the H-mode, $P_{\text{SOL}} = 15$ MW (L-mode) and $P_{\text{SOL}} = 25$ MW (H-mode). This gives $n_{\text{lim}}^{\text{ITER}} \simeq 1.4 \times 10^{20}$ m^{-3} (L-mode) and $n_{\text{lim}}^{\text{ITER}} \simeq 1.8 \times 10^{20}$ m^{-3} (H-mode), where both values are higher than the Greenwald density for ITER, $n_{GW}^{\text{ITER}} \simeq 1.2 \times 10^{20}$ m^{-3}. We underline that fusion power plants will operate with a much larger P_{SOL} than present day tokamaks, leading to higher values of density limit than the Greenwald scaling, with important implications for the design and operation of future fusion power plants.

6 Turbulence and flows in snowflake magnetic configurations

The present chapter is focused on the first study of plasma turbulence, equilibrium flows and heat flux at the target in alternative magnetic configurations by means of first-principle turbulence simulations. Among the various magnetic configurations that have been proposed to address the heat exhaust issue of future large scale fusion devices [5], we consider here a set of snowflake (SF) configurations [188]. The SF features a second-order null of the poloidal magnetic field, i.e. a point where all the first and second derivatives of the poloidal flux function vanish. As a consequence, the null-point is connected to the vessel wall through four legs, which define four strike points. It has been observed that these four strike points can distribute the exhaust power on a larger area than standard divertor configurations that feature two strike points. The simulations described in the present chapter consider the same physical model of Ch. 3. Namely, with respect to the full GBS model described in Ch. 2, we consider the electrostatic limit, we apply the Boussinesq approximation and we neglect the coupling to neutral dynamics.

The main results of this chapter have been recently published in Ref. [75].

6.1 Introduction

While ITER will employ a single-null X-point divertor, alternative exhaust solutions have been proposed in the recent years in order to mitigate the heat vessel loads in fusion reactors [5, 253]. Among the alternative configurations currently under consideration, we mention the super-X divertor, where the outer target is located at larger major radius than standard X-point configurations, keeping the radiative zone away from the core; the X-point divertor, where an additional X-point is generated close to the target in order to significantly increase the poloidal flux expansion; and the snowflake configuration, which features a second-order null of the poloidal magnetic field. An overview of the possible alternative exhaust solutions under consideration for DEMO can be found in Refs. [141, 168, 253]. Here, we focus on the SF configuration [188].

The SF configuration allows a distribution of the particle and heat fluxes on multiple legs, provides an increase of the connection length on flux surfaces close to the second-order null, and allows a stable radiation between two nulls in case of multiple X-points. On the other hand, the designed SF configuration for DEMO leads to a very high stress on the toroidal field coils, which makes the SF divertor challenging from an engineering point of view. In addition, the accessibility of the divertor region for installation and remote handling operations is expected to be difficult in a DEMO SF configuration [141].

SF configurations are obtained experimentally by generating two first-order X-points close to each other. When the two X-points coincide, a second-order null point is obtained. However, in practice, the two X-points never coincide perfectly. The X-point associated with the separatrix that encloses the plasma is denoted as primary, while the other, the secondary X-point, lays either in the private flux region of the primary X-point or in the common flux region. The first configuration is denoted as the snowflake plus (SF+), the latter as snowflake minus (SF−), while the configuration with the two X-points coinciding is usually referred to as the exact SF. In the SF−, the secondary X-point can be positioned either on the high-field side (HFS SF−) or on the low-field side (LFS SF−) with respect to the primary separatrix. All these configurations have been experimentally investigated in the TCV [110, 137, 163, 169], NSTX [207, 208], and DIII−D [206] tokamaks.

Experimental measurements in TCV have shown a reduction of the peak heat fluxes in SF configurations as compared to similar single-null (SN) configurations [169]. This was explained as the result of the presence of an additional cross-field transport channel into the private flux region. In Ref. [137], the effective SOL width in the LFS SF−, inferred from the measured power repartition between the two SOL regions created by the secondary X-point, was twice as large as that measured by a reciprocating probe at the outboard midplane, an observation interpreted as the result of an enhanced cross-field turbulent transport in the null-region. Numerical simulations of SF configurations, carried out by means of the EMC3-Eirene [127, 126] and the SOLPS [157] codes, are unable to reproduce these experimental observations and predict a negligible heat flux on the strike points connected to the secondary X-point [127]. These simulations assume constant diffusion parameters and neglect equilibrium drifts.

The discrepancies between experimental observations and simulations call for a detailed investigation of the presence of mechanisms leading to an enhanced cross-field transport. By evolving self-consistently the turbulent and the equilibrium cross-field transport, first-principles global turbulence simulations such as the one that are allowed by the GBS code can point out the existence of regions where the perpendicular transport is strong and the mechanisms behind it. The present chapter describes the first simulation based on a turbulent model of SF configurations.

The present chapter is organized as follows. The SF magnetic configurations implemented in GBS are presented in Sec. 6.2. An overview of simulations results as well as the

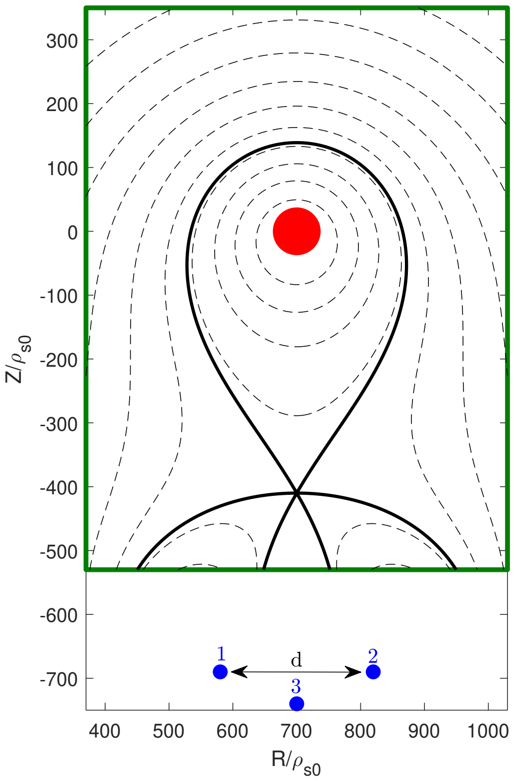

Figure 6.1 – Contour plot of the poloidal flux function, Ψ, in the exact SF configuration implemented in GBS (black dashed line). The separatrix is shown as a solid black line. The GBS boundary domain is indicated by a solid green line. The three blue circles represent the position of the current filaments, located outside the simulation domain, responsible of creating the SF configuration, while the red circle represents the center of the plasma current.

analysis of the heat flux distribution is reported in Sec. 6.3. The role of turbulence in SF configurations is discussed in Sec. 6.4. The conclusions follow in Sec. 6.5.

6.2 The snowflake magnetic equilibrium

Similarly to the equilibrium considered in Ch. 3-5, the magnetic poloidal flux Ψ of a SF configuration is analytically obtained by integrating the Biot-Savart law in the infinite aspect-ratio limit by considering three straight current filaments and a current density with Gaussian profile, which mimics the plasma current. The position of the filaments and the plasma current is shown in Fig. 6.1. The plasma current is centered at (R_p, Z_p), its integral value is I_p and its width σ. We denote (R_i, Z_i) and I_i, with $i = 1, 2, 3$, the position of the three filaments and their current, respectively. The position of the filaments are chosen, for instance, to develop a left-right symmetric equilibrium in the exact SF case. This imposes $R_1 + R_2 = 2R_p$, $R_3 = R_p$, $I_1 = I_2 \equiv \alpha I_p$ and $Z_1 = Z_2$. The distance between the first and the second filament, $d \equiv R_2 - R_1$, and α are derived by following the procedure described in Ref. [188]. In practice, we impose $\nabla\Psi$, $\partial_R \nabla\Psi$ and $\partial_Z \nabla\Psi$ to vanish at the second-order X-point and we obtain

$$\alpha = -\frac{Z_1'\sigma^2\left[Z_3' - (\beta Z_p' + Z_3')\exp\left(Z_p'^2/2\sigma^2\right)\right]^2}{\exp\left(Z_p'^2/\sigma^2\right)\left[K_1 - K_2\exp\left(-Z_p'^2/2\sigma^2\right)\right]}\,, \tag{6.1}$$

$$d = -\frac{2Z_1'\left[K_3\exp\left(Z_p'^2/2\sigma^2\right) - K_4\right]^{1/2}}{\left[K_1\exp\left(Z_p'^2/2\sigma^2\right) - K_2\right]^{1/2}}\,, \tag{6.2}$$

where $\beta = I_3/I_p$,

$$K_1 = \sigma^2\left[Z_3'^2(Z_p' + Z_1') + \beta Z_p'^2(Z_1' + Z_3')\right]\,, \tag{6.3}$$

$$K_2 = Z_3'^2(Z_p'^2 Z_1' + Z_p'\sigma^2 + Z_1'\sigma^2)\,, \tag{6.4}$$

$$K_3 = \sigma^2\left[\beta Z_p'^2(Z_3' - Z_1') + Z_3'^2(Z_p' - Z_1')\right]\,, \tag{6.5}$$

$$K_4 = Z_3'^2\left[\sigma^2(Z_p' - Z_1') - Z_p'^2 Z_1'\right]\,, \tag{6.6}$$

with $Z_p' = Z_p - Z_X$, $Z_1' = Z_1 - Z_X$, and $Z_3' = Z_3 - Z_X$, being Z_X the vertical position of the X-point. The SF+ and SF− configurations are obtained by varying the current of the $i = 1$ and $i = 2$ filaments.

In the following, we choose $\sigma = 63.3$, $I_p = 11.4$, $Z_p' = 410$, $Z_1' = -280$, $Z_3' = -330$ and $\beta = -7.0$ for all the SF configurations. This leads to a safety factor of $q_0 \simeq 1$ at the magnetic axis and $q_{95} \simeq 5$ at the tokamak edge. The parameters α and d are then evaluated from Eqs. (6.1) and (6.2), leading to $\alpha \simeq 3.91$ and $d \simeq 240$ for the exact SF. The values of the current in the three filaments for the four configurations are reported in Table 6.1. The ion-∇B drift direction points upwards (unfavourable for H-mode access).

In order to evaluate the benefits deriving from the SF on the power exhaust compared to standard exhaust solutions, we consider a single-null (SN) configuration with core conditions similar to the exact SF. The SN configuration is obtained by using the same set of filaments as well as the same physical and numerical parameters as in the SF simulations, but $\alpha = 0.3$, $d = 1000$, $Z_p' = 410$, $Z_1' = 0$, $Z_3' = -480$ and $\beta = 1.17$. The value of the current in the three filaments in the SN is also reported in Table 6.1.

The SF and SN configurations are designed to have similar flux-averaged safety factor and magnetic shear profiles in the core, as shown in Fig. 6.2. The low-field side (LFS) connection length, $L_\parallel$, defined as the length of a magnetic field line connecting the outer midplane to the LFS target, is displayed in Fig. 6.2 (c) for all the configurations. The

Table 6.1 – Values of the current in the three filaments normalized to the plasma current for all the considered configurations. Negative currents flow in the direction opposite to the plasma current.

Configuration	$\mathbf{I_1/I_p}$	$\mathbf{I_2/I_p}$	$\mathbf{I_3/I_p}$
Exact SF	3.91	3.91	-7.00
SF+	3.94	3.94	-7.00
HFS SF−	3.91	3.72	-7.00
LFS SF−	3.72	3.91	-7.00
SN	0.3	0.3	1.17

SN configuration has a longer LFS connection length than the exact SF, the SF+ and the HFS SF− within a distance from the separatrix larger than approximately 0.1 ρ_{s0}, considerably shorter than the SOL width. This is typical for present-day devices, but the distance from the separatrix at which the $L_\parallel$ of a SF configuration is equal to $L_\parallel$ of a comparable SN configuration in fusion reactors is expected to be larger than the SOL width [169]. The connection length in the LFS SF− diverges at the location of the secondary separatrix, whose distance from the primary separatrix at the LFS midplane is approximately 7 ρ_{s0}.

6.3 Heat flux distribution at the target plates

The simulations presented here are carried out with the following parameters: $\rho_*^{-1} = 700$, $a/R_0 = 0.25$, $\nu_0 = 0.1$, $\tau = 1$, $L_R = 660$, $L_Z = 880$, $s_{n0} = 0.3$, $\Delta_n = 900$, $s_{T0} = 0.3$ and $\Delta_T = 800$. Regarding the numerical parameters, in all cases, the grid used is $N_R \times N_Z \times N_\varphi = 240 \times 320 \times 80$ and the time-step is 2×10^{-5} R_0/c_{s0}. The analysis that follows is performed when a quasi-steady state is reached, where sources, turbulent transport and losses at the vessel balance each other. A snapshot of the density on a poloidal plane is shown in Fig. 6.3 for all the magnetic configurations considered here.

In this section, we focus on the distribution of the equilibrium parallel heat flux among the four target plates of the exact SF, the SF+, the LFS SF−, and the HFS SF−. Since our simulations are in the sheath-limited regime, the parallel heat flux is dominated by the parallel convection, $q_\parallel = \overline{p_e v_{\parallel e}}$, (as in the previous chapters, any quantity f is written as a sum of the time and toroidal averaged component $\bar{f}$, denoted here as equilibrium, and the fluctuating component $\tilde{f}$, i.e. $f = \bar{f} + \tilde{f}$). The $q_\parallel$ flux is proportional to the power reaching the wall through the sheath heat transmission coefficient [211].

Fig. 6.4 shows $q_\parallel$ in the proximity of the four strike points, which are denoted, from the HFS to the LFS, as SP1, SP2, SP3, and SP4, and whose position is displayed in Fig. 6.3. The distance from the separatrix is evaluated at the midplane in order to remove the

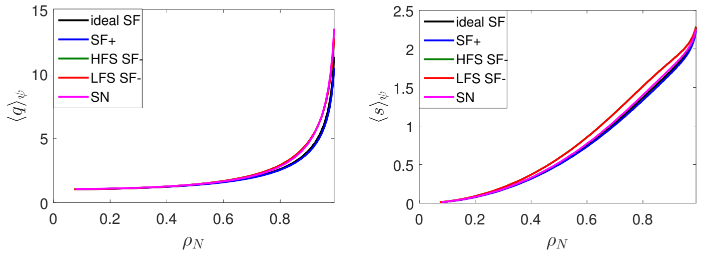

(a) Safety factor (b) Magnetic shear

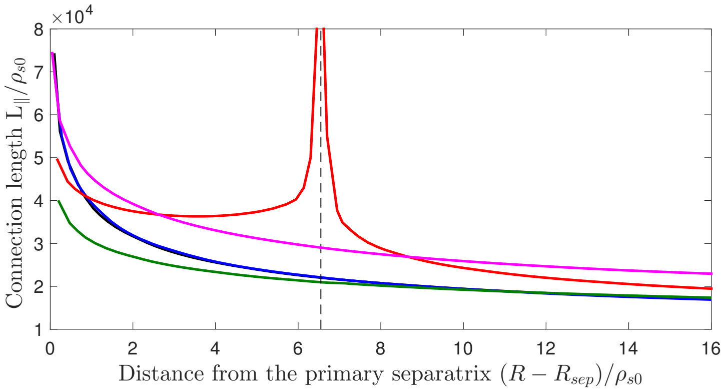

(c) Low-field side connection length

Figure 6.2 – Flux-surface averaged safety factor, $\langle q \rangle_\Psi$, and magnetic shear, $\langle s \rangle_\Psi$, inside the separatrix for all the considered configurations as a function of $\rho_N = \sqrt{(\Psi - \Psi_0)/(\Psi_{\mathrm{LCSF}} - \Psi_0)}$, where Ψ_{LCFS} and Ψ_0 are the poloidal flux values at the last closed flux surface and at the magnetic axis, respectively (panels (a) and (b)). The low-field side connection length is shown in panel (c). The vertical dashed line at the distance $R - R_{sep} \simeq 7$ from the primary separatrix, where $L_\parallel$ diverges, corresponds to the location of the secondary separatrix of the LFS SF$-$.

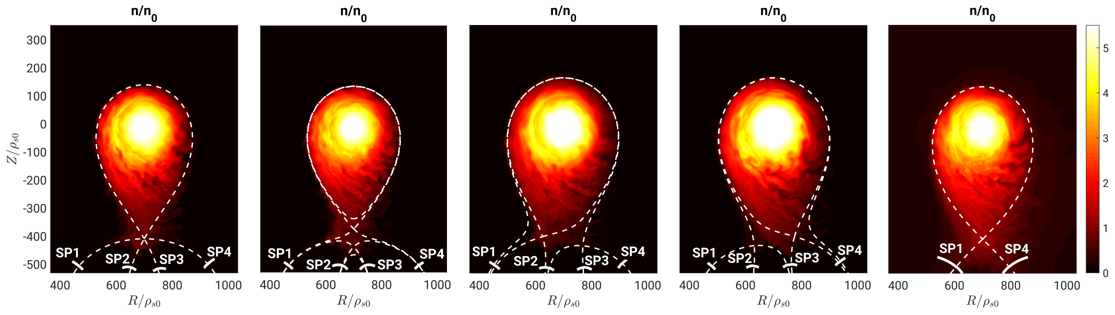

(a) Exact SF (b) SF+ (c) LFS SF$-$ (d) HFS SF$-$ (e) SN

Figure 6.3 – Typical snapshot of density, n, on a poloidal plane for the exact SF (a), the SF+ (b), the LFS SF$-$ (c), the HFS SF$-$ (d), and the SN (e). The dashed white line indicates the separatrices and the solid white lines the locations where the parallel heat flux is evaluated. Starting from the HFS, we label the strike points as SP1, SP2, SP3 and SP4 for the SF configurations, and SP1 and SP4 for the SN configuration.

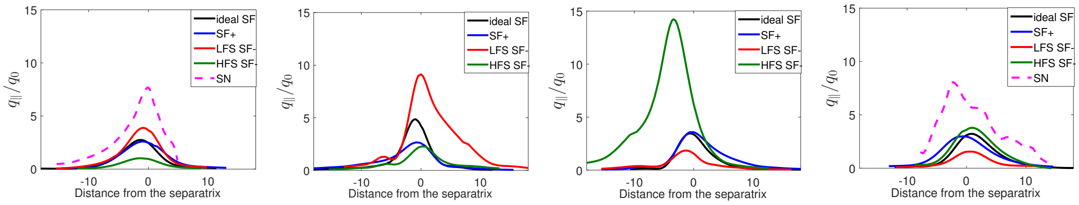

(a) SP1 (b) SP2 (c) SP3 (d) SP4

Figure 6.4 – Equilibrium parallel heat flux at the target plates, normalized to $q_0 = n_0 T_{e0} c_{s0}$, as a function of the distance from the separatrix, which is evaluated at the midplane and normalized to ρ_{s0}. The position of the strike points is shown in Fig. 6.3 (solid white lines). The positive (negative) sign of the distance refers to a region to the right (left) of the separatrix.

Table 6.2 – Fraction of the deposited power on the different strike points for all the considered magnetic configurations. See Fig. 6.3 for the position of the strike points.

	SP1	**SP2**	**SP3**	**SP4**
Exact SF	28%	20%	18%	34%
SF+	30%	14%	18%	38%
LFS SF−	28%	53%	9%	10%
HFS SF−	6%	8%	60%	26%
SN	46%	–	–	54%

effect of the flux expansion at the target, which is different for all the configurations and could be compensated by a poloidal tilt of the target in a dedicated device. The fraction of the deposited power on the strike points is listed in Table 6.2. As an aside, we note that the SOL width at the LFS midplane computed from the pressure profile is similar for all the configurations and its value is approximately 10 ρ_{s0}. This recalls experimental observations that show a weak dependence of the upstream SOL width on the different magnetic configurations [137, 169].

In the exact SF, in absence of perpendicular transport, we expect that the heat flux flows along the magnetic field lines to SP1 and SP4. On the other hand, we notice that the integrated heat flux redistributes quite homogeneously among the four strike points (see Table 6.2). The activation of the inner strike points (SP2 and SP3) is due to a convection cell induced by the equilibrium $\mathbf{E} \times \mathbf{B}$ drift, $\mathbf{q}_{\mathrm{E}}^{\mathrm{eq}} = \bar{p}_e \bar{\mathbf{v}}_{\mathrm{E}}$, which is present in the region around the null-point (see Fig. 6.5 (a)), while the turbulent flux is negligible in the null-point region, as also observed experimentally in the SN configuration [234]. We point out that the convective cell width is comparable to the SOL width evaluated at the X-point, i.e. retaining the effect of the flux expansion. In agreement with our simulation, experimental observations suggest that the $\mathbf{E} \times \mathbf{B}$ drift in SF configurations provides

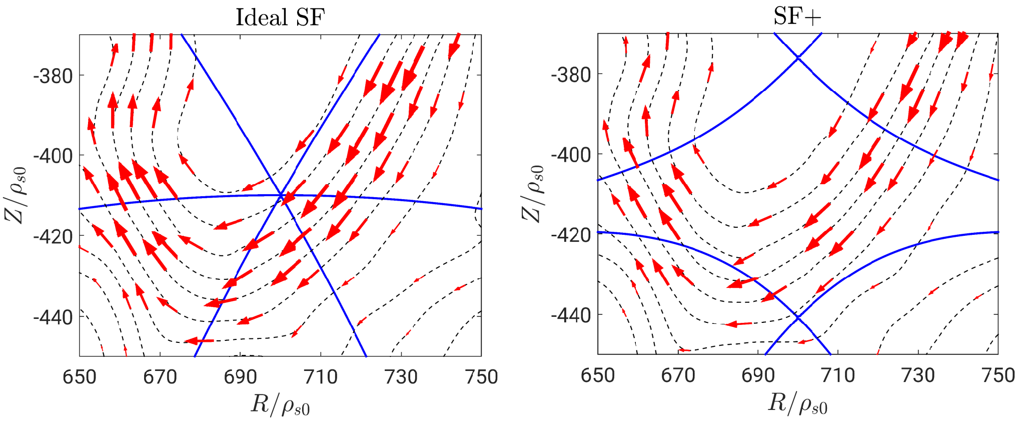

(a) Exact SF (b) SF+

Figure 6.5 – Equilibrium $\mathbf{E}\times\mathbf{B}$ heat flux in the null-point region for the exact SF (a) and SF+ configurations. The size of the arrows is proportional to the intensity of the heat flux. Black dashed lines indicate contour levels of the electrostatic potential while the solid blue line indicates the separatrix.

an important transport mechanism in the null-region and contributes to the heat flux distribution among the four strike points [26]. This mechanism has also been pointed out by measurements in the null-region of SN configurations [195, 194]. We note that Refs. [189, 224] argue that an electromagnetic instability, the churning mode, may provide the redistribution of the heat flux over the four divertor legs. Our simulation shows that the redistribution occurs also when electromagnetic fluctuations are not included.

In the SF+, the $\bar{\mathbf{v}}_{\rm E}$ drift in the region between the two X-points activates SP2 and SP3 (see Fig. 6.5 (b)). However, the equilibrium parallel heat flux on SP2 and SP3 is reduced with respect to the exact SF. This reminds of experimental observations in TCV [169] that show a decrease of the heat flux on the secondary strike points (SP2 and SP3) as the distance between the two X-points increases. We highlight that, in our simulation, the distance between the two X-points is comparable to the SOL width evaluated at the primary X-point, corresponding to the width of the convective cell (see Fig. 6.5 (b)). This is sufficient to lead to a reduction of 40% of the flux to SP2. In order to have significant activation of SP2 and SP3, we expect that the vertical distance between the two X-points must be comparable to the SOL width evaluated at the primary X-point. Such a request may be challenging for DEMO, whose SOL width is foreseen to be smaller than 1 mm [49].

Regarding the LFS SF− configuration, we notice that the strike points connected to the secondary X-point are only partially activated, i.e. only 9% and 10% of the total power is deposited on SP3 and SP4, respectively. In Fig. 6.6, we show $\mathbf{q}_{\rm E}^{\rm eq}$ around the primary and secondary X-point. The intensity of the circulation cell around the secondary X-point is an order of magnitude smaller than around the primary X-point and $\mathbf{q}_{\rm E}^{\rm eq}$ is localized around the X-point in a region of size smaller than the SOL width. It follows that, since the distance between the two X-points is approximately twice as large as the SOL width evaluated at the primary X-point, the convective cell around the primary X-point does not affect the heat fluxes in the proximity of the secondary X-point.

In the HFS SF− configuration, we observe that SP1 and SP2 are only partially activated (see Fig. 6.4) and most of the power (60%) flows to SP3. In this case, a very strong equilibrium $\mathbf{E}\times\mathbf{B}$ drift is found in the region around the primary X-point (see Fig. 6.6 (c)), such that it leads to a strong heat transport from the divertor leg connected to SP4 to the divertor leg connected to SP3. Around the secondary X-point $\mathbf{q}_{\mathrm{E}}^{\mathrm{eq}}$ is more than one order of magnitude smaller (see Fig. 6.6 (d)) and therefore its role is negligible.

We compare now the parallel heat flux for the SF and SN configurations. The peak value of the parallel heat flux in the SN configuration is more than twice as high as the one in the exact SF (Fig. 6.4), as a consequence of the uniform parallel heat flux distribution among all the four divertor legs. This highlights the benefit of the heat flux redistribution. The same is valid for the SF+, although the integrated power in SP2 and SP3 is reduced with respect to the exact case. In the case of the LFS SF− configuration, the peak value of the parallel heat flux, which occurs in SP2, is comparable with the peak value of the parallel heat flux in the SN configuration. This is a consequence of the fact that in the LFS SF− configuration the heat flux is not as well distributed among all the strike points. Worst considerations can be drawn for the HFS SF−, where the peak value of the parallel heat flux, which occurs in SP3, is 50% larger than the one in the SN.

6.4 The role of turbulence in the heat flux distribution

In order to highlight the role played by turbulence in SF configurations, especially in the LFS SF−, we consider the distribution of the heat flux between the LFS strike points of this configuration (SP2, SP3, and SP4), more precisely between the LFS strike point connected to the primary X-point, i.e. SP2, and the strike points connected to the secondary X-point, i.e. SP3 and SP4. For this purpose, we first consider $q_{\|}$ at the LFS midplane in a region where the parallel flow is directed towards the LFS targets [110]. We integrate $q_{\|}$ over the SOL region between the primary and the secondary separatrix and over the whole SOL region. The ratio between these two integrals, equal to 0.87 in our simulation, is larger than the ratio of the integrated power reaching SP2 to the power reaching the three LFS strike points, which is approximately 0.74. Therefore, cross-field transport must occur between the midplane region and the strike points. In fact, we observe in Fig. 6.7 (a) the presence of a region in the LFS between the two separatrices of strong turbulent $\mathbf{E}\times\mathbf{B}$ perpendicular flux, $\mathbf{q}_{\mathrm{E}}^{\mathrm{t}} = \overline{\widetilde{p}_e\ \widetilde{\mathbf{v}}_{\mathrm{E}}}$. Therefore, heat is transported across the secondary separatrix and parallel flows to the secondary X-point. This reduces the heat flux reaching SP2. Due to the presence of the small but not completely negligible $\mathbf{E}\times\mathbf{B}$ convective cell around the secondary X-point, the heat flux on the SOL region outside the secondary separatrix is partially distributed towards SP3

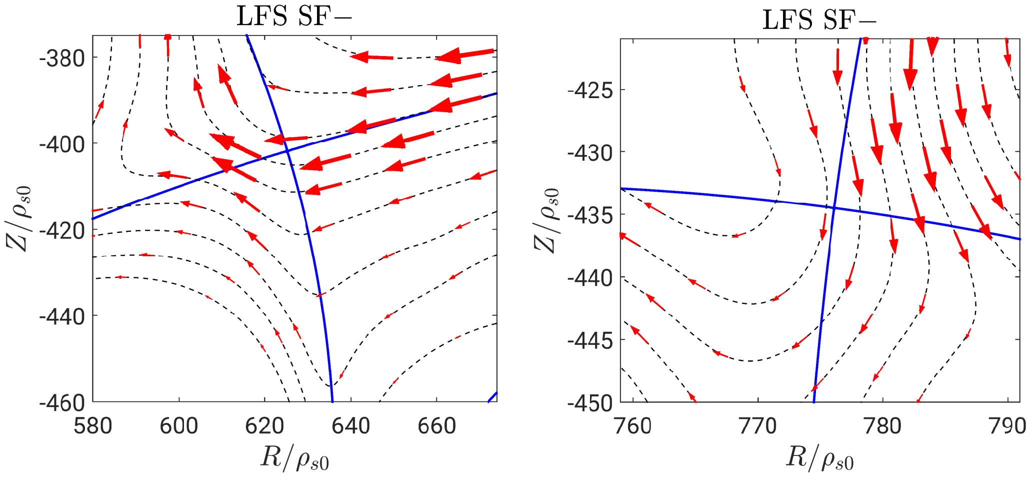

(a) Primary X-point (b) Secondary X-point

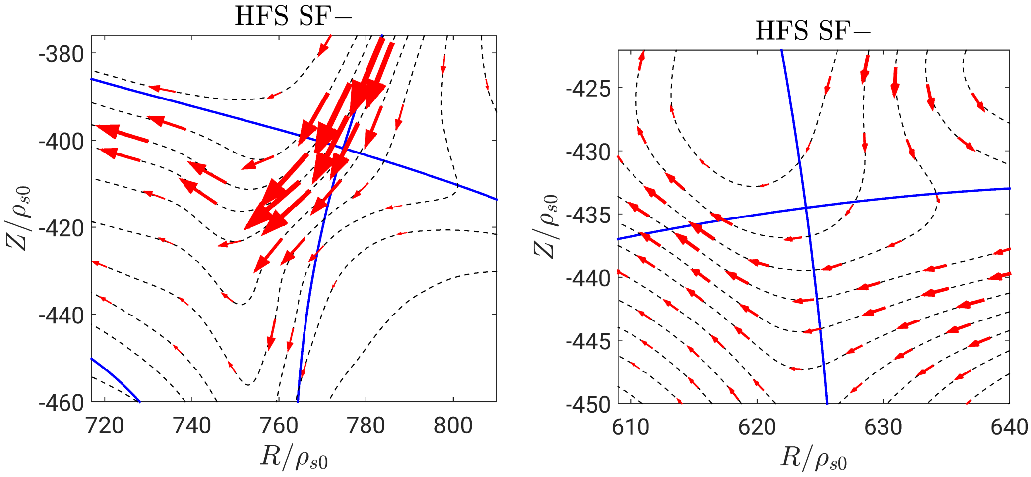

(c) Primary X-point (d) Secondary X-point

Figure 6.6 – Equilibrium $\mathbf{E} \times \mathbf{B}$ heat flux for the LFS (top line) and HFS (bottom line) SF− configurations around the primary [(a) and (c)] and secondary [(b) and (d)] X-points. The size of the arrows is proportional to the intensity of the heat flux. Black dashed lines represent the contour levels of the electrostatic potential. The separatrix is indicated by a solid blue line. In (b) and (d), the arrow size is multiplied by a factor of 10 with respect to (a) and (c).

and SP4. We note that the presence of turbulent structures in the region between the two nulls of the LFS SF− has been experimentally observed in Ref. [235]. On the other hand, $\mathbf{q}_{\mathrm{E}}^{\mathrm{eq}}$ is important only in the region around the primary X-point and cannot provide a mechanism to transport heat across the secondary separatrix. Moreover, there is no strong perpendicular equilibrium $\mathbf{E} \times \mathbf{B}$ flux that connects the two X-points. This explains the small heat flux exhausted at SP3 and SP4.

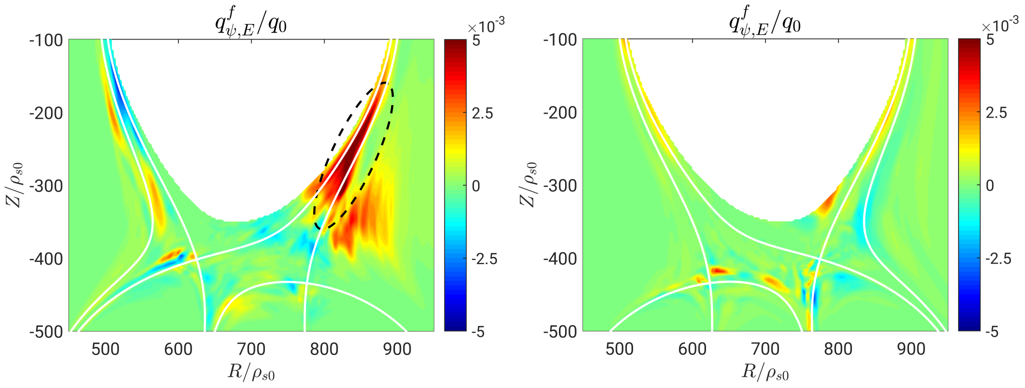

(a) LFS SF−

(b) HFS SF−

Figure 6.7 – Intensity of the $\mathbf{E} \times \mathbf{B}$ turbulent heat flux projected along $\nabla\Psi$, $q^f_{\Psi,E}$, in the LFS and HFS SF− configurations normalized to $q_0 = nT_{e0}c_{s0}$ ((a) and (b) respectively). The dashed black line highlights the region of strong turbulent transport. The white solid lines represent the two separatrices.

Analogously to the LFS SF− configuration, the secondary X-point of the HFS SF− splits the SOL in two regions. In order to investigate possible effects due to turbulence, the same analysis as in the LFS SF− is performed, but in this case at the HFS. By integrating $q_\parallel$ at the HFS midplane, where the parallel heat fluxes are directed towards the HFS targets, over the region inside and outside the secondary separatrix, we expect that 85% of the total HFS power flows towards SP3. In fact, the integrated power on SP3 normalized to the total power flowing in the HFS SOL and reaching the HFS strike points (SP1, SP2, and SP3) is approximately 81%, in good agreement with the expected value. As shown in Fig. 6.7, there is no strong perpendicular turbulent transport across the secondary separatrix in the case of HFS SF−. The fact that the perpendicular turbulent transport is enhanced only on the LFS of the LFS SF−, where large radial pressure gradients exist in the bad curvature region, indicates that it is driven by ballooning-like modes. This result confirms the hypothesis of Ref. [137], where the measured power on SP4 was found to be significantly larger than expected, and ballooning-like turbulent transport in the SOL between the primary and secondary separatrices was suggested as possible explanation.

For both the SF− configurations, the distance between the two separatrices can be optimized in order to achieve a better heat flux redistribution [110, 225]. The optimization requires that the distance between the primary and secondary separatrix is set to fractions of the SOL width. The enhancement of perpendicular turbulent transport for the LFS SF− increases the distance at which the uniform heat flux distribution is reached, which is particularly beneficial for DEMO-like reactors. On the other hand, the width of the $\mathbf{E} \times \mathbf{B}$ convection cell around the primary X-point is approximately a factor of 2 smaller in SF− configurations than in the other SF configurations, decreasing the potential importance of $\mathbf{q}_{\mathrm{E}}^{\mathrm{eq}}$.

6.5 Conclusions

In the present chapter, the results of the first global turbulence simulations in various snowflake configurations are presented. These simulations point out that the activation of the secondary strike points in the exact SF and in the SF+ configurations, experimentally observed in Ref. [169], can be explained by the presence of an equilibrium $\mathbf{E}\times\mathbf{B}$ convective cell in the region around the primary X-point. The effect of the convective cell is strongly reduced as the distance between the two X-points becomes larger than the SOL width evaluated at the primary X-point, which is the case for our SF− configurations. In addition, the turbulence simulation in the LFS SF− configuration shows the presence of a region of enhanced cross-field turbulent transport driven by ballooning-like modes, thus confirming the hypothesis in Ref. [137] based on experimental observations. No enhancement of turbulent transport is instead observed in the other snowflake configurations considered here.

The simulations presented in this chapter point out some potential benefits of SF configurations with respect to the standard SN magnetic configuration, such as the activation of the four strike points due to the presence of an equilibrium $\mathbf{E} \times \mathbf{B}$ convective cell around the second order null of the poloidal magnetic field. Understanding the origin of this $\mathbf{E} \times \mathbf{B}$ convective cell is therefore important to extrapolate these results to future magnetic fusion devices. Besides more detailed theoretical investigations, the results presented here call for the need of further GBS simulations with the full model described in Ch. 2, which will allow investigating the effect of electromagnetic perturbations and Boussinesq approximation on the presence and robustness of this $\mathbf{E} \times \mathbf{B}$ convective cell around the X-point. Simulations with electromagnetic effects are also needed to address the churning mode and its effect on the heat flux distribution [189, 224]. Finally, results of GBS simulations that evolve the neutral dynamics are needed to investigate possible advantages of detachment in SF configurations.

7 Conclusions and outlook

In the present thesis, different turbulent transport regimes in the tokamak boundary are identified and analyzed by means of three-dimensional, global, flux-driven, two-fluid turbulence simulations carried out by using the GBS code. Analytical expressions of the cross-field turbulent heat-flux at the separatrix are derived from a quasi-linear theory and then used to estimate the equilibrium pressure gradient length in the tokamak boundary. Thanks to these theoretical estimates and exploring also alternative divertor solutions, the thesis addresses some of the key aspects related to the design and the operation of future tokamaks, such as the heat flux to the target plates and the physics behind the density limit, providing a theoretical interpretation of this limit based on edge turbulent transport. In particular, theory-based scaling laws for the pressure decay length in the SOL of L-mode single-null tokamak discharges and for the crossing of the density limit are provided and successfully validated against a multi-machine database.

Following the introduction, Ch. 2 describes a new version of the GBS code, recently submitted for publications [73]. The GBS domain is extended to encompass the whole plasma volume, thus retaining the interplay among core, edge and SOL physics, while avoiding the use of an artificial boundary with the core. A new non-field aligned coordinate system is adopted, significantly extending the GBS capability to handle complex magnetic geometries, which can also be the result of a magnetic reconstruction of an experimental discharge. The implementation of the Poisson and Ampère equations is carefully optimized by means of an iterative solver based on the PETSc library, leading to a speed-up of medium size tokamak simulations of approximately a factor of 40. The physical model is improved by coupling the plasma model to a single-species kinetic neutral model, leading to the first simulation of a TCV discharge in lower single-null with the self-consistent evolution of plasma turbulence and neutral dynamics.

In Ch. 3, results of electrostatic GBS simulations are leveraged to study the effect of collisionality and heat source on plasma turbulence at the tokamak boundary. Three edge turbulent transport regimes are identified: (i) a regime of suppressed turbulence at low values of collisionality and large values of heat source, which shows some similarities with the H-mode regime, (ii) a regime of developed turbulence at intermediate values of collisionality and heat source, which can be associated to the L-mode regime, (iii) and a regime at large values of collisionality, characterized by a very large turbulent transport, not compatible with a tokamak operational scenario and therefore associated to a regime that is beyond the density limit. An analytical estimate of the equilibrium pressure gradient length is derived in all the identified regimes. The main results of this chapter are published in Ref. [72].

In Ch. 4, we focus on the SOL plasma dynamics of the L-mode regime identified in Ch. 3. Theory-based scaling laws of the pressure and density decay lengths are derived in the near and far SOL. The theoretical scaling law of the pressure decay length in the near SOL is derived from a balance among the heat source, the cross-field turbulent heat flux across the separatrix and the parallel heat losses at the vessel wall, and it is compared to the results of GBS simulations at different values of collisionality and heat source, showing a good agreement between the theoretical predictions and the numerical results, with differences that are below 20 %. The scaling law of the near SOL pressure decay length is also compared to experimental measurement of the power fall-off length taken from a multi-machine database that includes discharges of the C-mod, COMPASS, JET, MAST and TCV tokamaks. The result of this comparison shows that the theoretical scaling is able to reproduce well the experimental data, with a high value of $R^2 \simeq 0.85$. The theoretical scaling laws of the far SOL pressure and density decay lengths are derived by balancing the perpendicular and parallel transport in the far SOL due to blobs, and then compared to GBS results, showing differences between the theoretical predictions and the numerical results up to 40 %. As a preliminary comparison, the theoretical predictions of the far SOL pressure decay length are compared to experimental measurements at the outboard midplane of TCV L-mode lower single-null discharges, showing a weak correlation between the theoretical scaling and experimental data, thus calling for further theoretical and experimental investigations. The main results of this chapter are published in Ref. [74].

In Ch. 5, the effects of electromagnetic perturbations and of the Boussinesq approximation on turbulence and equilibrium profiles are investigated by using GBS simulations. The electromagnetic phase space of edge turbulence is derived by analysing the results of GBS simulations at various values of β, collisionality and heat source. Depending on the values of these parameters, the main instability driving turbulence is identified. We show the presence of a transition from resistive ballooning modes to drift-waves as collisionality decreases and from resistive ballooning modes to ideal ballooning modes as β increases. The transition to the ideal ballooning instability is associated to the crossing of the β-limit observed in experiments. In addition, a transition to a regime of extremely large turbulent transport is observed at large values of collisionality, independently of the value of β. This transition is associated to the crossing of the density limit. We show that the density limit can be seen as the result of enhanced turbulent transport at the tokamak boundary and we derive a theory-based scaling law of the maximum edge density achievable in tokamaks, which is in better agreement with a multi-machine database of density limit discharges in the AUG, JET and TCV tokamaks than the widely used Greenwald empirical scaling.

In Ch. 6, the results of the first three-dimensional turbulence simulations of snowflake configurations are presented. The parallel heat flux distribution over the four legs is analyzed in different snowflake geometries and compared to a standard single-null configuration. The activation of the secondary strike points in the exact SF and SF+ configurations is shown to be due to an equilibrium $\mathbf{E} \times \mathbf{B}$ flow that transports particles and heat from the SOL to the private flux region. The role of turbulence in snowflake configurations is investigated, pointing out the presence of enhanced turbulence in a region between the two separatrices of the LFS SF−, which contributes to the heat flux redistribution among the LFS strike points.

Despite the progresses in the simulation of plasma turbulence in the tokamak boundary with the GBS code described here and the physics understanding of its dynamics, some limitations persist that prevent us to simulate plasma turbulence in the boundary of large-scale fusion devices with realistic parameters. This is a necessary step to assess the extrapolation of our understanding to these configurations. For this purpose, as an important step towards the simulation of ITER and DEMO, GBS is being ported to Graphics Processing Units (GPUs). In fact, a GPU can process data several orders of magnitude faster than a CPU due to massive parallelism, thus strongly reducing the time required to perform simulations of plasma turbulence in large scale magnetic fusion devices. In addition, the flexibility of the GBS geometry is being improved by adopting a curvilinear coordinate system that will allow us to carry out simulations with a realistic wall geometry [91]. The neutral model is also being extended by including multiple species whose dynamics is expected to become important in the detached regimes required to safely operate fusion power plants [41]. Finally, we remind that the use of a fluid model is limited to the study of high collisional plasma. Therefore, its applicability is questionable in the hot boundary of an H-mode plasma, where kinetic effects are expected to play an important role. For this reason, kinetic effects will be included in the GBS plasma model by adding further moments of the electron and ion distribution functions [64, 102]. Ultimately, this will allow the exploration of the boundary turbulent regimes with a more reliable model.

Bibliography

[1] J. W. Ahn, G. F. Counsell, and A. Kirk. L-mode SOL width scaling in the MAST spherical tokamak. *Plasma Physics and Controlled Fusion*, 48(8):1077, 2006.

[2] P. R. Amestoy, A. Buttari, J.-Y. L'Excellent, and T. Mary. Performance and scalability of the block low-rank multifrontal factorization on multicore architectures. *ACM Transactions on Mathematical Software (TOMS)*, 45(1):1, 2019.

[3] G. Y. Antar, S. I. Krasheninnikov, P. Devynck, R. P. Doerner, E. M. Hollmann, J. A. Boedo, S. C. Luckhardt, and R. W. Conn. Experimental evidence of intermittent convection in the edge of magnetic confinement devices. *Physical Review Letters*, 87(6):065001, 2001.

[4] J. F. Artaud, F. Imbeaux, J. Garcia, G. Giruzzi, T. Aniel, V. Basiuk, A. Bécoulet, C. Bourdelle, Y. Buravand, J. Decker, et al. METIS: a fast integrated tokamak modelling tool for scenario design. *Nuclear Fusion*, 58(10):105001, 2018.

[5] N. Asakura, K. Shinya, K. Tobita, K. Hoshino, et al. Investigation of advanced divertor magnetic configuration for demo tokamak reactor. *Fusion Science and Technology*, 63(1T):70, 2013.

[6] ASDEX Team. The H-Mode of ASDEX. *Nuclear Fusion*, 29(11):1959, 1989.

[7] F. Avino, A. Fasoli, I. Furno, P. Ricci, and C. Theiler. X-point effect on plasma blob dynamics. *Physical Review Letters*, 116(10):105001, 2016.

[8] R. Aymar, P. Barabaschi, and Y. Shimomura. The ITER design. *Plasma Physics and Controlled Fusion*, 44(5):519, 2002.

[9] S. Balay, S. Abhyankar, M. F. Adams, J. Brown, P. Brune, K. Buschelman, L. Dalcin, A. Dener, V. Eijkhout, W. D. Grop, D. Karpeyev, D. Kaushik, M. G. Knepley, D. A. May, L. C. McInnes, et al. PETSc Web page. https://www.mcs.anl.gov/petsc, 2019.

[10] C. F. Beadle and P. Ricci. Understanding the turbulent mechanisms setting the density decay length in the tokamak scrape-off layer. *Journal of Plasma Physics*, 86(1):175860101, 2020.

[11] M. G. Bell, G. L. Schmidt, P. C. Efthimion, B. Grek, R. A. Hulse, D. K. Owens, H. K. Park, A. T. Ramsey, J. F. Schivell, and G. Taylor. Attainment of high plasma densities in TFTR with injection of multiple deuterium pellets. *Nuclear Fusion*, 32(9):1585, 1992.

[12] A. Bencze, M. Berta, A. Buzás, P. Hacek, J. Krbec, M. Szutyányi, COMPASS Team, et al. Characterization of edge and scrape-off layer fluctuations using the fast Li-BES system on COMPASS. *Plasma Physics and Controlled Fusion*, 61(8):085014, 2019.

[13] M. Bernert, T. Eich, A. Kallenbach, D. Carralero, A. Huber, P. T. Lang, S. Potzel, et al. The H-mode density limit in the full tungsten ASDEX Upgrade tokamak. *Plasma Physics and Controlled Fusion*, 57(1):014038, 2014.

[14] M. N. A. Beurskens, T. H. Osborne, P. A. Schneider, E. Wolfrum, L. Frassinetti, et al. H-mode pedestal scaling in DIII-D, ASDEX Upgrade, and JET. *Physics of Plasmas*, 18(5):056120, 2011.

[15] N. Bisai, A. Das, S. Deshpande, R. Jha, P. Kaw, A. Sen, and R. Singh. Edge and scrape-off layer tokamak plasma turbulence simulation using two-field fluid model. *Physics of Plasmas*, 12(7):072520, 2005.

[16] D. Biskamp. *Nonlinear magnetohydrodynamics*, volume 1. Cambridge university press, 1997.

[17] K. Bodi, G. Ciraolo, Ph. Ghendrih, F. Schwander, E. Serre, and P. Tamain. Impact of the Boussinesq approximation in tokamak scrape–off layer turbulence. In *38th EPS Conference on Plasma Physics P1.121*, 2011.

[18] J. A. Boedo. Edge turbulence and SOL transport in tokamaks. *Journal of Nuclear Materials*, 390:29, 2009.

[19] J. A. Boedo, N. Crocker, L. Chousal, R. Hernandez, J. Chalfant, H. Kugel, P. Roney, J. Wertenbaker, and NSTX Team. Fast scanning probe for the NSTX spherical tokamak. *Review of Scientific Instruments*, 80(12):123506, 2009.

[20] J. A. Boedo, J. S. DeGrassie, B. Grierson, T. Stoltzfus-Dueck, D. J. Battaglia, et al. Experimental evidence of edge intrinsic momentum source driven by kinetic ion loss and edge radial electric fields in tokamaks. *Physics of Plasmas*, 23(9):092506, 2016.

[21] J. A. Boedo, D. Rudakov, R. Moyer, S. Krasheninnikov, D. Whyte, G. McKee, G. Tynan, et al. Transport by intermittent convection in the boundary of the diii-d tokamak. *Physics of Plasmas*, 8(11):4826, 2001.

[22] J. A. Boedo, D. L. Rudakov, R. A. Moyer, G. R. McKee, R. J. Colchin, M. J. Schaffer, P. G. Stangeby, W. P. West, S. L. Allen, T. E. Evans, et al. Transport by intermittency in the boundary of the DIII-D tokamak. *Physics of Plasmas*, 10(5):1670, 2003.

[23] S. I. Braginskii. Transport processes in a plasma. *Reviews of Plasma Physics*, 1, 1965.

[24] D. Brunner, B. LaBombard, A. Q. Kuang, and J. L. Terry. High-resolution heat flux width measurements at reactor-level magnetic fields and observation of a unified width scaling across confinement regimes in the Alcator C-Mod tokamak. *Nuclear Fusion*, 58(9):094002, 2018.

[25] K. H. Burrell. Effects of E× B velocity shear and magnetic shear on turbulence and transport in magnetic confinement devices. *Physics of Plasmas*, 4(5):1499, 1997.

[26] G.P. Canal, T. Lunt, H. Reimerdes, B.P. Duval, B. Labit, and W.A.J. Vijvers. Enhanced $E \times B$ drift effects in the TCV snowflake divertor. *Nuclear Fusion*, 55(12):123023, 2015.

[27] D. Carralero, S. Artene, M. Bernert, G. Birkenmeier, M. Faitsch, P. Manz, P. de Marne, U. Stroth, M. Wischmeier, E. Wolfrum, et al. On the role of filaments in perpendicular heat transport at the scrape-off layer. *Nuclear Fusion*, 58(9):096015, 2018.

[28] D. Carralero, M. Siccinio, M. Komm, S. A. Artene, F. A. D'isa, J. Adamek, L. Aho-Mantila, G. Birkenmeier, M. Brix, G. Fuchert, et al. Recent progress towards a quantitative description of filamentary SOL transport. *Nuclear Fusion*, 57(5):056044, 2017.

[29] B. A. Carreras, P. H. Diamond, and G. Vetoulis. Role of neutrals in the phase transition model. *Physics of Plasmas*, 3(11):4106, 1996.

[30] T. A. Carter. Intermittent turbulence and turbulent structures in a linear magnetized plasma. *Physics of Plasmas*, 13(1):010701, 2006.

[31] C. S. Chang, S. Ku, P. H. Diamond, Z. Lin, et al. Compressed ion temperature gradient turbulence in diverted tokamak edge. *Physics of Plasmas*, 16(5):056108, 2009.

[32] C. S. Chang, S. Ku, A. Loarte, V. Parail, F. Koechl, M. Romanelli, R. Maingi, J.-W. Ahn, T. Gray, J. Hughes, et al. Gyrokinetic projection of the divertor heat-flux width from present tokamaks to ITER. *Nuclear Fusion*, 57(11):116023, 2017.

[33] L. Chôné, P. Beyer, Y. Sarazin, G. Fuhr, C. Bourdelle, and S. Benkadda. LH transition dynamics in fluid turbulence simulations with neoclassical force balance. *Physics of Plasmas*, 21(7):070702, 2014.

[34] L. Chôné, P. Beyer, Y. Sarazin, G. Fuhr, C. Bourdelle, and S. Benkadda. Mechanisms and dynamics of the external transport barrier formation in non-linear plasma edge simulations. *Nuclear Fusion*, 55(7):073010, 2015.

[35] L. Chôné, T. P. Kiviniemi, S. Leerink, P. Niskala, and R. Rochford. Improved boundary condition for full-f gyrokinetic simulations of circular-limited tokamak plasmas in ELMFIRE. *Contributions to Plasma Physics*, 58(6-8):534, 2018.

[36] S. Chu, Y. Cui, and N. Liu. The path towards sustainable energy. *Nature Materials*, 16(1):16, 2017.

[37] R. M. Churchill, C. S. Chang, S. Ku, and J. Dominski. Pedestal and edge electrostatic turbulence characteristics from an XGC1 gyrokinetic simulation. *Plasma Physics and Controlled Fusion*, 59(10):105014, 2017.

[38] G. Cima, R. V. Bravenec, A. J. Wootton, T. D. Rempel, R. F. Gandy, C. Watts, and M. Kwon. Core temperature fluctuations and related heat transport in the Texas Experimental Tokamak-Upgrade. *Physics of Plasmas*, 2(3):720, 1995.

[39] G. M. Contessa, L. Affinito, M. Angelone, M. Guardati, S. Sandri, and R. Villari. DTT-Divertor Tokamak Test facility-Interim Design Report, 2019.

[40] J. G. Cordey, K. Thomsen, A. Chudnovskiy, O. J. W. F. Kardaun, T. Takizuka, et al. Scaling of the energy confinement time with β and collisionality approaching ITER conditions. *Nuclear fusion*, 45(9):1078, 2005.

[41] A. Coroado and P. Ricci. A self-consistent multi-component model of plasma turbulence and kinetic neutral dynamics for the simulation of the tokamak boundary. *arXiv preprint arXiv:2110.13335*, 2021.

[42] G. De Dominici, G. Fuhr, P. Beyer, C. Bourdelle, L. Chôné, et al. Flux driven pedestal formation in tokamaks: turbulence simulations validated against the isotope effect. *arXiv preprint arXiv:1912.09792*, 2019.

[43] D. Dickinson, C. M. Roach, S. Saarelma, R. Scannell, A. Kirk, and H. R. Wilson. Kinetic instabilities that limit β in the edge of a tokamak plasma: a picture of an H-mode pedestal. *Physical Review Letters*, 108(13):135002, 2012.

[44] G. Dif-pradalier, E. Caschera, P. Ghendrih, P. Donnel, et al. Evidence for Global Edge – Core Interplay in Fusion Plasmas. *Plasma Fusion Res.*, 12:1203012, 2017.

[45] M. Dorf and M. Dorr. Progress with the 5D full-F continuum gyrokinetic code COGENT. *Contributions to Plasma Physics*, page e201900113, 2020.

[46] J. F. Drake, Y. T. Lau, P. N. Guzdar, A. B. Hassam, S. V. Novakovski, et al. Local negative shear and the formation of transport barriers. *Physical Review Letters*, 77(3):494, 1996.

[47] B. D. Dudson, A. Allen, G. Breyiannis, E. Brugger, et al. BOUT++: Recent and current developments. *Journal of Plasma Physics*, 81(1):365810104, 2015.

[48] D. A. D'Ippolito, J. R. Myra, and S. J. Zweben. Convective transport by intermittent blob-filaments: Comparison of theory and experiment. *Physics of Plasmas*, 18(6):060501, 2011.

[49] T. Eich, A. W. Leonard, R. A. Pitts, W. Fundamenski, R. J. Goldston, T. K. Gray, A. Herrmann, A. Kirk, A. Kallenbach, O. Kardaun, et al. Scaling of the tokamak near the scrape-off layer H-mode power width and implications for ITER. *Nuclear Fusion*, 53(9):093031, 2013.

[50] T. Eich and P. Manz. The separatrix operational space of asdex upgrade due to interchange-drift-alfvén turbulence. *Nuclear Fusion*, 61(8):086017, 2021.

[51] T. Eich, P. Manz, R. J. Goldston, P. Hennequin, P. David, M. Faitsch, B. Kurzan, B. Sieglin, E. Wolfrum, et al. Turbulence driven widening of the near-SOL power width in ASDEX Upgrade H-Mode discharges. *Nuclear Fusion*, 60(5):056016, 2020.

[52] T. Eich, B. Sieglin, A. Scarabosio, W. Fundamenski, R. J. Goldston, and A. Herrmann. Inter-ELM Power Decay Length for JET and ASDEX Upgrade: Measurement and Comparison with Heuristic Drift-Based Model. *Physical Review Letters*, 107:215001, 2011.

[53] B. Esposito, G. Granucci, P. Smeulders, S. Nowak, J. R. Martin-Solis, L. Gabellieri, et al. Disruption avoidance in the Frascati Tokamak Upgrade by means of magnetohydrodynamic mode stabilization using electron-cyclotron-resonance heating. *Physical Review Letters*, 100(4):045006, 2008.

[54] M. Faitsch, T. Eich, B. Sieglin, and JET Contributors. Correlation between near scrape-off layer power fall-off length and confinement properties in JET operated with carbon and ITER-like wall. *Plasma Physics and Controlled Fusion*, 62(8):085004, 2020.

[55] M. Faitsch, R. Maurizio, A. Gallo, S. Coda, T. Eich, B. Labit, A. Merle, H. Reimerdes, B. Sieglin, C. Theiler, et al. Dependence of the L-Mode scrape-off layer power fall-off length on the upper triangularity in TCV. *Plasma Physics and Controlled Fusion*, 60(4):045010, 2018.

[56] R. D Falgout and U. M. Yang. hypre: A library of high performance preconditioners. In *International Conference on Computational Science*, page 632. Springer, 2002.

[57] A. Fasoli, B. Labit, M. McGrath, S. H. Müller, G. Plyushchev, M. Podestà, and F. M. Poli. Electrostatic turbulence and transport in a simple magnetized plasma. *Physics of Plasmas*, 13(5):055902, 2006.

[58] G. Federici, R. Kemp, D. Ward, C. Bachmann, T. Franke, S. Gonzalez, C. Lowry, et al. Overview of EU DEMO design and R&D activities. *Fusion Engineering and Design*, 89(7-8):882, 2014.

[59] N. Fedorczak, M. Peret, H. Bufferand, G. Ciraolo, Ph. Ghendrih, and P. Tamain. A spectral filament model for turbulent transport and scrape off layer width in circular geometry. *Nuclear Materials and Energy*, 19:433, 2019.

[60] M. Fichtmüller, G. Corrigan, R. Simonini, and JET Joint Undertaking. Core-Edge Coupling and the Effect of the Edge on Overall Plasma Peformance. *Czechoslovak Journal of Physics*, 48:25, 1998.

[61] S. J. Fielding, J. Hugill, G. M. McCracken, J. W. M. Paul, et al. High-density discharges with gettered torus walls in DITE. *Nuclear Fusion*, 17(6):1382, 1977.

[62] M. Francisquez, B. Zhu, and B. N. Rogers. Global 3D Braginskii simulations of the tokamak edge region of IWL discharges. *Nuclear Fusion*, 57(11):116049, 2017.

[63] S. J. Freethy, G. D. Conway, I. Classen, A. J. Creely, T. Happel, A. Köhn, B. Vanovac, and A. E. White. Measurement of turbulent electron temperature fluctuations on the ASDEX Upgrade tokamak using correlated electron cyclotron emission. *Review of Scientific Instruments*, 87(11):11E102, 2016.

[64] B. J. Frei, R. Jorge, and P. Ricci. A gyrokinetic model for the plasma periphery of tokamak devices. *Journal of Plasma Physics*, 86(2):905860205, 2020.

[65] J. P. Freidberg. *Plasma Physics and Fusion Energy.* Cambridge University Press, 2008.

[66] D. Frigione, L. Pieroni, V. Zanza, G. M. Apruzzese, F. Alladio, M. L. Apicella, R. Bartiromo, M. Borra, G. Bracco, G. Buceti, et al. High density operation on Frascati tokamak upgrade. *Nuclear Fusion*, 36(11):1489, 1996.

[67] I. Furno, B. Labit, M. Podestà, A. Fasoli, S. H. Müller, F. M. Poli, P. Ricci, C. Theiler, S. Brunner, A. Diallo, et al. Experimental observation of the blob-generation mechanism from interchange waves in a plasma. *Physical Review Letters*, 100(5):055004, 2008.

[68] D. Galassi, C. Theiler, T. Body, F. Manke, P. Micheletti, J. Omotani, et al. Validation of edge turbulence codes in a magnetic X-point scenario in TORPEX. *Accepted for publication in Physics of Plasmas*, 2021.

[69] A. Gallo, N. Fedorczak, S. Elmore, R. Maurizio, H. Reimerdes, C. Theiler, C. K. Tsui, J. A. Boedo, M. Faitsch, H. Bufferand, et al. Impact of the plasma geometry on divertor power exhaust: experimental evidence from TCV and simulations with SolEdge2D and TOKAM3X. *Plasma Physics and Controlled Fusion*, 60(1):014007, 2017.

[70] D. A. Gates and L Delgado-Aparicio. Origin of tokamak density limit scalings. *Physical Review Letters*, 108(16):165004, 2012.

[71] W. Gekelman, H. Pfister, Z. Lucky, J. Bamber, D. Leneman, and J. Maggs. Design, construction, and properties of the large plasma research device- The LAPD at UCLA. *Review of Scientific Instruments*, 62(12):2875, 1991.

[72] M. Giacomin and P. Ricci. Investigation of turbulent transport regimes in the tokamak edge by using two-fluid simulations. *Journal of Plasma Physics*, 86(5):905860502, 2020.

[73] M. Giacomin, P. Ricci, A. Coroado, G. Fourestey, D. Galassi, E. Lanti, D. Mancini, N. Richart, L. N. Stenger, and N. Varini. The GBS code for the self-consistent simulation of plasma turbulence and kinetic neutral dynamics in the tokamak boundary. *Submitted to Journal of Computational Physics*, 2021, http://arxiv.org/abs/2112.03573.

[74] M. Giacomin, A. Stagni, P. Ricci, J. A. Boedo, J. Horacek, H. Reimerdes, and C. K. Tsui. Theory-based scaling laws of near and far scrape-off layer widths in single-null L-mode discharges. *Nuclear Fusion*, 61(7):076002, 2021.

[75] M. Giacomin, L. N. Stenger, and P. Ricci. Turbulence and flows in the plasma boundary of snowflake magnetic configurations. *Nuclear Fusion*, 60(2):024001, 2020.

[76] G. Giruzzi, M. Yoshida, J. F. Artaud, Ö. Asztalos, E. Barbato, P. Bettini, A. Bierwage, A. Boboc, T. Bolzonella, S. Clement-Lorenzo, et al. Physics and operation oriented activities in preparation of the JT-60SA tokamak exploitation. *Nuclear Fusion*, 57(8):085001, 2017.

[77] R. J. Goldston. Heuristic drift-based model of the power scrape-off width in low-gas-puff H-mode tokamaks. *Nuclear Fusion*, 52(1):013009, 2011.

[78] B. Goncalves, C. Hidalgo, C. Silva, M. A. Pedrosa, and K. Erents. Statistical description of the radial structure of turbulence in the JET plasma boundary region. *Journal of Nuclear Materials*, 337:376, 2005.

[79] M. Greenwald. Density limits in toroidal plasmas. *Plasma Physics and Controlled Fusion*, 44(8):R27, 2002.

[80] M. Greenwald, J. L. Terry, S. M. Wolfe, S. Ejima, et al. A new look at density limits in tokamaks. *Nuclear Fusion*, 28(12):2199, 1988.

[81] G. Grenfell, B. Ph. van Milligen, U. Losada, T. Estrada, et al. The impact of edge radial electric fields on edge–scrape-off layer coupling in the TJ-II stellarator. *Nuclear Fusion*, 60(1):014001, 2019.

[82] R. J. Groebner, K. H. Burrell, and R. P. Seraydarian. Role of edge electric field and poloidal rotation in the L-H transition. *Physical Review Letters*, 64(25):3015, 1990.

[83] O. Gruber, V. Mertens, J. Neuhauser, F. Ryter, W. Suttrop, M. Albrecht, M. Alexander, K. Asmussen, G. Becker, K. Behler, et al. Divertor tokamak operation at high densities on ASDEX Upgrade. *Plasma Physics and Controlled Fusion*, 39(12B):B19, 1997.

[84] T. S. Hahm, L. Wang, and J. Madsen. Fully electromagnetic nonlinear gyrokinetic equations for tokamak edge turbulence. *Physics of Plasmas*, 16(2):022305, 2009.

[85] R. J. Hajjar, P. H. Diamond, and M. A. Malkov. Dynamics of zonal shear collapse with hydrodynamic electrons. *Physics of Plasmas*, 25(6):062306, 2018.

[86] F. D. Halpern, S. Jolliet, J. Loizu, A. Mosetto, and P. Ricci. Ideal ballooning modes in the tokamak scrape-off layer. *Physics of Plasmas*, 20(5):052306, 2013.

[87] F. D. Halpern, P. Ricci, S. Jolliet, J. Loizu, J. Morales, et al. The GBS code for tokamak scrape-off layer simulations. *Journal of Computational Physics*, 315:388, 2016.

[88] F. D. Halpern, P. Ricci, S. Jolliet, J. Loizu, and A. Mosetto. Theory of the scrape-off layer width in inner-wall limited tokamak plasmas. *Nuclear Fusion*, 54(4):043003, 2014.

[89] F. D. Halpern, P. Ricci, B. Labit, I. Furno, S. Jolliet, et al. Theory-based scaling of the SOL width in circular limited tokamak plasmas. *Nuclear Fusion*, 53(12):122001, 2013.

[90] F. L. Hinton. Thermal confinement bifurcation and the L- to H-mode transition in tokamaks. *Physics of Fluids B: Plasma Physics*, 3(3):696, 1991.

[91] J. Hinz, M. Möller, and C. Vuik. Elliptic grid generation techniques in the framework of isogeometric analysis applications. *Computer Aided Geometric Design*, 65:48, 2018.

[92] R. Hong, G. R. Tynan, P. H. Diamond, L. Nie, et al. Edge shear flows and particle transport near the density limit of the HL-2A tokamak. *Nuclear Fusion*, 58(1):016041, 2017.

[93] J. Horacek, J. Adamek, M. Komm, J. Seidl, P. Vondracek, A. Jardin, Ch. Guillemaut, et al. Scaling of L-mode heat flux for ITER and COMPASS-U divertors, based on five tokamaks. *Nuclear Fusion*, 60(6):066016, 2020.

[94] J. Horacek, R. A. Pitts, J. Adamek, G. Arnoux, J. G. Bak, S. Brezinsek, M. Dimitrova, et al. Multi-machine scaling of the main sol parallel heat flux width in tokamak limiter plasmas. *Plasma Physics and Controlled Fusion*, 58(7):074005, 2016.

[95] J. Horacek, R. A. Pitts, and J. P. Graves. Overview of edge electrostatic turbulence experiments on TCV. *Czechoslovak Journal of Physics*, 55(3):271, 2005.

[96] J. Horacek, P. Vondracek, R. Panek, R. Dejarnac, M. Komm, R. A. Pitts, M. Kocan, R. J. Goldston, P. C. Stangeby, E. Gauthier, et al. Narrow heat flux channels in the compass limiter scrape-off layer. *Journal of Nuclear Materials*, 463:385, 2015.

[97] T. A. Howson, I. De Moortel, and P. Antolin. The effects of resistivity and viscosity on the kelvin-helmholtz instability in oscillating coronal loops. *Astronomy & Astrophysics*, 602:A74, 2017.

[98] A. Huber, S. Brezinsek, M. Groth, P. C. De Vries, V. Riccardo, G. Van Rooij, G. Sergienko, G. Arnoux, A. Boboc, P. Bilkova, et al. Impact of the ITER-like wall on divertor detachment and on the density limit in the JET tokamak. *Journal of Nuclear Materials*, 438:S139, 2013.

[99] A. Iiyoshi, A. Komori, A. Ejiri, M. Emoto, H. Funaba, et al. Overview of the large helical device project. *Nuclear Fusion*, 39(9Y):1245, 1999.

[100] J. Jacquinot. Fifty years in fusion and the way forward. *Nuclear Fusion*, 50(1):014001, 2009.

[101] F. Jenko and W. Dorland. Nonlinear electromagnetic gyrokinetic simulations of tokamak plasmas. *Plasma Physics and Controlled Fusion*, 43(12A):A141, 2001.

[102] R. Jorge, P. Ricci, and N. F. Loureiro. A drift-kinetic analytical model for scrape-off layer plasma dynamics at arbitrary collisionality. *Journal of Plasma Physics*, 83(6), 2017.

[103] N. Katz, J. Egedal, W. Fox, A. Le, and M. Porkolab. Experiments on the propagation of plasma filaments. *Physical Review Letters*, 101(1):015003, 2008.

[104] N. A. Kirneva, R. Behn, G. P. Canal, S. Coda, B. P. Duval, et al. High density experiments in TCV ohmically heated and L-mode plasmas. *Plasma Physics and Controlled Fusion*, 57(2):025002, 2014.

[105] T. Klinger, T. Andreeva, S. Bozhenkov, C. Brandt, R. Burhenn, B. Buttenschön, et al. Overview of first Wendelstein 7-X high-performance operation. *Nuclear Fusion*, 59(11):112004, 2019.

[106] S. Ku, C. S. Chang, R. Hager, R. M. Churchill, G. R. Tynan, et al. A fast low-to-high confinement mode bifurcation dynamics in the boundary-plasma gyrokinetic code XGC1. *Physics of Plasmas*, 25(5):056107, 2018.

[107] A. Q. Kuang, B. LaBombard, D. Brunner, O. E. Garcia, R. Kube, and A. Theodorsen. Plasma fluctuations in the scrape-off layer and at the divertor target in Alcator C-Mod and their relationship to divertor collisionality and density shoulder formation. *Nuclear Materials and Energy*, 19:295, 2019.

[108] R. Kube, O. E. Garcia, B. LaBombard, J. L. Terry, and S. J. Zweben. Blob sizes and velocities in the Alcator C-Mod scrape-off layer. *Journal of Nuclear Materials*, 438:S505, 2013.

[109] R. Kube, Odd Erik Garcia, Audun Theodorsen, Daniel Brunner, A.Q. Kuang, Brian LaBombard, and James L. Terry. Intermittent electron density and temperature fluctuations and associated fluxes in the Alcator C-Mod scrape-off layer. *Plasma Physics and Controlled Fusion*, 60(6):065002, 2018.

[110] B. Labit, G. P. Canal, N. Christen, B. P. Duval, B. Lipschultz, T. Lunt, F. Nespoli, H. Reimerdes, et al. Experimental studies of the snowflake divertor in TCV. *Nuclear Materials and Energy*, 12:1015, 2017.

[111] B. LaBombard, R. L. Boivin, M. Greenwald, J. Hughes, B. Lipschultz, et al. Particle transport in the scrape-off layer and its relationship to discharge density limit in Alcator C-Mod. *Physics of Plasmas*, 8(5):2107, 2001.

[112] B. LaBombard, J. W. Hughes, D. Mossessian, M. Greenwald, B. Lipschultz, et al. Evidence for electromagnetic fluid drift turbulence controlling the edge plasma state in the Alcator C-Mod tokamak. *Nuclear Fusion*, 45(12):1658, 2005.

[113] B. LaBombard, J. E. Rice, A. E. Hubbard, J. W. Hughes, M. Greenwald, et al. Transport-driven Scrape-Off-Layer flows and the boundary conditions imposed at the magnetic separatrix in a tokamak plasma. *Nuclear Fusion*, 44(10):1047, 2004.

[114] P. T. Lang, C. Angioni, M. Bernert, A. Bock, T. M. J. Engelhardt, R. Fischer, O. J. W. F. Kardaun, B. Ploeckl, M. Prechtl, W. Suttrop, et al. H-mode confinement in the pellet-enforced high-density regime of the all-metal-wall tokamak ASDEX Upgrade. *Nuclear Fusion*, 60(9):092003, 2020.

[115] J. D. Lawson. Some criteria for a power producing thermonuclear reactor. *Proceedings of the Physical Society. Section B*, 70(1):6, 1957.

[116] B. Li, B. N. Rogers, P. Ricci, and K. W. Gentle. Plasma transport and turbulence in the Helimak: Simulation and experiment. *Physics of Plasmas*, 16(8):082510, 2009.

[117] Z.-Y. Li, X.-Q. Xu, N.-M. Li, V. S. Chan, and X.-G. Wang. Prediction of divertor heat flux width for ITER using BOUT++ transport and turbulence module. *Nuclear Fusion*, 59(4):046014, 2019.

[118] B. Lipschultz. Review of MARFE phenomena in tokamaks. *Journal of Nuclear Materials*, 145:15, 1987.

[119] B. Lipschultz, B. LaBombard, E. S. Marmar, M. M. Pickrell, J. L. Terry, R. Watterson, and S. M. Wolfe. Marfe: an edge plasma phenomenon. *Nuclear Fusion*, 24(8):977, 1984.

[120] A. Loarte, S. Bosch, A. Chankin, S. Clement, A. Herrmann, D. Hill, K. Itami, J. Lingertat, B. Lipschultz, K. McCormick, et al. Multi-machine scaling of the divertor peak heat flux and width for L-mode and H-mode discharges. *Journal of Nuclear Materials*, 266:587, 1999.

[121] A. Loarte, B. Lipschultz, A.S Kukushkin, G.F Matthews, et al. Chapter 4: Power and particle control. *Nuclear Fusion*, 47(6):S203, 2007.

[122] J. Loizu, J. A. Morales, F. D. Halpern, P. Ricci, and P. Paruta. Scrape-off-layer current loops and floating potential in limited tokamak plasmas. *Journal of Plasma Physics*, 83(6), 2017.

[123] J. Loizu, P. Ricci, F. D. Halpern, and S. Jolliet. Boundary conditions for plasma fluid models at the magnetic presheath entrance. *Physics of Plasmas*, 19(12):122307, 2012.

[124] J. Loizu, P. Ricci, F. D. Halpern, S. Jolliet, and A. Mosetto. On the electrostatic potential in the scrape-off layer of magnetic confinement devices. *Plasma Physics and Controlled Fusion*, 55(12):124019, 2013.

[125] D. Lortz and J. Nührenberg. Ballooning stability boundaries for the large-aspect-ratio tokamak. *Physics Letters A*, 68(1):49, 1978.

[126] T. Lunt, G. P. Canal, B. P. Duval, Y. Feng, B. Labit, P. McCarthy, H. Reimerdes, W. A. J. Vijvers, and M. Wischmeier. Numerical study of potential heat flux mitigation effects in the tcv snowflake divertor. *Plasma Physics and Controlled Fusion*, 58(4):045027, 2016.

[127] T. Lunt, G. P. Canal, Y. Feng, H. Reimerdes, B. P. Duval, B. Labit, W. A. J. Vijvers, D. Coster, K. Lackner, and M. Wischmeier. First EMC3-Eirene simulations of the TCV snowflake divertor. *Plasma Physics and Controlled Fusion*, 56(3):035009, 2014.

[128] C. F. Maggi, H. Weisen, J. C. Hillesheim, A. Chankin, E. Delabie, et al. Isotope effects on LH threshold and confinement in tokamak plasmas. *Plasma Physics and Controlled Fusion*, 60(1):014045, 2017.

[129] D. Mancini, P. Ricci, N. Vianello, M. Giacomin, and A. Coroado. Investigation of the density shoulder formation by using self-consistent simulations of plasma turbulence and neutral kinetic dynamics. *Nuclear Fusion*, 61(12):126029, 2021.

[130] N. R. Mandell, A. Hakim, G. W. Hammett, and M. Francisquez. Electromagnetic full-f gyrokinetics in the tokamak edge with discontinuous galerkin methods. *Journal of Plasma Physics*, 86(1), 2020.

[131] P. Manz, T. Happel, U. Stroth, T. Eich, D. Silvagni, et al. Physical mechanism behind and access to the i-mode confinement regime in tokamaks. *Nuclear Fusion*, 60(9):096011, 2020.

[132] M. Maraschek, A. Gude, V. Igochine, H. Zohm, E. Alessi, M. Bernert, C. Cianfarani, S. Coda, B. Duval, B. Esposito, et al. Path-oriented early reaction to approaching disruptions in ASDEX Upgrade and TCV in view of the future needs for ITER and DEMO. *Plasma Physics and Controlled Fusion*, 60(1):014047, 2017.

[133] Y. Martin, R. Behn, I. Furno, B. Labit, H. Reimerdes, TCV Team, et al. H-mode access during plasma current ramp-up in TCV. *Nuclear Fusion*, 54(11):114006, 2014.

[134] Y. R. Martin, T. Takizuka, et al. Power requirement for accessing the H-mode in ITER. *Journal of Physics: Conference Series*, 123:012033, 2008.

[135] G. F. Matthews, P. Edwards, T. Hirai, M. Kear, et al. Overview of the iter-like wall project. *Physica Scripta*, 2007(T128):137, 2007.

[136] R. Maurizio, S. Elmore, N. Fedorczak, A. Gallo, H. Reimerdes, B. Labit, C. Theiler, C. K. Tsui, W. A. J. Vijvers, TCV Team, et al. Divertor power load studies for attached L-mode single-null plasmas in TCV. *Nuclear Fusion*, 58(1):016052, 2018.

[137] R. Maurizio, C.K. Tsui, B.P. Duval, H. Reimerdes, C. Theiler, J. Boedo, B. Labit, U. Sheikh, and M. Spolaore. The effect of the secondary x-point on the scrape-off layer transport in the TCV snowflake minus divertor. *Nuclear Fusion*, 59(1):016014, 2019.

[138] R. M. McDermott, B. Lipschultz, J. W. Hughes, P. J. Catto, A. E. Hubbard, et al. Edge radial electric field structure and its connections to H-mode confinement in Alcator C-Mod plasmas. *Physics of Plasmas*, 16(5):056103, 2009.

[139] V. Mertens, W. Junker, M. Laux, M. Schittenhelm, K. Buchl, F. Mast, A. Carlsont, A. Field, C. Fuchs, O. Gehre, et al. Experimental investigation of marfes and the density limit in the ASDEX upgrade. *Plasma Physics and Controlled Fusion*, 36(8):1307, 1994.

[140] V. Mertens, M. Kaufmann, J. Neuhauser, J. Schweinzer, J. Stober, et al. High density operation close to Greenwald limit and H mode limit in ASDEX upgrade. *Nuclear fusion*, 37(11):1607, 1997.

[141] F. Militello, L. Aho-Mantila, R. Ambrosino, T. Body, H. Bufferand, G. Calabro, et al. Preliminary analysis of alternative divertors for DEMO. *Nuclear Materials and Energy*, 26:100908, 2021.

[142] F. Militello, W. Fundamenski, V. Naulin, and A. H. Nielsen. Simulations of edge and scrape off layer turbulence in mega ampere spherical tokamak plasmas. *Plasma Physics and Controlled Fusion*, 54(9):095011, 2012.

[143] F. Militello, V. Naulin, and A. H. Nielsen. Numerical scalings of the decay lengths in the scrape-off layer. *Plasma Physics and Controlled Fusion*, 55(7):074010, 2013.

[144] F. Militello and J. T. Omotani. On the relation between non-exponential scrape off layer profiles and the dynamics of filaments. *Plasma Physics and Controlled Fusion*, 58(12):125004, 2016.

[145] F. Militello and J. T. Omotani. Scrape off layer profiles interpreted with filament dynamics. *Nuclear Fusion*, 56(10):104004, 2016.

[146] G. H. Miller, E. I. Moses, and C. R. Wuest. The national ignition facility: enabling fusion ignition for the 21st century. *Nuclear Fusion*, 44(12):S228, 2004.

[147] A. Mosetto, F. D. Halpern, S. Jolliet, J. Loizu, and P. Ricci. Turbulent regimes in the tokamak scrape-off layer. *Physics of Plasmas*, 20(9):092308, 2013.

[148] A. Mosetto, F. D. Halpern, S. Jolliet, J. Loizu, and P. Ricci. Finite ion temperature effects on scrape-off layer turbulence. *Physics of Plasmas*, 22(1):012308, 2015.

[149] V. Mukhovatov, M. Shimada, A. N. Chudnovskiy, A. E. Costley, Y. Gribov, G. Federici, et al. Overview of physics basis for ITER. *Plasma physics and controlled fusion*, 45(12A):A235, 2003.

[150] J. R. Myra, D. A. D'Ippolito, D. A. Russell, M. V. Umansky, and D. A. Baver. Analytical and numerical study of the transverse Kelvin–Helmholtz instability in tokamak edge plasmas. *Journal of Plasma Physics*, 82(2), 2016.

[151] J. R. Myra, D. A. Russell, and D. A. D'Ippolito. Collisionality and magnetic geometry effects on tokamak edge turbulent transport. I. A two-region model with application to blobs. *Physics of Plasmas*, 13(11):112502, 2006.

[152] F. Nespoli, I. Furno, B. Labit, P. Ricci, F. Avino, et al. Blob properties in full-turbulence simulations of the TCV scrape-off layer. *Plasma Physics and Controlled Fusion*, 59(5):055009, 2017.

[153] F. Nespoli, B. Labit, I. Furno, J. Horacek, C. K. Tsui, J. A. Boedo, R. Maurizio, H. Reimerdes, C. Theiler, P. Ricci, et al. Understanding and suppressing the near scrape-off layer heat flux feature in inboard-limited plasmas in TCV. *Nuclear Fusion*, 57(12):126029, 2017.

[154] A.H. Nielsen, G.S. Xu, J. Madsen, V. Naulin, J. Juul Rasmussen, and B.N. Wan. Simulation of transition dynamics to high confinement in fusion plasmas. *Physics Letters A*, 379(47-48):3097, 2015.

[155] D. S. Oliveira, Body. T., et al. Validation of edge turbulence codes against the TCV-X21 diverted L-mode reference case. *Submitted to Nuclear Fusion*, 2021.

[156] L. W. Owen, B. A. Carreras, R. Maingi, P. K. Mioduszewski, T. N. Carlstrom, and R. J. Groebner. Assessment of effects of neutrals on the power threshold for LH transitions in DIII-D. *Plasma Physics and Controlled Fusion*, 40(5):717, 1998.

[157] Q. Pan, D. Told, E. L. Shi, G. W. Hammett, and F. Jenko. Full- f version of GENE for turbulence in open-field-line systems. *Physics of Plasmas*, 25(6):062303, 2018.

[158] R. Panek, T. Markovic, P. Cahyna, R. Dejarnac, J. Havlicek, J. Horacek, M. Hron, M. Imrisek, P. Junek, M. Komm, et al. Conceptual design of the compass upgrade tokamak. *Fusion Engineering and Design*, 123:11, 2017.

[159] P. Paruta, C. Beadle, P. Ricci, and C. Theiler. Blob velocity scaling in diverted tokamaks: A comparison between theory and simulation. *Physics of Plasmas*, 26(3):032302, 2019.

[160] P. Paruta, P. Ricci, F. Riva, C. Wersal, C. Beadle, and B. Frei. Simulation of plasma turbulence in the periphery of diverted tokamak by using the GBS code. *Physics of Plasmas*, 25(11):112301, 2018.

[161] S. V. Patnakar. Numerical heat transfer and fluid flow, 1980.

[162] J. L. Peterson and G. W. Hammett. Positivity preservation and advection algorithms with applications to edge plasma turbulence. *SIAM Journal on Scientific Computing*, 35(3):B576, 2013.

[163] F. Piras, S. Coda, B. P. Duval, B. Labit, J. Marki, S. Yu Medvedev, J.-M. Moret, A. Pitzschke, and O. Sauter. “Snowflake” H Mode in a Tokamak Plasma. *Physical Review Letters*, 105(15):155003, 2010.

[164] R. A. Pitts, S. Carpentier, F. Escourbiac, T. Hirai, V. Komarov, S. Lisgo, A. S. Kukushkin, A. Loarte, M. Merola, A. Sashala Naik, et al. A full tungsten divertor for ITER: Physics issues and design status. *Journal of Nuclear Materials*, 438:S48, 2013.

[165] R. A. Pitts, G. Vayakis, G. F. Matthews, and V. A. Vershkov. Poloidal SOL asymmetries and toroidal flow in DITE. *Journal of nuclear materials*, 176:893, 1990.

[166] H. Qin, R.H. Cohen, W.M. Nevins, and X.Q. Xu. Geometric gyrokinetic theory for edge plasmas. *Physics of Plasmas*, 14(5):056110, 2007.

[167] J. Rapp, P. C. De Vries, F. C. Schüller, W. Biel, R. Jaspers, H. R. Koslowski, A. Krämer-Flecken, A. Kreter, M. Lehnen, A. Pospieszczyk, et al. Density limits in TEXTOR-94 auxiliary heated discharges. *Nuclear Fusion*, 39(6):765, 1999.

[168] H. Reimerdes, R. Ambrosino, P. Innocente, A. Castaldo, P. Chmielewski, et al. Assessment of alternative divertor configurations as an exhaust solution for DEMO. *Nuclear Fusion*, 60(6):066030, 2020.

[169] H. Reimerdes, G. P. Canal, B. P. Duval, B. Labit, T. Lunt, W. A. J. Vijvers, S. Coda, G. De Temmerman, T. W. Morgan, F. Nespoli, and B. Tal. Power distribution in the

snowflake divertor in TCV. *Plasma Physics and Controlled Fusion*, 55(12):124027, 2013.

[170] P. Ricci, F. D. Halpern, S. Jolliet, J. Loizu, A. Mosetto, et al. Simulation of plasma turbulence in scrape-off layer conditions: the GBS code, simulation results and code validation. *Plasma Physics and Controlled Fusion*, 54(12):124047, 2012.

[171] P. Ricci and B. N. Rogers. Transport scaling in interchange-driven toroidal plasmas. *Physics of Plasmas*, 16(6):062303, 2009.

[172] P. Ricci and B. N. Rogers. Turbulence phase space in simple magnetized toroidal plasmas. *Physical Review Letters*, 104(14):145001, 2010.

[173] P. Ricci and B. N. Rogers. Plasma turbulence in the scrape-off layer of tokamak devices. *Physics of Plasmas*, 20(1):010702, 2013.

[174] P. Ricci, B. N. Rogers, and S. Brunner. High- and low-confinement modes in simple magnetized toroidal plasmas. *Physical Review Letters*, 100(22):6, 2008.

[175] P. Ricci, C. Theiler, A. Fasoli, I. Furno, K. Gustafson, D. Iraji, and J. Loizu. Methodology for turbulence code validation: Quantification of simulation-experiment agreement and application to the TORPEX experiment. *Physics of Plasmas*, 18(3):032109, 2011.

[176] E. Righi, D. V. Bartlett, J. P. Christiansen, G. D. Conway, J. G. Cordey, et al. Isotope scaling of the H mode power threshold on JET. *Nuclear Fusion*, 39(3):309, 1999.

[177] F. Riva, E. Lanti, S. Jolliet, and P. Ricci. Plasma shaping effects on tokamak scrape-off layer turbulence. *Plasma Physics and Controlled Fusion*, 59(3):035001, 2017.

[178] F. Riva, P. Ricci, F. D. Halpern, S. Jolliet, J. Loizu, and A. Mosetto. Verification methodology for plasma simulations and application to a scrape-off layer turbulence code. *Physics of Plasmas*, 21(6):062301, 2014.

[179] F. Riva, C. K. Tsui, J. A. Boedo, P. Ricci, and TCV Team. Shaping effects on scrape-off layer plasma turbulence: A rigorous validation of three-dimensional simulations against TCV measurements. *Physics of Plasmas*, 27(1):012301, 2020.

[180] B. N. Rogers and W. Dorland. Noncurvature-driven modes in a transport barrier. *Physics of Plasmas*, 12(6):062511, 2005.

[181] B. N. Rogers and J. F. Drake. Enhancement of turbulence in tokamaks by magnetic fluctuations. *Physical Review Letters*, 79(2):229, 1997.

[182] B. N. Rogers, J. F. Drake, and A. Zeiler. Phase space of tokamak edge turbulence, the L- H transition, and the formation of the edge pedestal. *Physical Review Letters*, 81(20):4396, 1998.

[183] B. N. Rogers and P. Ricci. Low-frequency turbulence in a linear magnetized plasma. *Physical Review Letters*, 104(22):225002, 2010.

[184] DL Rudakov, JA Boedo, RA Moyer, Peter C Stangeby, JG Watkins, DG Whyte, L Zeng, NH Brooks, RP Doerner, TE Evans, et al. Far sol transport and main wall plasma interaction in diii-d. *Nuclear fusion*, 45(12):1589, 2005.

[185] D. A. Russell, J. R. Myra, and D. A. D'Ippolito. Collisionality and magnetic geometry effects on tokamak edge turbulent transport. II. Many-blob turbulence in the two-region model. *Physics of Plasmas*, 14(10):102307, 2007.

[186] F. Ryter, M. Cavedon, T. Happel, R.M. McDermott, et al. L-H transition physics in hydrogen and deuterium: key role of the edge radial electric field and ion heat flux. *Plasma Physics and Controlled Fusion*, 58(1):014007, 2015.

[187] F. Ryter, S. K. Rathgeber, L. B. Orte, M. Bernert, G. D. Conway, et al. Survey of the H-mode power threshold and transition physics studies in ASDEX Upgrade. *Nuclear Fusion*, 53(11):113003, 2013.

[188] D. D. Ryutov. Geometrical properties of a "snowflake" divertor. *Physics of Plasmas*, 14(6):064502, 2007.

[189] D. D. Ryutov, R. H. Cohen, W. A. Farmer, T. D. Rognlien, and M. V. Umansky. The 'churning mode' of plasma convection in the tokamak divertor region. *Physica Scripta*, 89(8):088002, 2014.

[190] R. Sánchez, B. Ph. van Milligen, D. E. Newman, and B. A. Carreras. Quiet-time statistics of electrostatic turbulent fluxes from the JET tokamak and the W7-AS and TJ-II stellarators. *Physical Review Letters*, 90(18):185005, 2003.

[191] O. Sauter, S. Brunner, D. Kim, G. Merlo, R. Behn, Y. Camenen, et al. On the non-stiffness of edge transport in l-mode tokamak plasmas. *Physics of Plasmas*, 21(5):055906, 2014.

[192] A. Scaggion, Y. Martin, H. Reimerdes, et al. H-mode access with different X-point height in TCV. In *39th EPS Conference on Plasma Physics 2012, EPS 2012 and the 16th International Congress on Plasma Physics*, 2012.

[193] A. Scarabosio, T. Eich, A. Herrmann, B. Sieglin, JET-EFDA contributors, et al. Outer target heat fluxes and power decay length scaling in L-mode plasmas at JET and AUG. *Journal of Nuclear Materials*, 438:S426, 2013.

[194] M. J. Schaffer, B. D. Bray, J. A. Boedo, T. N. Carlstrom, R. J. Colchin, C. L. Hsieh, R. A. Moyer, G. D. Porter, T. D. Rognlien, and J. G. Watkins. E×B circulation at the tokamak divertor X point. *Physics of Plasmas*, 8(5):2118, 2001.

[195] M.J. Schaffer, J.A. Boedo, R.A. Moyer, T.N. Carlstrom, and J.G. Watkins. Large E×B convection near the divertor X-point. *Journal of Nuclear Materials*, 290-293:530, 2001.

[196] J. Schirmer, G. D. Conway, H. Zohm, W. Suttrop, et al. The radial electric field and its associated shear in the ASDEX Upgrade tokamak. *Nuclear Fusion*, 46(9):S780, 2006.

[197] B. Schmid, P. Manz, M. Ramisch, and U. Stroth. Collisional scaling of the energy transfer in drift-wave zonal flow turbulence. *Physical Review Letters*, 118(5):055001, 2017.

[198] B. Scott. Three-dimensional computation of drift Alfvén turbulence. *Plasma Physics and Controlled Fusion*, 39(10):1635, 1997.

[199] K. C. Shaing and C. T. Hsu. Critical neutral density for high-mode bifurcation in tokamaks. *Physics of Plasmas*, 2(6):1801, 1995.

[200] B. W. Shanahan and B. D. Dudson. Blob dynamics in TORPEX poloidal null configurations. *Plasma Physics and Controlled Fusion*, 58(12):125003, 2016.

[201] U. A. Sheikh, M. Dunne, L. Frassinetti, P. Blanchard, B. P. Duval, B. Labit, et al. Pedestal structure and energy confinement studies on TCV. *Plasma Physics and Controlled Fusion*, 61(1):014002, 2018.

[202] E. L. Shi, G. W. Hammett, T. Stoltzfus-Dueck, and A. Hakim. Gyrokinetic continuum simulation of turbulence in a straight open-field-line plasma. *Journal of Plasma Physics*, 83(3):1, 2017.

[203] B. Sieglin, T. Eich, M. Faitsch, A. Herrmann, A. Scarabosio, et al. Investigation of scrape-off layer and divertor heat transport in ASDEX Upgrade L-mode. *Plasma Physics and Controlled Fusion*, 58(5):055015, 2016.

[204] D. Silvagni, T. Eich, M. Faitsch, T. Happel, B. Sieglin, P. David, et al. Scrape-off layer (SOL) power width scaling and correlation between SOL and pedestal gradients across L, I and H-mode plasmas at ASDEX Upgrade. *Plasma Physics and Controlled Fusion*, 62(4):045015, 2020.

[205] J. A. Snipes, R. L. Boivin, C. Christensen, C. Fiore, D. Garnier, et al. Characteristics of high-confinement modes in Alcator C Mod. *Physics of Plasmas*, 3(5):1992, 1996.

[206] V. A. Soukhanovskii, S. L. Allen, M. E. Fenstermacher, C. J. Lasnier, M. A. Makowski, A. G. McLean, et al. Developing physics basis for the snowflake divertor in the DIII-D tokamak. *Nuclear Fusion*, 58(3):036018, 2018.

[207] V. A. Soukhanovskii, R. E. Bell, A. Diallo, S. Gerhardt, S. Kaye, E. Kolemen, B. P. LeBlanc, et al. Snowflake divertor configuration studies in National Spherical Torus Experiment. *Physics of Plasmas*, 19(8):082504, 2012.

[208] V. A. Soukhanovskii, R. E. Bell, A. Diallo, S. Gerhardt, S. Kaye, E. Kolemen, B.P. LeBlanc, et al. Advanced divertor configurations with large flux expansion. *Journal of Nuclear Materials*, 438:S96, 2013.

[209] L. Spitzer J. Physics of fully ionized gases. *Interscience Tracts on Physics and Astronomy*, 3, 1.

[210] M. Spolaore, V. Antoni, E. Spada, H. Bergsåker, R. Cavazzana, J. R. Drake, E. Martines, G. Regnoli, G. Serianni, and N. Vianello. Vortex-induced diffusivity in reversed field pinch plasmas. *Physical Review Letters*, 93(21):215003, 2004.

[211] P. C. Stangeby. *The plasma boundary of magnetic fusion devices.* CRC Press, 2000.

[212] A. Stegmeir, D. Coster, A. Ross, O. Maj, et al. GRILLIX: a 3D turbulence code based on the flux-coordinate independent approach. *Plasma Physics and Controlled Fusion*, 60(3):035005, 2018.

[213] A. Stegmeir, A. Ross, T. Body, M. Francisquez, W. Zholobenko, D. Coster, O. Maj, P. Manz, F. Jenko, B. N. Rogers, et al. Global turbulence simulations of the tokamak edge region with GRILLIX. *Physics of Plasmas*, 26(5):052517, 2019.

[214] T. Stoltzfus-Dueck. Transport-driven toroidal rotation in the tokamak edge. *Physical Review Letters*, 108(6):065002, 2012.

[215] H. P. Summers, W. J. Dickson, M. G. O'mullane, N. R. Badnell, A. D. Whiteford, D. H. Brooks, J. Lang, S. D. Loch, and D. C. Griffin. Ionization state, excited populations and emission of impurities in dynamic finite density plasmas: I. The generalized collisional–radiative model for light elements. *Plasma Physics and Controlled Fusion*, 48(2):263, 2006.

[216] H. J. Sun, E. Wolfrum, T. Eich, B. Kurzan, S. Potzel, U. Stroth, et al. Study of near scrape-off layer (SOL) temperature and density gradient lengths with Thomson scattering. *Plasma Physics and Controlled Fusion*, 57(12):125011, 2015.

[217] T. Sunn Pedersen, A. Dinklage, Y. Turkin, R. Wolf, et al. Key results from the first plasma operation phase and outlook for future performance in Wendelstein 7-X. *Physics of Plasmas*, 24(5):055503, 2017.

[218] P. Tamain, H. Bufferand, G. Ciraolo, C. Colin, et al. The TOKAM3X code for edge turbulence fluid simulations of tokamak plasmas in versatile magnetic geometries. *Journal of Computational Physics*, 321:606, 2016.

[219] H. Tanaka, N. Ohno, N. Asakura, Y. Tsuji, H. Kawashima, S. Takamura, Y. Uesugi, et al. Statistical analysis of fluctuation characteristics at high-and low-field sides in L-mode SOL plasmas of JT-60U. *Nuclear Fusion*, 49(6):065017, 2009.

[220] P. W. Terry. Suppression of turbulence and transport by sheared flow. *Reviews of Modern Physics*, 72(1):109, 2000.

[221] C. Theiler, I. Furno, P. Ricci, A. Fasoli, B. Labit, S. H. Müller, and G. Plyushchev. Cross-field motion of plasma blobs in an open magnetic field line configuration. *Physical Review Letters*, 103(6):065001, 2009.

[222] D. M. Thomas, R. J. Groebner, K. H. Burrell, T. H. Osborne, and T. N. Carlstrom. The back transition and hysteresis effects in DIII-D. *Plasma Physics and Controlled Fusion*, 40(5):707, 1998.

[223] C. K. Tsui, J. A. Boedo, J. R. Myra, B. Duval, B. Labit, C. Theiler, N. Vianello, W. A. J. Vijvers, H. Reimerdes, S. Coda, et al. Filamentary velocity scaling validation in the TCV tokamak. *Physics of Plasmas*, 25(7):072506, 2018.

[224] M. V. Umansky and D. D. Ryutov. Toroidally symmetric plasma vortex at tokamak divertor null point. *Physics of Plasmas*, 23(3):030701, 2016.

[225] P. J. Vail, O. Izacard, and E. Kolemen. Optimization of the snowflake divertor for power and particle exhaust on NSTX–U. *Nuclear Materials and Energy*, 19:516, 2019.

[226] V. A. Vershkov and S. V. Mirnov. Role of impurities in current tokamak experiments. *Nuclear Fusion*, 14(3):383, 1974.

[227] N. Vianello, D. Carralero, C. K. Tsui, V. Naulin, M. Agostini, I. Cziegler, B. Labit, C. Theiler, E. Wolfrum, D. Aguiam, et al. Scrape-off layer transport and filament characteristics in high-density tokamak regimes. *Nuclear Fusion*, 60(1):016001, 2019.

[228] N. Vianello, C. Tsui, C. Theiler, S. Allan, J. Boedo, B. Labit, H. Reimerdes, K. Verhaegh, et al. Modification of SOL profiles and fluctuations with line-average density and divertor flux expansion in TCV. *Nuclear Fusion*, 57(11):116014, 2017.

[229] E. Viezzer, T. Pütterich, C. Angioni, A. Bergmann, R. Dux, E. Fable, R. M. McDermott, U. Stroth, E. Wolfrum, et al. Evidence for the neoclassical nature of the radial electric field in the edge transport barrier of ASDEX Upgrade. *Nuclear Fusion*, 54(1):012003, 2013.

[230] T. Vu, F. Felici, C. Galperti, M. Maraschek, A. Pau, N. Rispoli, O. Sauter, B. Sieglin, TCV Team, MST Team, et al. Integrated real-time supervisory management for off-normal-event handling and feedback control of tokamak plasmas. *IEEE Transactions on Nuclear Science*, 2021.

[231] F. Wagner, G. Becker, K. Behringer, D. Campbell, et al. Regime of improved confinement and high beta in neutral-beam-heated divertor discharges of the ASDEX tokamak. *Physical Review Letters*, 49(19):1408, 1982.

[232] F. Wagner and U. Stroth. Transport in toroidal devices-experimentalist's view. *Plasma Physics and Controlled Fusion*, 34(13):1803, 1992.

[233] D. N. Wakam and J. Erhel. Parallelism and robustness in GMRES with the Newton basis and the deflated restarting, 2011.

[234] N. R. Walkden, J. Harrison, S.A. Silburn, T. Farley, S. S. Henderson, A. Kirk, F. Militello, and A. Thornton. Quiescence near the X-point of MAST measured by high speed visible imaging. *Nuclear Fusion*, 57(12):126028, 2017.

[235] N. R. Walkden, B. Labit, H. Reimerdes, J. Harrison, T. Farley, P. Innocente, and F. Militello. Fluctuation characteristics of the TCV snowflake divertor measured with high speed visible imaging. *Plasma Physics and Controlled Fusion*, 60(11):115008, 2018.

[236] N. R. Walkden, F. Militello, J. Harrison, T. Farley, S. Silburn, and J. Young. Identification of intermittent transport in the scrape-off layer of MAST through high speed imaging. *Nuclear Materials and Energy*, 12:175, 2017.

[237] C. Wersal and P. Ricci. A first-principles self-consistent model of plasma turbulence and kinetic neutral dynamics in the tokamak scrape-off layer. *Nuclear Fusion*, 55(12):123014, 2015.

[238] J. Wesson and D. J. Campbell. *Tokamaks*, volume 149. Oxford University Press, 2011.

[239] J. A. Wesson, R. D. Gill, M. Hugon, F. C. Schüller, J. A. Snipes, et al. Disruptions in JET. *Nuclear Fusion*, 29(4):641, 1989.

[240] M. Wiesenberger, L. Einkemmer, M. Held, A. Gutierrez-Milla, X. Saez, and R. Iakymchuk. Reproducibility, accuracy and performance of the Feltor code and library on parallel computer architectures. *Computer Physics Communications*, 238:145, 2019.

[241] Wolfram Research, Inc. Mathematica, Version 12.2. Champaign, IL, 2020.

[242] A. Wynn, B. Lipschultz, I. Cziegler, J. Harrison, A. Jaervinen, G. F. Matthews, J. Schmitz, B. Tal, M. Brix, C. Guillemaut, et al. Investigation into the formation of the scrape-off layer density shoulder in JET ITER-like wall L-mode and H-mode plasmas. *Nuclear Fusion*, 58(5):056001, 2018.

[243] G. S. Xu, V. Naulin, W. Fundamenski, C. Hidalgo, J. A. Alonso, C. Silva, B. Goncalves, A. H. Nielsen, J. J. Rasmussen, S. I. Krasheninnikov, et al. Blob/-hole formation and zonal-flow generation in the edge plasma of the JET tokamak. *Nuclear Fusion*, 49(9):092002, 2009.

[244] G. Q. Yu and S. I. Krasheninnikov. Dynamics of blobs in scrape-off-layer/shadow regions of tokamaks and linear devices. *Physics of Plasmas*, 10(11):4413, 2003.

[245] G. Q. Yu, S. I. Krasheninnikov, and P. N. Guzdar. Two-dimensional modelling of blob dynamics in tokamak edge plasmas. *Physics of Plasmas*, 13(4):042508, 2006.

[246] P. N. Yushmanov, T. Takizuka, K. S. Riedel, O. J. W. F. Kardaun, J. G. Cordey, et al. Scalings for tokamak energy confinement. *Nuclear Fusion*, 30(10):1999, 1990.

[247] P. Zanca, F. Sattin, D. F. Escande, and JET Contributors. A power-balance model of the density limit in fusion plasmas: application to the L-mode tokamak. *Nuclear Fusion*, 59(12):126011, 2019.

[248] P. Zanca, F. Sattin, D. F. Escande, G. Pucella, and O. Tudisco. A unified model of density limit in fusion plasmas. *Nuclear Fusion*, 57(5):056010, 2017.

[249] A. Zeiler, J.F. Drake, and B. Rogers. Nonlinear reduced Braginskii equations with ion thermal dynamics in toroidal plasma. *Physics of Plasmas*, 4(6):2134, 1997.

[250] B. Zhu, M. Francisquez, and B. N. Rogers. Global 3D two-fluid simulations of the tokamak edge region: Turbulence, transport, profile evolution, and spontaneous E× B rotation. *Physics of Plasmas*, 24(5):055903, 2017.

[251] B. Zhu, M. Francisquez, and B. N. Rogers. GDB: A global 3D two-fluid model of plasma turbulence and transport in the tokamak edge. *Computer Physics Communications*, 232:46, 2018.

[252] H. Zohm, C. Angioni, E. Fable, G. Federici, et al. On the physics guidelines for a tokamak DEMO. *Nuclear Fusion*, 53(7):073019, 2013.

[253] H. Zohm, F. Militello, T. W. Morgan, W. Morris, H. Reimerdes, and M. Siccinio. The EU strategy for solving the DEMO exhaust problem. *Fusion Engineering and Design*, 166:112307, 2021.

Maurizio Giacomin

Curriculum Vitae

✉ *maurizio.giacomin@epfl.ch*
Birth Date: 12 July 1993

Education

11/2017–current	**Ph.D. in Physics**, École Polytechnique Fédérale de Lausanne (EPFL) - Swiss Plasma Center (SPC), Lausanne, Switzerland.
10/2015–09/2017	**Master degree in Physics**, Grade: 110/110 *cum laude* and two extra exams (6 ECTS each), Padua University, Department of Physics and Astronomy, Padua, Italy.
10/2012–07/2015	**Bachelor degree in Physics**, Grade: 110/110 *cum laude*, Padua University - Department of Physics and Astronomy, Padua, Italy.
09/2007–06/2012	**High school diploma**, Grade: 100/100 *cum laude*, Istituto Tecnico Industriale "A. Rossi", Vicenza, Italy.

Research Experiences

11/2017–present **Ph.D. candidate**, École Polytechnique Fédérale de Lausanne (EPFL) - Swiss Plasma Center (SPC), Lausanne, Switzerland, under supervision of Prof. Paolo Ricci.

- Thesis title: *Investigation of turbulent transport regimes in the plasma boundary of magnetic fusion devices.*
- Co-developer of the GBS code.

03/2017–08/2017 **Master thesis project**, Max-Planck-Institut für Plasmaphysik (IPP), Munich, Germany, under supervision of Prof. Ursel Fantz, Dr. Dirk Wünderlich and Dr. Gianluigi Serianni.

- Thesis title: *Application of collisional radiative models for atomic and molecular hydrogen to a negative ion source for fusion.*
- Main developer of the web application *Yacora on the Web*, `www.yacora.de`

03/2015–06/2015 **Bachelor thesis project**, Consorzio RFX, Padua, Italy, under supervision of Dr. Gianluigi Serianni and Dr. Piero Agostinetti.

- Thesis title: *Characterization of the extracted current density profile from calorimetric measurements in the BATMAN experiment.*

Teaching Experiences

Supervision of Master Thesis

- Riccardo Saura, Politecnico di Milano, 2021: *Turbulent regime evaluation in the tokamak shaped edge layer.*
- Louis Nicolas Stenger, EPFL, 2020: *Investigation of Plasma Turbulence and Flows in Snowflake Magnetic Configurations.*
- Adriano Stagni, Politecnico di Milano, 2020: *Investigation of the near and far SOL pressure and density fall-off lengths in L-mode diverted tokamak plasmas.*

Supervision of Semester Project

- Chiara Galletti, EPFL, 2020: *Investigation of the effect of plasma triangularity on turbulence at the tokamak boundary.*
- Matteo Nessi, EPFL, 2020: *Investigation of turbulence and flows in the plasma boundary with different divertor positions.*
- Matteo Nessi, EPFL, 2019: *Understanding the circulation pattern around the X-point in the snowflake magnetic configuration.*
- Louis Nicolas Stenger, EPFL, 2019: *Study of Plasma Turbulent Dynamics in the Tokamak Periphery in Presence of Snowflake Magnetic Geometry.*
- Louis Nicolas Stenger, EPFL, 2018: *Scrape-Off Layer Width Determination in a X-Point Diverted Geometry Using Plasma Particle Fluxes.*

Teaching Assistantship

- Nonlinear dynamics, chaos and complex systems, EPFL, 2018, 2019, 2020.
- General Physics II: thermodynamics, EPFL, 2020, 2021.
- General Physics IV: quantum mechanics, EPFL, 2018, 2019.

Awards

2017 **Master Thesis Prize**, *Prize awarded by the Consorzio RFX to the most outstanding master thesis in "Plasma Physics and Controlled Nuclear Fusion".*

2017 **FuseNet Scholarship**, *Financial support from FuseNet to spend 6 months at IPP working on the master thesis project on fusion.*

Publications

First author

- M. Giacomin, A. Pau, P. Ricci, *et al.* "Theory-based scaling of the density limit in tokamaks", submitted to **Physical Review Letters**.
- M. Giacomin, P. Ricci, G. Fourestey, D. Galassi, E. Lanti, D. Mancini, D. S. Oliveira, N.Richart, N. Varini, "The GBS code for turbulence simulation of the plasma boundary", submitted to **Journal of Computational Physics**.
- M. Giacomin, A. Stagni, P. Ricci, J. A. Boedo, J. Horacek, H. Reimerdes, C. K. Tsui, "Theory-based scaling laws of near and far scrape-off layer widths in single-null L-mode discharges", **Nuclear Fusion**, 61, 076002 (2021).
- M. Giacomin and P. Ricci, "Investigation of turbulent transport regimes in the tokamak edge by using two-fluid simulations", **Journal of Plasma Physics** 86.5 (2020).

- M. Giacomin, L. N. Stenger, P. Ricci, "Turbulence and flows in the plasma boundary of snowflake magnetic configurations", **Nuclear Fusion** 60.2, 024001 (2020).

Co-author

- D. Mancini, P. Ricci, N. Vianello, M. Giacomin, A. Coroado, "Investigation of the density shoulder formation by using self-consistent simulations of plasma turbulence and neutral kinetic dynamics", **Nuclear Fusion**, 61.12, 126029 (2021).
- D. Galassi, C. Theiler, T. Body, F. Manke, *et al.*, "Turbulence dynamics around the X-point in TORPEX and comparison with multi-code 3D flux-driven simulations", accepted for publication in **Physics of Plasmas (2021)**.
- D. S. Oliveira, T. Body, D. Galassi, C. Theiler, *et al.*, "Validation of edge turbulence codes against the TCV-X21 diverted L-mode reference case", submitted to **Nuclear Fusion**.
- A. M. Stefanini, G. Montagnoli, M. D'Andrea, M. Giacomin, *et al.*, "New insights into sub-barrier fusion of ^{28}Si + ^{100}Mo", **Journal of Physics G: Nuclear and Particle Physics**, 48 055101 (2021).
- D. Wünderlich, M. Giacomin, R. Ritz, U. Fantz, "Yacora on the Web: Online collisional radiative models for plasmas containing H, H_2 or He", **Journal of Quantitative Spectroscopy and Radiative Transfer**, 240, 106695 (2020).
- P. Agostinetti, M. Giacomin, G. Serianni, P. Veltri, F. Bonomo, L. Schiesko, "Preliminary results concerning the simulation of beam profiles from extracted ion current distributions for mini-STRIKE", **Review of Scientific Instruments** 87.2 (2016).

Conference Contributions and Invited Talks

11/2021 **63rd Annual Meeting of the APS Division of Plasma Physics**, *Theoretical interpretation of the operational density limit based on edge turbulent transport*, Pittsburgh, Pennsylvania, `Invited talk`.

09/2021 **Plasma Edge Theory Workshop - 2021**, *Theory-based scaling laws of the near scrape-off layer width in L-mode discharges and density limit crossing, including comparison with experiments*, Lausanne, Switzerland, `Oral contribution`.

09/2021 **Virtual 25th Joint EU-US Transport Task Force Meeting**, *Theory-based scaling laws of the near scrape-off layer width in L-mode discharges and density limit crossing, including comparison with experiments*, York, United Kingdom, `Oral contribution`.

07/2021 **30th ITPA Scrape-Off-Layer and Divertor Topical Group workshop**, *Theory-based scaling laws of the near and far scrape-off layer widths in L-mode discharges*, Virtual, `Oral contribution`.

10/2020 **Joint Varenna-Lausanne International Workshop**, *Turbulence and flows in the plasma boundary of snowflake magnetic configurations*, Lausanne, Switzerland, `Invited talk`.

10/2019 **18th European Fusion Theory Conference**, *Properties of plasma turbulence in the periphery of diverted tokamaks*, Ghent, Belgium, `Oral contribution`.

08/2018 **Swiss Physics Society Annual Meeting**, *Turbulence simulations in diverted geometry*, Lausanne, Switzerland, `Poster`.

Skills

- **Teaching and mentoring:** Undergraduate teaching experience and supervision of many undergraduate students.
- **Software:** Matlab, Python, Mathematica, MS Office.
- **Programming languages:** Fortran, MPI, Latex, C++, CUDA.
- **High Performance Computing:** Experience on large scale supercomputers.

Languages

○ **Italian**	Native speaker
○ **English**	Fluent
○ **French**	Fluent
○ **German**	Basic